UNIVERSITY OF SOUTHAMPTON

Synthesis and Structural Characterisation of Mixed-Metal Oxide Pigment Systems

A thesis submitted for the degree of
Doctor of Philosophy

by

C. Owens

School of Chemistry
Faculty of Science, Engineering and Mathematics
Southampton

September 2004

UNIVERSITY OF SOUTHAMPTON

ABSTRACT

FACULTY OF SCIENCE, ENGINEERING AND MATHEMATICS
SCHOOL OF CHEMISTRY

Doctor of Philosophy

Synthesis and Structural Characterisation of Mixed-Metal Oxide Pigment Systems

by Craig Owens

The synthesis and characterisation of the $NaCaV_{1-x}Mn_xO_4$ (x = 0, 0.02, 0.04, 0.06, 0.08 and 1.0) system has been carried out. Structural characterisation was performed through the use of powder X-ray diffraction, powder neutron diffraction and UV-Visible spectroscopy. These techniques reveal that the MnO_4^{3-} complex ion can be stabilised within the $NaCaVO_4$ structure by isotopic substitution of the VO_4^{3-} unit. The MnO_4^{3-} ion imparts it own coordination geometry upon the host lattice, with the effect of making the MO_4^{3-} a more regular coordination environment. The limit of substitution occurs at x = 0.08. Degradation of the colour over time makes this system unsuitable for use as a pigment.

The preparation of the solid solution $Cu_2Al_{1-x}Ga_x{}^{11}BO_5$ (x = 0, 0.2, 0.4, 0.6, 0.8, 1.0) has been successfully completed with colours ranging from dark intense green to a lighter olive green. Structural characterisation has utilised powder neutron diffraction and CIELab colour measurements. The replacement of Al^{3+} with Ga^{3+} enlarges the average metal-oxygen distances, which in turn alters the copper coordination and hence the observed colour. $Cu_2Al_6{}^{11}B_4O_{17}$ has been prepared by conventional solid-state methods and has been structurally characterised using powder neutron diffraction.

The crystal structure of cobalt pyroborate ($Co_2B_2O_5$) has been further refined using powder neutron diffraction.The structure of $Co_{2.45}BO_5$ has been determined from a single crystal X-ray refinement and is shown to adopt the Ludwigite structure. The structure contains four distorted octahedral CoO_6 environments and planar BO_3 units.

Twelve materials in the $(Co, Zn, Mg)_2TiO_4$ inverse spinel system have been prepared and structurally characterised using powder neutron diffraction and combined EXAFS/PND refinements. Reverse Monte Carlo simulations indicate that Ti^{4+} occupies a distorted '5+1' octahedral environment with one Ti-O bond *ca.* 0.4 Å longer than the remaining five and have also been used to solve the cation distribution for the quaternary system $Co_{0.8}Mg_{0.6}Zn_{0.6}TiO_4$.

The preparation of the $Co_{1-x}Al_2O_4$ (x = 0, 0.1, 0.2, 0.3) series from CoO and Al_2O_3 using conventional solid state synthesis results in the formation of sub-stoichiometric compounds with scrambling of the cations over the tetrahedral and octahedral sites. The observed darkening of the colour occurs due to octahedrally coordinated Co^{3+}, which leads to mixed-valence charge transfer transitions.

Table of Contents

PREFACE

Table of Contents

CHAPTER 2: EXPERIMENTAL TECHNIQUES

Acknowledgements

I would like to thank Professor Mark Weller for his advice and support throughout the preparation of this thesis. Thanks also go to Norman Binsted for his continued commitment to assisting me with the production of the EXAFS data.

I would also like to thank the members of the Weller Research Group both past and present, including; Jon Reading (for helping me get to grips with all things solid state), Bob Hughes (for proof-reading this work, I'll never forget that leather blouson), Nicola Kenyon, Dr Andrew Hector and Paul Vincent (for your company on the many trips to Daresbury) and Matt Oliver (for a great weekend in Prague). To the rest of you in the group who didn't get a mention, sorry, my mind isn't what it used to be – but thanks anyway!

Thanks also to my parents who have been extremely understanding and helpful throughout. Finally, to Joanne, without her constant encouragement and support this thesis might never have been completed and to Joshua Rhys who has been such an inspiration.

Abbreviations

EXAFS	Extended X-ray Absorption Fine Structure
FT	Fourier Transform
HRPXD	High Resolution Power X-ray Diffraction
IR	Infra-red
PND	Powder Neutron Diffraction
PXD	Powder X-ray Diffraction
TOF	Time of Flight
UV-Vis	Ultra-violet – visible

Dedication

To my family.

Chapter 1

Introduction

1 Introduction

1.1 Inorganic Pigments

Inorganic pigments account for around 96% of all the pigments synthesised world-wide. They therefore form a very important class of inorganic materials with applications ranging from ceramics and building materials, to artist's colours and cosmetics. Total world production, of white, black and coloured pigments reached 5.7 million tons in 1999, with titanium dioxide accounting for around 68% of the total [1] and the world market value for coloured pigments (inorganic and organic) was estimated at $7.5 billion.

There are many different types of coloured inorganic pigments. Some are based on transition metal oxides such as transition metal doped rutile [2]. Others are based on charge transfer compounds such as cadmium sulphide. Recently, there has been an increased effort to find new inorganic pigments, suitable for production on an industrial scale. This increase has for the most part, been brought about by new health and safety restrictions on the use of heavy metals, in particular cadmium, lead and chromium. New less toxic, inorganic pigments such as those based on cerium have recently begun commercial production [3].

1.1.1 Definition

A pigment is a coloured, black, white or fluorescent particulate organic or inorganic solid, which is usually insoluble in and essentially physically and chemically unaffected by, the vehicle or substrate into which it is incorporated. A pigment will alter appearance by selective absorption and/or scattering of light. The pigment is usually dispersed in a vehicle for application in, for example, the manufacture of paints, plastics or other polymeric materials and inks. The pigment will retain its own unique crystalline or particulate structure throughout the incorporation period [4].

1.1.2 Pigment Classification [4]

The many different types and classes of pigments can be grouped together into five categories as shown in the table below.

Table 1-1: Classification of pigments

Type	*Definition*
White	Optical effect caused by non-selective light scattering (e.g. TiO_2)
Coloured	Optical effect caused by selective light absorption and selective light scattering (e.g. Fe oxides and Cd, Cr, Co pigments)
Black	Optical effect caused by non-selective light absorption (e.g. Carbon black, Fe oxide black)
Lustre	Optical effect caused by regular reflection or interference (e.g. Al flakes)
Luminescent	Optical effect caused by capacity to absorb radiation and emit it as light of longer wavelength (e.g. Ag doped ZnS (fluorescent), Cu doped ZnS)

1.2 Coloured Pigments

Some of the most common coloured inorganic pigments are discussed below.

1.2.1 Iron Oxide Pigments

Naturally occurring iron oxides and iron oxide hydroxides were used as pigments in prehistoric times [5]. The Egyptians, Greeks and Romans also used them as colouring materials.

Natural iron oxide pigments are based around Fe_2O_3; examples include hematite (α-Fe_2O_3), a red pigment and goethite (α-FeOOH), a yellow pigment. These pigments, along with synthetic iron oxide pigments, provide a wide variety of colours ranging from yellow, red and orange to browns and black. The importance of these pigments is based on their high chemical and thermal stability, non-toxicity and low price. Applications include coatings, artists' materials, rubber and plastics.

Pigment manufacturer Ferro, produces the pigments PK 1095 [6] and PK 3080 [7], which are based on the composition $(Fe,Cr)_2O_3$, and are brown and black respectively.

Iron oxide pigments are not considered to be toxic and this is reflected in their use as colorants for food and pharmaceutical products.

1.2.2 Mixed Metal Oxide Pigments

The colour of these pigments arises through the incorporation of certain transition metal cations into a stable oxide lattice. The ions that are of interest for pigmentation are those which are themselves coloured [8, 9], colouration is a result of partially filled d or f shells, permitting transitions between levels within those shells, with the absorption of energy at

optical frequencies. The most common colouring ions are those of the first transition series V, Cr, Mn, Fe, Co, Ni and Cu.

These materials can be described as solid solutions, whereby two, or more, substances with the same basic formula and crystal structure can form a stable, homogenous material. The spinel, hematite and rutile type oxide lattices are of great value as mixed metal oxide pigments due to their good chemical and thermal stability.

Examples of mixed metal oxide pigments include *Nickel rutile yellow,* a light yellow pigment with the composition $(Ti_{0.85}Sb_{0.10}Ni_{0.05})O_2$, and *Spinel Black*, which has the composition $CuFe_{0.5}Cr_{1.5}O_4$.

The excellent stability of oxide materials allows these pigments to be used for applications where resistance to chemicals and weathering is important; examples include exterior paints and masonry coatings. The stability of these pigments renders them relatively inert and toxicological investigations [10, 11] for some spinel and rutile-based pigments have shown that despite the presence of a heavy metal component the pigments can be classified as non-toxic.

1.2.3 Cadmium Pigments

After discovering the element in 1817 Friedrich Stromeyer suggested the use of cadmium as an artists' pigment and although cadmium based pigments were not commercially available until around 1840 the colours of cadmium compounds were being used to decorate ceramics by 1830.

Cadmium pigments give excellent red and yellow colours and are also very durable. They are used mainly in the plastics industry but also play an important role in the colouring of enamels, ceramic glazes and glass. Cadmium pigments are usually based around cadmium sulphide/selenide mixed with mercury and zinc sulphides.

Although the solubility of these pigments is low, small amounts of cadmium will dissolve in dilute hydrochloric acid (stomach acid), which will cause it to build up within the body. Despite this cadmium pigments are not classified as toxic (except pure CdS). However, many are classified as 'suspect carcinogens' [12, 13]. Therefore, their use is becoming increasingly restricted due to the associated health risks during both their manufacture and in some of their applications.

1.2.4 Chromate Pigments

In the early nineteenth century the French chemist Nicolas-Louis Vauquelin investigated Crocoite (Siberian red lead) a bright red mineral and discovered that it contained a new metallic element that formed brightly coloured compounds. For this reason he proposed the

name *Chrome.* Crocoite is the mineral form of lead chromate, which when prepared synthetically has a bright yellow colour.

Chromate pigments produce colours ranging from light yellows to oranges and reds. Examples include chrome yellow (lead chromate) [14], molybdate orange and molybdate red which are mixed phase pigments of general formula $Pb(Cr,Mo,S)O_4$. Due to their low cost they have applications in many areas, including paints, plastics and road markings. However, as with cadmium pigments, the use of lead and chromate pigments in certain applications is becoming more restricted, especially in food packaging and children's toys. Indeed an EU directive (94/62/EC) bans, since 30 June 2001, any and all packaging which contains heavy metal concentrations exceeding 100 parts per million (ppm). The heavy metals are named as lead, cadmium, mercury and chromium(VI).

1.2.5 Ultramarine Pigments

Natural blue ultramarine is derived from *lapis lazuli*, a semiprecious stone and was used as a pigment by artists in the Middle Ages. However, natural ultramarine was expensive, so in 1824 the French Society for Encouragement of National Industry offered a prize for the first practical synthetic route to ultramarine. Synthetic ultramarines were first produced in 1828 by Guimet [15] and Gmelin [16] and are currently commercially available in three colours: - blue, violet and pink.

Ultramarine pigments consist of an aluminosilicate lattice, with the sodalite structure and trapped within the lattice are sodium ions and sulphur free radicals that are stabilised due their entrapment. Unlike the previous pigments mentioned, the colour of ultramarine pigments is due the sulphur free radicals rather than the presence of any transition metals. These pigments are considered to be safe during both manufacture and use, and have good stability. They therefore have a wide range of applications including plastics, printing inks, detergents [17] and cosmetics.

1.3 Origin of Colour

Colour has several different origins and it is knowledge of exactly what causes the colours in certain systems which allows us to design compounds which specifically favour the generation of desired colours. For example, placing cobalt in a tetrahedral environment is often known to cause blue colouration. Colour is normally perceived where a particular system absorbs certain wavelengths of visible light and reflects the unaffected wavelengths back to the eye. Most absorption occurs in coloured systems by the incident wavelengths being of the same energy as an electronic transition within the structure. As energy levels are quantised there are only certain transitions allowed within a given structure. Knowledge of the types of transitions and the effect that a perturbation in the structure can have on these transitions gives us some amount of control over the colour of the compounds.

1.3.1 Types of electronic transitions

Colour in inorganic materials is often associated with the presence of one or more transition metal species. In such materials the colour can normally be described by the absorption of visible light by d-d transitions and/or charge transfer processes.

1.3.1.1 d-d transitions

The colours of transition metal complexes can usually be ascribed to the presence of d-electrons in conjunction with a ligand(s). An octahedrally coordinating ligand splits the d-orbitals of the central metal atom into two sets called the e_g and t_{2g} sets. The energy separation of the sets (Δ_{Oct}) is small and the excitation $e_g \leftarrow t_{2g}$ typically occurs in the visible region of the spectrum. Other metal-ligand co-ordination arrangements occur, such as square planar or tetrahedral, giving rise to different splitting of the d-orbitals and hence different colours. The presence of alternative ligands or a different metal centre will also affect the splitting and hence the observed colour.

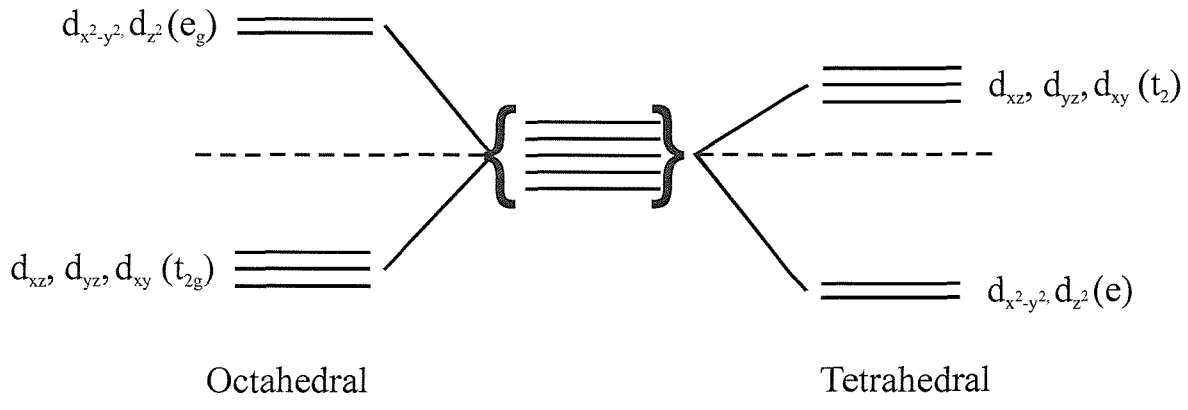

Figure 1-1. Octahedral and tetrahedral splitting of d orbitals

A problem arises in that d-d transitions are formally forbidden in octahedral complexes. The Laporte selection rule [18] for centrosymmetric complexes states that the only allowed transitions are those accompanied by a change in parity. That is, u ↔ g and g ↔ u transitions are allowed but g ↔ g and u ↔ u transitions are forbidden. $e_g \leftrightarrow t_{2g}$ transitions are only permitted when the symmetry of the molecule is reduced by a vibration or a distortion from a perfect octahedron (thus removing the centre of symmetry).

In the case of the tetrahedral arrangement the xy, xz and yz orbitals interact more strongly with the ligand electrons than the z^2 and (x^2-y^2) ligands so the energy level diagrams are inverted from the octahedral case, with a splitting energy of Δ_t. As transitions within the tetrahedral system (with no centre of symmetry) are Laporte allowed, these transitions are correspondingly more intense and tend to dominate the electronic spectrum relative to the octahedral transitions.

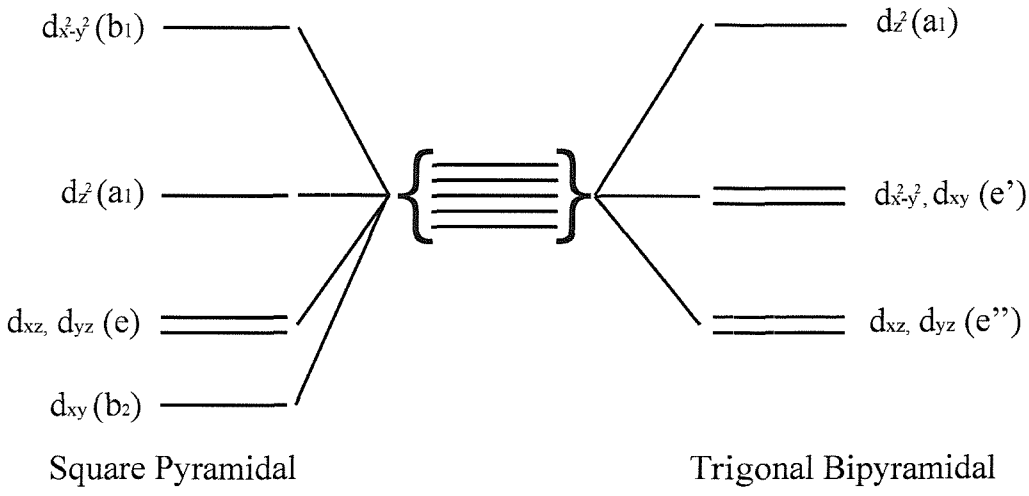

Figure 1-2. Square planar and trigonal bipyramidal splitting of d orbitals

In the case of the regular five coordinate species, square pyramidal and trigonal bipyramidal, there are several splitting parameters which depend on the metal-ligand distance and the ligand-metal-ligand bond angles that are not fixed by symmetry. No unique diagram therefore exists, however the diagram above shows the important features.

Each different geometry and related splitting parameters are therefore of great interest in this study, as for a given transition metal the electronic transitions will give different colours. It is also evident that changing both the metal and the ligands and introducing distortions into the system will allow us to control the colour of the final compound.

1.3.1.2 Intensity of electronic transitions

The intensity of the absorptions observed are governed by the following selection rules.

- $\Delta S = 0$ *Spin selection rule*
- $\Delta L = \pm 1$ and if the molecule is centrosymmetric, $g \leftrightarrow u$ *Laporte selection rule.*
- Product of symmetry of ground and excited states corresponds to x, y and z in the character tables. *Symmetry selection rule.*

Examples of these transitions are shown below

Table 1-2. Electronic transitions

Band Type	*Absorption Intensity* ε *- extinction coefficient*	*Type of Transition*
Spin forbidden	$\varepsilon < 1$	d-d (Mn^{2+}, d^5)
Laporte forbidden	$\varepsilon = 20$ -100	d-d (O_h)
Laporte allowed	ε = ca. 250	d-d (T_d)
Fully symmetry allowed	$\varepsilon = 1000$ - 5000	charge transfer

The values for extinction coefficient given above are approximate and based on solution UV data. For solid state UV analysis, calculation of the extinction coefficient cannot be carried out easily as the concentration of a solid sample is difficult to quantify accurately. However, from the relative sizes of the values given it is evident that simple qualitative analysis can be carried out to assign the general transition types to solid state UV data.

1.3.1.3 Charge transfer transitions

Colour in some inorganic solids arises from the absorption of light as a result of the promotion of an electron from a localised orbital on one atom to a higher energy, but still localised, orbital on an adjacent atom. Processes of this type are known as a *charge transfer transitions* which are, according to spectroscopic selection rules, 'allowed transitions', therefore the corresponding absorption bands are intense. Chromate pigments owe their intense yellow colour to the transfer of an electron from an oxygen atom to the central chromium atom in the tetrahedral complex anion $(CrO_4)^{2-}$, this is known as a *ligand to metal charge transfer (LMCT).* Another type of charge transfer is a *metal to ligand charge transfer (MLCT)*, which is responsible for the red colour observed in tris(bipyridyl)iron(II) [19].

1.3.1.4 Mixed valence transitions

Compounds, containing elements in more than one oxidation state, are called mixed valence compounds. Many of these are coloured due to transitions between these two differing oxidation states. A good example is Prussian Blue ($KFe[Fe(CN)_6]$) [20]. This contains Fe in both II and III oxidation states. The iron species is bonded to the carbon atom of the CN ligand and the adjacent iron species is linked to the nitrogen atom of the same ligand. This creates a three dimensional network of alternating FeC_6 and FeN_6 octahedra.

The colour arises from a small amount of a charge transfer state being mixed in with the ground state wavefunction of the ligand. The delocalisation and mixing of the ground and charge transfer states will therefore be much more favourable for small energy differences between ground and excited states and if the Fe (II) and Fe (III) sites are adjacent and overlap strongly or are bridged by a covalent ligand (CN).

1.3.1.5 π,π^* and π^*,π transitions

Although of no direct relevance to this project it is worth noting that the colour in organic systems has a similar origin. In this case absorption promotes a π electron into an antibonding π^* orbital. The energy of this transition is *ca.* 7 eV which corresponds to an absorption at 180 nm. As the level of conjugation in a system increases the absorption shifts into the visible and hence the higher the level of conjugation the darker the colour.

1.4 Perception of Colour

We perceive colour by means of cones in the retina. There are three types of cones sensitive to wavelengths that approximately correspond to red, green and blue lights. Together with information from rod cells (which are not sensitive to colour merely differences in light and dark) the cone information is encoded and sent to higher brain centres along the optic nerve. The encoding, known as opponent process theory [21], consists of three opponent channels, these are:

- Red-Green
- Blue-Yellow
- Black-White

The fact that these signals are opposing is the reason why it is not possible to perceive green shades of red or yellow shades of blue. However, you can see red and green shades of blue and yellow.

For human colour description purposes the following terms have been defined by the Commission Internationale de l'Eclairages (CIE).

Brightness.

"*The attribute of visual sensation according to which, an area appears to exhibit more or less light. (An image may be blurred or enhanced by modification of this attribute.)*"

Hue.

"*The attribute of a visual sensation according to which an area appears to be similar to one, or to proportions of two, of the perceived colours red, yellow, green and blue.*"

Colourfulness.

"*The attribute of visual sensation, according to which an area appears to exhibit, more or less of its hue. (Sky blue is transformed to a deep blue by changing this attribute.)*"

1.5 Quantification of Colour

It is important to be able quantify the colour produced by a pigment for comparison purposes. The colour of the pigment is greatly influenced by the medium in which the pigment is incorporated. So for a pigment of given particle size one could obtain different colour measurements from different media. Common media include linseed oil, PVA glue, varnish and high impact polystyrene. There are many systems for representing colour and these are called colour spaces.

1.5.1 Colour spaces

A colour space is a method by which we can specify, create and visualise colour. As humans, we may define a colour by its attributes of brightness, hue and colourfulness. A computer will define a colour in terms of the excitations of red, green and blue phosphors on the CRT screen. A printing press defines a colour in terms of the reflectance and absorbance of cyan, magenta, yellow and black inks on the paper. In effect a colour space is a mathematical representation of our perceptions.

If we imagine that each of the three attributes used to describe a colour are axes in a 3-dimensional space then this defines a colour space. The colours that we can perceive can be represented by the CIE system, other colour spaces are subsets of this perceptual space. For instance RGB colour space, as used by television displays, can be visualised as a cube with red, green and blue axes. This cube lies within our perceptual space, since the RGB space is smaller and represents fewer colours than we can see. The CMY space would be represented by a second cube, with a different orientation and a different position, within the perceptual space.

Different colour spaces are better for different applications; some equipment has limiting factors that dictate the size and type of colour space that can be used. Some colour spaces are perceptually linear, i.e. a 10 unit change in stimulus will produce the same change in perception wherever it is applied. Many colour spaces, particularly in computer graphics, are not linear in this way. Some colour spaces are intuitive to use, *i.e.* it is easy for the user to navigate within them and creating desired colours is relatively easy.

1.5.1.1 RGB, CMY, and CMYK

The most popular colour spaces are RGB (Red/Green/Blue) and CMY (Cyan/Magenta/Yellow) and are used in monitors and printers respectively.

RGB are known as additive primary colours because, a colour is produced by *adding* different quantities of the three components, red, green, and blue. CMY are known as subtractive (or secondary) colours, because the colour is generated by *subtracting* different quantities of cyan, magenta and yellow from white light.

The primaries used by artists, cyan, magenta and yellow, are different from the primaries of computer devices because they are concerned with mixing pigments rather than lights or dyes.

Table 1-3. Interconversion between RGB and CMY colour spaces

RGB → CMY	*CMY → RGB*
Red = 1-Cyan (0←Cyan←1)	Cyan = 1-Red (0←Red←1)
Green = 1-Magenta (0←Magenta←1)	Magenta = 1-Green (0←Green←1)
Blue = 1-Yellow (0←Yellow←1)	Yellow = 1-Blue (0←Blue←1)

On printer devices, a component of black is added to the CMY, and the second colour space is then called CMYK (Cyan/Magenta/Yellow/blacK). This component is actually used because cyan, magenta, and yellow set to the maximum should produce a black colour. (The RGB components of the white are completely subtracted from the CMY components.) but the resulting colour is not physically a 'true' black.

1.5.1.2 CIELAB/CIELUV

Two, three-dimensional colour spaces were recommended by the CIE in 1976 [22]. The CIE 1976 L*u*v* or CIELUV colour space is a linear transform of the x, y chromaticity co-ordinates and hence it is often used in applications involving additive colour mixing, such as television. The CIE 1976 L*a*b* or CIELAB system, like CIELUV, was designed to provide approximate perceptual uniformity which makes them suitable for expressing differences in colour. It has applications dealing with subtractive colourant mixtures such as those found in the textile, plastic, paint, and printing industries. It is possible to derive hue and chroma (colourfulness) attributes from a*, b* by converting the rectangular a*, b* axes into polar coordinates.

1.6 Common Inorganic Pigment Structures

Inorganic pigments are chemically very stable. Oxide pigments, for example, can even have a protective effect on the substrate to which the pigment is being applied [23]. The stability and chemical resistance of these compounds is often due to their mineral-like structures; two of the most common inorganic pigment structures are the *spinel* and *rutile* oxide lattices.

1.6.1 Spinel

The crystal structure of spinel pigments, which owe their name to the naturally occurring mineral magnesium aluminate ($MgAl_2O_4$), is based around a cubic close packed arrangement of oxygen ions.

In the unit cell, which contains 32 oxygen atoms, 1/8 of the possible 64 tetrahedral sites are occupied by magnesium ions (in the $MgAl_2O_4$ example) and 1/2 of the possible 32 octahedral sites are occupied by aluminium ions. Magnesium aluminate itself is colourless, but colour can be introduced by replacing the 'colourless ions' (Mg^{2+}, Al^{3+}) with 'coloured' ones, such as cobalt, chromium, nickel, titanium, copper, iron, etc. One of the oldest and most well known synthetic pigments is Cobalt Blue ($CoAl_2O_4$), a cobalt-aluminium spinel.

An inverse spinel structure also exists, where by one type of metal ion occupies the tetrahedral and half of the octahedral sites in the lattice, and the remaining octahedral sites are occupied by the other cation. Examples include Zn_2TiO_4, alternatively this can be written $[Zn]^{tet}[ZnTi]^{oct}O_4$, thus indicating that the zinc ions occupy both tetrahedral and octahedral sites. Usually the two types of cations (Zn and Ti in this case) are disordered over the octahedral sites.

The structures of the normal and inverse spinels, as described here, are ideal limiting structures and in practice the structure obtained is often a mixture of the two, where the cation distribution over the tetrahedral and octahedral sites appears to be random, for example $[Co_{0.06}Ge_{0.94}]^{tet}[Co_{1.94}Ge_{0.06}]^{oct}O_4$ [24]. However, a number of factors influence the cation distribution including cation size, oxidation state and ligand field stabilisation energies. The cation distribution within binary spinel oxides, of general formula $M^{2+}M^{3+}{}_2O_4$ and $M^{4+}M^{2+}{}_2O_4$, has been studied in detail [25,26,27,28].

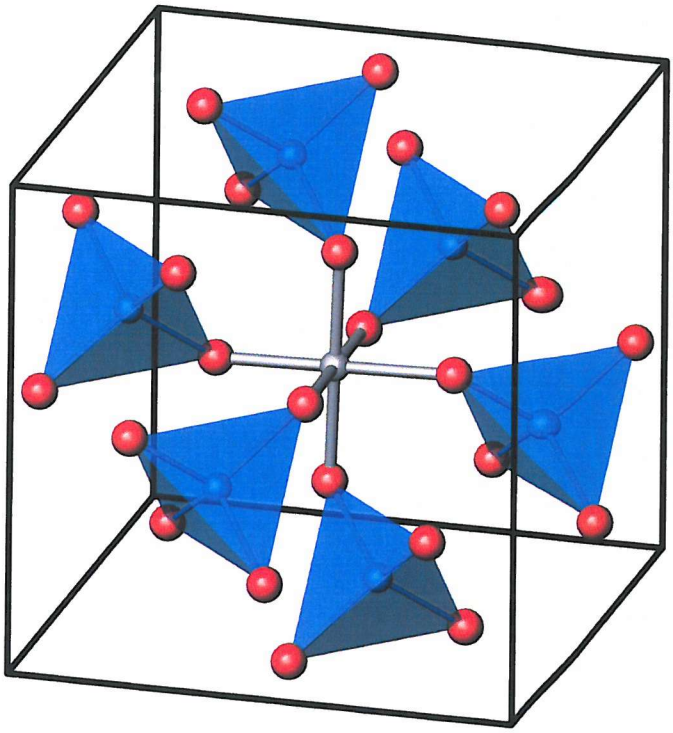

Figure 1-3: A view of the Spinel structure showing the tetrahedral sites (blue) surrounding an octahedral site (grey). Oxygen atoms are shown as red spheres.

There are a large number of commercially available spinel pigments, making it the most common structure found in inorganic pigments. A few examples are shown in the table below

Table 1-4: Some inorganic pigments with the spinel structure.

Composition	Manufacturer	Colour
$CoCr_2O_4$	Ferro	Turquoise
$(Co,Ni,Zn)_2(Ti,Al)O_4$	Bayer	Green
Co_2TiO_4	Ferro	Green
$Co(Al,Cr)_2O_4$	Bayer	Blue/Green
$CoAl_2O_4$	Bayer	Blue
$(Zn,Fe)Fe_2O_4$	Ferro	Brown
$Cu(Cr,Fe)_2O_4$	Bayer	Black
$(Fe,Mn)(Fe,Mn)_2O_4$	Ferro	Black

1.6.2 Rutile

Rutile pigments as with spinel pigments, are based on and owe their name to, a naturally occurring mineral, TiO_2 (rutile) which crystallises in the tetragonal system. In the rutile lattice titanium ions are surrounded by six neighbouring oxygen atoms, forming a slightly distorted octahedron. F. Hund [29] showed that by substituting the titanium ions for

transition metal ions, coloured pigments can be obtained. An example of a rutile pigment is the light yellow colour obtained when the titanium is partially substituted for a mixture of antimony and nickel, such that the composition becomes $(Ti_{0.85}Sb_{0.10}Ni_{0.05})O_2$.

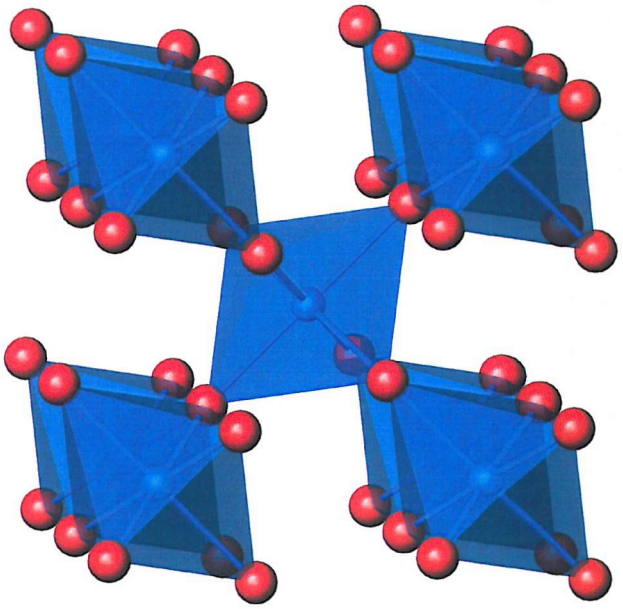

Figure 1-4: A view of the Rutile structure (Ti shown in blue, O shown in red).

Commercially available rutile pigments are generally yellow to brown in colour. Examples include $(Ti_{0.8}Ni_{0.05}Sb_{0.15})O_2$, a light yellow pigment produced by Bayer, and (Ti, Mn, Sb)O_2 a brown pigment produced by Ferro.

1.6.3 Framework Structures

Another approach to the production of pigments is to synthesise an inert, colourless framework structure containing a chromophore. This can be achieved by *in situ* encapsulation of the chromophore at the time of synthesis or by post synthesis modification of the framework or the encapsulated species. An example of a framework pigment is Ultramarine Blue. Ultramarine ($Na_8[AlSiO_4]_6S_2, S_3^-$) pigments consist of an aluminosilicate lattice, with the sodalite structure and trapped within the lattice are sodium ions and sulphur free radicals that are stabilised due their entrapment. In the case of *Ultramarine Blue*, the intense blue colouration is due to the S_3^- and S_2^- species encapsulated within the sodalite cage. Other anions such as the permanganate ion (MnO_4^-) can also be incorporated into the sodalite structure resulting in a deep violet colour.

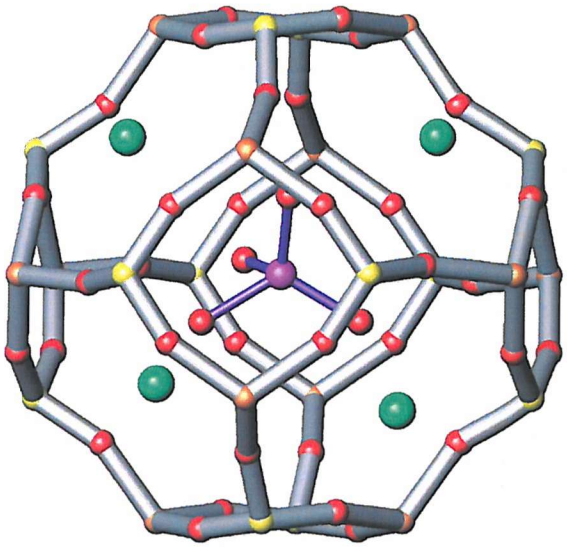

Figure 1-5: Permanganate sodalite. Aluminium and silicon atoms are shown in yellow and orange, oxygen atoms in red, sodium atoms in green and manganese is shown in purple.

A different approach is to prepare a framework that is itself coloured. This can be realised by inserting transition metals into the zeolite framework. Examples include $CsCoPO_4$ [30], which has an intense deep blue colour, and $RbCuPO_4$ [31], which has a sky blue colour.

1.7 Borate Chemistry

Boron, although a Group III element, bears a strong resemblance to Group IV silicon, in terms of its chemistry. It is a rare element, only found in about 3ppm in the earth's crust and is never found freely in nature. Most often it can be found as boron oxide, B_2O_3 [32]. In metal borates, boron can bond to either three or four oxygen atoms to give a trigonal planar or tetrahedral unit, respectively. In a similar manner to the metal silicates, it is the number of different ways these units can link, which leads to the complexity of borate structures [32]. Borates are extremely stable systems – both chemically and thermally – and, as such, would be ideal for use as pigments [33].

1.7.1 Orthoborates

The simplest metal borate structure is that of the orthoborates, such as the rare-earth orthoborates and the mineral $Mg_3(BO_3)_2$. These contain discrete, planar, triangular BO_3^{3-} units [34]. Structurally, the simplest orthoborates are those of empirical formula $M^{III}BO_3$, such as $FeBO_3$ [37].

1.7.2 Pyroborates

Complexes such as $M_2B_2O_5$ (where M = Fe^{2+}, Co^{2+} or Mg^{2+}) contain the finite $B_2O_5^{4-}$ ion, which is made up from two of the basic borate triangles sharing one oxygen each [34].

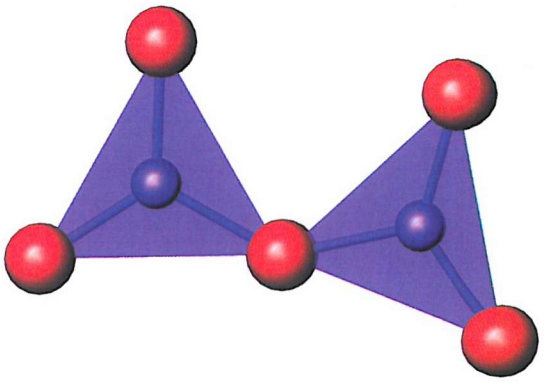

Figure 1-6: $B_2O_5^{4-}$ unit found in pyroborates

1.7.3 Metaborates

The metaborates arise from the linking of two oxygen atoms of the basic BO_3^{3-} unit. This can give rise to either infinite chains of empirical formula $(BO_2)_n^{n-}$ or finite ring structures of the same empirical formula, the simplest of these being $B_3O_6^{3-}$. $NaBO_2$ and KBO_2 both contain the cyclic units, therefore the correct empirical formulae should be $Na_3B_3O_6$ and

$K_3B_3O_6$ respectively – whereas $Ca(BO_2)_2$ incorporates the infinite chains within its structure [34, 35].

1.7.4 Other More Complex Borate Structures

As well as binding to three oxygen atoms, boron can also bind to a fourth oxygen to form a tetrahedron. This binding to a fourth oxygen arises due to the subsequent completion of the octet of valence electrons, thus forming a very stable arrangement [32]. There are many structures involving tetrahedral borate units, again the differences between these structures arising from the different number of oxygen atoms shared in each case. An example of a compound containing only tetrahedrally co-ordinated boron is Fe_3BO_6 [36].

1.8 Phosphate Chemistry

The transition metal phosphates form a large group of coloured compounds similar to the transition metal silicates. Indeed, the structural chemistry of phosphates has much in common with that of silicates [37]. Just as SiO_4 tetrahedra link together to form $Si_2O_7^{6-}$ ions, ring and chain ions of composition $(SiO_3)_n$ in the metasilicates, layers, and infinite 3-dimensional complexes, so PO_4 tetrahedra can link up to form pyro- and meta- phosphate ions and also the $P_3O_{10}^{5-}$ ion. Any arrangement where every PO_4 group shares three of its oxygen atoms with other PO_4 groups is necessarily electrically neutral; layer structures comparable with those of the silicates are therefore not possible.

1.8.1 Orthophosphates

Discrete PO_4^{3-} ions exist in normal orthophosphates, acid phosphates such as KH_2PO_4 where they are held together by hydrogen bonds as well as positive ions and in orthophosphoric acid itself. The structures of a number of orthophosphates, particularly those of the Group III elements, illustrate the similarity of the oxygen chemistry of phosphorus to that of silicon.

Table 1-5. Some phosphate materials and related silicate counterparts.

Phosphates	*Silicates with similar or related structures*
BPO_4, $(BAsO_4)$	β-cristobalite, SiO_2
$AlPO_4$, $(AlAsO_4)$	Quartz, SiO_2
YPO_4, $(YAsO_4, YVO_4)$	$ZrSiO_4$
$LiMnPO_4$	Mg_2SiO_4
$Cu_2(OH)PO_4$, $(Zn_2(OH)AsO_4)$	Al_2OSiO_4

1.8.2 Pyrophosphates

Linking of two PO_4 tetrahedra to form the $P_2O_7^{4-}$ ion occurs in pyrophosphoric acid and the pyrophosphates [38]. Only normal ($M^I_4P_2O_7$, $M^{II}_2P_2O_7$, $M^{IV}P_2O_7$) and dihydrogen salts appear to form anhydrous salts. The non-existence of the anhydrous forms $M_3HP_2O_7$ and $MH_3P_2O_7$ is due to the fact that stable P_2O_7 frameworks linked by hydrogen bonds are not possible for these particular H:O ratios.

1.8.3 Metaphosphates

In comparison with the chemistry of the ortho- and pyro-phosphates, that of the metaphosphates is complex. In these compounds the condensation of PO_4 tetrahedra has proceeded further to the formation of rings or chains, of composition $(PO_3)_n^{n-}$, analogous to those in metasilicates. In contrast to $Si_3O_9^{6-}$ and $Si_6O_{13}^{2-}$ ions, however, only $P_3O_{12}^{9-}$ and $P_4O_{12}^{4-}$ ions have as yet been shown to exist in the metaphosphates.

1.8.4 Phosphate links

In an analogous manner to silicates, phosphate groups are also known to act as links in framework structures formed from metal polyhedra as in $NiNH_4(PO_3)_3$ [39] and $CoNH_4(PO_3)_3$ [40] where metal octahedra are linked via each corner by a $[P_2O_7]$ group creating a three dimensional channel structure analogous to those found in zeolites.

1.9 Transition Metal Chemistry

1.9.1 Cobalt

Cobalt produces a diverse range of coloured pigments ranging in colour from black and brown to violet and even yellow. The blue colours exhibited by some cobalt pigments have been used for decorating ceramics since antiquity. The development of modern cobalt pigments began with Sven Rinmann, a Swedish chemist, who discovered a green cobalt-based paint around 1780. Louis-Jacques Thénard, was commissioned by the French government to devise an alternative pigment to expensive ultramarine and in 1802 he discovered Cobalt Blue ($CoAl_2O_4$). Cerulean Blue was discovered by Andreas Höpfner in 1805 and was essentially a solid solution between cobalt tin oxide and cobalt chromium oxide. Fischer's Yellow ($K_3[Co(NO_2)_6]\cdot H_2O$), named after Nikolaus Wolfgang Fischer, became available in 1831 and a violet pigment, Cobalt Violet, based on cobalt phosphate was developed by Jean Salvétat in 1859. Some commercially available cobalt pigments are listed in the table below.

Table 1-6: Some commercially available cobalt pigments.

Colour	*Composition*	*Manufacturer*
Black	$(Co,Fe)(Fe,Cr)_2O_4$	Ferro
Violet	Co_3PO_4	Ferro
Dark Blue	$CoO\text{-}Al_2O_3\text{-}SiO_2$	Mahavir Minerals
Blue	$CoAl_2O_4$	Bayer
Light Blue	$Co(Al,Cr)_2O_4$	Bayer
Turquoise	$CoCr_2O_4$	Ferro
Green	$(Co,Ni,Zn)_2(Ti,Al)O_4$	Bayer
Yellow	$K_3[Co(NO_2)_6]\cdot H_2O$	Brada Fine Colour

Cobalt has two common oxidation states +2 and +3 and these are exhibited in a number of compounds. Obvious examples where cobalt achieves these oxidation states are the oxides of the element: CoO and Co_3O_4. In the former cobalt occupies a tetrahedral site and the oxide has the rock-salt structure. Co_3O_4, which can be written $Co^{II}Co^{III}{}_2O_4$, has the normal spinel structure with the Co^{II} ions in the tetrahedral and the Co^{III} ions in the octahedral sites within the cubic close packed oxide lattice.

1.9.1.1 Tetrahedrally coordinated Co^{II}

Compounds that contain Co^{2+} ions tetrahedrally coordinated by oxide ions are often blue in colour, examples include $CoAl_2O_4$. The colour in most cobalt pigments is due to the d-d transitions which take place as particular wavelengths of light are absorbed. The spin allowed d-d transitions of Co^{2+} in tetrahedral coordination are [41]:

$$\nu_1: {}^4A_2(F) \rightarrow {}^4T_2(F)$$
$$\nu_2: {}^4A_2(F) \rightarrow {}^4T_1(F)$$
$$\nu_3: {}^4A_2(F) \rightarrow {}^4T_1(P)$$

In terms of colour the most important of these transitions is ν_3 as this gives rise to a broad and intense absorption band usually between 500 – 700 nm [42, 43]. The transitions ν_1 and ν_2 occur in the infrared region and therefore do not affect the observed colour of a material.

1.9.1.2 Octahedrally coordinated Co^{II}

In contrast to tetrahedrally coordinated Co^{2+}, compounds such as Co_2GeO_4 that contain octahedral cobalt (II) are weakly coloured and are often pink. The d-d transitions that occur for octahedral complexes are typically weaker than those for tetrahedral complexes. The visible spectrum is dominated by the ${}^4T_1(F) \rightarrow {}^4T_1(P)$ transition.

1.9.2 Copper

Copper is primarily seen in blue, green and black pigments. Well known examples include Egyptian Blue and Scheele's Green. Egyptian blue, $CaCuSi_4O_{10}$, has been used since Babylonian times as a cheaper substitute for *lapis lazuli* and has been investigated by several geologists and mineralogists [44, 45]. Scheele's green ($Cu(AsO_2)_2$) was discovered by Carl Wilhelm Scheele in 1775 and was cheap to manufacture therefore it was used in applications such as paint and printing. The naturally occurring copper minerals, Malachite (green) and Azurite (blue), were also used as pigments in ancient times.

The divalent state is the most commonly observed oxidation state for copper and the usual coordination numbers are four, five and six. However, the d^9 configuration makes Cu^{II} susceptible to Jahn-Teller distortion when placed in regular octahedral or tetrahedral coordinations, i.e. an environment of regular cubic symmetry. For this reason regular symmetrical geometries are rarely observed for Cu^{II}.

1.9.2.1 Square planar Cu^{II}

Due to the Jahn-Teller effect Cu^{II} is not typically found in regular tetrahedral coordination geometry and occurs in square planar geometry [46], which can be regarded at the limit of extension of an octahedron along a four-fold axis. However, some spinel-type Cu^{II} compounds do exhibit approximate tetrahedral geometry, examples include $CuCr_2O_4$ [47] and the pigment Spinel Black ($Cu(Cr,Fe)_2O_4$) [48]. In these cases the copper ion causes the crystal structure to distort from the regular cubic structure usually associated with most spinel materials.

The colour of Egyptian Blue arises from the presence of Cu^{II} in a square planar coordination geometry. Previous studies [49, 50] of the UV/Vis spectra for Egyptian blue and similar materials ($MCuSi_4O_{10}$ M = Sr, Ba) reveal that there are three transitions responsible for their colour: a weak band at around 770 nm ($^2B_{2g} \leftarrow {}^2B_{1g}$) and two overlapping bands, one at around 630 nm ($^2E_g \leftarrow {}^2B_{1g}$) and the other at around 540 nm ($^2A_{1g} \leftarrow {}^2B_{1g}$).

1.9.2.2 Five Coordinate Geometry

Cu^{II} is often seen to occupy sites with coordination numbers of five, typically displaying geometries denoted as '4+1' as a result of the Jahn-Teller effect. In this geometry the Cu^{II} often has four relatively strong coplanar bonds and one weaker elongated apical bond. Examples of compounds which contains this '4+1' arrangement are $Cu_3(PO_4)_2$ and $YBa_2Cu_3O_7$.

The crystal structure of copper (II) phosphate ($Cu_3(PO_4)_2$), reported by Shoemaker *et al.* [51], contains two Cu^{II} sites and is, as with many Cu^{II} compounds, blue in colour. The Cu(1) atom occupies a slightly distorted (Cu(1) – O 2 x 1.924 Å and 2 x 1.982 Å) square planar site. The Cu(2) site is described as 'an irregular polyhedron of five O atoms', with four bonds at an average distance of 1.965 Å and a fifth at 2.265 Å. In fact the geometry of the site can be described as intermediate between square pyramidal and trigonal bipyramidal.

1.9.2.3 Six Coordinate Geometry

Due to the Jahn-Teller effect on Cu^{II}, the formation of a regular octahedral geometry CuX_6 where all CuX bonds are equal in length has not yet been observed. Instead, the tetragonally distorted '4+2' structure is observed, where there are 4 relatively strong equatorial bonds and two longer, weaker axial bonds. The four equatorial bonds are of comparable length to those found in the square planar and 4+1 arrangements already mentioned, *ca.* 1.95-2.0 Å. The two axial bonds are slightly longer; normally these are not shorter than 2.2 Å.

1.9.3 Manganese

A number of colours are seen for manganese compounds ranging from white, through green, blue and violet to brown and black. Manganese (II) carbonate, a white material, is mixed with calcium carbonate and used in some watercolour paints. A brown pigment is produced [52] when Mn^{II} is incorporated into the stable rutile lattice to give the composition $(Ti,Sb,Mn)O_4$ and a black pigment containing manganese is also commercially available and has the composition $(Fe,Mn)(Fe,Mn)_2O_4$.

1.9.3.1 Manganese Violet

Manganese violet ($NH_4MnP_2O_7$) was developed, by Leykauf, as a pigment in 1868 as a replacement for the more expensive cobalt violet and continues to be commercially produced today [53]. The violet colour is characteristic of manganese (III) in an octahedral coordination environment and much work has focused on the pigment's structure [54, 55] and the origin of its colour [56].

1.9.3.2 Permanganate Sodalite

The sodalite structure containing permanganate ($Na_8[AlSiO_4]_6(MnO_4)_2$) was first reported by Haworth and Weller [57] in 1991. The material, when incorporated into plastics, gives a violet colour that is stronger than many commercially produced pigments such as Manganese Violet, described above. The encapsulation of coloured species into zeolitic frameworks is of commercial interest due to the existence of many species, which, although brightly coloured, are also thermally and chemically unstable under the conditions encountered in pigment applications. Permanganate sodalite is not produced commercially as a pigment due to its poor light stability.

1.9.3.3 The Hypomanganate Ion (MnO_4^{3-})

MnO_4^{3-} is an intensely coloured charge transfer species with an extinction coefficient higher than that for permanganate. The use of the permanganate ion in pigment systems has previously been investigated [57]. However, the MnO_4^- ion is light and heat sensitive, due to the ease of reduction of the Mn(VII) centre, even when incorporated into zeolite structures. Similar problems exist with the manganate, MnO_4^{2-}, ion. Hence while intensely coloured materials containing these species are well known they have no application in pigments.
However the MnO_4^{3-} ion, with a Mn(V) centre is less easily reduced, therefore it has decreased light and heat sensitivity and can be incorporated into stable solid state structures at high temperature. An example of this is $Ba_3Mn_2O_8$, which has an intense green colour [58] and is readily produced by reaction of MnO_2 and $BaCO_3$ under oxygen at 1000°C. The

structure of this compound consists of discrete tetrahedral MnO_4^{3-} ions co-ordinated to two types of Ba-O polyhedra, one 10-coordinate and one 6-coordinate. The later polyhedra can also be described as having a 12-fold coordination if a further 6 x Ba-O at 3.298 Å are included in the coordination sphere. The barium content and ease of dissolution of this compound in dilute acids negates its possible use as a pigment. Attempts to produce other simple manganate (V) compounds have been unsuccessful.

The MnO_4^{3-} ion is isovalent with the tetrahedral anions VO_4^{3-} and PO_4^{3-}, and can therefore be substituted into vanadates and phosphates without any problems of charge compensation. Several research groups have studied the substitution of Mn^{5+} into materials such as $Ba_3(VO_4)_2$ [59, 60], $Sr_2(VO_4)Cl$ [61] and apatite-type compounds [62, 63] and materials with colours ranging from deep blue to green are reported.

1.10 Structure Determination and Pigment Design

Throughout this work the emphasis is placed upon accurate determination of the crystal structures under consideration and the elucidation of the associated colour-affecting properties.

An understanding of the origins of pigment colouration is a key consideration in the development of novel pigment systems. By performing in-depth investigations of existing pigment systems it is possible to extract information regarding the coordination environments for each ion, the electronic transitions causing the observed colour and the particular species responsible for the given colour. This knowledge, along with an understanding of synthetic techniques enables the preparation of a number of related systems, which may have an array of different colours.

1.10.1 Cation Substitution

The replacement of metal cations within an existing metal oxide pigment system with other metal cations will have significant implications for both the colour and the structure of the material.

The variation in colour can be due to a number of factors and in most cases the actual colour change is due to a combination of these factors. Some of the factors caused by cation substitution are listed below.

1) Dilution of the chromophore
2) Distortion of the structure/coordination environments
3) Direction of the chromophore onto sites with differing coordination geometries

The substitution of one colourful species with another will lead to some degree of tunability of pigment colour. However, the replacement of colourful species with colourless ones may not simply dilute the colour of the pigment. In fact the colour may be enhanced if the final coordination environment of the chromophore can be favourably altered or indeed if the chromophore can be directed towards a more favourable coordination.

Much of this work is concerned with the replacement of transition metal cations within existing pigment systems.

1.10.2 Synthetic Method

A number of synthetic methods are available to industrial pigment manufacturers and in a number of cases the colour of the pigment may deteriorate or be enhanced if a different synthetic method is used. The origins of the colour change may arise from a change in the crystal structure, changes in oxidation state of constituent elements, impurity phases, particle

size, changes in cation distribution across mixed sites or subtle changes in coordination geometry, among other things. Therefore, when directly comparing similar materials, for reasons other than synthetic method, it is essential that the preparatory method is identical in each case.

1.11 Aims of this Work

The aims of this work are to investigate a number of coloured mixed metal-oxide systems in order to gain an understanding of colour generating environments for transition metal species through the use of structural characterisation using both neutron and X-ray diffraction techniques, EXAFS and UV visible spectroscopy. Among the systems of interest are existing cobalt-containing pigments, metal borate systems and manganese (V) containing oxide materials. In each case the materials are either prepared as novel examples of coloured systems or are characterised in greater depth than in previous studies.

1.12 References

[1] Market Report, SRI Consulting, Menlo Park, California, (2001).

[2] Hund F. Bayer, US 3022186, (1959).

[3] Vilmin G., *Chemistry & Industry* - "Green process gives rare earth reds", **19,** 761 (1997)

[4] Buxbaum G. (Editor); *Industrial Inorganic Pigments VCH,* Weinheim, Federal Republic of Germany (1993).

[5] Jolly J.L.W., Collins C.T.; *Iron Oxide Pigments,* part 2, Information Circular-Bureau of Mines 8813, Washington (1980)

[6] Pigment PK 1095; *Inorganic Pigments for Paint and Plastic,* Ferro Ltd. (1995)

[7] Pigment PK 3080; *Inorganic Pigments for Paint and Plastic,* Ferro Ltd. (1995)

[8] Eppler R.A.; *Physics of Electronic Materials*, Part B, Chapter 31 1021-1046, Edited by Hench L.L. and Dove D.B., Marcel Dekker, New York (1972)

[9] Kreidl N.J.; *Physics of Electronic Materials*, Part B, Chapter 27 915-963, Edited by Hench L.L. and Dove D.B., Marcel Dekker, New York (1972)

[10] Bomhard E.; *Toxicol. Lett.,* **14** 189-194 (1982)

[11] Steinhoff D., Mohr U.; *Exp. Pathol.*, **41** 169-174 (1991)

[12] Rusch G., O'Grodnick J.S., Rinehart W.E.; *Am. Ind. Hyg. Assoc. J.,* **47** 12 754 (1986).

[13] Oldiges H., Hochrainer D., Glaser M.; *Toxicol. Environ. Hem.,* **19** 217 (1988).

[14] Hund F.; *Farbe und Lack*, **73** 111-120 (1967)

[15] Guimet J.; *Bull. Soc. Enc. Ind. Nat.,* **27** 346 (1828)

[16] Gmelin C.; *Bull. Soc. Enc. Ind. Nat.,* **27** 216 (1828)

[17] Reckitt's Colours Limited; *'The Cost of Whiteness'*, Hull, UK.

[18] Shriver D.F., Atkins P.W., & Langford C.H.; *Inorganic Chemistry, 2nd Ed.,* 600-602, Oxford Science Publications (1994).

[19] Shriver D.F., Atkins P.W., & Langford C.H.; *Inorganic Chemistry, 2nd Ed.,* 590, Oxford Science Publications (1994).

[20] Williams A., *A theoretical approach to inorganic chemistry*, Berlin, Springer-Verlag, (1979)

[21] Hurvich L. M., Jameson D., *Journal Optical Society of America*, **45**, 602 (1955)

[22] Commission Internationale de l'Eclairage *CIE Technical Report*, **116** (1995)

[23] Kämpf, G., Papenroth, W. *Farbe und Lack* **83** 18-29 (1977).

[24] Hirota K., Inoue T., Mochida N., Ohtsuka A.; *Nippon Seramikkusu Kyokai Gakujutsu Ronbunshi,* **98** 976-986 (1990)

[25] Eppler R.A.; *J. Am. Ceram. Soc,* **66** 794-801 (1983).

[26] Garcia Casado P., Rasines I.; *J.Solid State Chem.,* **52** 187-193 (1984)

[27] Sawada H.; *Mats. Res. Bull.,* **31** 355-360 (1996)

[28] McClure D.S.; *J. Phys. Chem. Solids,* **3** 311 (1957)

[29] F. Hund. Bayer, US 3022186, (1959).

[30] Henry P.F., Hughes E.M., Weller M.T.; *J. Chem. Soc. Dalton Trans.,* 555 (2000)

[31] Henry P.F., Hughes R.W., Ward S.C., Weller M.T.; *Chem. Comm.*, 1959-1960 (2000)

[32] Kemp P.H., *The Chemistry of Borates – Part 1*, Borax Consolidated Ltd, London (1956)

[33] Weller M.T., *The Design and Synthesis of New Inorganic Pigments*, Private Communication.

[34] Greenwood N.N., Earnshaw A., *Chemistry of the Elements*, 1st Edition, Pergamon Press (1984)

[35] Farmer J.B.; *Adv. Inorg. Chem. Radiochem.*, **25** 187 (1982)

[36] Diehl R., Brandt G.; *Acta. Cryst.*, **B31** 1662-1665 (1975)

[37] Wells A.F., *Structural Inorganic Chemsitry*, 3rd Edition Oxford University Press (1962)

[38] Levi G.R.., Peyronel G.; *Z. Krist.,* **92**, 190 (1935)

[39] Tordjman I., Tranqui D., Durif A., Averbuch M.T., *Bull. Franc. Miner. Cristallogr.,* **72**, 1949(1977)

[40] Tranqui D., Grenier J.C., Durif A., Guitel J.C., *Bull. Franc. Miner. Cristallogr.,* **90**, 252 (1967)

[41] Carlin R.L.; Electronic structure and stereochemistry of cobalt(II), *Transition Metal Chemistry*, **1** 1-33 (1965)

[42] Mimani T., Ghosh S.; *Current Science,* **78** 7 892-896 (2000)

[43] Corma F, Lambies V; *Rev. Chim. Miner.*, **17** 110-117 (1980)

[44] Fouque F., *Bull. Soc. Franc. Miner.,* **12**, 36 (1889)

[45] Jope E. M., Huse G., *Nature,* **146**, 26 (1940)

[46] Pack M.J.; *Ph.D. Thesis*, Southampton University, (1998)

[47] Prince E.; *Acta Crystallogr.,* **10** 554 (1957)

[48] Fast Black 100, *Lightfast™ Mixed Metal Oxide Pigments*, Bayer Inorganic Pigments US, (1998)

[49] Clark M.G., Burns R.G., *Inorg. Chem.* **5**, 1268 (1966)

[50] Clark M.G., Burns R. G., *J. Chem. Soc.* **A**, 1034 (1967)

[51] Shoemaker G.L., Anderson J.B., Kostiner E.; *Acta Cryst.* **B33** 2969-2972 (1977)

[52] Manganese Rutile Brown, *Sicotan® Pigments,* BASF (2002)

[53] Manganese Violet Pigment, Holliday Pigments, France.

[54] Lee J. D., Browne L. S., *J. Chem. Soc.*, **A,** 560 (1968)

[55] Riskin, Kalinskaya, *J. Appl. Chem.*, **40,** 16 (1967)

[56] Hughes E.M., *Ph.D. Thesis*, Southampton University, (1999)

[57] Weller M. T., Haworth K., *J. Chem. Soc., Chem. Commun.*, **10**, 373 (1991)

[58] Weller M.T., Skinner S.J: *Acta Crystallogr.* **C55** 154 (1999)

[59] Merkle L.D., Pinto A., Verdún H.R McIntosh B.: *Appl. Phys. Lett.* Vol. **61** 2386 (1992).

[60] Buijsse B., Schmidt J., Chan I.Y., Singel D.J.: *Phys. Rev. B-Condensed Matter*, Vol. **51** 6215 (1995).

[61] Albrecht C., Cohen S., Mayer I., Reinen D.: *J. Solid State Chem.* **107** 218 (1993).

[62] Lachwa H., Reinen D.: *Inorg. Chem.* **28** 1044 (1989)

[63] Dardenne K., Vixen D., Huguenin D.: J. Solid State Chem. **146** 464 (1999).

Chapter 2

Experimental Techniques

2 Experimental Techniques

Due to the nature of the materials studied in this thesis, a variety of characterisation techniques have been used to gain a full and accurate understanding of the systems and their structures. Powder X-ray diffraction has been used for phase identification and structural analyses, powder neutron diffraction for structural analyses, EXAFS to determine local coordination environments of particular elements and UV-Visible spectroscopy to identify the electronic transitions responsible for the colour in each case.

2.1 Powder X-ray Diffraction (PXD)

Powder X-ray diffraction is one of the principal techniques used in solid-state chemistry. It is used to study polycrystalline samples and involves the diffraction of X-rays by the planes of atoms within a crystal.

2.1.1 Theory

Diffraction of X-rays occurs in solids, as the X-ray wavelength is of the same order of magnitude as the interatomic spacings within a crystal (*ca.* 10^{-10} m) and Max von Laue recognised that a crystal may act as a 3-dimensional diffraction grating for X-rays [1].

If one considers a plane wave incident on two parallel lattice planes separated by a perpendicular distance d (Figure 2-1), for constructive interference to occur the path length difference between the two diffracted beams must correspond to an integral number of wavelengths. Simple trigonometry yields the Bragg equation (Equation 2-1).

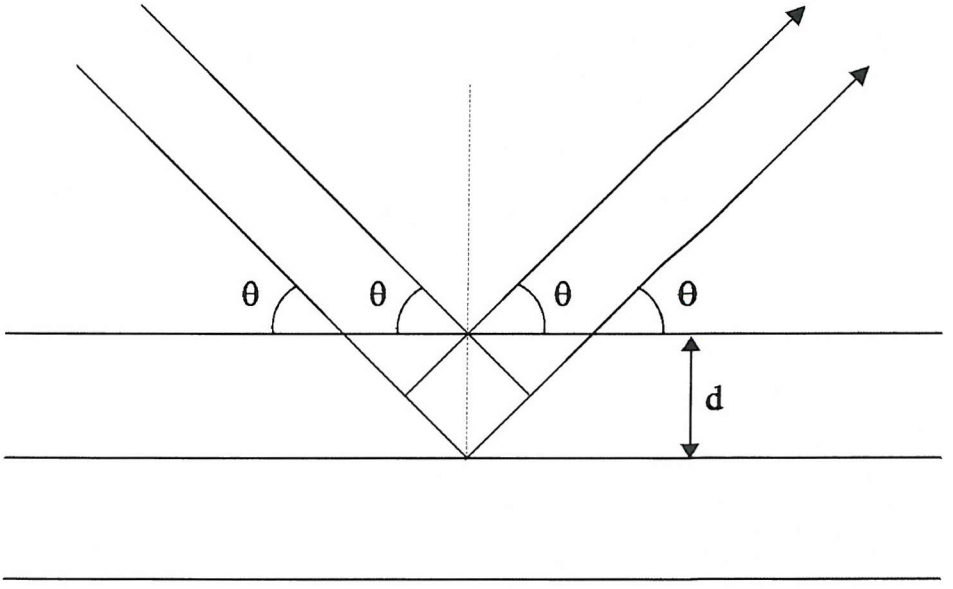

Figure 2-1. Illustration showing diffraction from points on parallel lattice planes.

Equation 2-1

$$n\lambda = 2d\sin\theta$$

where n = 1,2,3...

λ = wavelength of incident X-rays.

d = separation of planes ('d-spacing')

θ = glancing angle of the X-rays.

At angles other than the Bragg angle, the diffracted beams are out of phase and interfere destructively. The interplanar separations, d, in the crystal are calculated by measuring the diffraction maxima, of which only the first order diffraction maxima (n = 1) are generally seen. The crystal system can be derived from these d values by identification of the planes involved (Table 2-1). Planes are defined by the Miller indices, *h, k, l*, which are the reciprocal values of the positions where the plane intersects the *a*, *b* and *c* axes in the unit cell respectively.

In theory a crystal should display diffraction from each of its lattice planes giving rise to an observed maxima in the diffraction pattern. However, intensity is not always observed from every plane due to the existence of reflection conditions or systematic absences. These result from symmetry elements of the structure and are determined by the lattice types such as body centred (I) and face centred (F), as well as space symmetry elements such as glide planes and screw axes[2, 3].

Table 2-1: Expressions for d-spacings in the different crystal systems in terms of lattice parameters *a*, *b* and *c* and Miller indices *h*, *k* and *l*.

Crystal system	*Expression for* d_{hkl}
Cubic	$\frac{1}{d_{hkl}^2} = \frac{h^2+k^2+l^2}{a^2}$
Tetragonal	$\frac{1}{d_{hkl}^2} = \frac{h^2+k^2}{a^2} + \frac{l^2}{c^2}$
Orthorhombic	$\frac{1}{d_{hkl}^2} = \frac{h^2}{a^2} + \frac{k^2}{b^2} + \frac{l^2}{c^2}$
Hexagonal	$\frac{1}{d_{hkl}^2} = \frac{4}{3}\left(\frac{h^2+hk+k^2}{a^2}\right) + \frac{l^2}{c^2}$
Monoclinic	$\frac{1}{d_{hkl}^2} = \frac{1}{\sin^2\beta}\left(\frac{h^2}{a^2} + \frac{k^2\sin^2\beta}{b^2} + \frac{l^2}{c^2} - \frac{2hl\cos\beta}{ac}\right)$
Triclinic	$\frac{1}{d_{hkl}^2} = \frac{\left(\begin{array}{c}\frac{h^2}{a^2}\sin^2\alpha + \frac{k^2}{b^2}\sin^2\beta + \frac{l^2}{c^2}\sin^2\gamma + \frac{2hk}{ab}(\cos\alpha\cos\beta - \cos\gamma) \\ + \frac{2kl}{bc}(\cos\beta\cos\gamma - \cos\alpha) + \frac{2hl}{ac}(\cos\gamma\cos\alpha - \cos\beta)\end{array}\right)}{1 - \cos^2\alpha - \cos^2\beta - \cos^2\gamma + 2\cos\alpha\cos\beta\cos\gamma}$

2.1.2 Powder Diffraction

In a powder sample there are many very small crystals (10^{-7} – 10^{-4} m in dimension) orientated in a random manner. Each of these crystallites will diffract in the normal way. Due to the random nature of the crystallite orientation the incident beam will therefore be diffracted in all possible directions as governed by the Bragg equation [1]. The effect of this is that each lattice spacing in the crystal will give rise to a cone of diffraction, which would be observed as circles on a flat plate.

2.1.3 Instrumentation

Throughout this study, all constant temperature PXD experiments were carried out by mounting the powdered sample, flat, on a recessed aluminium sample holder. The diffraction data were collected on a Siemens D5000 Diffractometer, employing monochromated Cu-$K_{\alpha 1}$ radiation (λ = 1.5406 Å). The terminology, Cu-$K_{\alpha 1}$, above refers to the source of the X-rays. In this instance, a copper target atom is ionised by ejection of a core electron (1s – K shell) on exposure to an electron beam of sufficient energy. The filling of a vacant 1s orbital is

given the symbol K. This can be achieved in copper atoms by decay from the 3p or 2p levels. The X-rays generated by a 1s ← 2p transition are termed K_α and have wavelength of 1.5406 Å. Those generated by 1s ← 3p transition are termed K_β and have a wavelength of 1.3922 Å. The numeric term arises from one specific spin alignment in the np level.

Initial phase identification experiments were performed by collecting data, for 25 minutes, over the 2θ range 20-70 °. Longer collection times, typically 15 hours, and wider 2θ ranges , usually 10-110 ° were also employed to enable a more detailed study of the material's structure.

The data obtained were imported into a personal computer where they could be stored and manipulated with the aid of EVA and the JCPDS database [4], allowing phase identification, peak location and fingerprinting to be performed.

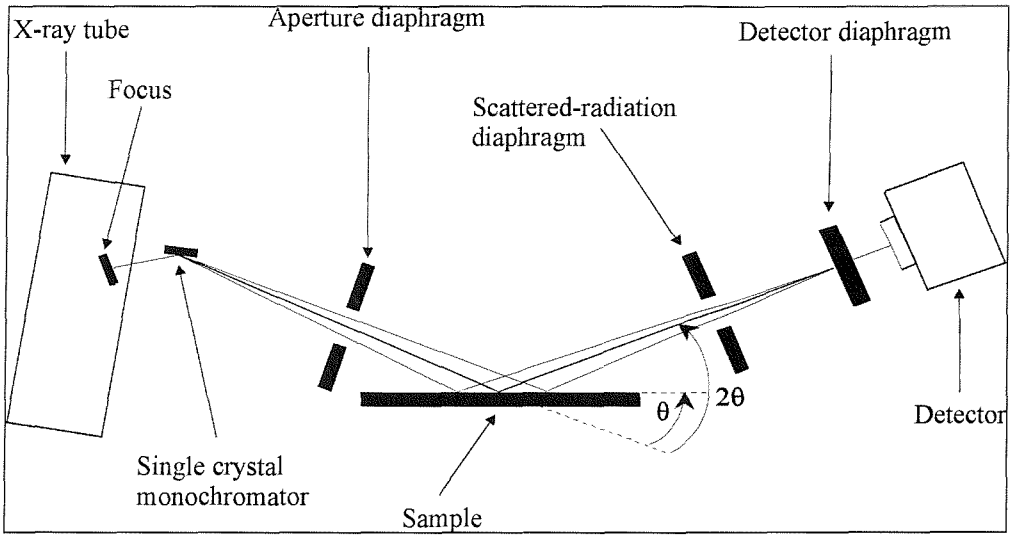

Figure 2-2: Schematic Representation of the Siemens D5000 Diffractometer

2.1.4 Cell Parameter Determination

Lattice parameters were determined using the CELL [5] refinement program that uses an iterative least squares process to minimise the equation: -

Equation 2-2

$$M = \sum_i W_i \left(\sin_i^2 \theta^{obs} - \sin_i^2 \theta^{calc}\right)^2$$

Where W_i = a weighting factor

M = weighted minimised difference for observed 2θ data.

In complete structural determinations, the cell parameters were determined within the overall refinement process (Section 2.4).

2.2 Synchrotron Powder X-ray Diffraction

2.2.1 High Resolution PXD

High-resolution PXD data were collected on station 9.1 at the Daresbury Laboratory Synchrotron Radiation Source. The radiation is produced by high-energy electrons, which are accelerated to velocities near to the speed of light and injected into a storage ring where they are held by powerful bending magnets. These high-energy electrons emit intense 'white' radiation (synchrotron radiation) tangentially to their path, over a wide range of energies. Ports around the ring allow the radiation to exit and travel along beam lines to experimental stations.

2.2.2 Monochromation

The polychromatic beam from the ring is incident on to a channel-cut Si (111) monochromator crystal, which is water cooled to maintain thermal stability. The practical wavelength range of the diffractometer is from 0.4Å to 1.5Å. A wavelength of 0.4858 Å was used in the collection of all the data presented here.

2.2.3 Detectors

The incident beam is monitored using a scintillation detector, which records the scattering from a kapton foil.

The intensity of the diffracted beam was measured using a curved image-plate system, which was placed, at a distance of 40cm from the sample.

2.2.4 Sample Mounting

Powdered samples were transferred to glass capillaries, 2.5cm in length. The capillary was then mounted on a spinning goniometer.

All data were collected at room temperature and each sample run typically lasted 30 - 45 minutes.

2.3 Powder Neutron Diffraction (PND)

Time of flight (TOF) powder neutron diffraction (PND) has been used in some cases to supplement the PXD data. The main difference between the two diffraction techniques, mentioned, is the way in which the radiation is scattered. In PXD, the X-rays are scattered by the electrons of the atoms and the scattering power is a function of the atomic number. However, neutrons are scattered by the atomic nuclei and the neutron scattering power has no simple dependence on the atomic number. The ability of a nucleus to scatter neutrons is dependent on both the potential scattering and the resonant scattering, which varies across the periodic table giving neighbouring elements and isotopes very different scattering lengths. PND is an essential technique when studying cation distributions over a number of mixed sites, especially when the cations concerned have similar X-ray scattering powers, such as cobalt, nickel and iron. PND can also prove to be very useful when trying to locate light atoms in the presence of heavy ones.

The suitability of neutrons to the diffraction technique is a result of a number of properties including a wavelength comparable to the atomic separation and an intrinsic magnetic moment, allowing both crystal and magnetic structures to be investigated. In this work, PND has primarily been used to locate oxygen positions and occupancies and to study the distribution of cations of similar atomic number over a number of mixed sites.

2.3.1 de Broglie Equation

Neutrons, due to their wave-particle duality, may be used for diffraction experiments in a similar way to X-rays. The wavelength of a given neutron is governed by the de Broglie equation [6]:

Equation 2-3

$$\lambda = \frac{h}{mv}$$

where: λ = wavelength

h = Planck's constant

m = mass of a neutron

v = velocity of a neutron

2.3.2 Instrumentation

PND data, throughout the course of this work, were collected using the medium resolution instrument POLARIS and the high intensity, high-resolution instrument GEM both at the ISIS facility at the Rutherford Appleton Laboratory (RAL), Oxfordshire. This facility employs a spallation neutron source, which provides a pulsed beam of neutron radiation and has a d-spacing range of 0.2-3.2 Å. A wide range of neutron energies is produced, making this a variable wavelength technique. In a conventional diffraction experiment, according to the Bragg equation (2.1.1), λ is fixed with d and θ as variables. However, for a TOF experiment λ and d are variables with θ being fixed. The diffracted neutrons are detected by fixed angle detectors according to their 'time of flight' (time taken for a neutron to travel from the source to the detector) and hence their wavelength over a fixed distance.

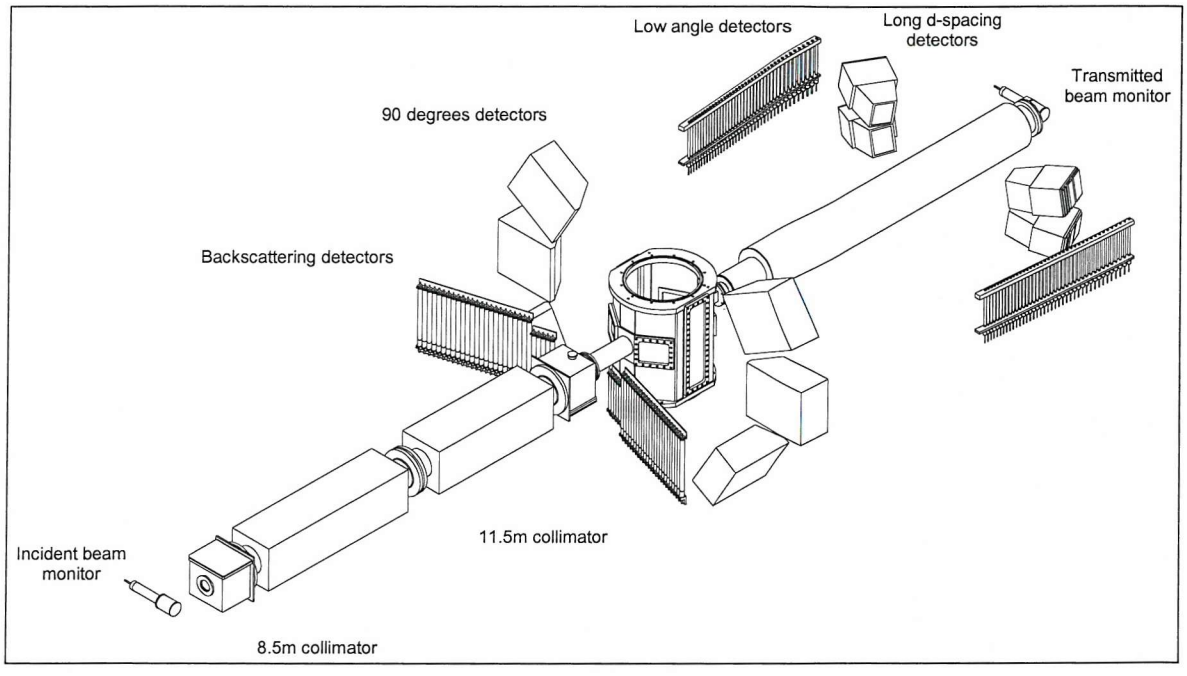

Figure 2-3: Schematic of the POLARIS instrument

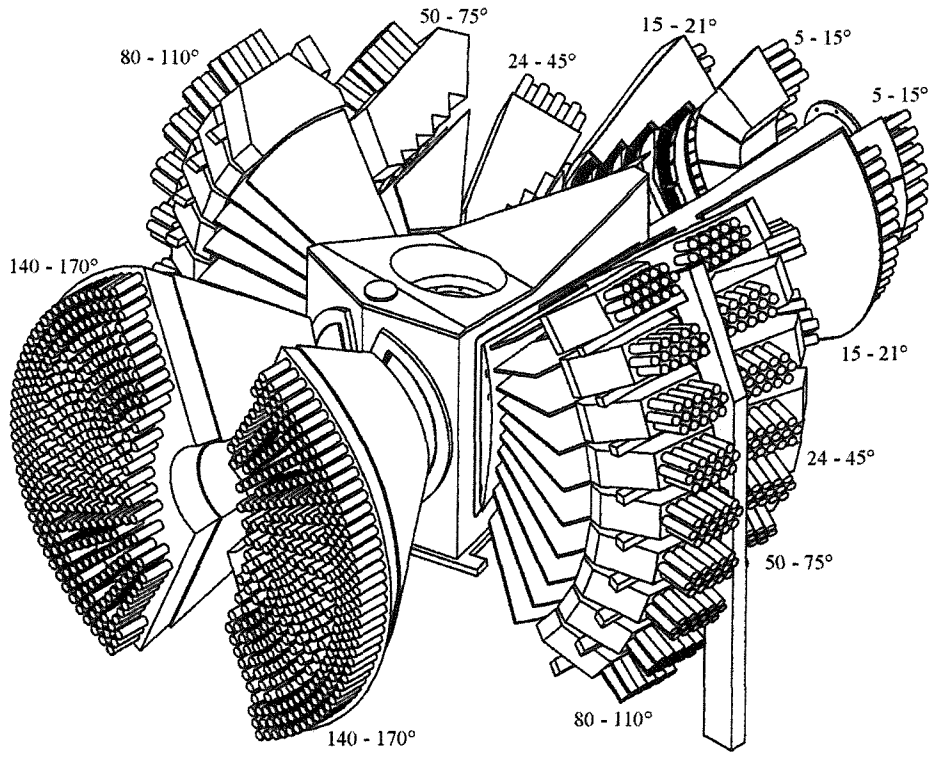

Figure 2-4: Schematic of the GEM instrument

Diffractometers utilising a pulsed neutron source operate in a fundamentally different way to a conventional reactor-based, constant wavelength diffractometer. TOF diffractometers measure the Bragg reflections at fixed scattering angles and monitor the time of arrival of a neutron after the initial burst produced at the target. Conventional diffractometers measure the Bragg reflections by scanning a detector over a range of angles from low to high 2θ.

The relationship between TOF and d-spacing is a linear one and is derived from the de Broglie equation and Bragg's law:

Equation 2-4

$$\lambda = \frac{h}{m_n v_n}$$

Equation 2-5

$$\lambda = 2d\sin\theta$$

If the total distance travelled by a neutron (source→sample + sample→detector) is equal to L and the corresponding time of flight is t then;

Equation 2-6

$$v_n = \frac{L}{t}$$

hence

Equation 2-7

$$\left[\frac{h}{m_n}\right]\cdot\left[\frac{t}{L}\right] = 2d\sin\theta$$

therefore

Equation 2-8

$$t = 2dL\left(\frac{m_n}{h}\right)\sin\theta$$

$$\therefore t \propto d$$

Therefore, for a 12 m instrument like POLARIS, a 1 Å d-spacing reflection will be detected in a backscattering bank at a TOF of ~5000 μs.

2.3.3 Data Collection

The samples were mounted in a cylindrical vanadium can, which is then placed within an evacuated sample chamber. All data were collected at room temperature with typical collection times being around 1 hour.

2.4 Structural Refinement

All structural refinements were carried out using the General Structure Analysis Suite (GSAS) [7], which employs the Rietveld method [8,9].

2.4.1 The Rietveld Method

The single crystal method of structure determination is not always applicable to solid state chemistry as the standard experimental procedures (high temperature sintering and frequent regrinding) lead to samples with very small crystal size. Single crystal experiments typically require *ca.* 0.01 mm^3 crystals and larger crystals (*ca.* 1 mm^3) are required for neutron experiments as the neutron beam has a significantly lower flux (*ca.* 10^3 lower).

A powder diffraction pattern of a crystalline material can be considered as a collection of individual reflection profiles, each with a peak height, peak position, peak width, peak shape and an integrated area which is proportional to the Bragg intensity, I_k where k represents the Miller indices *h, k,* and *l* [10]. A technique was devised to utilise the full information content at each step of the powder pattern, which allowed structure determination using a method of profile refinement.

The Rietveld method [8, 9] is based upon a comparison of an observed diffraction pattern with a theoretical model and refines a number of structural/positional parameters, including lattice parameters, atomic coordinates and site occupancies and profile parameters, including peak shape, zero point and asymmetry. Once a calculated profile has been obtained, least-squares refinements are carried out until the best fit is obtained between the entire observed powder diffraction pattern and the entire calculated pattern based on simultaneously refined models for the structural and profile parameters.

In order to refine X-ray and time of flight neutron data, different versions of the Rietveld method have been used.

2.4.2 Theoretical considerations

It may be shown that for any regular array of stationary atoms, the structure factor F, is the sum of the contributions of the scattering amplitudes, f, and the phases, ϕ, of each atom [11], leading to the expression:

Equation 2-9

$$F = \sum_{j=1}^{N} f_j \exp[i\phi_j]$$

In a unit cell, the total phase shift of an atom j, at a point (x_j, y_j, z_j) from the origin is the sum of the phase shifts in each direction. When the phase shift is evaluated, the structure factor for one unit cell becomes:

Equation 2-10

$$F_{hkl} = \sum_{j=1}^{N} f_j \exp\left[2\pi i\left(hx_j + ky_j + lz_j\right)\right]$$

where h, k and l are the Miller Indices that define the plane from which the reflection takes place. For very small crystals, it may be shown that the intensity of the scattered beam is proportional to the square of the structure factor.

Equation 2-11

$$I_{hkl} = kL^2|F_{hkl}|^2$$

where k = scaling constant

L = the Lorentz factor, a geometric function of the method of data collection and hence the instrument used.

In real crystals, the scattered intensity is modified by imperfections in the lattice structure. Defects and substitutional disorder cause local structural irregularities, particularly in non-stoichiometric materials. In addition, thermal motion causes a reduction in scattered intensity as a result of time dependent vibrations of the atoms about their mean positions: the atoms in a plane *hkl* are displaced randomly from their ideal in-plane positions, disrupting the in-plane behaviour of their combined scattering. The correction to a structure factor reflected by a plane, *hkl*, takes the form [11]:

Equation 2-12

$$T_{hkl} = \exp\left[-B_{hkl}\frac{\sin^2\theta}{\lambda^2}\right]$$

so that for a unit cell, the structure factor becomes:

Equation 2-13

$$F_{hkl} = \sum_{j=1}^{N} f_j n_j \exp\left[-B_j\frac{\sin^2\theta}{\lambda^2}\right].\exp\left[2\pi i(hx_j + ky_j + lz_j)\right]$$

where n_j is the occupation factor of the j^{th} atom, equal to one in a structure free from defects. However, this assumes that the displacements due to thermal motion are isotropic, which is rarely the case, except in some highly symmetric special positions of cubic space groups. A more rigorous analysis [8] describes the anisotropy of thermal motion in the form of an ellipsoid, replacing the equation above with:

Equation 2-14

$$T_{hkl} = \exp\left[-\tfrac{1}{4}\left(B_{11}h^2a^{*2} + B_{22}k^2b^{*2} + B_{33}l^2c^{*2} + 2B_{12}hka^*b^* + 2B_{23}klb^*c^* + 2B_{13}hla^*c^*\right)\right]$$

A number of expressions can be used to simulate the thermal motion (T_{hkl}), but the form given here is used to describe the anisotropic temperature factors used throughout this work. (Values of U are quoted throughout this work and these are related to B in Equation 2-14 by $B = 8\pi^2U$)

The intensity of the scattered beam at a particular point is also dependent on the multiplicity of the particular *hkl* reflection. Therefore, for a specific *hkl* reflection in a given crystal symmetry class, there can be a number of equivalent planes diffracting at the same angle to give an increased intensity.

2.4.3 Data Refinement

The Rietveld method is now widely recognised to be uniquely valuable for structural analyses of nearly all classes of crystalline materials not available as single crystals. The typical process followed for the refinement of powder diffraction data was as follows:

i) Determination of an approximate model of the structure by comparison with other known structures and their diffraction patterns.

ii) Refinement of the overall scale factor and background parameters.

iii) Refinement of the lattice parameters, zero point error and possible sample displacement correction in order to accurately locate the Bragg reflections. A preliminary refinement of the peak shape parameters is often carried out at this stage.

iv) Location of atom positions in the structure by allowing them to vary. This alters the peak intensities and allows improvement of the peak shape.

v) Refinement of the isotropic temperature factors is allowed when the atomic position is known in order to define its thermal motion.

vi) Full refinement of peak shape parameters, in addition to any asymmetry or preferred orientation parameters that might be required.

vii) Variation of the anisotropic temperature factors is carried out if possible. This can lead to a significant improvement in the fit, however, its use is often not feasible with X-ray data.

In this work the Rietveld method was used for refinement of data collected on both the single wavelength powder X-ray diffractometer and time of flight neutron instruments. The differences between data sources influence the data preparation that was required and the instrumental parameters that were refined, however, the method itself is the same. In all cases, the 'best-fit' sought is the best least squares fit to all the intensities at each step. The quantity minimised in the least-squares refinement is the function M and is the sum over all the data points:

Equation 2-15

$$M = \sum_i w_i (y_i^{obs} - y_i^{calc})^2$$

Where: w_i = a weighting factor given by $1/y_i^{obs}$

y_i^{obs} = observed intensity at each step/point i ($2\theta_I$ for PXD)

y_i^{calc} = calculated intensity at each step.

For PXD, the calculated intensities y_i^{calc} are determined from the structural model by summing the calculated contributions from neighbouring Bragg reflections (k) plus the background b_i :

Equation 2-16

$$y_i^{calc} = s\sum_k L_k |F_k|^2 \phi(2\theta_i - 2\theta_k) P_k A + y_{bi}$$

where s = scale factor

L_k contains Lorentz polarisation and multiplicity factors

ϕ = reflection profile function

F_k = structure factor for the k^{th} Bragg reflection

P_k = preferred orientation function

A = an absorption factor

y_{bi} = background intensity at i^{th} step

Preferred orientation arises when there is a stronger tendency for the crystallites to be ordered in one way / set of ways and is defined by :

Equation 2-17

$$P_k = \left[G_2 + (1 - G_2)\exp(-G_1\alpha_k^2)\right]$$

where G_1 and G_2 are refinable parameters and α_k is the angle between the presumed cylindrical symmetry axis and the preferred orientation axis direction.

Since a comparison of intensities is performed at every point, it is essential for the construction of the calculated profile to accurately describe the shape of the Bragg reflections *i.e.* peak shape. Peak shape is generally dictated by the instrument; for the Siemens D5000 the peak shape is pseudo-Voigt, and described by the function

Equation 2-18

$$\eta L + (1 - \eta)G$$

where L and G are the Lorentzian and Gaussian contributions to the peak shape and η is the mixing parameter which can be refined as a linear function of 2θ ;

Equation 2-19

$$\eta = N_A + N_B(2\theta)$$

where N_A and N_B are refinable parameters.

The Gaussian (G) and Lorentzian (L) contributions to the peak shape are represented by the equations ;

Equation 2-20

$$G = \frac{(4\ln 2)^{1/2}}{H_k\sqrt{\pi}} \exp\left(-4\ln 2\left(2\theta_i - 2\theta_k\right)^2 / H_k^2\right)$$

and

Equation 2-21

$$L = \frac{2}{\pi H_k} 1 \Big/ \left[1 + 4\frac{(2\theta_i - 2\theta_k)^2}{H_k^2}\right]$$

where $2\theta_k$ is the calculated position for the k^{th} Bragg peak corrected for the counter zeropoint and H_k is the full-width-at-half-maximum (FWHM) of the k^{th} Bragg reflection.

The full width at half maximum (FWHM), H_k, of a peak has been shown to vary with the scattering angle $2\theta_k$ [12] and is modelled as:

Equation 2-22

$$H_k^2 = U\tan^2\theta + V\tan\theta + W$$

where U, V and W are the refinable parameters and are both instrument and sample dependent. Therefore, this formula can account for peak broadening effects resulting from particle size.

At low scattering angles the peak shape shows marked asymmetry due to the detector and sample heights. This results in the peak maximum shifting to slightly lower angle while the integrated intensity remains unchanged. This can be corrected by the use of a semi-empirical correction factor of the form

Equation 2-23

$$1-\frac{sP(2\theta_i-2\theta_k)^2}{\tan\theta_k}$$

where P = the asymmetry parameter

s = +1, 0, -1 when $(2\theta_I - 2\theta_k)^2$ is positive, zero or negative.

The refineable parameters for any least squares refinement fall into two distinct groups. The first group defines the structural parameters, which describe the contents of the unit cell and include the overall temperature factors, coordinates and occupancies of each atom. The second group contains the profile parameters, which define the position, shape and FWHM of each peak and consist of the profile scale factor, unit cell parameters, U, V, W, zeropoint, asymmetry and preferred orientation correction. In order to make a quantitative assessment of the agreement between the observed and calculated profiles, a number of reliability factors are defined, $R_{profile}$, $R_{expected}$, $R_{weighted\ profile}$. The R-factors are given by;

Equation 2-24

$$R_{profile} = R_p = 100\left[\frac{\sum_i \left|y_i^{obs} - y_i^{calc}\right|}{\sum_i y_i^{obs}}\right]$$

Equation 2-25

$$R_{exp\,ected} = R_{exp} = 100\left[\frac{(N-P+C)}{\sum_i \omega_i (y_i^{obs})^2}\right]^{1/2}$$

Where R_{exp} is defined from the statistics of the refinement and N is the number of observations, P is the number of refinable parameters and C the number of constraints.

From a mathematical point, $R_{weighted\ profile}$ (R_{wp}) is the most meaningful of the R-factors because the numerator is the residual being minimised. For the same reason, it is also the one that best reflects the progress of the refinement and is given by:

Equation 2-26

$$R_{wp} = 100\left[\frac{\sum_i \omega_i \left[y_i^{obs} - y_i^{calc}\right]^2}{\sum_i \omega_i \left[y_i^{obs}\right]^2}\right]^{1/2}$$

The final measure of the whole fit, that is minimised during the refinement is the chi-squared parameter and is defined as:

Equation 2-27

$$\chi^2 = \left[\frac{R_{weightedprofile}}{R_{\exp}}\right]^2$$

Therefore, for a good fit, the $R_{weighted\ profile}$ should approach the statistically expected R-factor (R_{exp}). The goodness of fit can also be measured by examining a plot of the profile fit; for a good fit, the difference line between the calculated and observed patterns should be as flat as possible.

2.4.4 Neutron Diffraction Data Refinement

The refinement of neutron diffraction data has significant advantages over the X-ray method. As previously described, the scattering length of a particular atom is related to the size of the nucleus and not the number of electrons it possesses. Neutron diffraction experiments are not affected by a form factor and consequently, allow the collection of a much larger angular range data set. In addition, preferred orientation effects are reduced due to the nature of the sample mounting in a neutron diffraction experiment.

The time-of-flight data from POLARIS and GEM were refined using the GSAS package, which employs the Rietveld technique as previously discussed. In this type of refinement, 2θ data is replaced by TOF data which is readily converted to d-spacing using Equation 2-8. However, for TOF data refined by this method, a d-spacing dependant absorption correction is applied due to the range of incident neutron energies.

In addition, the peak shape is more complex and is often fitted in terms of Gaussian, Lorentzian and exponential expressions rather than the mainly Gaussian expression used for single wavelength neutron diffraction data.

2.5 Solid State Ultraviolet/Visible (UV/Vis) Spectroscopy

UV visible spectra were acquired using a Perkin Elmer UV\Vis\NIR Lambda 19 spectrometer set up for diffuse reflectance spectroscopy utilising tungsten and deuterium lamps. The Kubelka-Munk [13, 14] function is applied to the spectrum. Selection of the required wavelength is achieved automatically through the use of diffraction gratings during the scan. Powdered samples were mounted in a quartz fronted aluminium holder and the spectra recorded between 200 and 800 nm using barium sulphate as a reference sample.

2.6 Extended X-ray Absorption Fine Structure – EXAFS

Since the advent of synchrotron radiation many forms of X-ray spectroscopy have been developed and utilised. In particular the technique of EXAFS has been used widely to investigate the local environment of a specific element up to distances typically 4-5 Å from the central atom.

EXAFS relates to the oscillatory variation of the X-ray absorption function as a function of photon energy beyond an absorption edge. The absorption, often stated in terms of the absorption coefficient (μ), can be ascertained from measurement of the attenuation of X-rays as they pass through a material. If the X-ray photon energy (E) is matched to the binding energy of a core level of an atom in a material, a sudden increase in absorption coefficient is observed, known as the absorption edge. For condensed matter, the variation of absorption coefficient at energies above the absorption edge produces a fine oscillatory structure called EXAFS [15].

EXAFS is a weak phenomenon so an intense source of X-rays is required to achieve an acceptable signal to noise ratio. Synchrotron radiation sources provide intense, highly collimated X-radiation over a wide range of energies that is ideal for the accumulation of EXAFS data in acceptable acquisition times.

2.6.1 The Absorption Edge

When an X-ray beam travels through a material a reduction in intensity is observed due to absorption. This absorption occurs at characteristic energies, which occur as steps or edges and are characteristic of the absorbing atom. The absorption is a result of an electron being excited from a core energy level, to an excited state close to or beyond the continuum. The edges are labelled according to the element and energy level from which the electron is ejected. For example, a 1s electron excitation is labelled K-edge, a 2s electron is an L_I-edge, and L_{II} and L_{III}-edges for $2p_{1/2}$ and $2p_{3/2}$ excitations respectively.

The absorption edge has further fine structure as shown in Figure 2-5. The region just before the edge to approximately 30 eV beyond it is known as the X-ray absorption near edge structure (XANES) region and consists of sharp spikes and oscillations caused by electronic transitions between bound states (before and on the edge) and multiple scattering effects (beyond the edge). Analysis of this region is complex and hence it is used mainly for the qualitative comparison between samples.

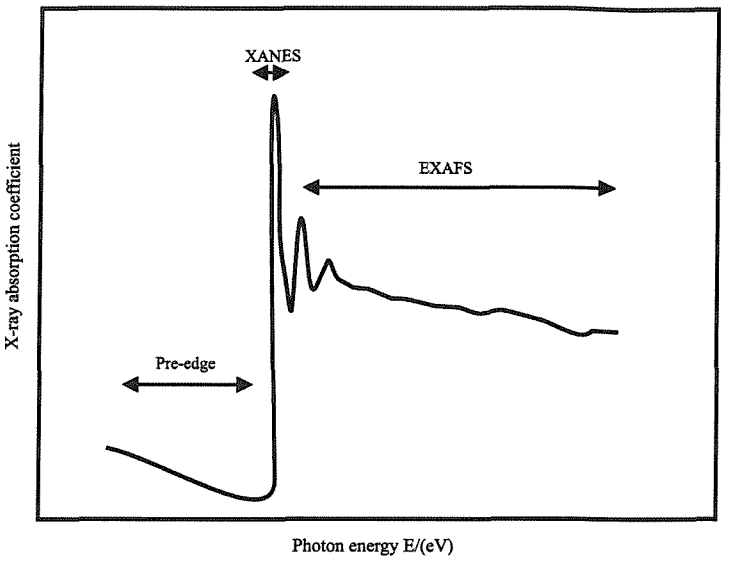

Figure 2-5. A typical X-ray absorption spectrum

The region from approximately 30 eV to 1000 eV beyond the edge consists of sinusoidal oscillations, which are termed extended X-ray absorption fine structure (EXAFS). EXAFS oscillations are observed for all materials, except monatomic gases. This effect is caused by the presence of fixed atoms as near neighbours to the absorber.

2.6.2 EXAFS Theory

EXAFS is defined as a final state interference effect, involving scattering of outgoing photoelectrons by the neighbouring atoms [15, 16].

The probability that an atom will absorb an X-ray photon and eject a core electron is dependent on the initial and final states of the electron. The initial state is a localised core level that corresponds to the absorption edge and the final state is the free electron. The ejected electron can be considered as an outgoing spherical wave, which will be backscattered by any neighbouring atoms producing incoming electron waves. The nature of the interference of the incoming and outgoing waves is dictated by the electron wavelength (λ). Thus the backscattered waves will either add or subtract from the outgoing waves at the centre depending on their relative phase. The total amplitude of the electron wave function will be correspondingly enhanced or reduced, giving rise to the sinusoidal variation of absorption *vs.* photon energy that is EXAFS.

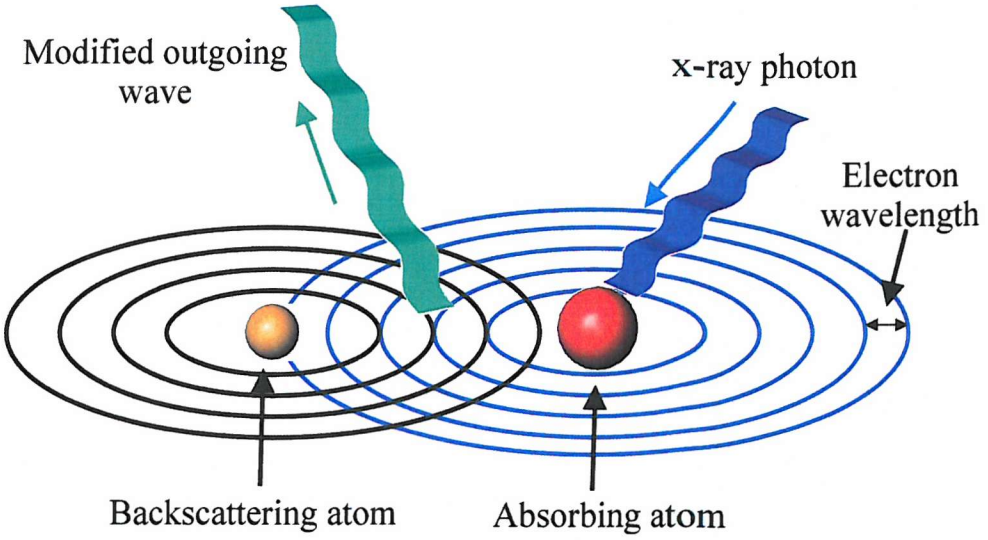

Figure 2-6. Modification of the outgoing wave by a neighbouring atom.

The electron wavelength is given by the expression;

Equation 2-28

$$\lambda = \frac{2\pi}{k}$$

where k is the photoelectron wavevector, given by,

Equation 2-29

$$k = \sqrt{\left(\frac{2m}{h}(E - E_0)\right)}$$

where E = X-ray photon energy

m = mass of an electron

E_0 = threshold energy of the absorption edge

h = Planck's constant

As the X-ray energy changes, so does the photoelectron wavevector k and hence the wavelength λ, thus causing an oscillation between constructive and destructive interference. As the final electron state is governed by this interference and the probability of the absorption is dependent on the final state, oscillations are seen in absorption with varying photon energy.

In order to treat EXAFS theoretically the oscillations have to be isolated from the normal atomic absorption and machine absorption. The EXAFS intensity or interference function $\chi(E)$ is defined by:

Equation 2-30

$$\chi(E)=\frac{\mu(E)-\mu_0(E)}{\mu_0(E)}$$

where $\mu(E)$ = observed absorption coefficient for photon energy E

$\mu_0(E)$ = background absorptions/absorption coefficient of free atom

As $\mu_0(E)$ cannot be obtained experimentally, an approximation is taken to give a smooth absorption coefficient through the oscillations.

In order to relate $\chi(E)$ to the structural parameters required, $\chi(E)$ is plotted as a function of the photoelectron wavevector k ($Å^{-1}$) *i.e.* E is converted to k. When plotted in this manner, the EXAFS oscillations decrease rapidly in intensity with increasing k and the determination of structural parameters would be dominated by the strong oscillations at low k. To prevent this occurring, the EXAFS is weighted by a function of k, most often k^3, which amplifies the contribution made by the later oscillations.

The k^3 weighted EXAFS oscillations then undergo Fourier transformation over the k range, which creates peaks that approximately compare to the interatomic distances. The peaks are of differing intensity reflecting the number and size of backscattering atoms. At this stage, the peaks are broad and shells of backscatterers at similar distances may fall under the same peak, so it is not possible to directly resolve the structural parameters. In addition, the intensities cannot be accurately quantified and the peak distances may be displaced from their true distances by 0.2 - 0.5 Å depending on a number of variables; the phase shifts of the elements involved, the position of E_0 chosen and the weighting.

In order to obtain quantitative information, curve fitting between a theoretical model and the experimental EXAFS is carried out.

2.6.3 The Plane Wave Equation (Small-Atom Approximation)

The conversion of EXAFS into the photoelectron wavevector k is formally derived in the plane wave theory of Lee and Pendry [17]:

Equation 2-31

$$\chi(k)=\frac{1}{k}\sum_{s} N_s S_i \frac{|f_s(\pi,k)|}{(R_{as})^2}\exp(-2\sigma_{as}^2 k^2)\exp\left(\frac{-2R_{as}}{\lambda}\right)\sin(2kR_{as}+2\delta_1+\alpha_s)$$

where S_i = an amplitude reduction factor due to absorber multiple excitations.

N_s = number of equivalent backscatters in each shell s.

R_{as} = interatomic distance between the absorber and backscatterer.

$f_s(\pi,k)$ = backscattering amplitude of the backscattering atom.

σ_{as}^2 = mean square variation of R_{as}.

λ = elastic mean free path.

δ_1 = phase shift due to absorber.

α_s = phase shift due to backscatterer.

This is the plane wave equation and is based on the approximation that the outgoing spherical electron wave may be treated as a plane wave in the vicinity of the backscatterers. This approximation is valid if the effective size of the backscattering atom is small compared with the interatomic distance between the central atom (absorber) and backscatterer, hence the terminology 'small-atom approximation'.

Essentially, the plane wave equation can be described as the sum of a series of damped sine waves from all neighbouring atoms. Each shell of equivalent backscatterers produces an individual interference pattern in the form of a damped sine wave. For backscatterers at longer distances from the absorber, the amplitude of the sine waves is greatly reduced ($\propto 1/R_{as}^2$).

In this single-scattering theory, the backscattering pathways are considered independent, *i.e.* they do not interact with each other. Therefore, the interference pattern due to each shell can be summed and the EXAFS comes from a summation over all the atoms neighbouring the absorber.

Some of the variables and functions involved in the phase and damping of the EXAFS oscillations are described;

2.6.3.1 Phaseshifts – $\sin(2kR_{as} + 2\delta_1 + \alpha_s)$

The frequency of each EXAFS wave is dependent on the distance between the absorbing atom and the neighbouring atom, as the photoelectron wave must travel from the absorber to the scatterer and back. On leaving the absorber and travelling to the backscatterer the outgoing photoelectron wave undergoes a phaseshift ($kR_{as} + \delta_1$) where δ_1 is the phaseshift due to the potential of the central atom (Coulombic interaction). It then experiences a further phaseshift (α_s) when backscattered by the neighbouring atom. Finally it undergoes the

phaseshift ($kR_{as} + \delta_1$) when returning to the back scatterer, giving a total phaseshift ($2kR_{as} + 2\delta_1 + \alpha_s$). The phaseshifts are calculated for the atom types present in a sample and both backscatterer and absorber phaseshifts vary with k and increase with atomic number Z. In addition the backscattering amplitude, $f_s(\pi,k)$, is highly correlated with phase functions and shows trends with variation in k and Z.

2.6.3.2 Debye-Waller Term – $\exp(-2\sigma_{as}^2k^2)$

The Debye-Waller factor σ plays an important part in EXAFS spectroscopy and has two components σ_{stat}, due to static disorder, and σ_{vib}, due to thermal vibrations.

Static disorder results from the atoms in a shell of backscatterers being at a slightly different distances from the absorber. The thermal motion of the atoms also causes further uncertainty in the distances. This in turn causes a deviation in R_{as} and in cases where the disorder is large, damping of the EXAFS occurs as the oscillations are broadened. In general, shells at larger distances have higher Debye-Waller factors. The relative variation in vibration between the absorber and scatterer is important and closer shells tend to move in sympathy with the central atom whereas the variation is greater for shells at larger distances.

The thermal contribution and hence the Debye-Waller factor can be minimised by cooling the sample. This also increases the intensity of the oscillations, giving a better signal to noise ratio and enhances the resulting fit, particularly for distant shells.

2.6.3.3 Inelastic Scattering Losses

There are two categories of inelastic scattering process which the photoelectron experiences as it leaves the X-ray absorbing atom, travels to the neighbouring atoms and returns, that may reduce the EXAFS amplitude. The foremost is a result of multiple excitations at the central atom and the second is associated with excitation of the surrounding environment such as neighbouring atoms – mean free path.

2.6.3.3.1 Multiple Excitations Amplitude Reductions (Passive Electrons) - S_i

When a photoelectron is ejected from a core hole, excess energy ($E - E_0$) can excite the remaining passive electrons (any electrons other than the core/active electron). These passive electrons may be excited in *shake-up* (excited to a bound state) or *shake off* (excited to continuum / ejected) processes. Since the total energy must be conserved, the original photoelectron must have a kinetic energy less than ($E - E_0$), i.e. a loss of intensity, implying its EXAFS contribution will be shifted in energy and phase. The result is a further damping in the experimentally observed EXAFS, which is modelled by the factor S_i. The degree of amplitude reduction is dependent upon the central absorber. The surrounding chemical

environment has a negligible effect. Therefore, the multiple excitation amplitude reduction factor remains constant having been set with standard components.

2.6.3.3.2 Inelastic Mean Free Path – exp(-2R_{as} / λ)

The outgoing photoelectron wave has a limited lifetime and path length as a result of energy losses to its surroundings. This type of inelastic scattering decreases the interaction between the outgoing and the backscattered waves by reducing the intensity and coherency of the interference effects. The term *exp(-2R_{as} / λ)* in Equation 2-31 is a factor used to describe this damping and is dependent upon the ratio of the interatomic distance R_{as}, to the electron mean free path, λ.

In contrast to the multiple excitation process, the mean free path scattering losses are dominated by weakly bound electrons (outer electrons such as valence electrons) which are dependent upon chemical environment, i.e. they are sensitive to the chemical environment of the absorber. This effect is particularly important for light-atom scatterers where the number of valence electrons is a substantial amount of the total number of electrons, and for higher shells where the emitted photoelectron travels a greater distance

2.6.4 Curved Wave Theory

The plane wave approximation assumes the atomic radii are smaller than the interatomic distance and approximates outgoing/incoming spherical electron waves by plane waves neglecting curvature of the electron wave at the scattering atom. This formalism is sufficient for high-energy data. Although, in practice the plane wave equation is not valid at low k (less than 4 Å) and consequently a better formalism is the curved wave theory. This is applied for actual EXAFS data and achieves a better fit across the whole k range [18]. The theory describes the initial and final states in terms of angular momentum with the result being a more complex expression with all the effects of the scattering atom incorporated in a matrix form. All of the factors involved in the plane wave equation are present but in different mathematical formulations. Computations using the full theory are time-consuming, and in practice a modified version derived by Gurman *et al.* [19] is used in both the data analysis program EXCURV98 [20] and the combined refinement program (section 2.6.8) [21, 22]. This simplifies the full spherical wave expression, as all terms except the diagonal matrix elements are negligible, although the exactness of the original theory is retained.

2.6.5 Multiple Scattering

Multiple scattering (MS) occurs when the photoelectron encounters more than one backscatterer before returning to the absorber. The EXAFS expression (Equation 2-31) is based on the single-scattering approximation where the outgoing wave is backscattered only once before combining with the unscattered wave. This assumes that in most cases single-scattering pathways between the absorber and shells of backscatterers have much greater amplitude than multiple pathways and photoelectron waves returning to the central atom from MS pathways are thought to mostly cancel each other out. However, in compounds where two backscatterers are arranged approximately collinearly with the absorber, MS effects have been shown to significantly increase the amplitude of EXAFS [23, 24].

The natural assumption would be that the intervening backscatter would block the more distant one, reducing the EXAFS contribution from it. In contrast, experiments have revealed that the EXAFS due to the latter is strongly enhanced. This is because the intervening atom has a focusing effect on the photoelectron, forward scattering it with greater intensity than would occur if it were absent, and with a change of phase.

The relative importance of the pathways varies with angle. At low angles the first order, single scattering is dominant, but the higher order pathways become more influential as the angle approaches 180 °.

2.6.6 Instrumentation

EXAFS spectra were collected at the Daresbury Laboratory Synchrotron Radiation Source (SRS) on stations 8.1 and 9.2. Both stations employ double crystal monochromators, which produce a tuneable monochromatic beam of synchrotron radiation at the desired energy.

2.6.6.1 Station 8.1

Station 8.1 is designed to function as a high flux bending magnet station for dilute sample studies in the range 3.5 – 11 keV. The station consists of bent double crystal monochromator (Si(111) or Si(220)). The crystals are bent in order to match the vertical dispersion of the source, hence eliminating the requirement of vertical slits to maintain resolution. The first crystal is also water cooled for temperature stabilisation. The beam line is maintained at high vacuum making it possible to minimise the beryllium window thickness between the synchrotron and the beam line itself, which is particularly important at lower energies [25].

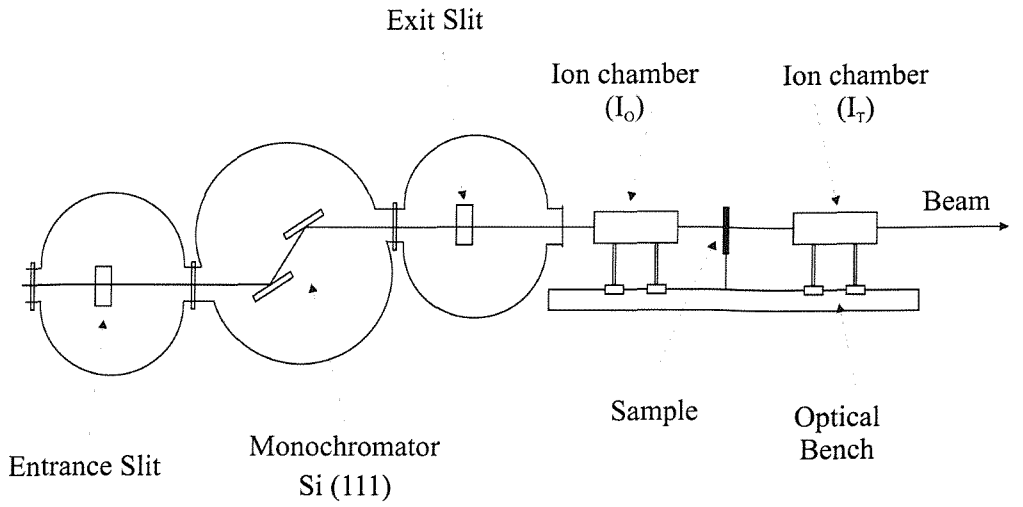

Figure 2-7: Schematic representation of a typical EXAFS beam-line

2.6.6.2 Station 9.2

Station 9.2 operates with a water-cooled, harmonic rejecting double crystal (Si (220)) monochromator in conjunction with a 5 Tesla wiggler magnet, which results in radiation of a higher energy [26]. This allows the study of energies in the range 6 – 33 keV. Entrance slits define the beam size, both horizontally and vertically, before it reaches the monochromator. The beam then passes through a further set of slits prior to entering the experimental area.

2.6.6.3 Harmonic Rejection

The required wavelength (and hence the energy) of X-rays for a certain experiment can be selected according to the Bragg equation:

$$n\lambda = 2d\sin\theta$$

where n = an integer (1 for the fundamental, 2, 3 etc. for higher harmonics)

λ = desired wavelength

d = crystal spacing (fixed for Si(111) or Si(220))

θ = angle between monochromator crystals and beam

However, in addition to the selected wavelength, the monochromator would also allow higher harmonics (n = 2, 3 etc.) to be incident on the sample. This could result in the EXAFS data being distorted as the higher harmonics would not be absorbed in the same way as the fundamental. For this reason they are removed by *harmonic rejection*. This is controlled by tilting one monochromator crystal with respect to the other in order to only allow 50, 60 or

70% of the maximum intensity through, thus rejecting most of the harmonic content while retaining 50% or more of the fundamental.

2.6.6.4 Absorption Detection

The absorbance is monitored using two inert gas filled ion chambers, I_0 before the sample and I_t after the sample. The relative absorbance is then calculated from the natural log of the ratio between the two readings ($\ln I_0/I_t$).

2.6.6.5 Sample Preparation

A calculated [27] amount of sample, designed to give an optimum μ value of 2.0, was diluted with around 50mg of polyvinyl alcohol (PVA) and pelletised. Sample homogeneity is a key consideration when preparing samples as unevenly distributed sample can cause irregular absorption across the sample. The prime advantage of using a pelletised sample is that the disc produced presents a more homogenous, uniform sample. Finally, the pellets were mounted on specially designed aluminium sample holders and secured with Kapton tape. Experiments were set to scan over a particular energy range to incorporate the edge jump for the element being studied. Scan durations were typically 30 – 45 minutes, and a minimum of two scans were carried out so that the data sets could be averaged during analysis to help improve the signal to noise ratio.

2.6.7 Data Analysis

The analysis of EXAFS data initially involves a background subtraction to isolate the EXAFS followed by fitting of the experimental data to a theoretical model. These stages can be achieved using two programs: PAXAS [28] and EXCURV98 [20].

2.6.7.1 PAXAS

PAXAS, the program used for the background subtraction of EXAFS data, removes the EXAFS oscillations due to atomic and machine absorption from the background absorption. The data is recorded experimentally as absorption versus monochromator angle (millidegrees), and is converted, by PAXAS, into absorption versus energy (eV) using the relevant monochromator d-spacing.

2.6.7.2 EXCURV98

The second type of program utilised is the EXAFS curve-fitting program EXCURV98 [29] which uses theoretical models to curve-fit and ultimately provide structural parameters.

Initially, the phase shifts used in the theoretical model are generated by *ab-initio* calculations. The type and number of atoms, distance from absorbing nucleus and thermal motion parameters, are then introduced to generate a theoretical spectrum and these are subsequently varied during the refinement.

EXCURV98 program uses a least squares refinement process to minimise the equation:

Equation 2-32

$$FI = \sum_i \left[k_i^3 \left(\chi_i^T(k) - \chi_i^E(k)\right)\right]^2$$

where $\chi^T(k)$ and $\chi^E(k)$ = theoretical and experimental EXAFS

FI (Fit Index) = weighted minimised sum for theoretical and experimental EXAFS.

This term can be used to indicate an improving fit but it is not comparable between data sets as it is dependent on energy range, number of points and magnitude of EXAFS. To allow comparison of the quality of fits, the *R*-factor is calculated where

Equation 2-33

$$R = \frac{\int \left|\chi^T(k) - \chi^E(k)\right| k^3 .dk}{\int \left|\chi^E(k)\right| k^3 .dk} \times 100$$

2.6.8 P – Combined Refinement Program

The Combined Refinement Program is a similar program to EXCURV98, however, powder diffraction data are also included in a simultaneous refinement of both data sets using one set of structural coordinates. The program itself was written and developed by Mr. Norman Binsted at Southampton University.

The techniques of EXAFS and PXD have often been combined in the study of materials. In most cases this is due to the complementarity of the methods with EXAFS being used to elucidate information about local environments and short-range order, whilst powder diffraction data can provide information about the structure as a whole.

2.6.8.1 Powder X-ray Diffraction

PXD is an important technique used in the characterisation of polycrystalline inorganic materials, but is dependent upon long-range order being present in a material. The form of the PXD pattern obtained is dependent upon the crystal structure a material adopts. This

structure is defined by the lattice type, crystal class, unit cell parameters and the distribution of the various ion types within the unit cell, which in turn determines the number and position of the observed reflections. The atom types and their distribution throughout the unit cell determine the intensity of the observed reflections. Rietveld refinement of the PXD data allows the derivation of a number of structural parameters exclusive to the material under study, such as lattice parameters, atomic positions, fractional occupancies, temperature factors and bond lengths.

However a number of drawbacks to the technique do exist. The ability of an atom to scatter X-rays is proportional to its atomic number and as a result it is often difficult to locate light atoms because the scattered intensity is very weak. This is a particular problem when the other atoms present are very heavy. Similarly, it is difficult to distinguish elements that have very similar atomic numbers or are isoelectronic. Also, when doping very small quantities of a different atom type into a structure, it is often difficult to locate the position of the dopant.

2.6.8.2 EXAFS

Extended X-ray Absorption Fine Structure (EXAFS) is an atom specific technique giving short-range data on the local environment of a particular element within a structure. The information available from EXAFS includes interatomic distances, the approximate nature of the neighbouring atoms (i.e. to which row of the periodic table they belong) and the approximate number of each atom type at each distance.

EXAFS does not require the presence of long-range order, therefore, it can be used to extract structural information in many phases where diffraction techniques are not definitive, such as glasses, liquids and amorphous solids. EXAFS is particularly useful in determination of minor/trace elements due to the sensitivity of the technique. It is highly element specific and therefore the data obtained from EXAFS analysis contain only the relationship between atoms of the X-ray absorbing element and its neighbours, whereas X-ray diffraction methods result in an average correlation function for the sample as a whole.

However, a number of limitations exist for EXAFS as a technique. The margin of error in the determination of structural parameters beyond the first shell is high and is therefore not as accurate as other structural methods. EXAFS is a weak phenomenon and as such an intense source of X-radiation is required to achieve an acceptable signal to noise ratio. This is provided by synchrotron radiation sources, where beam time is limited and expensive.

Due to the element specificity of EXAFS, impurity phases that contain the absorbing element will interfere with the data leading to poor results, however, other impurities will not affect

the EXAFS measurements. Further complications can arise in multi-element samples where the respective absorption edges are close together and overlap.

Finally, if the absorbing element exists in more than one environment, then the EXAFS will not characterise the separate conditions because the derived parameters are the average for that element. Therefore minor species of the probed element may not be detected.

2.6.8.3 Combined refinement

There are a number of advantages in refining EXAFS and powder diffraction spectra simultaneously, one being that no additional structural variable needs to be introduced in order to describe the EXAFS distances, even when very many shells are fitted. Consequently, the method is a far more rigorous test of the structural model than either of the techniques performed independently and should lead to a better-determined refinement.

2.6.8.4 Theory

The EXAFS theory employed in the combined refinement program (P) is very similar to that previously discussed in section 2.6. The method used is based on the fast spherical wave formalism of Gurman, Binsted and Ross [19, 30]. Ground state photoelectron potentials are calculated according to the Mattheis prescription [31, 32, 33]. Excited state corrections to the exchange and correlation potential are based on the theory of Hedin and Lundquist [34], as implemented by Lee and Beni [35]. The phaseshifts are calculated following the method of Fox and Goodwin [36]. The PXD calculations are based on the DBW code of Wiles, Sakthivel and Young [37] employing the Rietveld method (section 2.4.1).

2.6.8.5 Parameters

Theory calculation, refinement and restraints are all governed by a large number of variables. The parameters available within the combined refinement program are grouped into nine types, as described below.

1) **Cell** parameters – define the unit cell.
2) **Atomic** parameters – define fractional coordinates of the atoms within the cell, their occupancies, isotropic temperature factors and Debye-Waller factors.
3) **Shell** parameters – are defined by the number of atoms in a particular shell and the characteristics of the atom within the shell.
4) **Unit** parameters – used in the refinement of proteins and have not been used in this work.
5) **Phaseshift** parameters – are defined by the atomic number of the atoms involved.

6) **Control** parameters – examples are numerous (≈ 85) and include NS (number of shells and AH, BH and CH (peak shape parameters).
7) **XANES** parameters – used only by XANES calculation not covered in this work.
8) **Restrained refinement, bond and correlation** parameters – are defined by two shell numbers and sometimes a symmetry index.
9) **Group** symbols – define the cell or cluster symmetry.

2.6.8.6 Method

Initially, raw EXAFS and powder diffraction data sets are read into the combined refinement program – the EXAFS data is previously background subtracted using PAXAS [28] (section 2.6.7.1), powder diffraction (PD) data can be read into the program in either DBW format or GSAS format. The structural model is first defined as for a PD Rietveld analysis, in terms of a space group, positional coordinates and occupancies.

For each atom for which EXAFS data are available, the program calculates the radial distribution up to a pre-defined limit (normally 5 to 10 Å). If necessary, several clusters are generated for each structurally unique site occupied by the element in question. In some cases mixed or partially occupied sites are required and this can be included in the refinement. For each cluster, the program then determines the point group, which allows the table of radial coordinates to be reduced to a set of shell coordinates and occupation numbers, and a point group operator. One benefit of this is the efficient treatment of multiple scattering (MS) making full use of symmetry without the need for a path-sort to find equivalent paths. It is important to include MS even when it does not seem to make a large contribution to the final result. MS is particularly sensitive to short interatomic distances, and hence its inclusion helps to eliminate solutions where distances tend to refine to values that are significantly shorter than actual values. The PD and EXAFS theories are then calculated and combined EXAFS and PD curve fitting is performed using a least squares refinement. This involves minimisation of the weighted sum of squares of residuals employing non-linear least squares routine VA05A in the Harwell library [38].

In addition to the structural parameters required to describe the model, the control parameters generally refined are the PD isotropic thermal parameters, peak shape and background parameters, scale factor, and zero offset. The EXAFS energy zero EF (one per spectrum) and one or more phaseshift parameters are also refined, e.g. individual muffin-tin radii.

The quantity minimised during refinement is given by:

Equation 2-34

$$W_{exafs}\Phi_{exafs} + W_{pd}\Phi_{pd}$$

W_{exafs} and W_{pd} are the weights attached to the EXAFS and PD data sets respectively. For a combined refinement the values are normally set such that $W_{exafs} = W_{pd} = 0.5$. For EXAFS of PD only refinements the weightings $W_{exafs} = 1.0$ or $W_{pd} = 1.0$ are used respectively.

The EXAFS contribution (Φ_{exafs}) is given by:

Equation 2-35

$$\phi_{exafs} = \sum_i^N w_i^2 \left(\chi_i^{\exp}(k) - \chi_i^{th}(k)\right)^2$$

$\chi^{exp}(k)$ and $\chi^{exp}(k)$ are the experimental and theoretical EXAFS. K is the magnitude of the photoelectron wavevector. w_i, the weighting attached to a particular data point i, is normally defined for an EXAFS data point by:

Equation 2-36

$$w_i^{1/2} = \frac{k_i^n}{\sum_i^N k_j^n \left|\chi_j^{\exp}(k)\right|}$$

where n is selected to give an envelope of approximately comstant amplitude for $k^n \chi^{exp}(k)$.

Similarly the PD contribution is given by:

Equation 2-37

$$\phi_{pd} = \sum_i^N w_i \left(y_i^{\exp} - y_i^{th}\right)^2$$

where the sum over all experimental data points i with experimental and theoretical counts y^{exp} and y^{th} respectively. For a PD observation the point weighting is taken to be $w_i = 1/y_i^{exp}$.

An R-factor is defined as:

Equation 2-38

$$R_{exafs} = \sum_i^N \frac{1}{\sigma_i}\left(\left|\chi_i^{\exp}(k) - \chi_i^{th}(k)\right|\right) \times 100\%$$

which gives a meaningful indication of the quality of the fit to EXAFS data in k-space. A value of around 20% is normally considered to be a reasonable fit, with values of 10% or less being difficult to obtain on unfiltered data. R factors for PD data are as previously stated in section 2.4.

An absolute index of goodness to fit, which takes account of the degree of over determinacy in the system is given by the reduced chi squared function. The difficulty in comparing the weights for each of the data points w_i for the two techniques, and the fact that it is rarely

possible to use experimental values of w_i for EXAFS analysis (accurate distance determination requires a constant amplitude envelope over a wide k-range), complicates the derivation of a useful overall statistical criteria. An expression:

Equation 2-39

$$chi^2 = 1/(N_{ind} - p)(N_{ind} / N_{obs})\sum_i^{N_{obs}} W\, w_i \left(f_{\exp} - f_{th}\right)^2$$

is used, where N_{ind} is the number of independent data points and p the number of parameters. N_{ind} is normally less than N (number of data points). The sum is over all observations N_{obs} and W is W_{exafs}, W_{pd} or W_d according to whether the term is due to EXAFS, powder diffraction or constraint respectively. This expression does not have any absolute significance due to the artificial nature of the weightings, but changes do provide a valid statistical measure of the effect of introducing or removing variables – introducing an additional variable should result in an overall reduction in chi^2.

2.7 Synthesis Techniques

2.7.1 Conventional High-Temperature Solid-State Synthesis

The direct reaction of a mixture of solid starting materials, at high temperatures and over extended periods of time, is the most widely used method for the preparation of polycrystalline solids. In the preparation of mixed metal oxide materials, for example, a stoichiometric mixture of the component oxides is used. However, in some cases using the oxide is difficult, particularly where it may be hygroscopic or air sensitive, and often a carbonate or another oxo-salt, which will decompose on heating to give the oxide, is used. This facilitates more accurate weighing of the starting materials, which are then ground to produce an intimate mixture using a pestle and mortar, transferred to an alumina crucible and heated to the required temperature.

The reaction process between oxide starting materials occurs by diffusion of the metal cations at particle interfaces. In oxide materials the cations are the most mobile as they are usually smaller than the oxide ions. The rate of diffusion of reactants is usually very slow and therefore long reaction times are required. The most common method of increasing the rate at which the cations diffuse is by raising the reaction temperature.

A reaction between two solids will only occur when the relevant reactant particles are in contact, therefore, by maximising the number of interfaces it is possible to increase the reaction rate. This can be achieved by frequent and thorough grinding of the material both before and during the reaction to increase the overall surface area or by pelletising the ground reactants. The grinding process also aids homogeneity and thus improves the formation of a single-phase product.

2.7.2 Precursor Methods

An alternative method of producing a homogenous and very finely divided reactant mixture is through the use of precursor methods. These techniques typically involve the decomposition of a material to yield finely divided and reactive particles, which will increase the reaction rate. Examples of such precursors include metal carbonates, nitrates and hydroxides.

2.7.3 Special Atmospheres

Where a particular oxidation state or reaction stoichiometry is required the reaction environment may be controlled using a tube furnace. This allows a continuous supply of a particular gas e.g. oxygen to be passed over the reaction mixture during heating.

In some cases one or more of the components may be volatile at the necessary reaction temperature. Here the reaction mixture can be sealed in an evacuated quartz tube to prevent any loss of material.

2.8 References

[1] Woolfson M.M.., *An Introduction to X-ray Crystallography,* Cambridge University Press (1970)

[2] Cheetham A. K., Day P., *Solid State Chemistry:Techniques,* Oxford Science Publications, Clarenden Press, Oxford, 54 (1988)

[3] Hahn T., *International Tables For Crystallography,* Reidel D., Dordrecht **A.**, 26 (1983)

[4] International Centre for Diffraction Data, 12 Campus Boulevard, Newton Square, Pennsylvania 19073-3273 USA.

[5] CELL (Program to calculate cell parameters from indexed powder data), University of Oxford.

[6] Atkins P.; *Physical Chemistry,* 4th Edition Oxford University Press, 298 (1992)

[7] Larson A.C., Von Dreele R.B.; *General Structure Analysis System (GSAS).* Los Alamos National Laboratory Report LAUR, 86 (2000).

[8] Rietveld H.M.; *Acta Crystallogr.* **21** A228 (1966b)

[9] Rietveld H.M.; *J. Appl. Crystallogr.* **2** 65-71 (1969b)

[10] Weller M.T., *Inorganic Materials Chemsitry*, Oxford University Press , (1992)

[11] Buerger M.J., *Contemporary Crystallography,* McGraw-Hill (1970)

[12] Caglioti G, Paoletti A., Ricci F.P, *Nucl. Instrum. Methods,* **35** 223 (1958)

[13] Kubelka P., Munk F., *Z. Tech. Phys.* **12** 539 (1931)

[14] Kubelka P., *J. Opt. Soc. Am.* **38** 448 (1948)

[15] Teo B.K.; *EXAFS: Basic Principles and Data Analysis,* Springler-Verlag, Berlin, (1986)

[16] Andrews P., Ph.D. Thesis University of Southampton, (1993)

[17] Lee P.A.., Pendry J.B., *Phys. Rev. B.* **11** 2795 (1975)

[18] Ashley C.A., Donaich S., *Phys. Rev. B.* **11** 1279 (1975)

[19] Gurman S.J., Binsted N., Ross I., *J. Phys. C.* **17** 143 (1984)

[20] Binsted N., Campbell J.W., Gurman S.J., Stephenson PC; SERC Daresbury Laboratory EXCURV98 computer program, (1998)

[21] Binsted N., Weller M.T., Evans J.; *Physica B* **208/209** 129 (1994)

[22] Binsted N., Pack M.J., Weller M.T., Evans J.; *J. Am. Chem. Soc.* **118** 10200 (1996)

[23] Teo, B.; *J. Am. Chem. Soc.* **103** 3990 (1981)

[24] Koningsberger D.C., R. Prins, Eds, *X-ray Absorption: Principles, Applications, Techniques of EXAFS, SEXAFS and XANES,* Wiley Interscience, New York, (1988)

[25] Mosselmans J.F.W.; *Station 8.1 Manual*, Daresbury Laboratory (1994)

[26] van Dorsen G.; *Station 9.2 manual,* Daresbury Laboratory (1995)

[27] Binsted N.; *Program for Calculating EXAFS Pellet Weights,* Southampton University.

[28] Binsted N.; *PAXAS (Program for the Analysis of X-ray Absorption Spectra),* University of Southampton, (1988)

[29] Binsted N., Campbell J.W., Gurman S.J. and Stephenson P.C., ***EXCURV98*** *computer program*, SERC Daresbury Laboratory (1992)

[30] Gurman S.J., Binsted N., Ross I.; *J. Phys. C.*, **19** 1845 (1986).

[31] Mattheis LF; *Phys. Rev. B*, **8** 3719 (1973).

[32] Loucks T.L.; *Augmented Plane Wave Method*, W.A. Benjamin (New York) 1, (1967).

[33] Binsted N., Norman D.; *Phys. Rev. B*, **B49** 15531 (1994).

[34] Hedin L., Lundquist S.; *Solid State Physics,* **23** 1 (1969).

[35] Lee P.A., Beni G.; *Phys. Rev. B,* **15** 2862 (1977).

[36] Fox L., Goodwin E.T.; *Trans. Cam. Phil. Soc.,* **45** 373 (1949).

[37] Wiles D.B., Sakthivel A., Young R.A.; Georgia Institute of Technology, (1991).

[38] AERE Harwell, Harwell Subroutine Library: a catalogue of subroutines. Harwell Report AERE R 9185 (HMSO), 1-72 (1987).

Chapter 3

Manganese (V) Systems

3 Mn^{V} Systems

Mn^{V} is a d^2 transition metal ion which, when doped into tetrahedral sites within stable oxide matrices, exhibits bright colours due to a large absorption cross section [1, 2]. Indeed materials containing the Mn^{5+} ion tetrahedrally coordinated by four oxygen ions show colours ranging from deep blues through turquoise to dark green [3, 4, 5]. Thus ceramic oxide materials of this nature are of considerable interest as possible inorganic pigments.

A particular driving force for this research is that many current green pigments contain either chromium or cobalt, e.g. Cr_2O_3 and Co_2TiO_4. The former is a problem due to increasingly strict regulations that restrict the use of pigments containing heavy metals and is a particular problem due to the CrO_4^{2-} complex ion, which is carcinogenic, whilst cobalt is a relatively expensive element.

Compounds containing Mn^{V} are relatively rare, mainly due to its relative instability when compared with Mn^{II}, Mn^{III}, Mn^{IV} and Mn^{VII}, particularly when incorporated into an oxide matrix. Most of the literature work has focused on the isomorphous substitution of Mn^{V} for P^{V}, V^{V} and to a lesser extent As^{V} and in all cases it is seen that a condition necessary for the stabilisation of the Mn^{5+} ion is the presence of cations with pronounced base properties [1, 6] i.e. an alkali metal or an alkaline earth metal. Indeed the majority of this work has been concerned with doped apatite and spodiosite type structures (Figure 3-1) [1, 2, 7, 8, 9, 10, 11, 12, 13, 14, 15, 16] of general formula $A_{10}(B_{1-x}Mn_xO_4)_6X_2$ and $A_2B_{1-x}Mn_xO_4X$ (where A = Ca, Sr or Ba, B = P, V or As and X = F or Cl) respectively.

Its is also possible to incorporate the Mn^{V} ion into a number of other structures. Olazcuaga *et al.* [17] were able to stabilise Mn^{5+} in the following materials, A_3MnO_4 (where A = Na or K) and $ABMnO_4$ (where A = Na or K, B = Sr or Ba) and showed that all of the materials were isotypical with the corresponding orthovanadates. In all cases Mn^{V} is seen to adopt tetrahedral oxo coordination. The optical properties of Mn^{V} doped Li_3PO_4 and Li_3VO_4, which are isotypic with the A_3MnO_4 phases mentioned above, have also been examined in detail [7, 14]. A further aspect of compounds containing tetrahedrally coordinated Mn^{V}, besides their possible pigment applications, is the near-IR laser activity exhibited by some of these materials, including $Ba_3(V_{1-x}Mn_xO_4)_2$ [18, 19]. A complete structural investigation of $Ba_3(MnO_4)_2$, using PND, was performed by Weller *et al.* in 1999 [3] and despite the intense green colour of this compound its application as a pigment is somewhat limited by the presence of barium and the detrimental effect it has on the environment.

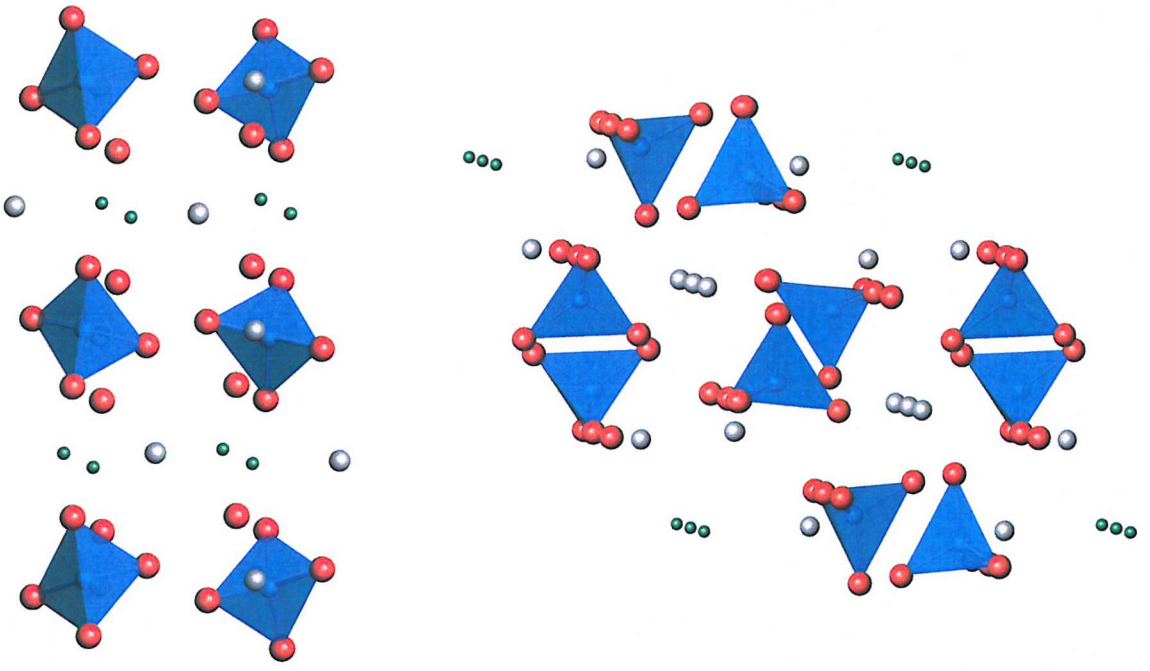

Figure 3-1: Views of the Spodiosite (left) and Apatite structures showing the BO_4 tetrahedra (where B = P, V, As, Mn).

In this section the stabilisation of Mn^V is reported through incorporation into the $NaCaV_{1-x}Mn_xO_4$ and $Na_3Ca_2V_{3-x}Mn_xO_{11}$ systems and the preparation of a complete solid solution is attempted. The effect of coordination environment and overall quantity of Mn^V on the colour of the material is studied.

The aim of this work was to find alternative hosts for the Mn^V ion with light, cheap and non-toxic counter cations and ideally with modest levels of incorporation.

3.1 $NaCaV_{1-x}Mn_xO_4$

$NaCaVO_4$, previously studied by le Flem & Olazcuaga [20] and Ijdo [21] contains discrete VO_4^{3-} tetrahedra in conjunction with Na^+ and Ca^{2+}, which are both considered to have base properties, making it an ideal template for the incorporation of the MnO_4^{3-} species.

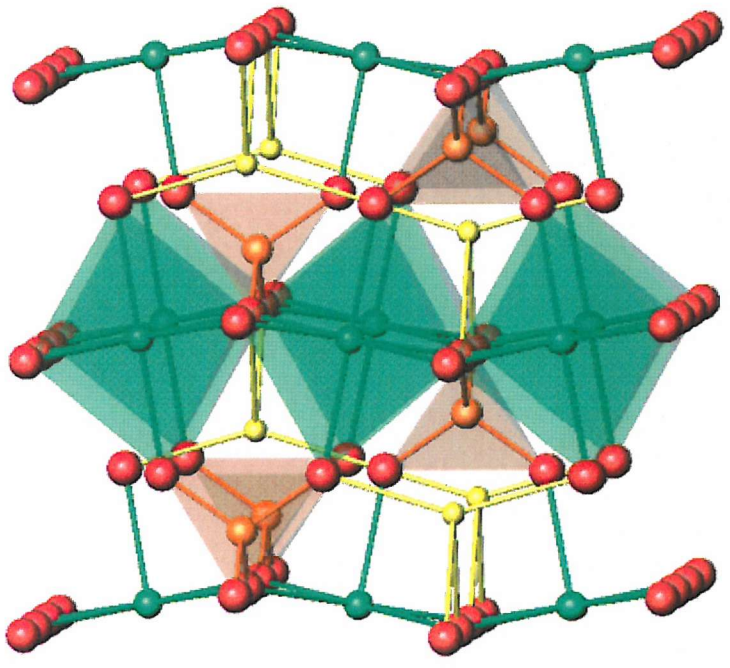

Figure 3-2: A view of the $NaCaVO_4$ structure showing VO_4 tetrahedra (orange), CaO_6 octahedra (green) and NaO_4 tetrahedra (yellow). Red spheres represent oxygen atoms.

As mentioned previously Olazcuaga *et al.*, have reported the preparation of materials of general formula $ABMnO_4$ (where A = Na or K, B = Sr or Ba) although evidently no calcium analogues were considered, i.e. $ACaMnO_4$ (where A = Na or K). The presence of calcium would be preferable to strontium or barium in a possible pigment material.

3.1.1 Synthesis

The $NaCaV_{1-x}Mn_xO_4$ (x = 0, 0.02, 0.04, 0.06, 0.08, 0.1, 0.12, 0.14, 0.16, 0.18 and 0.2) series was prepared by heating stoichiometric mixtures of sodium oxalate, calcium carbonate, manganese (III) oxide and vanadium (V) oxide (all >99%). The precursors were intimately mixed by grinding before being transferred to an alumina boat and heated under flowing oxygen to 900 °C for 48 hours. Further heating to 550 °C for 7 days yielded the final product which powder X-ray powder diffraction data revealed was the desired $NaCaVO_4$ structure

type phase. Attempts to prepare samples with $x \geq 0.1$ resulted in products with significant intensity reflections of additional phases present in the powder diffraction patterns.

The products were further studied using PXD, PND and UV-visible spectroscopy.

3.1.2 Powder X-ray Diffraction

PXD data for the series $NaCaV_{1-x}Mn_xO_4$ ($x = 0, 0.02, 0.04, 0.06, 0.08, 0.1$) were recorded on a Siemens D5000 diffractometer using Cu $K\alpha_1$ radiation ($\lambda = 1.5406$ Å) over the two-theta range 10° – 110° for 15 hours. The structure was refined using the model presented by Ijdo [21] for $NaCaVO_4$ and a least squares method as described in Chapter 2. The Mn/V fractional site occupancies for the tetrahedral site were fixed at values based upon the intended composition in each case. It was not possible to refine these site occupancies due to the near-isoelectronic nature of the Mn^{5+} and V^{5+} species. The refinements proceeded smoothly to convergence giving a good fit to the observed data and chemically sensible bond distances and angles in each case.

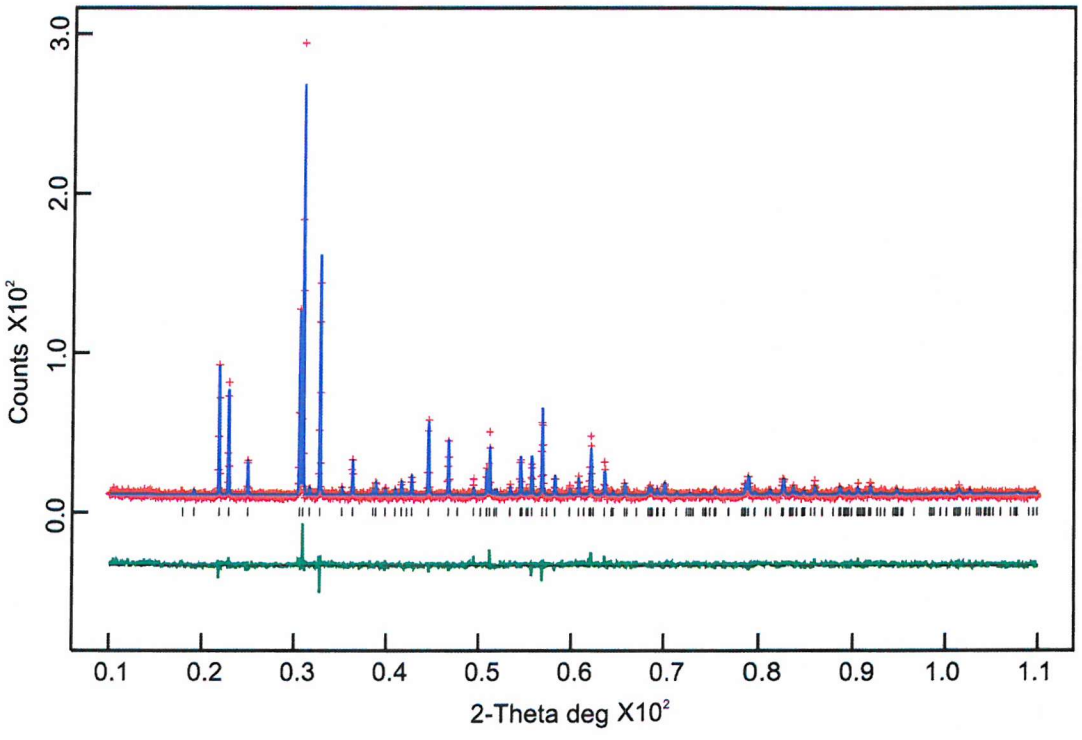

Figure 3-3:Observed (+++), Calculated (—), and difference (shown underneath) PXD profiles for $NaCaV_{0.92}Mn_{0.08}O_4$. Tick marks indicate reflection positions.

The derived lattice parameters, and hence cell volume (Figure 3-4), indicate a linear dependence upon the manganese concentration in accordance with Vegard's law. Often departure from Vegard's law [22] in solid solutions indicates clustering of the dopant [23]. It can therefore be assumed that the Mn^V ions are probably randomly distributed throughout the

materials. This trend also confirms that the manganese is being incorporated into the structure rather than forming impurity phases. However, the variation is slightly more complicated if the lattice parameters are considered separately, since *a* and *b* decrease as expected given the respective ionic radii for Mn^{5+} and V^{5+}, 0.33 Å and 0.35 Å, while *c* increases.

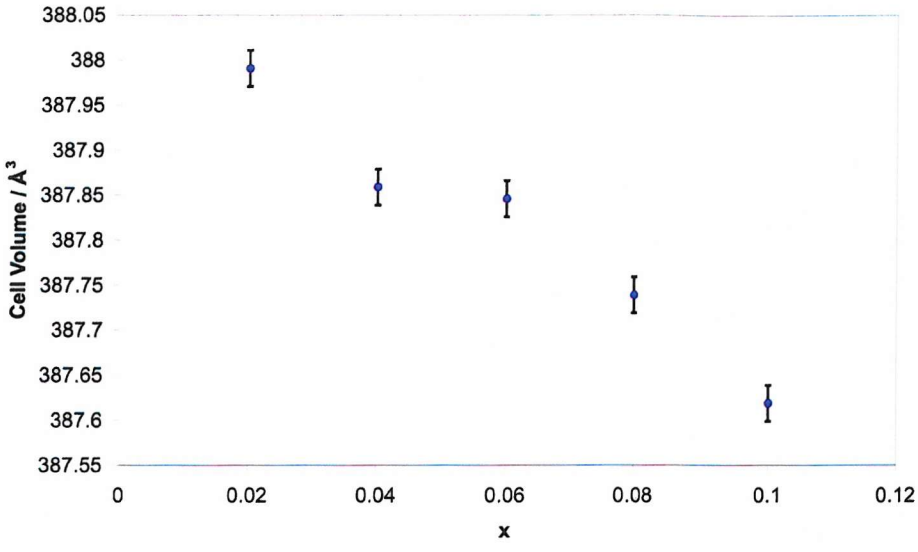

Figure 3-4: Variation of unit cell volume as a function of x for the $NaCaV_{1-x}Mn_xO_4$ system.

3.1.3 Powder Neutron Diffraction

Neutron diffraction is an excellent technique for the study of mixed metal oxide systems. Firstly because the scattering power of oxygen with respect to neutrons is greater than for X-rays, thus allowing the identification of oxygen atom positions to a greater degree of accuracy than for PXD. Secondly the scattering length of an element during X-ray diffraction is dependent upon the number of electrons, therefore neighbouring transition metal elements, in the periodic table, are very difficult to distinguish. However, the scattering lengths of neutrons for neighbouring atoms are often very different allowing fractional occupancies to be determined more readily. This allows the metal-oxygen polyhedra to be delineated more accurately than by X-ray diffraction thus yielding more accurate bond lengths and site occupancies.

In the case of the $NaCaV_{1-x}Mn_xO_4$ system, neutron diffraction data were used to extract details about the MO_4^{3-} (M = V, Mn) tetrahedral environment. The neutron scattering lengths

[24] of vanadium and manganese (V = -0.3824 fm and Mn = -3.73 fm) are sufficiently different to enable the determination of site occupancy values for the mixed site.

Time of flight (TOF) powder neutron diffraction data were collected on the GEM (x = 0, 0.02, 0.04, 0.06, 0.10) and POLARIS (x = 0.08, 0.20) diffractometers at the Rutherford Appleton Laboratory, Oxfordshire, UK. All samples were run at room temperature for 100 μAh and data obtained from the low angle, 75°, 90° and backscattering banks were used in the analysis. Rietveld refinements were performed using the PC package, GSAS [25]. Literature [21] values were used as the initial model for $NaCaVO_4$ (x = 0), subsequent refinements utilised the values obtained in the preceding refinement. A uniform approach to the structure refinement was undertaken for each of the data sets obtained with different x values to ensure consistent results. Initially the background was modelled and the lattice parameters were refined to accurately locate the reflections. The peak profiles were then refined and the atomic positions varied. Finally, isotropic temperature factors and fractional site occupancy of the V/Mn site were added to the refinement. Due to the very low concentration of manganese being considered and the extremely poor scattering length for vanadium, refinement of the site occupancies led to unreasonable values being obtained. Therefore, due to the absence of any secondary phases the site occupancies were constrained to agree with the intended stoichiometry. The temperature factors for the V/Mn site also yielded unreasonable values for the same reasons and were thus fixed at a sensible value. Finally, the refinement of the vanadium site position for x = 0 was not possible, again due to the poor neutron scattering length associated with vanadium.

The refinements proceeded smoothly to convergence giving a good fit to the observed data and chemically sensible bond distances and angles in each case. The refinement profile for $NaCaV_{0.92}Mn_{0.08}O_4$ and tables of crystallographic data and refinement statistics for each phase are presented in Figure 3-5 and Table 3-1 to Table 3-7.

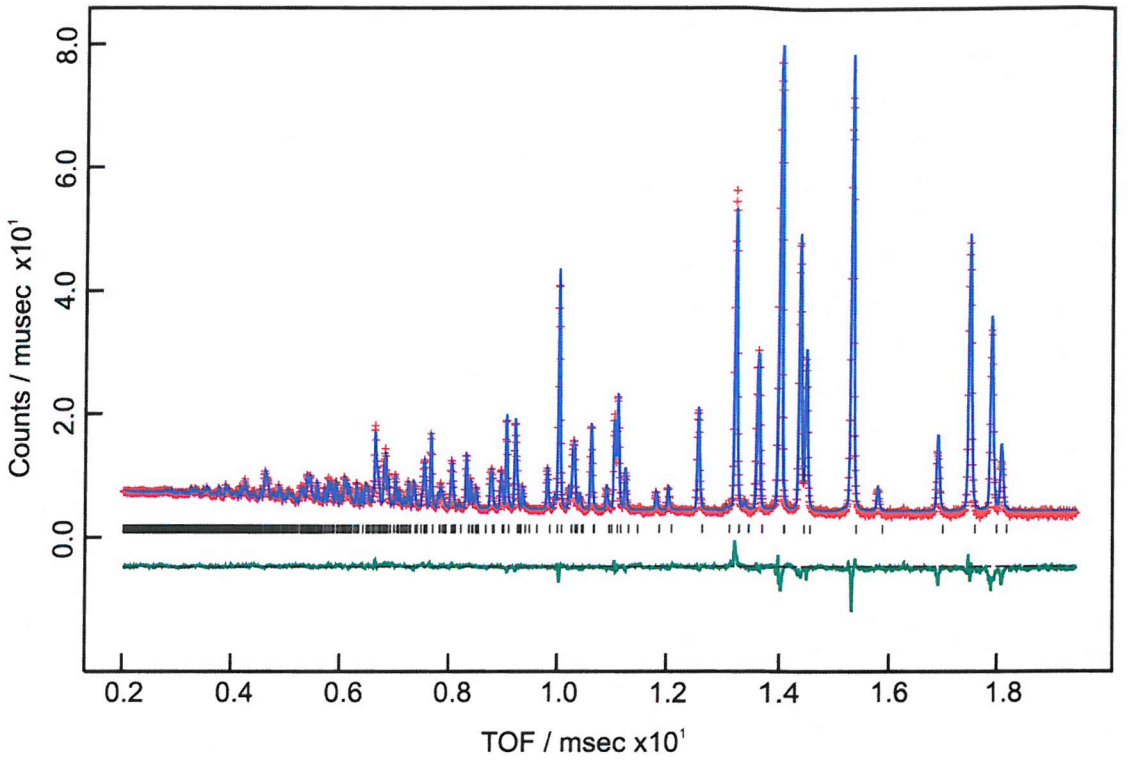

Figure 3-5:Observed (+++), Calculated (—), and difference (shown underneath) PND profiles for $NaCaV_{0.92}Mn_{0.08}O_4$. Tick marks indicate reflection positions.

Table 3-1. Refined crystallographic data for $NaCaVO_4$ (e. s. d. s are shown in parentheses).

Space group: *Cmcm*

Lattice parameters a = 5.8884(5) Å, b = 9.3301(8) Å, c = 7.1783(6) Å

Atom	*x*	*y*	*z*	*Frac.*	U_{iso} /Å^2
Na	0	.1809(2)	.25	1	.0194(4)
Ca	0	0.5	0	1	.0104(4)
V	0	.855	.25	1	.01
O1	.2592(1)	.46227(6)	.25	1	.0084(2)
O2	0	.25287(6)	.55923(8)	1	.0125(2)

Final fit parameters:χ^2 = 2.879, R_{wp} = 2.97 %, R_p = 2.85 %

Table 3-2. Refined crystallographic data for $NaCaV_{0.98}Mn_{0.02}O_4$ (e. s. d. s are shown in parentheses).

Space group: C*mcm*

Lattice parameters a = 5.85421(6) Å, b = 9.2771(1) Å, c = 7.13820(9) Å

Atom	*x*	*y*	*z*	*Frac.*	U_{iso} /Å^2
Na	0	.1815(2)	.25	1	.0183(5)
Ca	0	0.5	0	1	.0103(3)
V	0	.854(2)	.25	.98	.01
Mn	0	.854(2)	.25	.02	.01
O1	.2591(1)	.46238(8)	.25	1	.0080(2)
O2	0	.25280(8)	.5590(1)	1	.0122(2)

Final fit parameters:χ^2 = 8.307, R_{wp} = 3.89 %, R_p = 3.89 %

Table 3-3. Refined crystallographic data for $NaCaV_{0.96}Mn_{0.04}O_4$ (e. s. d. s are shown in parentheses).

Space group: C*mcm*

Lattice parameters a = 5.85793(6) Å, b = 9.2842(1) Å, c = 7.14490(8) Å

Atom	*x*	*y*	*z*	*Frac.*	U_{iso} /Å^2
Na	0	.1814(2)	.25	1	.0198(4)
Ca	0	0.5	0	1	.0101(3)
V	0	.853(2)	.25	.96	.01
Mn	0	.853(2)	.25	.04	.01
O1	.2588(1)	.46243(7)	.25	1	.0087(2)
O2	0	.25276(8)	.5592(1)	1	.0127(2)

Final fit parameters:χ^2 = 7.090, R_{wp} = 4.02 %, R_p = 3.85 %

Table 3-4. Refined crystallographic data for $NaCaV_{0.94}Mn_{0.06}O_4$ (e. s. d. s are shown in parentheses).

Space group: C*mcm*

Lattice parameters a = 5.85486(5) Å, b = 9.27945(9) Å, c = 7.14151(7) Å

Atom	*x*	*y*	*z*	*Frac.*	U_{iso} /Å^2
Na	0	.1816(2)	.25	1	.0193(4)
Ca	0	0.5	0	1	.0102(2)
V	0	.8524(9)	.25	.94	.01
Mn	0	.8524(9)	.25	.06	.01
O1	.2589(1)	.46249(6)	.25	1	.0082(2)
O2	0	.25287(7)	.5591(1)	1	.0124(2)

Final fit parameters:χ^2 = 5.174, R_{wp} = 3.46 %, R_p = 3.43 %

Table 3-5. Refined crystallographic data for $NaCaV_{0.92}Mn_{0.08}O_4$ (e. s. d. s are shown in parentheses).

Space group: C*mcm*

Lattice parameters a = 5.86557(7) Å, b = 9.2978(2) Å, c = 7.15788(9) Å

Atom	*x*	*y*	*z*	*Frac.*	U_{iso} /Å^2
Na	0	.1820(2)	.25	1	.0195(4)
Ca	0	0.5	0	1	.0084(2)
V	0	.8520(9)	.25	.92	.01
Mn	0	.8520(9)	.25	.08	.01
O1	.2590(1)	.46237(8)	.25	1	.0081(2)
O2	0	.25264(9)	.5586(1)	1	.0121(2)

Final fit parameters:χ^2 = 4.739, R_{wp} = 2.10 %, R_p = 4.03 %

Table 3-6. Refined crystallographic data for $NaCaV_{0.90}Mn_{0.10}O_4$ (e. s. d. s are shown in parentheses).

Space group: *Cmcm*

Lattice parameters a = 5.88501(7) Å, b = 9.3281(2) Å, c = 7.1795(1) Å

Atom	*x*	*y*	*z*	*Frac.*	U_{iso} /Å^2
Na	0	.1828(3)	.25	1	.0229(6)
Ca	0	0.5	0	1	.0084(3)
V	0	.846(1)	.25	.90	.01
Mn	0	.846(1)	.25	.10	.01
O1	.2601(2)	.46173(9)	.25	1	.0091(2)
O2	0	.2527(1)	.5588(1)	1	.0125(2)

Final fit parameters:$\chi^2 = 9.619$, $R_{wp} = 3.35$ %, $R_p = 2.73$ %

Table 3-7. Refined crystallographic data for $NaCaV_{0.80}Mn_{0.20}O_4$ (e. s. d. s are shown in parentheses).

Space group: *Cmcm*

Lattice parameters a = 5.8617(2) Å, b = 9.2930(3) Å, c = 7.1544(3) Å

Atom	*x*	*y*	*z*	*Frac.*	U_{iso} /Å^2
Na	0	.1831(6)	.25	1	.023(2)
Ca	0	0.5	0	1	.0069(6)
V	0	.855(3)	.25	.80	.01
Mn	0	.855(3)	.25	.20	.01
O1	.2606(4)	.4616(3)	.25	1	.0098(3)
O2	0	.2522(3)	.5592(3)	1	.0112(3)

Final fit parameters:$\chi^2 = 8.830$, $R_{wp} = 2.94$ %, $R_p = 3.86$ %

3.1.4 Impurity Phase

For all samples where $x \geq 0.1$ additional impurity peaks were present in the diffraction data. The impurity itself could not be identified but is assumed to contain manganese as the intensity of the reflections increases with increasing x. It can therefore be inferred that the limit of manganese substitution for the $NaCaV_{1-x}Mn_xO_4$ system occurs at x = 0.08.

3.1.5 Interatomic Distances and Angles

The metal-oxygen distances and bond angles, derived from the Rietveld refinements, are shown in Table 3-8 and Table 3-10, and compared with literature data for $NaCaVO_4$ in Table 3-9 and Table 3-10. The distances shown for the tetrahedral $(V, Mn)^{5+}$ site are averages of the metal-oxygen bond lengths within the structure as the site contains two different metals. One would expect the values therefore, to lie in-between the bond lengths of the end members $NaCaVO_4$ and $NaCaMnO_4$, where the site would be occupied exclusively by V^{5+} or Mn^{5+} respectively.

Table 3-8: Derived bond distances (Å) for the $NaCaMO_4$ ($M = V_{1-x}Mn_x$) system as a function of x. (e. s. d. s are shown in parentheses).

Distance / Å	*0*	*.02*	*.04*	*.06*	*.08*	*.10*
Na_O1 (x2)	2.484(2)	2.474(2)	2.476(2)	2.475(2)	2.484(2)	2.499(2)
Na_O2 (x2)	2.319(1)	2.303(1)	2.306(1)	2.304(1)	2.304(1)	2.311(2)
Ca_O1 (x4)	2.3818(5)	2.3680(5)	2.3686(5)	2.3678(4)	2.3733(5)	2.3856(6)
Ca_O2 (x2)	2.3446(7)	2.3317(8)	2.3340(7)	2.3326(6)	2.3378(8)	2.3452(9)
M_O1 (x2)	1.735(7)	1.731(8)	1.742(6)	1.743(5)	1.747(5)	1.779(6)
M_O2 (x2)	1.700(7)	1.686(8)	1.678(6)	1.676(5)	1.681(5)	1.651(5)
Average	**1.717**	**1.709**	**1.710**	**1.710**	**1.714**	**1.715**

Table 3-9: Literature bond distances (Å) for $NaCaVO_4$. (e. s. d. s are shown in parentheses).

Distance	Ijdo - $NaCaVO_4$ [21]
Na_O1 (x2)	2.474(4)
Na_O2 (x2)	2.317(2)
Ca_O1 (x4)	2.378(1)
Ca_O2 (x2)	2.334(2)
V_O1 (x2)	1.690(18)
V_O2 (x2)	1.734(20)
Average	**1.712**

Table 3-10: Derived bond angles (°) for the $NaCaMO_4$ ($M = V_{1-x}Mn_x$) system as a function of x. (e. s. d. s are shown in parentheses).

Angle	*0*	*.02*	*.04*	*.06*	*.08*	*.10*
O1_Na_O1	69.63(5)	69.51(6)	69.61(6)	69.54(5)	69.39(6)	68.80(7)
O1_Na_O2 (x4)	103.76(3)	103.66(4)	103.65(4)	103.62(3)	103.56(4)	103.46(4)
O2_Na_O2	146.32(7)	146.60(9)	146.61(9)	146.69(8)	146.9(1)	147.3(2)
O1_Ca_O1 (x2)	100.31(3)	100.33(3)	100.41(3)	100.39(3)	100.40(3)	100.19(4)
O1_Ca_O2 (x4)	90.50(2)	90.50(3)	90.47(3)	90.46(2)	90.57(3)	90.67(3)
O1_M_O1	109.6(6)	109.1(7)	108.4(6)	108.2(5)	108.0(5)	105.1(5)
O1_M_O2 (x4)	109.97(2)	109.96(2)	109.94(2)	109.96(2)	109.88(3)	109.77(4)
O2_M_O2	107.3(6)	107.9(7)	108.7(6)	108.8(5)	109.3(5)	112.5(5)
Average	**108.96**	**108.99**	**109.01**	**109.00**	**109.06**	**109.12**

Table 3-11: Literature bond angles (°) for $NaCaVO_4$. (e. s. d. s are shown in parentheses).

Angle	Ijdo - $NaCaVO_4$ [21]
O1_Na_O1	69.5(1)
O1_Na_O2 (x4)	103.8(1)
O2_Na_O2	146.2(2)
O1_Ca_O1 (x2)	100.1(1)
O1_Ca_O2 (x4)	90.4(1)
O1_M_O1	113.1(18)
O1_M_O2 (x4)	110.0(1)
O2_M_O2	103.5(17)
Average	**108.87**

3.1.6 $(V_{1-x}Mn_x)^{5+}$ Tetrahedral Site

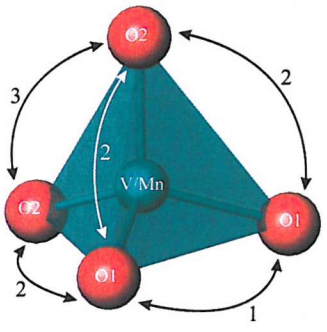

Figure 3-6: $V_{1-x}Mn_x$ (green) – oxygen (red) tetrahedral site in $NaCaV_{1-x}Mn_xO_4$

It can be seen from the derived data that there is a consistent variation in the geometry of the M^{5+} site as the manganese content is increased.

As x increases the M – O1 bond lengths show an overall increase, 1.735(7) Å (x = 0) to 1.747(5) Å (x = 0.08). Conversely the M – O2 bond lengths show an overall decrease, 1.700(7) Å (x = 0) to 1.681(5) Å (x = 0.08). The bond angles (Figure 3-6) also vary steadily with the incorporation of manganese and appear to do so in a linear fashion. The O1_M_O1 angle (1) decreases in size by 1.6 ° (x = 0 to x = 0.08) as shown in Figure 3-7, the four O1_M_O2 angles (2) remain approximately constant throughout the range and the O2_M_O2 angle (3) increases by 2 ° (Figure 3-7). These data suggest that the MnO_4^{3-} ion imposes its own geometry upon the host lattice rather than *vice versa.* Dardenne *et al.* [13] also found, for Mn^V substituted phosphates, that this ion imposes its own size upon the host lattice. This would be difficult to observe in cases where the Mn^V is doped into V^V sites due to the similarity in their respective ionic radii [26], 0.33 Å and 0.355 Å, and hence the observed bond lengths.

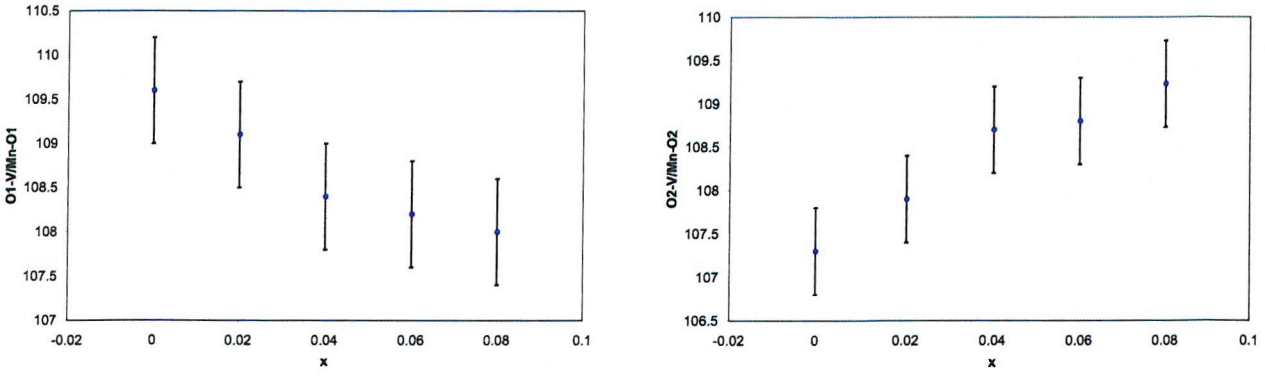

Figure 3-7: Variation of the O1-M-O1 (left) and O2-M-O2 (right) bond angles (where M = $V_{1-x}Mn_x$) as a function of x for the $NaCaV_{1-x}Mn_xO_4$ system.

3.1.6.1 Distortion of the $(V_{1-x}Mn_x)^{5+}$ Tetrahedral Site

A measure of the distortion of the tetrahedral site can be calculated using the following equation:

$$Td_{dist} = (\Sigma\ |\theta_{obs} - \theta_{Td}|) / 6 \qquad \textbf{Equation 3-1}$$

where θ_{obs} = the observed bond angle and θ_{Td} = the ideal tetrahedral angle (109.48 °).

The greater the calculated $Td_{distortion}$ value the greater the deviation from an ideal tetrahedral environment; a value of 0 indicates a perfect tetrahedron with no distortion.

The calculation was performed for materials in the series $NaCaV_{1-x}Mn_xO_4$ (x = 0, 0.02, 0.04, 0.06, 0.08) and results are presented in Table 3-12 and Figure 3-8.

Table 3-12: Tetrahedral distortion values for the MO_4^{3-} (M = V, Mn) site in $NaCaV_{1-x}Mn_xO_4$. Values calculated using equation 3-1.

x	$Td_{distortion}$
0	0.71
0.02	0.646667
0.04	0.616667
0.06	0.646667
0.08	0.543333

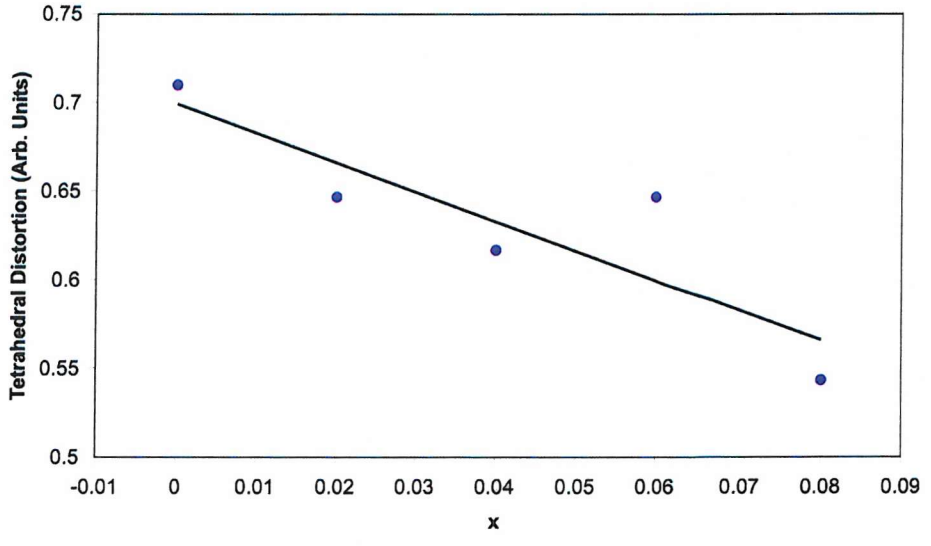

Figure 3-8: Tetrahedral distortion values as a function of x for the $NaCaV_{1-x}Mn_xO_4$ series.

The calculated $Td_{distortion}$ values suggest that the V/Mn coordination environment becomes more regular as x increases. This serves to further highlight the fact that the MnO_4^{3-} ion tends to impose its own geometry upon the host lattice, as mentioned earlier.

3.1.7 UV-Visible Spectroscopy

UV visible data were collected on undiluted samples for the $NaCaV_{1-x}Mn_xO_4$ system, according to the method outlined in Chapter 2. These are shown in Figure 3-11.

There are three spin-allowed *d-d* transitions expected for Mn^V (d^2 electronic configuration) in a regular tetrahedral environment, T_d:

$$^3A_2 \rightarrow {}^3T_2$$
$$^3A_2 \rightarrow {}^3T_1(^3F)$$
$$^3A_2 \rightarrow {}^3T_1(^3P)$$

The $^3A_2 \rightarrow {}^3T_2$ transition is symmetry forbidden and the $^3A_2 \rightarrow {}^3T_1(^3P)$ transition corresponds to a two-electron jump [15], therefore they are both expected to be weak. The $^3A_2 \rightarrow {}^3T_1(^3F)$ transition will give rise to a strong absorption band within the visible range.

The figure below (Figure 3-9) shows the orbital splitting for a deviation from the idealised tetrahedral environment. The lowering of symmetry from T_d to C_{3v} and C_s leads to a change of selection rules and the transition to the former $^3T_2$ state becomes symmetry allowed. It also leads to the splitting of states, which were degenerate in regular tetrahedral symmetry. It has been observed [13] that these modifications influence the colour of Mn^V doped materials by broadening of the $^3A_2 \rightarrow {}^3T_1(^3F)$ band and/or shifting some of the $^3T_2$ and $^3T_1(^3P)$ energy sub-states into the red and blue parts of the visible spectrum.

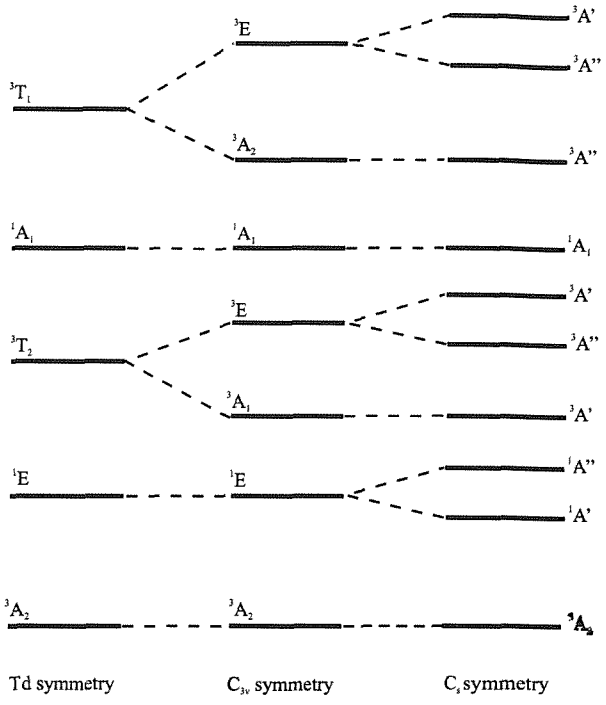

Figure 3-9: Schematic representation of the energy level structure of Mn^V according to the reduction of symmetry $T_d \rightarrow C_{3v} \rightarrow C_s$.

The diffuse reflectance spectrum for $NaCaV_{0.9}Mn_{0.1}O_4$ is shown below (Figure 3-10) and the different bands associated with *d-d* transitions for Mn^{5+} have been assigned according to literature results for other Mn^V doped materials [10, 15]. As expected the spectrum is dominated by the $^3A_2 \rightarrow {}^3T_1(^3F)$ transition, which occurs at *ca.* 700 nm and appears to be a broad single band suggesting that the Mn^V environment is a near-regular tetrahedral one. Further components to this band might suggest that the environment is distorted towards C_{3v} and C_s. The intense absorption band, labeled CT, corresponds to an oxygen ion to manganese orbital charge transfer and occurs at *ca.* 350 nm. The position and assignment of the absorption bands for $NaCaV_{0.9}Mn_{0.1}O_4$ are shown in Table 3-13.

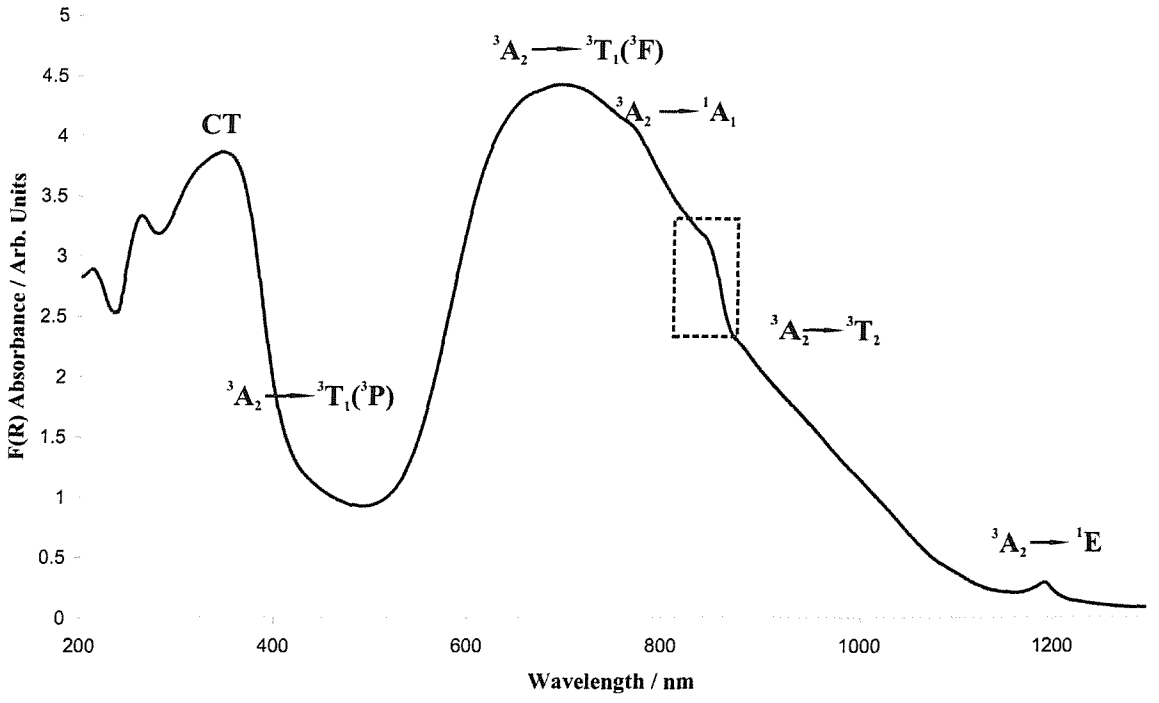

Figure 3-10: Diffuse reflectance spectrum of $NaCaV_{0.90}Mn_{0.10}O_4$ transformed according to the Kubelka-Munk function (the hashed box indicates a spectrometer glitch caused by transition through the wavelength range).

Table 3-13: Position and assignment of absorption bands for $NaCaV_{0.90}Mn_{0.10}O_4$.

Wavelength / nm	*Transition*
1190	$^3A_2 \rightarrow {}^1E$
ca. 880	$^3A_2 \rightarrow {}^3T_2$
763	$^3A_2 \rightarrow {}^1A_1$
ca. 694	$^3A_2 \rightarrow {}^3T_1(^3F)$
ca. 419	$^3A_2 \rightarrow {}^3T_1(^3P)$
344	CT

The colour of the compounds obtained in the system $NaCaV_{1-x}Mn_xO_4$, range from turquoise-blue to green as the manganese concentration increases. Close inspection of the spectra indicates that the change in colour is apparently caused by a red shift of the charge transfer band, which overlaps the weak $^3A_2 \rightarrow {}^3T_1(^3P)$ transition, leading to a sharper colour-determining minimum in the green part of the visible spectrum *ca.* 500nm. The position of the *d-d* transitions, however, appears to remain unchanged as x increases.

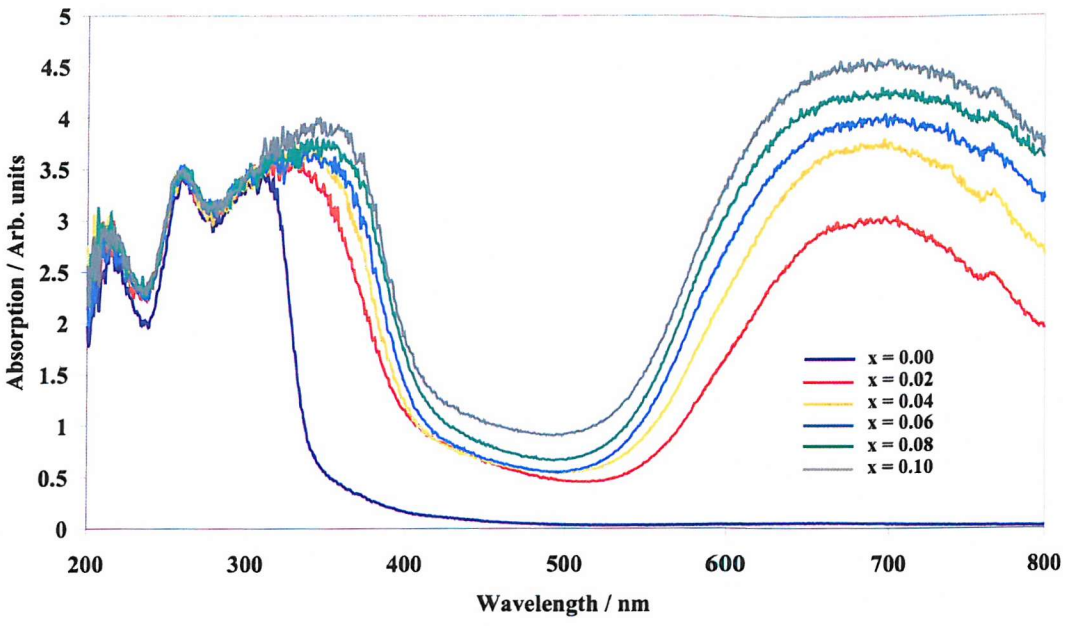

Figure 3-11: Diffuse reflectance spectra of the $NaCaV_{1-x}Mn_xO_4$ solid solution transformed according to the Kubelka-Munk function

The spectra shown in Figure 3-11 reveal an almost linear dependence of absorption intensity upon manganese content, x. The fact that it is not completely linear may be due to small discrepancies in the manganese content that cannot be detected accurately by PXD or PND alone.

3.1.8 Conclusions

The substitution of Mn^V into the tetrahedral V^{5+} site in $NaCaVO_4$ gives rise to intense turquoise to green colouration. The synthesis and characterisation of the $NaCaV_{1-x}Mn_xO_4$ solid solution has been achieved for x = 0, 0.02, 0.04, 0.06, 0.08 and 0.10, with the limit of substitution occurring at x = 0.08. Members of the solid solution where $x \geq 0.10$ were not observed as single phase products and the colour observed degraded over time, first to a weak grey/violet colour then to a dark grey/brown colour.

The MnO_4^{3-} ion imposes its own size and geometry upon the host lattice rather than adopting the environment of the ion it replaces in the host lattice.

This material is unsuitable for application as a pigment due to the degradation of the colour over time except for those materials with minimal manganese incorporation, whose colours are weak.

3.2 Synthesis and Structure of $Na_3Ca_2V_3O_{11}$

Sodium calcium orthovanadate pyrovanadate ($Na_3Ca_2(VO_4)(V_2O_7)$) was discovered by Murashova *et al.* [27] in 1988 and was characterised using single crystal X-ray diffraction. So far it is the only example of a double vanadate that contains both VO_4^{3-} and $V_2O_7^{4-}$ discrete anionic groups. As for $NaCaVO_4$ the main reason for studying this material is the presence of discrete VO_4^{3-} tetrahedra in conjunction with the basic nature of Na^+ and Ca^{2+}, possibly facilitating the incorporation of the MnO_4^{3-}. The complexity of the structure is also of interest, containing three types of Ca^{2+} environment, three types of Na^+ environment and three different VO_4 tetrahedra. Its also has eleven different oxygen positions, therefore powder neutron diffraction will be used to provide more accurate atomic positions and to study the various MO_x environments.

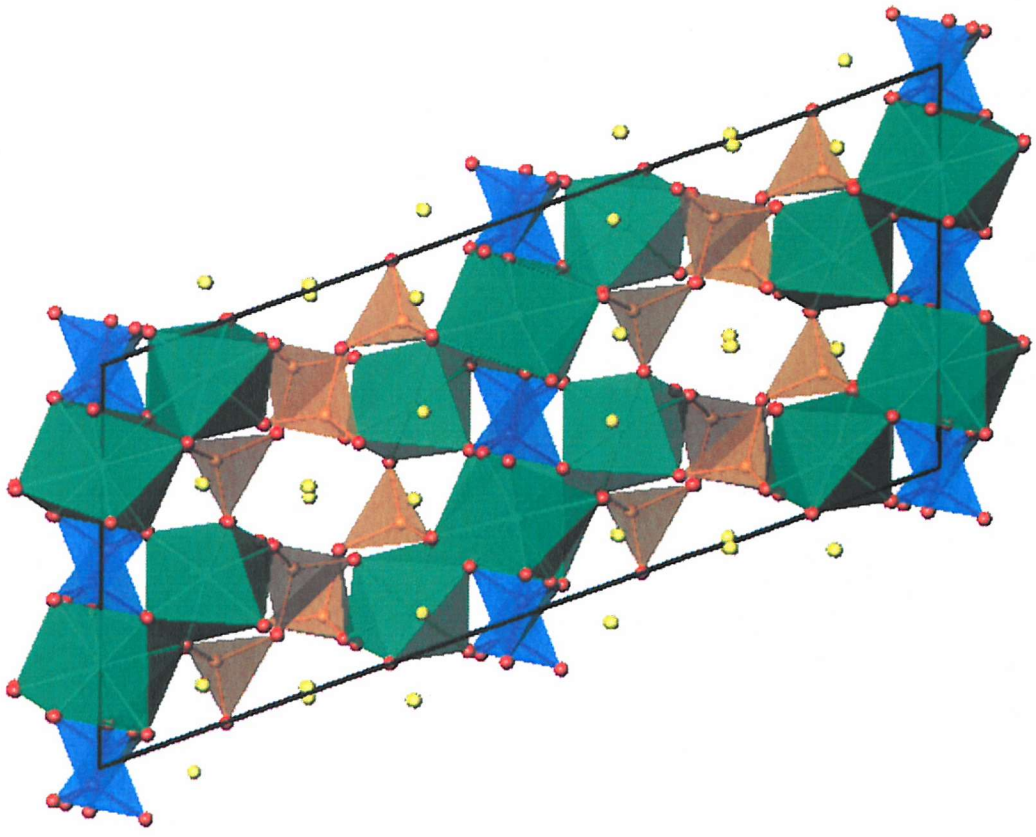

Figure 3-12: A view of the structure of $Na_3Ca_2(VO_4)(V_2O_7)$ showing VO_4^{3-} (blue) and $V_2O_7^{4-}$ (orange) units. Calcium polyhedra and sodium atoms are shown in green and yellow respectively. Red spheres represent oxygen atoms.

3.2.1 Synthesis

$Na_3Ca_2V_3O_{11}$ was prepared by heating stoichiometric mixtures of sodium carbonate, calcium carbonate and ammonium vanadate (NH_4VO_3) (all >99%). The precursors were intimately

mixed by grinding before being transferred to an alumina crucible and heated initially for 1 hour at 350 °C to allow decomposition of the precursors. Further heating to 600 °C for 20 hours yielded the final product which powder X-ray powder diffraction data revealed was the desired single-phase product.

Attempts to incorporate the MnO_4^{3-} species into this material resulted in light grey coloured multi-phase products. The use of elevated temperatures to aid the incorporation, as described for $NaCaV_{1-x}Mn_xO_4$ (section 3.1.1), caused the samples to melt and therefore could not be used.

The products were further studied using PXD and PND.

3.2.2 Powder X-ray Diffraction

PXD data for $Na_3Ca_2V_3O_{11}$ were recorded on a Siemens D5000 diffractometer using Cu $K\alpha_1$ radiation (λ = 1.5406 Å) over the two-theta range 10° – 110° for 15 hours. The structure was refined using the model presented by Murashova *et al.* (27) and a least squares method as described in Chapter 2. Due to the complexity of the structure it was not possible to obtain sensible temperature factors for all of the atomic positions individually, therefore these values were fixed at a sensible value. The refinement proceeded to convergence giving a reasonably good fit to the observed data and chemically sensible bond distances and angles. Refinement details are presented in Table 3-14.

Table 3-14: Refined crystallographic data for $Na_3Ca_2V_3O_{11}$ (e. s. d. s are shown in parentheses).

Space group: *C2/c*

Lattice parameters a = 23.7194(9) Å, b = 8.6563(4) Å, c = 10.8519(4) Å and β = 109.899(3) °

Atom	*x*	*y*	*z*	U_{iso} /Å^{2}x*100*
V(1)	-.01447(8)	0.262(3)	0.140(2)	1.00
V(2)	-0.2273(7)	0.248(3)	0.330(2)	1.00
V(3)	0.0013(9)	0.233(3)	-0.058(2)	1.00
Ca(1)	0	0.019(4)	0.25	1.00
Ca(2)	0	0.445(4)	0.25	1.00
Ca(3)	0.117(1)	-0.060(3)	0.105(3)	1.00
Na(1)	0.231(2)	0.466(5)	0.468(4)	1.00
Na(2)	0.331(2)	0.253(6)	0.165(3)	1.00
Na(3)	0.124(2)	0.539(5)	0.118(5)	1.00
O(1)	-0.135(3)	0.240(9)	0.0034(7)	1.00
O(2)	-0.226(3)	0.230(8)	0.174(5)	1.00
O(3)	-0.089(3)	0.428(8)	0.358(7)	1.00
O(4)	-0.1338(3)	0.092(7)	0.285(7)	1.00
O(5)	-0.237(3)	0.414(8)	0.422(7)	1.00
O(6)	-0.196(3)	0.104(6)	0.460(6)	1.00
O(7)	0.347(3)	0.247(7)	0.195(5)	1.00
O(8)	0.059(3)	0.140(7)	-0.009(6)	1.00
O(9)	-0.062(3)	0.214(6)	0.863(5)	1.00
O(10)	-0.0285(3)	0.275(6)	0.188(6)	1.00
O(11)	0.040(3)	0.387(7)	-0.082(6)	1.00

Final fit parameters:χ^2 = 0.2115, R_{wp} = 10.92 %, R_p = 8.41 %

3.2.3 Powder Neutron Diffraction

In order to delineate the oxygen positions more accurately, time of flight (TOF) powder neutron diffraction data were collected on the POLARIS diffractometer at the Rutherford Appleton Laboratory, Oxfordshire, UK. The sample was run at room temperature for 100 μAh and data obtained from the backscattering banks were used in the analysis. A Rietveld refinement was performed using literature [27] values as the initial model for $Na_3Ca_2V_3O_{11}$

and the PC package, GSAS [25]. A uniform approach to the structure refinement was undertaken as described previously. The temperature factors and positional coordinates for the three vanadium sites were fixed at sensible values, due to the poor neutron scattering length associated with vanadium. The refinement proceeded smoothly to convergence giving a good fit to the observed data and chemically sensible bond distances and angles. The refinement profile for $Na_3Ca_2V_3O_{11}$ and tables of crystallographic data and refinement statistics are presented in Table 3-15.

Table 3-15: Refined crystallographic data (PND) for $Na_3Ca_2V_3O_{11}$ (e. s. d. s are shown in parentheses).

Space group: *C2/c*

Lattice parameters a = 23.7994(6) Å, b = 8.6886(2) Å, c = 10.8834(3) Å and β = 109.897(2) °

Atom	*x*	*y*	*z*	U_i/U_e (×100)
V(1)	-0.141	0.271	0.189	0.5
V(2)	-0.221	0.295	0.316	0.5
V(3)	0.009	0.280	-0.063	0.5
Ca(1)	0	0.0302(2)	0.25	0.7(3)
Ca(2)	0	0.444(3)	0.25	0.6(2)
Ca(3)	0.1254(6)	-0.061(2)	0.1145(2)	0.8(1)
Na(1)	0.243(2)	0.429(2)	0.504(3)	3.8(6)
Na(2)	0.3736(7)	0.231(3)	0.111(2)	3.1(5)
Na(3)	0.1124(8)	0.5451(2)	0.090(2)	2.3(5)
O(1)	-0.1557(4)	0.254(2)	-0.0051(7)	0.9(2)
O(2)	-0.2132(3)	0.248(2)	0.1723(9)	1.2(2)
O(3)	-0.1032(6)	0.424(2)	0.229(2)	1.8(4)
O(4)	-0.0996(5)	0.088(2)	0.229(2)	1.2(3)
O(5)	-0.1937(5)	0.399(2)	0.418(2)	1.6(3)
O(6)	-0.2084(6)	0.0947(2)	0.398(2)	2.6(4)
O(7)	0.3040(5)	0.2878(2)	0.214(1)	2.6(4)
O(8)	0.0517(6)	0.092(2)	-0.039(2)	1.5(4)
O(9)	-0.0556(5)	0.217(2)	0.836(1)	1.1(3)
O(10)	-0.0108(4)	0.239(2)	0.1011(7)	0.2(2)
O(11)	0.0461(5)	0.404(2)	-0.058(2)	0.8(3)

Final fit parameters: $\chi^2 = 9.098$, $R_{wp} = 4.59$ %, $R_p = 5.49$ %

3.2.4 Interatomic distances and Angles

Metal-oxygen distances and bond angles, derived from the Rietveld refinements, are shown in Table 3-16 to Table 3-19.

3.2.4.1 Vanadium Tetrahedra

There are three different vanadium tetrahedra within the $Na_3Ca_2(VO_4)(V_2O_7)$ structure. One forms a discrete VO_4^{3-} unit, whilst the remaining two tetrahedra form a $V_2O_7^{4-}$ pyrovanadate unit. The derived values quoted below have relatively large errors associated with them due to the uncertainty surrounding the position of the vanadium centres. The distances and angles agree, within experimental errors, with those quoted by Murashova *et al.* [27].

3.2.4.2 Calcium Polyhedra

There are three different calcium polyhedra within the $Na_3Ca_2(VO_4)(V_2O_7)$ structure. Ca(1) forms a CaO_8 tetragonal antiprism (Figure 3-13), whilst both Ca(2) and Ca(3) form octahedra with different degrees of distortion.

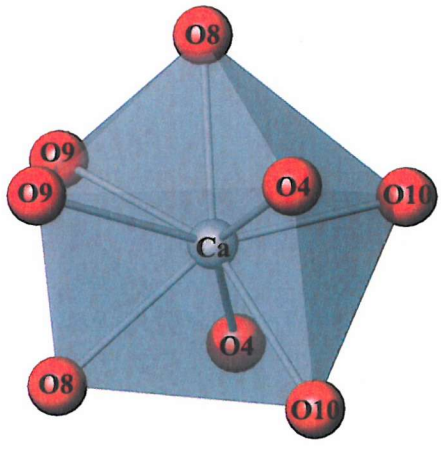

Figure 3-13: $Ca(1)O_8$ site in $Na_3Ca_2(VO_4)(V_2O_7)$. Calcium and oxygen atoms are shown as grey and red spheres respectively.

Table 3-16: Derived bond distances (Å) and angles (°) for the $Ca(1)O_8$ site in $Na_3Ca_2(VO_4)(V_2O_7)$ (e. s. d. s are shown in parentheses).

Vector	*Distance / Å*
Ca(1)_O4 (x2)	2.345(5)
Ca(1)_O8 (x2)	2.471(6)
Ca(1)_O9 (x2)	2.879(7)
Ca(1)_O10 (x2)	2.339(7)
Average	2.509

Angle	*Degrees*
O4_Ca(1)_O4	158.0(9)
O4_Ca(1)_O8	79.2(4)
O4_Ca(1)_O9	111.1(7)
O4_Ca(1)_O10	84.9(5)
O4_Ca(1)_O10	78.6(5)
O4_Ca(1)_O8	111.1(4)
O4_Ca(1)_O9	79.2(4)
O4_Ca(1)_O10	78.6(5)
O4_Ca(1)_O10	84.9(5)
O8_Ca(1)_O9	126.4(9)
O8_Ca(1)_O10	78.2(4)
O8_Ca(1)_O10	151.8(6)
O9_Ca(1)_O10	151.8(8)
O9_Ca(1)_O10	78.2(4)
O10_Ca(1)_O10	82.8(7)

Table 3-17: Derived bond distances (Å) and angles (°) for the $Ca(2)O_6$ and $Ca(3)O_6$ octahedral sites in $Na_3Ca_2(VO_4)(V_2O_7)$ (e. s. d. s are shown in parentheses).

Vector	*Distance / Å*
Ca(2)_O3 (x2)	2.397(6)
Ca(2)_O10 (x2)	2.375(9)
Ca(2)_O11 (x2)	2.408(7)
Average	2.393
Ca(3)_O1	2.327(9)
Ca(3)_O4	2.378(8)
Ca(3)_O6	2.438(9)
Ca(3)_O7	2.442(8)
Ca(3)_O8	2.360(8)
Ca(3)_O9	2.328(7)
Average	2.379

Angle	*Degrees*
O3_Ca(2)_O3	170.8(9)
O3_Ca(2)_O10 (x2)	90.1(6)
O3_Ca(2)_O10 (x2)	83.0(5)
O3_Ca(2)_O11 (x2)	79.4(5)
O3_Ca(2)_O11 (x2)	105.7(7)
O10_Ca(2)_O10	81.3(8)
O10_Ca(2)_O11 (x2)	84.1(4)
O10_Ca(2)_O11 (x2)	157.0(6)
O11_Ca(2)_O11	114.8(9)
O1_Ca(3)_O4	165.3(7)
O1_Ca(3)_O6	87.8(6)
O1_Ca(3)_O7	74.8(5)
O1_Ca(3)_O8	108.3(6)
O1_Ca(3)_O9	94.5(6)
O4_Ca(3)_O6	98.6(6)
O4_Ca(3)_O7	92.0(6)
O4_Ca(3)_O8	84.7(7)
O4_Ca(3)_O9	77.0(6)
O6_Ca(3)_O7	89.3(6)
O6_Ca(3)_O8	92.6(7)
O6_Ca(3)_O9	170.3(7)
O7_Ca(3)_O8	176.4(8)
O7_Ca(3)_O9	82.3(5)
O8_Ca(3)_O9	95.6(6)

3.2.4.3 Sodium Polyhedra

There are three different sodium polyhedra within the $Na_3Ca_2(VO_4)(V_2O_7)$ structure. Both Na(1) and Na(3) have six-coordinate environments, whereas Na(2) has a seven-oxygen coordination environment (Figure 3-14).

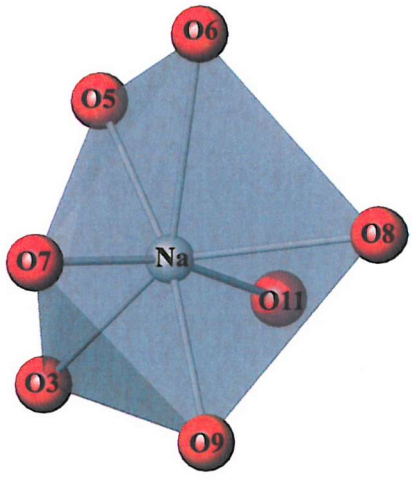

Figure 3-14: $Na(2)O_7$ site in $Na_3Ca_2(VO_4)(V_2O_7)$. Sodium and oxygen atoms are shown as grey and red spheres respectively.

Table 3-18: Derived bond distances (Å) and angles (°) for the $Na(1)O_6$ and $Na(3)O_6$ sites in $Na_3Ca_2(VO_4)(V_2O_7)$ (e. s. d. s are shown in parentheses).

Vector	*Distance / Å*
Na(1)_O1	2.58(2)
Na(1)_O1	2.91(2)
Na(1)_O2	2.37(3)
Na(1)_O2	2.38(3)
Na(1)_O5	2.22(3)
Na(1)_O6	2.36(3)
Average	2.470
Na(3)_O1	2.38(3)
Na(3)_O3	2.29(3)
Na(3)_O5	2.34(3)
Na(3)_O7	3.16(3)
Na(3)_O9	2.75(3)
Na(3)_O11	2.20(3)
Average	2.520

Angle	*Degrees*
O1_Na(1)_O2	66.2(7)
O1_Na(1)_O2	74.9(8)
O1_Na(1)_O5	81.9(5)
O1_Na(1)_O6	154.0(9)
O2_Na(1)_O2	96.9(6)
O2_Na(1)_O5	134.5(9)
O2_Na(1)_O6	95.6(9)
O2_Na(1)_O5	105.3(9)
O2_Na(1)_O6	127.3(9)
O5_Na(1)_O6	101.2(8)
O1_Na(3)_O3	148.6(9)
O1_Na(3)_O7	84.1(9)
O1_Na(3)_O9	83.4(7)
O1_Na(3)_O11	115.3(9)
O3_Na(3)_O7	96.7(9)
O3_Na(3)_O9	83.6(8)
O3_Na(3)_O11	96.0(9)
O7_Na(3)_O9	156(2)
O7_Na(3)_O11	94.7(4)
O9_Na(3)_O11	109.4(9)

Table 3-19: Derived bond distances (Å) and angles (°) for the Na(2)O_7 site in $Na_3Ca_2(VO_4)(V_2O_7)$ (e. s. d. s are shown in parentheses).

Vector	*Distance / Å*
Na(2)_O3	2.91(3)
Na(2)_O5	2.48(3)
Na(2)_O6	2.89(3)
Na(2)_O7	2.36(2)
Na(2)_O8	2.64(3)
Na(2)_O9	2.46(2)
Na(2)_O11	2.47(2)
Average	2.60

Angle	*Degrees*
O3_Na(2)_O6	44.6(5)
O3_Na(2)_O7	134.3(8)
O3_Na(2)_O8	90.5(6)
O3_Na(2)_O9	127.3(8)
O3_Na(2)_O11	41.3(6)
O6_Na(2)_O7	97.2(9)
O6_Na(2)_O8	109.3(8)
O6_Na(2)_O9	163.4(8)
O6_Na(2)_O11	85.1(5)
O7_Na(2)_O8	131.3(9)
O7_Na(2)_O9	81.3(6)
O7_Na(2)_O11	160.8(9)
O8_Na(2)_O9	83.5(7)
O8_Na(2)_O11	64.3(4)
O9_Na(2)_O11	91.1(7)

3.2.5 Discussion

The vanadium ions within the structure are tetrahedrally coordinated by oxygen atoms, with the V(1) and V(2) sites being linked by a bridging oxygen (O2) atom to form a pyrovanadate unit. Usually one would expect the V-O(bridging) bonds to be slightly longer than the remaining V-O bonds as reported by Murashova *et al.* [27], however that does not appear to be the case here. A possible reason for this discrepancy is that it was not possible to refine the vanadium position due to its poor neutron scattering length and therefore the assigned positional coordinates may be incorrect.

The inability of this material to stabilise the MnO_4^{3-} species in place of VO_4^{3-} may be due to the fact that the VO_4 units in this material are slightly larger and somewhat more distorted than those seen for $NaCaVO_4$ (section 3.1). As seen for $NaCaV_{1-x}Mn_xO_4$ the MnO_4^{3-} ion tends to impose its own geometry upon the host lattice, however the Mn^{5+} ion is slightly smaller than the V^{5+} ion (0.33 Å and 0.355 Å respectively) and would possibly be unstable in

a larger tetrahedron. Indeed the longer metal-oxygen distance would tend to favour Mn^{4+} (0.39 Å), which may explain the grey/brown coloured products for the attempted syntheses. The $Ca(2)O_6$ and $Ca(3)O_6$ polyhedra exhibit similar average Ca-O distances (2.393 Å and 2.379 Å respectively). The average metal-oxygen distance for the $Ca(1)O_8$ polyhedron is somewhat longer (2.509 Å) due to the higher oxygen coordination number. A similar situation exists for the sodium polyhedra, where the average bond length for six-coordinate sodium (2.495 Å) is shorter than that for seven-coordinate sodium (2.60 Å).

3.2.6 Conclusion

The crystal structure of sodium calcium orthovanadate pyrovanadate ($Na_3Ca_2(VO_4)(V_2O_7)$) has been further refined using powder neutron diffraction. However, despite several synthesis attempts, it was not possible to incorporate the MnO_4^{3-} species into the structure; multi-phase products were formed.

3.3 References

[1] Lachwa H., Reinen D.; *Inorg. Chem.*, **28** 1044 (1989).

[2] Grisafe D.A., Hummel F.A.; *J. Solid State Chem.*, **2** 167 (1970).

[3] Weller M.T., Skinner S.J.; *Acta Crystallogr.*, **C55** 154 (1999).

[4] Reinen D., Lachwa H., Allmann R.; *Z. Anorg. Allg. Chem.*, **542** 71 (1986).

[5] Albrecht C., Cohen S., Mayer I., Reinen D.; *J. Solid State Chem.*, **107** 218 (1993)

[6] Klemm W.; *Angew. Chem.*, **16** 469 (1954).

[7] Oetliker U., Herren M., Güdel H., Kesper U., Albrecht C., Reinen D.; *J. Chem. Phys.*, **100** 8656 (1994).

[8] Verdun H.R.; OSA Proceedings on Advanced Solid-State Lasers, **15** 315 (1993).

[9] Capobianco J.A., Cormier G., Moncorgé R., Manaa H., Bettineli M.; *Appl. Phys. Lett.*, **60** 163 (1992).

[10] Capobianco J.A., Cormier G., Morrison C.A., Moncorgé R.; *Opt. Mater.*, **1** 209 (1992).

[11] Herren M., Güdel H., Albrecht C., Reinen D.; *Chem. Phys. Lett.*, **183** 98 (1991)

[12] Capobianco J.A., Cormier G., Bettineli M., Moncorgé R., Manaa H.,; *J. Lumin.*, **54** 1 (1992).

[13] Dardenne K., Vivien D., Huguenin D.; *J. Solid State Chem.*, **146** 464 (1999).

[14] Reinen D., Rauw W., Kesper U., Atanasov M., Güdel H., Hazenkamp M., Oetliker U; *J. Alloys Compds.*, **246** 193 (1997).

[15] Scott M.A., Henderson B., Gallagher H.G., Han T.P.J.; *J. Phys. Condens. Matter*, **9** 9893 (1997).

[16] Herren M., Riedener T., Güdel H., Albrecht C., Kaschuba U., Reinen D.; *J. Lumin.*, **54** 1 (1992).

[17] Olazcuaga R., le Flem G., Hagenmuller P.; *Rev. Chim. Minér.*, **13** 9 (1976)

[18] Merkle L.D., Pinto A., Verdún H.R., McIntosh B.; *Appl. Phys. Lett.*, **61** 2386 (1992).

[19] Buijsse B., Schmidt J., Chan I.Y., Singel D.J.; *Phys. Rev. B-Condensed Matter*, **51** 6215 (1995)

[20] le Flem G., Olazcuaga R.; *Bull. Soc. Chim. Fr.*, 2769 (1968).

[21] Ijdo D.J.W.; *Acta Crystallogr.*, **B38** 923 (1982).

[22] Vegard L, *Z. Phys.*, **5**, 17 (1921).

[23] West A.R.; *Solid State Chemistry and its Applications*, Wiley, New York (1984).

[24] Munter A.; *Neutron News*, **3** 3 29-37 (1992).

[25] Larson A.C., Von Dreele R.B.; *General Structure Analysis System (GSAS).* Los Alamos National Laboratory Report LAUR, 86 (2000).

[26] Shannon R.D.; *Acta Crystallogr.*, **A32** 751 (1976).

[27] Murashova E.V., Velikodnyi Yu.A., Trunov V.K.; *Russ. J. Inorg. Chem.*, **33** 1621 (1988).

Chapter 4

Transition Metal Borate Systems

4 Transition Metal Borate Pigments

Metal borate materials have enormous structural diversity in the solid state, which makes borate chemistry as extensive as the more commonly studied areas of phosphate and silicate chemistry. Borate groups, when combined with the colourful properties of the transition elements, have the potential to produce a number of useful inorganic pigments with good physical and chemical properties.

In this section the cation distribution and its effect upon the colour of the $Cu_2Al_xGa_{1-x}BO_5$ system is studied. The coordination environments of Cu^{2+} in the system are examined and any variations, both structurally and in terms of colour, are considered as a function of x. $Cu_2Al_6B_4O_{17}$, an impurity phase obtained during the study of above system, is prepared as a single phase and structurally characterised using PND. The synthesis and structure of cobalt pyroborate $Co_2B_2O_5$ is refined using PND and the preparation and crystal structure of a single crystal of composition $Co_{2.45}BO_5$ is also presented.

4.1 $Cu_2Al_{1-x}Ga_xBO_5$

4.1.1 Introduction

The Ludwigite structure (space group *Pbam)* is one of the more common polytypes for borates of the first row transition metals and is based on Mg_2FeBO_5 [1] a naturally occurring mineral. Examples include Ni_2FeBO_5 [2,3], $Cu_{2-x}Co_xGaBO_5$ [4], Co_3BO_5 [5,6], Cu_2FeBO_5 [7], Fe_3BO_5 [8], $Ni_5TiB_2O_{10}$ [9], Ni_2CrBO_5 [10] and Ni_2VBO_5 [10]. The copper aluminium borate (Cu_2AlBO_5) and copper gallium borate (Cu_2GaBO_5) structures are both monoclinically distorted along the *a* axis by about 8 degrees [11] compared to the orthorhombic Ludwigite structure.

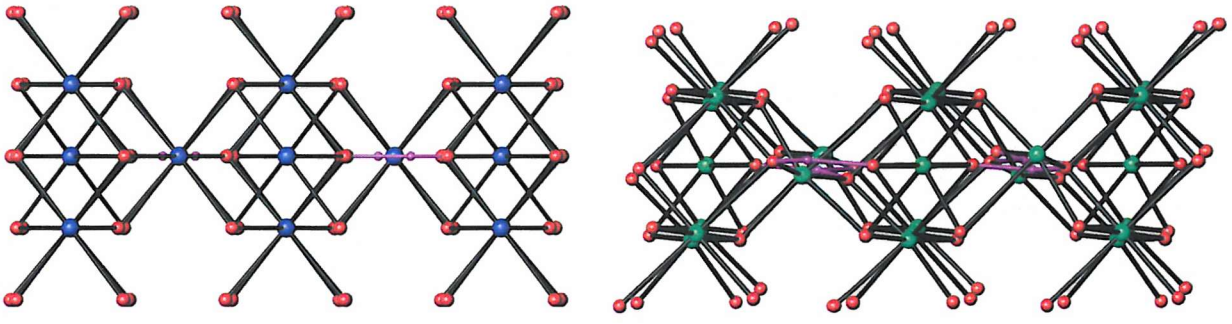

Figure 4-1: Views of the Ludwigite structure (left) and the monoclinically distorted structure of Cu_2AlBO_5.

Compounds in the CuO-Al_2O_3-B_2O_3 system have uses as selective mild dehydrogenation [12] and dehydrocyclisation catalysts [13].

Single crystal preparations of the transition metal borates with empirical formula Cu_2MBO_5 (where M = Ga or Al), have shown that both the gallium and the aluminium versions afford green crystals [11, 14]. It is known that the two systems crystallise with the same space group – $P2_1/c$ – and as such, the aim here was to prepare a solid solution in order to study the variation in colour and structure across the series.

Cu_2AlBO_5 contains four mixed cation sites each containing a combination of Cu^{2+} and Al^{3+} ions. Each of the four sites has a varying degree of distortion and, as such, the colour originating from the cations present on each particular site will differ. In contrast the reported structure refinements [14, 15] for Cu_2GaBO_5 reveal that only two of the cation sites contain both Cu^{2+} and Ga^{3+}, with the remaining cation sites contain only copper. It is therefore the aim of this study to determine how the natures of the four shared sites in

Cu_2AlBO_5 are affected when Al^{3+} is replaced with Ga^{3+} and how the substitution affects the colour of the materials produced.

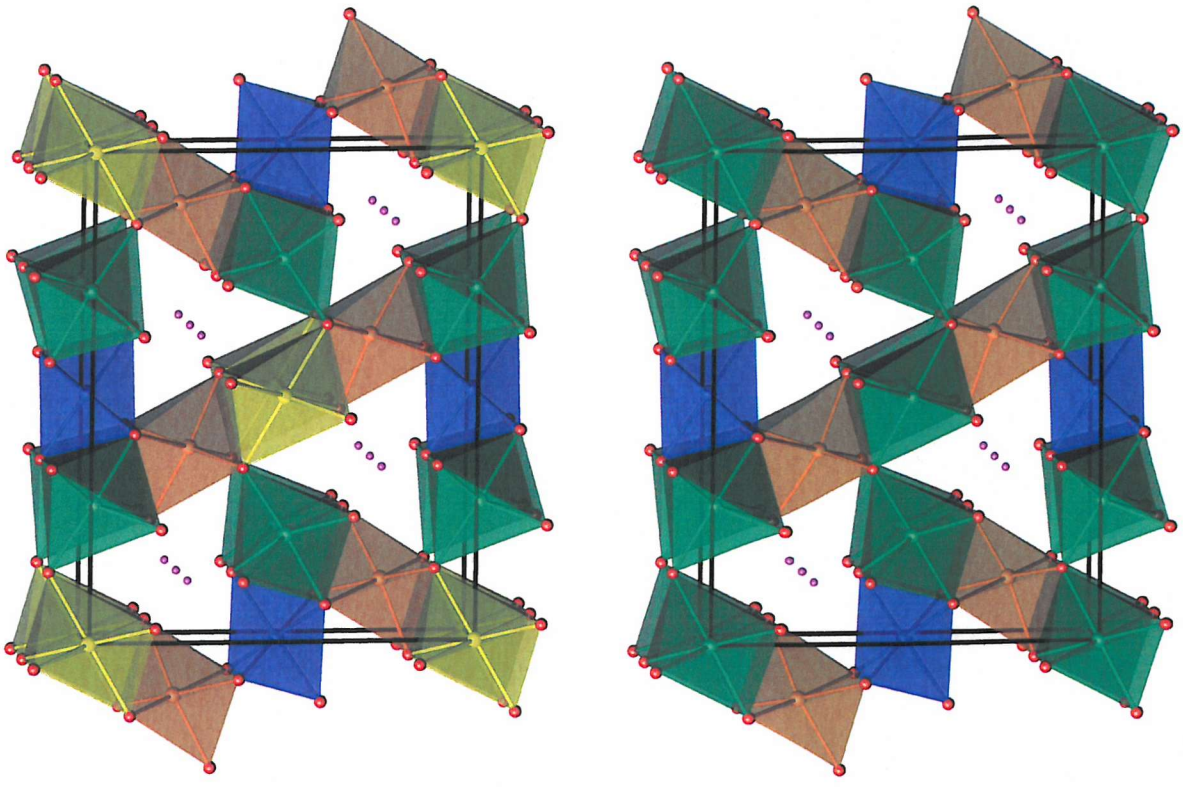

Figure 4-2: Views of the Cu_2AlBO_5 (left) and Cu_2GaBO_5 structures showing the shared Cu/Al sites (green, yellow, blue, orange) and Cu/Ga sites (blue, orange only).

4.1.2 Synthesis

The six members of the series $Cu_2Al_{1-x}Ga_xBO_5$ (where x = 0, 0.2, 0.4, 0.6, 0.8, 1.0) were prepared by grinding the reagents (CuO, Ga_2O_3 and 5% excess $B(OH)_3$) using an agate pestle and mortar, and then heated in air at 950°C, for 24 hours. After cooling, washing in hot water (to remove excess $B(OH)_3$) and regrinding, the colours ranged from an intense vibrant green, for the Cu/Al end member to an olive green, for the Cu/Ga end member. The products were studied using UV visible spectroscopy, PXD and PND. Preliminary PXD data showed that the main phase in each case was analogous to the Cu_2AlBO_5 structure. However, despite several attempts, some minor impurity phases could not be eliminated completely. These appear in varying amounts throughout the series and have been identified as CuO, $Cu_2Al_6B_4O_{17}$ and $CuGa_2O_4$.

4.1.3 Powder X-ray Diffraction

PXD data were acquired for the $Cu_2Al_{1-}xGaxBO_5$ series as described in Chapter 2, and a Rietveld refinement of the structure for Cu_2AlBO_5 was carried out using the model proposed

by Hriljac *et al.* [11] as a starting point and the PC package, GSAS [18]. Initially, the lattice parameters and diffractometer zero point correction were varied followed by the profile coefficients to fit the peaks. Atomic positions and thermal parameters were then added to the refinement. It was not possible to refine the fractional occupancies of the cation sites due to the complexity of the model (three different cations scattered over four different sites). Therefore these were fixed at the values determined by Hriljac *et al.* [11]. Sensible values were obtained for the refined temperature factors, which indicates that this distribution is probably reasonable. The refinement proceeded smoothly and convergence was achieved, giving a good fit to the observed data with chemically sensible bond distances and angles. Refinement details are presented in Figure 4-3 and Table 4-1. Lattice parameters for the remaining members of the series were determined using the CELL refinement program [16] as described in Chapter 2 and are presented in Table 4-2.

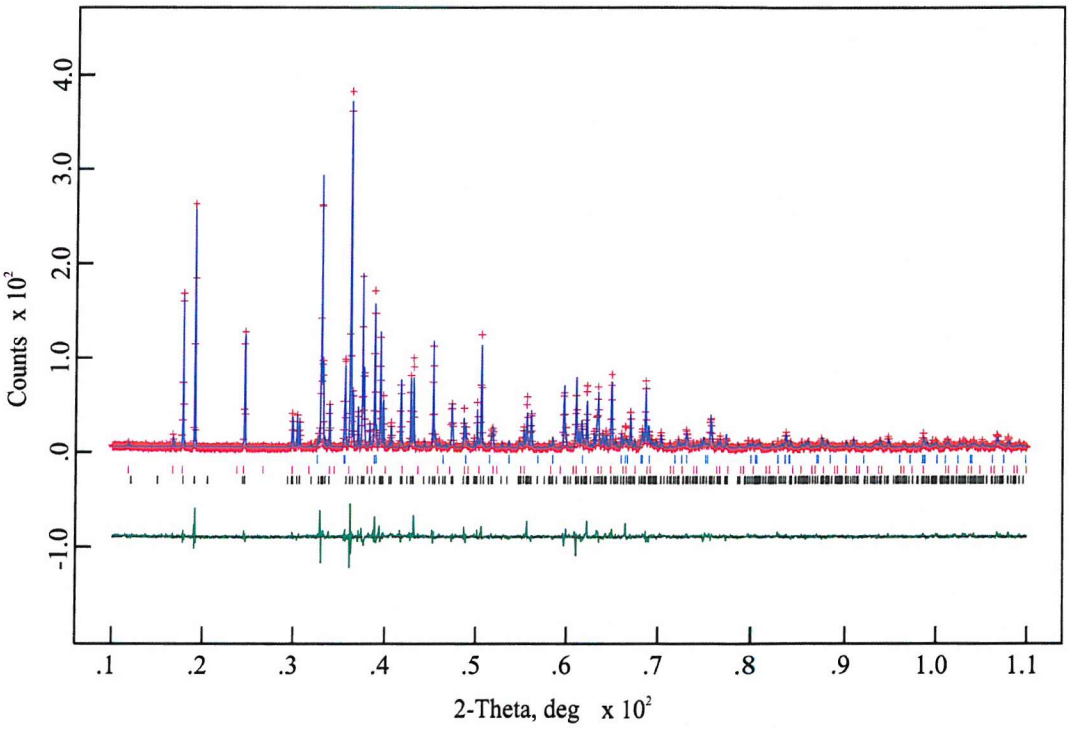

Figure 4-3: Observed (+++), Calculated (—), and difference (shown underneath) PXD profiles for Cu_2AlBO_5. Tick marks indicate reflection positions (Cu_2AlBO_5 (black), $Cu_2Al_6B_4O_{17}$ (red), CuO (blue)).

Table 4-1: Refined crystallographic data (PXD) for Cu_2AlBO_5 (e.s.d.s are shown in parentheses).

Space group: P $2_1/a$

Lattice parameters a = 9.3419(2) Å, b = 11.7388(2) Å, c = 3.06077(3) Å, β = 97.7478(9) °

Atom	*x*	*y*	*z*	*Frac.*	U_{iso} /Å^{2}x100
Cu(1)	0.9934(4)	0.9934(4)	0.0451(9)	.960	1.49(9)
Al(1)	0.9934(4)	0.9934(4)	0.0451(9)	.040	1.49(9)
Cu(2)	0.00	0.00	0.00	.925	1.1(1)
Al(2)	0.00	0.00	0.00	.075	1.1(1)
Cu(3)	0.00	0.500	0.500	.411	1.6(1)
Al(3)	0.00	0.500	0.500	.589	1.6(1)
Cu(4)	-0.2306(4)	-0.1173(4)	0.427(2)	.372	1.3(1)
Al(4)	-0.2306(4)	-0.1173(4)	0.427(2)	.628	1.3(1)
B	0.244(3)	-0.141(3)	0.488(6)	1	2.2(6)
O(1)	0.102(1)	0.146(1)	0.019(4)	1	1.7(3)
O(2)	0.158(1)	-0.0389(8)	0.483(3)	1	1.0(3)
O(3)	0.115(1)	0.366(1)	0.512(3)	1	1.4(3)
O(4)	-0.113(2)	0.4269(9)	-0.002(4)	1	4.8(4)
O(5)	-0.168(2)	0.2374(8)	-0.398(4)	1	1.1(3)

Final fit parameters: $\chi^2 = 0.2350$, $R_{wp} = 14.5$ %, $R_p = 11.2$ %

Table 4-2: Lattice parameters for the $Cu_2Al_xGa_{1-x}BO_5$ series obtained from PXD data using CELL (e.s.d.s are shown in parentheses).

x	*a / Å*	*b / Å*	*c / Å*	*β / °*
0[a]	9.3419(2)	11.7388(2)	3.06077(3)	97.7478(9)
0[b]	9.365(1)	11.778(2)	3.072(2)	97.71(2)
0.2	9.394(5)	11.775(2)	3.109(6)	99.36
0.4	9.443(5)	11.931(4)	3.121(2)	97.22
0.6	9.46(2)	11.924(9)	3.127(4)	98.07
0.8	9.458(5)	11.928(8)	3.126(3)	97.90
1.0	9.465(7)	11.935(7)	3.125(2)	97.90
1.0[c]	9.477(2)	11.921(3)	3.1146(2)	97.91(2)

[a] – values obtained from PXD Rietveld refinement. [b] – Literature values [11]. [c] – literature values [14].

An overall increase in the size of the unit cell is observed as a fraction of x for the series $Cu_2Al_xGa_{1-x}BO_5$ and can be explained in terms of the ionic radii of the cation being incorporated. The effective ionic radius [17] of an Al^{3+} ion in a six-coordinate environment is 0.535 Å whereas Ga^{3+} has a radius of 0.620 Å. This is also observed in the Variable Composition Diffractogram (Figure 4-4), where the shifting of the peak at 2θ *ca.* 17.7° to higher 2θ value corresponds to an increase in the size of the unit cell. The peak at 2θ = 16.75° corresponds to the impurity $Cu_2Al_6B_4O_{17}$, which decreases with increasing gallium content, which implies that there is no gallium analogue of the impurity - $Cu_2Ga_6B_4O_{17}$. The small peak at *ca.* 18.5° shows the presence of the $CuGa_2O_4$ impurity for the compositions where x = 0.8 and 1.0. For the compositions where x = 0, 0.2 and 0.4 a more complicated transition occurs at 2-theta = *ca.* 19°. For x = 0.2 and 0.4 there appears to be two peaks present possibly corresponding to the formation of two phases/domains each with a different composition.

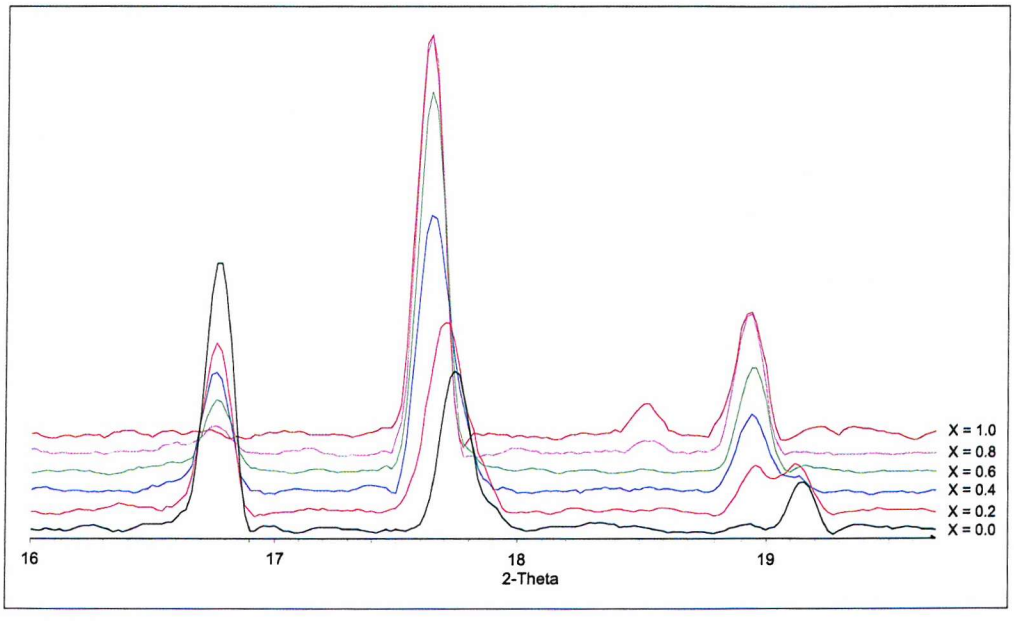

Figure 4-4: Variable composition diffractogram for the series $Cu_2Al_{1-x}Ga_xBO_5$ showing PXD data collected across the 2θ-range 16° to 20°.

4.1.4 Powder Neutron Diffraction

The collection of neutron diffraction data for boron containing samples is made difficult by the large absorption cross-section observed for natural isotope boron (767.(8.) barn). Natural

isotope boron consists of ^{10}B (20 %) and ^{11}B (80 %), whose absorption cross-sections are 3835.(9.) barn and 0.0055 barn respectively. Therefore, the study of borate materials is made possible through the preparation of samples containing solely ^{11}B. Samples in the series $Cu_2Al_{1-x}Ga_xBO_5$ (where x = 0, 0.2, 0.4, 0.6, 0.8, 1.0), were prepared as described in the synthesis section, using $^{11}B(OH)_3$.

In order to delineate the oxygen and boron positions more accurately, time of flight (TOF) powder neutron diffraction data were collected on the GEM diffractometer at the Rutherford Appleton Laboratory, Oxfordshire, UK. All data sets were collected at room temperature and data obtained from the low angle, 75°, 90° and backscattering banks were used in the analysis. Rietveld refinements were initially performed using the model refined from the PXD data (Cu_2AlBO_5) as a starting point, with subsequent refinements (as x increases) using the model obtained from the previous refinement, and the PC package, GSAS [18]. Initially the lattice parameters were refined to accurately locate the reflections. The peak profiles were then refined and the atomic positions varied. Finally, isotropic temperature factors were added to the refinements. It was intended that each refinement would be based upon the preceding one. However, as x increased the fit to the observed data became less satisfactory. The deterioration of the fit may be due to the fact that the fractional site occupancies and the gallium distribution were fixed for all samples except $CuGa^{11}BO_5$. The distribution for x = 0 was based upon that reported by Hriljac *et al.* [11], subsequent refinements assumed that gallium replaced aluminium like-for-like on each site. For the sample where x = 0.8, a better fit to the observed data was obtained by assuming that sites 1 and 2 contain only copper.

The refinements proceeded to convergence giving reasonably good fits to the observed data and chemically sensible bond distances and angles. The refinement profiles for $Cu_2Al(^{11}B)O_5$ are shown in Figure 4-5 and tables of crystallographic data and refinement statistics for each phase are presented in Table 4-3 to Table 4-8.

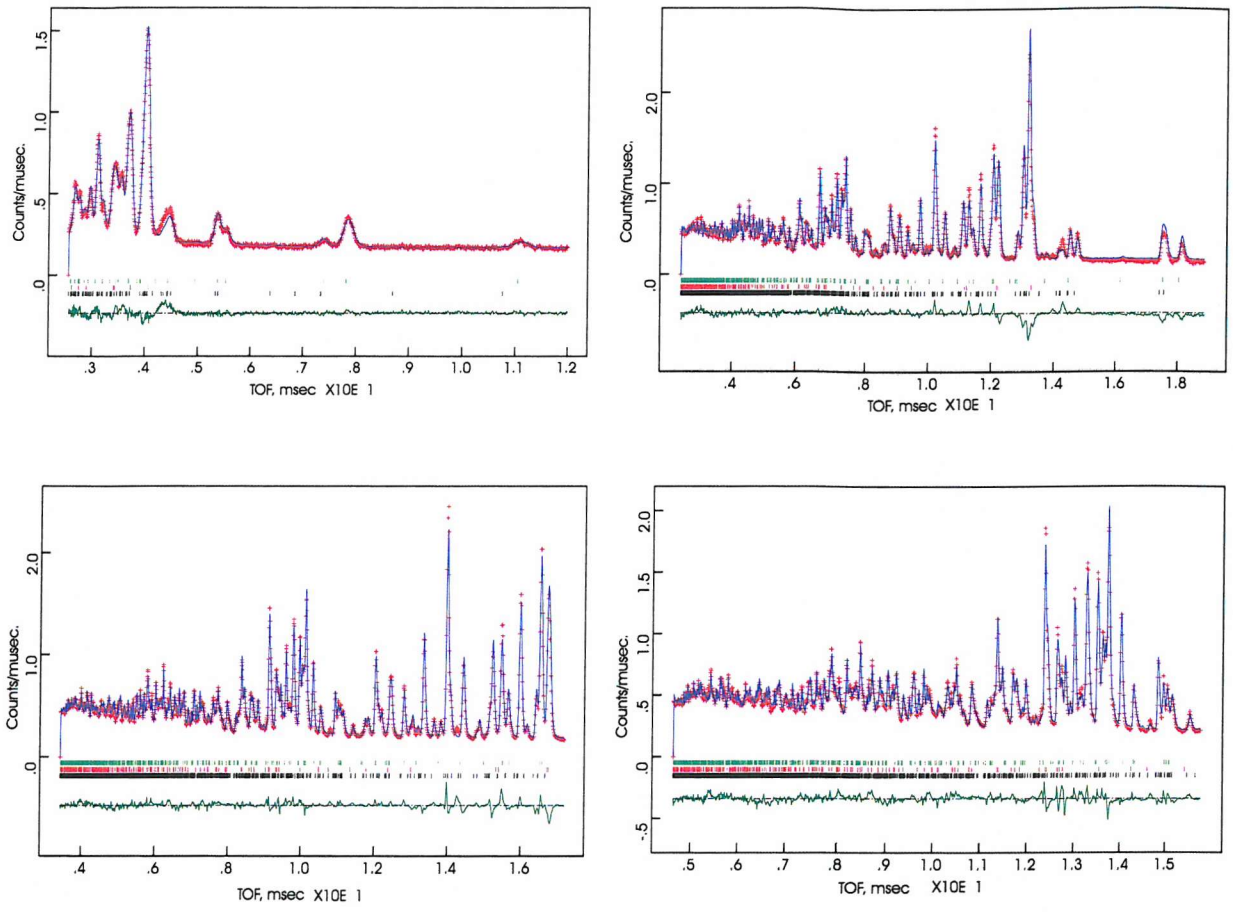

Figure 4-5: Observed (+++), Calculated (—), and difference (shown underneath) PND profiles from the low angle, 75 °, 90 ° and backscattering banks for $Cu_2Al(^{11}B)O_5$. Tick marks indicate reflection positions ($Cu_2Al(^{11}B)O_5$, CuO (red) and $Cu_2Al_6(^{11}B)_4O_{17}$ (green)).

Table 4-3: Refined crystallographic data for $Cu_2Al(^{11}B)O_5$ (e.s.d.s are shown in parentheses).

Space group: P $2_1/a$

Lattice parameters a = 9.382(1) Å, b = 11.791(2) Å, c = 3.0752(4) Å, β = 97.753(2) °

Atom	*x*	*y*	*z*	*Frac.*	U_{iso} /Å^{2}x100
Cu(1)	.9917(2)	.2812(2)	.0447(8)	.960	.52(5)
Al(1)	.9917(2)	.2812(2)	.0447(8)	.040	.52(5)
Cu(2)	0	0	0	.925	.09(7)
Al(2)	0	0	0	.075	.09(7)
Cu(3)	0	.5	.5	.411	.95(9)
Al(3)	0	.5	.5	.589	.95(9)
Cu(4)	-.2318(3)	-.1142(3)	.4275(8)	.372	.12(6)
Al(4)	-.2318(3)	-.1142(3)	.4275(8)	.628	.12(6)
B	.2375(3)	-.1361(3)	.4635(6)	1	.34(4)
O(1)	.1061(3)	.1462(3)	.0439(8)	1	.45(6)
O(2)	.1577(3)	-.0386(3)	.4752(9)	1	.77(6)
O(3)	.1174(3)	.3671(4)	.4970(9)	1	1.18(6)
O(4)	-.1114(5)	.4247(3)	.010(1)	1	3.1(1)
O(5)	-.1710(3)	.2384(3)	-.4006(8)	1	.16(5)

Final fit parameters: $\chi^2 = 19.66$, $R_{wp} = 5.50$ %, $R_p = 5.16$ %

Table 4-4: Refined crystallographic data for $Cu_2Al_{0.8}Ga_{0.2}(^{11}B)O_5$ (e.s.d.s are shown in parentheses).

Space group: P $2_1/a$

Lattice parameters a = 9.4124(5) Å, b = 11.8245(5) Å, c = 3.0863(2) Å, β = 97.825(4) °

Atom	*x*	*y*	*z*	*Frac.*	U_{iso} /Å^{2}x100
Cu(1)	.9913(4)	.2831(3)	.037(1)	.960	.50(9)
Al(1)	.9913(4)	.2831(3)	.037(1)	.032	.50(9)
Ga(1)	.9913(4)	.2831(3)	.037(1)	.008	.50(9)
Cu(2)	0	0	0	.925	.1(1)
Al(2)	0	0	0	.060	.1(1)
Ga(2)	0	0	0	.015	.1(1)
Cu(3)	0	.5	.5	.411	1.4(2)
Al(3)	0	.5	.5	.4712	1.4(2)
Ga(3)	0	.5	.5	.1178	1.4(2)
Cu(4)	-.2301(6)	-.1115(5)	.431(2)	.372	.1(1)
Al(4)	-.2301(6)	-.1115(5)	.431(2)	.5024	.1(1)
Ga(4)	-.2301(6)	-.1115(5)	.431(2)	.1256	.1(1)
B	.2382(5)	-.1376(5)	.462(2)	1	.25(8)
O(1)	.1076(6)	.1446(6)	.044(2)	1	.5(1)
O(2)	.1564(6)	-.0426(5)	.459(2)	1	1.1(2)
O(3)	.1174(5)	.3671(6)	.511(2)	1	1.2(1)
O(4)	-.1096(8)	.4248(6)	.023(3)	1	2.9(2)
O(5)	-.1703(6)	.2388(5)	-.400(2)	1	.3(1)

Final fit parameters: $\chi^2 = 23.75$, $R_{wp} = 6.76$ %, $R_p = 6.21$ %

Table 4-5: Refined crystallographic data for $Cu_2Al_{0.6}Ga_{0.4}(^{11}B)O_5$ (e.s.d.s are shown in parentheses).

Space group: P $2_1/a$

Lattice parameters a = 9.449(1) Å, b = 11.877(1) Å, c = 3.1045(4) Å, β = 97.893(8) °

Atom	*x*	*y*	*z*	*Frac.*	U_{iso} /Å^{2}x100
Cu(1)	.9983(8)	.2848(5)	.029(3)	.960	.7(2)
Al(1)	.9983(8)	.2848(5)	.029(3)	.024	.7(2)
Ga(1)	.9983(8)	.2848(5)	.029(3)	.016	.7(2)
Cu(2)	0	0	0	.925	.2(2)
Al(2)	0	0	0	.045	.2(2)
Ga(2)	0	0	0	.030	.2(2)
Cu(3)	0	.5	.5	.411	.6(3)
Al(3)	0	.5	.5	.3534	.6(3)
Ga(3)	0	.5	.5	.2356	.6(3)
Cu(4)	-.2273(8)	-.1139(6)	.437(2)	.372	.1(1)
Al(4)	-.2273(8)	-.1139(6)	.437(2)	.3768	.1(1)
Ga(4)	-.2273(8)	-.1139(6)	.437(2)	.2512	.1(1)
B	.2386(9)	-.136(1)	.459(2)	1	.2(2)
O(1)	.1080(9)	.1490(9)	.039(3)	1	.8(2)
O(2)	.154(1)	-.0428(8)	.447(3)	1	.9(2)
O(3)	.1168(8)	.364(1)	.534(3)	1	.9(2)
O(4)	-.115(2)	.4186(9)	.066(3)	1	2.1(3)
O(5)	-.166(1)	.2400(7)	-.387(3)	1	.5(2)

Final fit parameters: $\chi^2 = 52.13$, $R_{wp} = 9.73$ %, $R_p = 8.33$ %

Table 4-6: Refined crystallographic data for $Cu_2Al_{0.4}Ga_{0.6}(^{11}B)O_5$ (e.s.d.s are shown in parentheses).

Space group: P $2_1/a$

Lattice parameters a = 9.4688(4) Å, b = 11.9248(5) Å, c = 3.1151(2) Å, β = 97.833(3) °

Atom	*x*	*y*	*z*	*Frac.*	U_{iso} /Å^{2}x100
Cu(1)	1.0003(7)	.2811(5)	.037(2)	.960	1.9(2)
Al(1)	1.0003(7)	.2811(5)	.037(2)	.016	1.9(2)
Ga(1)	1.0003(7)	.2811(5)	.037(2)	.024	1.9(2)
Cu(2)	0	0	0	.925	.2(2)
Al(2)	0	0	0	.030	.2(2)
Ga(2)	0	0	0	.045	.2(2)
Cu(3)	0	.5	.5	.411	.5(2)
Al(3)	0	.5	.5	.2356	.5(2)
Ga(3)	0	.5	.5	.3534	.5(2)
Cu(4)	-.2247(6)	-.1179(5)	.429(2)	.372	.1(1)
Al(4)	-.2247(6)	-.1179(5)	.429(2)	.2512	.1(1)
Ga(4)	-.2247(6)	-.1179(5)	.429(2)	.3768	.1(1)
B	.2392(8)	-.1368(8)	.453(2)	1	.6(2)
O(1)	.1013(7)	.1475(6)	.049(2)	1	.3(2)
O(2)	.1567(7)	-.0426(5)	.460(2)	1	.2(2)
O(3)	.1229(8)	.3683(9)	.520(2)	1	1.7(2)
O(4)	-.1182(9)	.4160(7)	.042(3)	1	2.5(3)
O(5)	-.1698(9)	.2366(7)	-.374(3)	1	1.7(2)

Final fit parameters: $\chi^2 = 58.95$, $R_{wp} = 10.60$ %, $R_p = 9.22$ %

Table 4-7: Refined crystallographic data for $Cu_2Al_{0.2}Ga_{0.8}(^{11}B)O_5$ (e.s.d.s are shown in parentheses).

Space group: P $2_1/a$

Lattice parameters a = 9.4680(4) Å, b = 11.9318(5) Å, c = 3.1162(2) Å, β = 97.829(4) °

Atom	*x*	*y*	*z*	*Frac.*	U_{iso} /Å^{2}x100
Cu(1)	.9970(5)	.2829(4)	.035(2)	1	.3(1)
Cu(2)	0	0	0	1	.1(1)
Cu(3)	0	.5	.5	.400	.2(2)
Al(3)	0	.5	.5	.120	.2(2)
Ga(3)	0	.5	.5	.480	.2(2)
Cu(4)	-.2250(6)	-.1178(4)	.429(2)	.300	.3(1)
Al(4)	-.2250(6)	-.1178(4)	.429(2)	.140	.3(1)
Ga(4)	-.2250(6)	-.1178(4)	.429(2)	.560	.3(1)
B	.2339(5)	-.1342(6)	.464(2)	1	.4(2)
O(1)	.0986(7)	.1487(6)	.040(2)	1	.4(2)
O(2)	.1530(7)	-.0391(5)	.461(2)	1	.6(2)
O(3)	.1153(7)	.3590(8)	.494(2)	1	1.5(2)
O(4)	-.1144(8)	.4165(5)	.025(3)	1	1.5(2)
O(5)	-.1656(7)	.2391(5)	-.393(2)	1	.2(2)

Final fit parameters: $\chi^2 = 68.02$, $R_{wp} = 10.95$ %, $R_p = 9.31$ %

Table 4-8: Refined crystallographic data for $Cu_2Ga(^{11}B)O_5$ (e.s.d.s are shown in parentheses).

Space group: P $2_1/a$

Lattice parameters a = 9.4689(6) Å, b = 11.9340(8) Å, c = 3.1163(2) Å, β = 97.796(3) °

Atom	*x*	*y*	*z*	*Frac.*	U_{iso} /Å^{2}x100
Cu(1)	.9937(5)	.2818(3)	.044(2)	1	1.0(1)
Cu(2)	0	0	0	1	.2(1)
Cu(3)	0	.5	.5	.3(2)	.1(2)
Ga(3)	0	.5	.5	.7(2)	.1(2)
Cu(4)	-.2259(4)	-.1181(3)	.431(1)	.4(1)	.21(9)
Ga(4)	-.2259(4)	-.1181(3)	.431(1)	.6(1)	.21(9)
B	.2339(5)	-.1364(5)	.474(2)	1	.68(8)
O(1)	.0991(5)	.1469(5)	.044(2)	1	.7(1)
O(2)	.1577(6)	-.0407(4)	.471(2)	1	.6(1)
O(3)	.1190(5)	.3651(6)	.480(2)	1	1.1(1)
O(4)	-.1126(7)	.4203(5)	-.017(2)	1	1.8(2)
O(5)	-.1657(6)	.2372(4)	-.412(2)	1	.6(2)

Final fit parameters:χ^2 = 46.16, R_{wp} = 9.25 %, R_p = 6.92 %

4.1.5 Interatomic Distances and Bond Angles

Selected interatomic bond distances and angles were extracted from the PND refinements and are presented in Table 4-9 to Table 4-13. The values quoted for the mixed six-coordinate sites are averages of the metal-oxygen bond lengths and angles within the structure as the sites contain up to three different cations.

4.1.5.1 M(1) site

In each compound of this series the M(1) site is occupied all but exclusively by Cu^{2+}. Indeed for Cu_2GaBO_5 the fractional occupancies used for the PND data refinement and those presented by Bluhm and Schaefer [14] imply that there is no site mixing for the M(1) site and that the site contains solely copper ions. The d^9 electronic configuration of Cu^{II} makes it susceptible to Jahn-Teller distortions if placed in an environment that has regular octahedral symmetry. The presence of Cu^{2+} leads to a coordination that is best described as 4+2, where by the axial M(1)-O distances are, on average, between 20 – 25% longer than the equatorial

bonds. The shorter, stronger M(1)-O bonds range from 1.857(9) Å to 2.015(7) Å in length, with the two weaker axial interactions ranging in length from 2.232(9) Å to 2.656(9) Å.

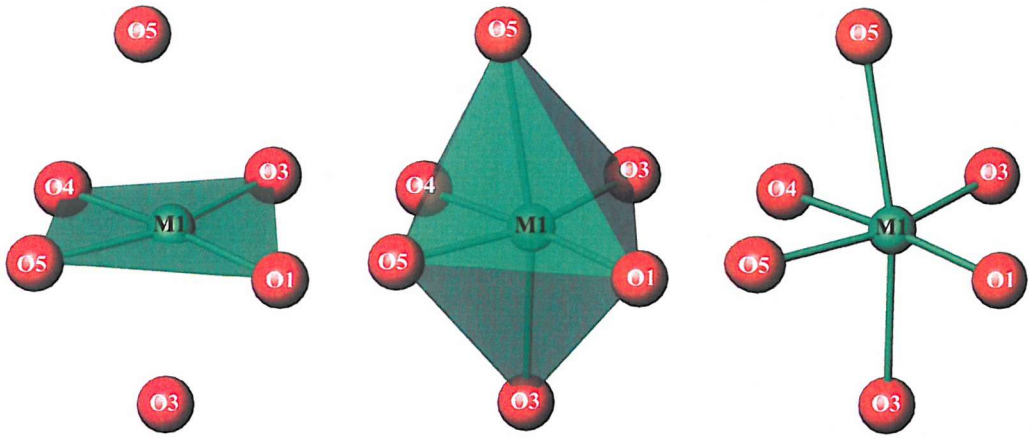

Figure 4-6: M(1) (green) – oxygen (red) distorted octahedral site in $Cu_2Al_{1-x}Ga_xBO_5$.

Table 4-9: Selected Bond lengths and Angles for the M(1) site in $Cu_2Al_{1-x}Ga_xBO_5$ extracted from powder neutron diffraction data (GEM). (M = Cu, Al, Ga - shared site).

x	0	0.2	0.4	0.6	0.8	1.0
M(1)_O1	1.921(4)	1.968(8)	1.946(9)	1.857(9)	1.867(9)	1.894(7)
M(1)_O3	2.407(4)	2.358(8)	2.232(9)	2.351(9)	2.331(9)	2.460(7)
M(1)_O3	1.978(4)	2.015(7)	2.031(9)	2.054(9)	1.921(8)	1.949(6)
M(1)_O4	1.944(5)	1.923(9)	1.928(9)	1.963(9)	1.909(8)	1.931(7)
M(1)_O5	1.973(4)	1.962(7)	1.955(9)	1.988(9)	1.966(8)	2.000(7)
M(1)_O5	2.489(4)	2.516(7)	2.600(9)	2.656(9)	2.563(8)	2.476(7)
O3_M(1)_O3	98.3(2)	97.4(4)	98.4(5)	100.5(5)	98.8(4)	99.4(4)
O3_M(1)_O4	174(4)	176(9)	175(9)	176(9)	177(9)	175(7)
O3_M(1)_O5	99.7(3)	99.4(4)	98.9(7)	98.8(6)	97.6(5)	96.9(4)
O3_M(1)_O4	80.6(2)	80.1(4)	79.8(5)	81.1(4)	83.2(4)	83.8(3)
O3_M(1)_O5	162.1(9)	163(2)	160.3(5)	159.1(5)	163(2)	163(2)
O4_M(1)_O5	81.6(2)	83.3(4)	82.3(5)	79.1(5)	80.3(4)	79.9(4)

4.1.5.2 M(2) Site

The M(2) site, as with the M(1) site, is mainly occupied by Cu^{2+} ions and can also be described as a 4+2 environment due to the Jahn-Teller distortions caused by Cu^{II}. The length range of equatorial M(2)-O distances across the series is 1.94(1) Å to 2.006(6) Å, with the axial bond ranging from 2.376(3) Å to 2.449(8) Å.

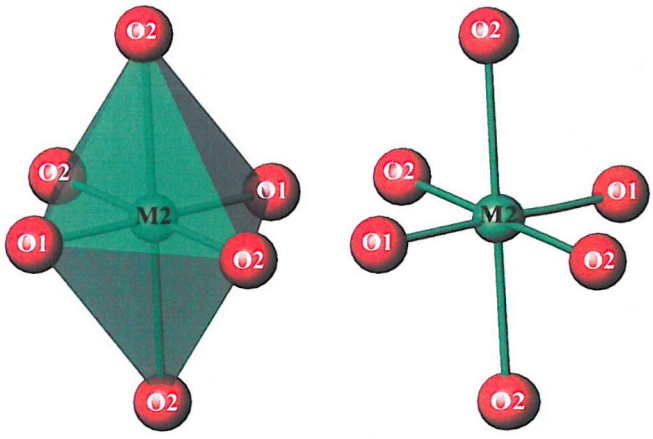

Figure 4-7: M(2) (green) – oxygen (red) distorted octahedral site in $Cu_2Al_{1-x}Ga_xBO_5$.

Table 4-10: Selected Bond lengths and Angles for the M(2) site in $Cu_2Al_{1-x}Ga_xBO_5$ extracted from powder neutron diffraction data (GEM). (M = Cu, Al, Ga - shared site).

x	0	0.2	0.4	0.6	0.8	1.0
M(2)_O1 (x2)	1.986(4)	1.983(7)	2.00(1)	1.999(7)	2.001(7)	1.985(6)
M(2)_O2 (x2)	2.376(3)	2.425(5)	2.449(8)	2.444(6)	2.408(6)	2.419(5)
M(2)_O2 (x2)	1.987(4)	1.963(6)	1.94(1)	1.983(7)	1.953(7)	2.006(6)
O1_M(2)_O2	180.0(3)	180.0(5)	180.0(7)	180.0(5)	180.0(5)	180.0(4)
O1_M(2)_O2	80.3(2)	81.2(3)	81.8(4)	82.3(3)	82.7(3)	82.3(2)
O1_M(2)_O2	99.7(2)	98.9(4)	98.2(5)	97.7(4)	97.3(4)	97.8(3)
O2_M(2)_O2	99.7(2)	98.9(4)	98.2(4)	97.7(4)	97.3(4)	97.8(3)
O2_M(2)_O2	80.3(3)	81.1(5)	81.8(8)	82.3(6)	82.7(4)	82.3(5)
O2_M(2)_O2	180.0(3)	180.0(5)	180.0(7)	180.0(5)	180.0(6)	180.0(4)

4.1.5.3 M(3) Site

Again the M(3) site exhibits a distorted octahedral environment, which tends towards a 4+2 arrangement. Here though the distortion is less pronounced, with the axial bonds being, on average, only ~ 16% longer than the equatorial bonds. This is consistent with a smaller fractional occupancy of Cu^{2+} ions on this site (around 40 %). The average bond length for each environment increases as the gallium content is increased, which can be explained by considering the relative sizes of the Al^{3+} (0.535 Å) and Ga^{3+} (0.62 Å) ions in a six-coordinate environment [17].

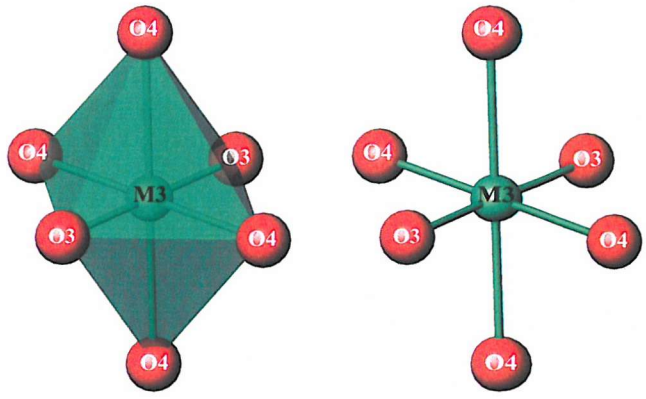

Figure 4-8: M(3) (green) – oxygen (red) distorted octahedral site in $Cu_2Al_{1-x}Ga_xBO_5$.

Table 4-11: Selected Bond lengths and Angles for the M(3) site in $Cu_2Al_{1-x}Ga_xBO_5$ extracted from powder neutron diffraction data (GEM). (M = Cu, Al, Ga - shared site).

x	0	0.2	0.4	0.6	0.8	1.0
M(3)_O3 (x2)	1.916(4)	1.919(7)	1.95(1)	1.951(9)	2.007(8)	1.971(6)
M(3)_O4 (x2)	1.929(4)	1.900(8)	1.88(1)	1.963(9)	1.979(8)	2.043(7)
M(3)_O4 (x2)	2.187(4)	2.216(7)	2.394(9)	2.371(8)	2.308(7)	2.177(6)
O3_M(3)_O3	180.0(4)	180.0(6)	180.0(9)	180.0(7)	180.0(6)	180.0(5)
O3_M(3)_O4	82.6(3)	83.1(4)	83.2(6)	83.8(5)	79.3(4)	80.45(2)
O3_M(3)_O4	97.4(2)	96.9(3)	96.8(4)	96.2(3)	100.7(3)	99.6(2)
O3_M(3)_O4	97.4(3)	96.9(4)	96.8(6)	96.2(5)	100.7(4)	99.6(3)
O3_M(3)_O4	82.6(2)	83.1(3)	83.2(4)	83.8(3)	79.3(3)	80.45(2)
O4_M(3)_O4	180.0(4)	180.0(6)	180.0(9)	180.0(7)	180.0(6)	180.0(5)

4.1.5.4 M(4) Site

The M(4) site is again a distorted octahedral one. However, in this case the coordination tends towards a square pyramidal arrangement, with one of the axial bonds being around 0.5 Å longer than the other five M(4)-O distances. As with the M(3) site the average bond distances increase, as expected, with increasing gallium content.

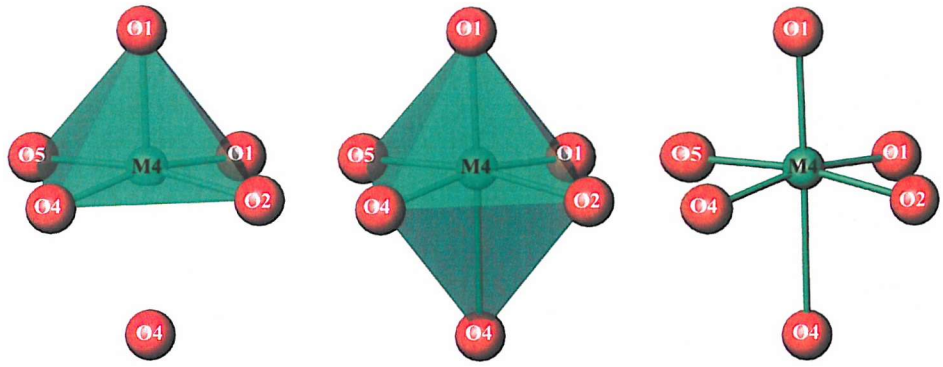

Figure 4-9: M(4) (green) – oxygen (red) distorted octahedral site in $Cu_2Al_{1-x}Ga_xBO_5$.

Table 4-12: Selected Bond lengths and Angles for the M(4) site in $Cu_2Al_{1-x}Ga_xBO_5$ extracted from powder neutron diffraction data (GEM). (M = Cu, Al, Ga - shared site).

x	0	0.2	0.4	0.6	0.8	1.0
M(4)_O1	2.024(4)	2.023(7)	2.015(9)	2.043(8)	2.042(8)	2.056(6)
M(4)_O1	1.912(4)	1.897(8)	1.89(1)	1.903(9)	1.943(8)	1.925(6)
M(4)_O2	1.941(4)	1.963(8)	2.00(1)	2.035(8)	2.006(8)	2.012(6)
M(4)_O4	1.911(5)	1.961(9)	2.04(2)	1.98(1)	1.97(1)	1.916(8)
M(4)_O4	2.462(5)	2.449(9)	2.32(1)	2.40(1)	2.467(9)	2.579(7)
M(4)_O5	1.958(4)	1.999(8)	2.00(1)	2.00(1)	1.993(9)	2.006(7)
O1_M(4)_O1	102.7(2)	103.8(4)	105.4(5)	104.2(4)	102.8(4)	103.0(3)
O1_M(4)_O2	93.0(2)	94.8(4)	95.3(5)	95.0(4)	94.2(3)	93.5(3)
O1_M(4)_O4	90.5(2)	89.1(3)	84.1(4)	86.7(3)	89.7(3)	92.7(3)
O1_M(4)_O5	96.8(2)	95.9(4)	96.0(5)	96.7(4)	98.9(3)	100.5(3)
O1_M(4)_O2	83.3(2)	83.4(4)	83.2(5)	83.4(4)	82.9(4)	83.6(3)
O1_M(4)_O4	167(3)	167(4)	170(6)	169(5)	167(4)	164.3(3)
O1_M(4)_O5	95.2(2)	94.8(4)	97.3(5)	98.9(4)	98.0(3)	97.4(3)
O2_M(4)_O4	96.4(3)	98.1(6)	99.2(7)	97.0(6)	98.1(6)	95.0(3)
O2_M(4)_O5	170.1(2)	169.3(4)	168.1(6)	167.1(5)	166.2(9)	165.4(3)
O4_M(4)_O5	82.8(3)	81.4(5)	78.4(7)	78.3(5)	78.1(4)	80.1(3)

4.1.5.5 BO_3^{3-} Group

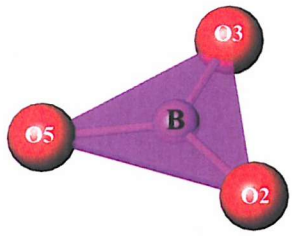

Figure 4-10: BO_3^{3-} group in $Cu_2Al_{1-x}Ga_xBO_5$. Boron and oxygen atoms are represented as purple and red spheres respectively.

Table 4-13: Selected Bond lengths and Angles for the BO_3^{3-} Group in $Cu_2Al_{1-x}Ga_xBO_5$ extracted from powder neutron diffraction data (GEM).

x	0	0.2	0.4	0.6	0.8	1.0
B_O2	1.376(4)	1.362(9)	1.36(2)	1.37(1)	1.368(9)	1.351(8)
B_O3	1.351(4)	1.351(6)	1.36(1)	1.298(9)	1.418(8)	1.381(6)
B_O5	1.359(4)	1.357(8)	1.41(2)	1.37(1)	1.412(9)	1.366(7)
O2_B_O3	121.2(3)	122.0(6)	125.6(9)	122.1(9)	127.1(6)	121.3(5)
O2_B_O5	120.3(3)	118.1(4)	115.8(8)	117.1(7)	119.3(5)	120.1(4)
O3_B_O5	118.5(4)	119.7(6)	117.7(9)	120.4(9)	113.4(7)	118.5(6)

4.1.6 Discussion

In each of the compounds studied here there are four different metal sites, each containing varying amounts of Cu^{2+}, Al^{3+} and Ga^{3+} ions. The copper ions appear to show preference for sites 1 and 2, whilst the 3+ cations remain, almost exclusively on sites 3 and 4. Hriljac *et al.* give an explanation for this ordering [11] by considering the metal-oxygen-boron (m-o-b) interactions within the Ludwigite type structure. Metal sites 1 and 2 each have four of these interactions whilst sites 3 and 4 have only two each, the remaining interactions being of the metal-oxygen-metal (m-o-m) type. The B-O bond has a relatively high covalency, therefore the oxygen ion within an m-o-b interaction will have reduced ionic character; the 2- charge on the ion will be reduced. For this reason sites 1 and 2 will have a lower effective charge than sites 3 and 4, thus favouring the occupancy of those sites by divalent cations, namely Cu^{2+}.

4.1.7 UV-Visible Spectroscopy

UV visible data were collected on undiluted samples for the $Cu_2Al_{1-x}Ga_xBO_5$ system, according to the method outlined in Chapter 2. These are shown in Figure 4-12.

The Cu^{II} d^9 transition metal ion adopts the ground state configuration $t_{2g}^6 e_g^3$ when situated in a strictly octahedral environment. The ground state electronic configuration $t_{2g}^6 e_g^3$ yields the term ^2E_g, whilst the excited electronic configuration corresponds to the $^2T_{2g}$ term. Therefore only a single electron transition $^2E_g \rightarrow {}^2T_{2g}$ is expected in an octahedral crystal field. However, the Jahn-Teller effect for Cu^{II} leads to a lowering of the symmetry and therefore splits the both ^2E_g ground state and the $^2T_{2g}$ excited state. In most cases a tetragonally elongated 4+2 arrangement is observed, as described in Chapter 1. This distortion causes the energy level diagram to split as shown in Figure 4-11.

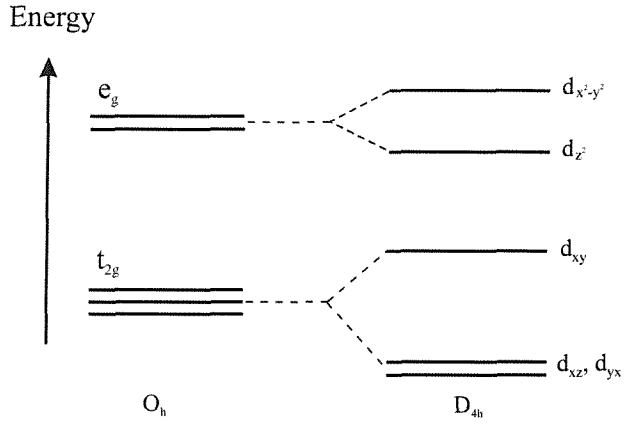

Figure 4-11: Schematic representation of the energy level structure of Cu^{II} according to the reduction of symmetry $O_h \rightarrow D_{4h}$.

The lowering of symmetry has the effect of broadening the observed absorption band. This happens because the three transitions now present occur very close together and, unless the spectrum is taken at a very low temperature, the bands may not be fully resolved.

The UV-Vis spectra observed for the $Cu_2Al_{1-x}Ga_xBO_5$ system present a broad absorption band centred at around 700-750 nm. This band is characteristic of the $^2E_g \rightarrow {}^2T_{2g}$ transition for the Cu^{II} cation in an octahedral environment [19, 20]. The broadness of the band can be attributed to the fact that the metal sites 1 and 2 are distorted due to the Jahn-Teller effect and have axial bonds that are somewhat longer than the four equatorial bonds. The broadness of the band is also a result of the four individual copper environments observed for these materials. Despite the broadness of the observed absorption one can clearly see that the centre of the band appears to shift toward longer wavelengths. It is possible that this is due to differing sizes [17] and electronegativities [21] of aluminium (0.535 Å, 3.32 eV) and galium

ions (0.620 Å, 3.2 eV) and the differing distortion they create on coordination to sites 1 and 2; those which contain mainly copper. The metal-oxygen distances are longer for the gallium analogue and the O-Cu-O angles also differ. The value of Δ_{oct} will therefore be modified and thus the absorption positions for a given transition will be shifted.

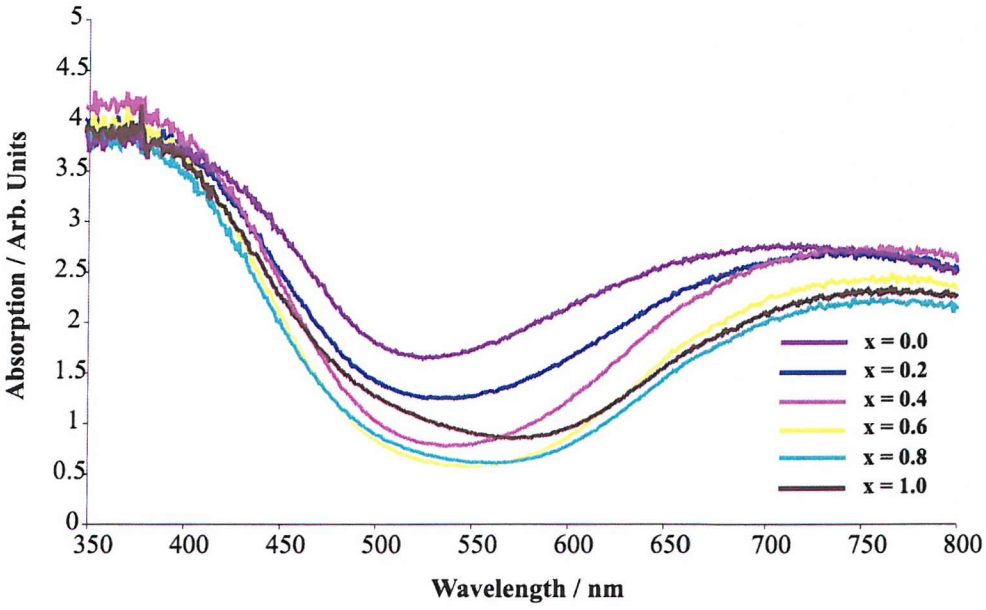

Figure 4-12: Diffuse reflectance spectra of the $Cu_2Al_{1-x}Ga_xBO_5$ series transformed according to the Kubelka-Munk function.

4.1.8 Colour Measurements

CIE L*, a*, b* (CIELAB) colour measurements were performed using a Perkin-Elmer Lambda 35 UV-Vis spectrometer. Results for the $Cu_2Al_{1-x}Ga_xBO_5$ series are presented in Table 4-14.

CIELAB allows the specification of colour perceptions in terms of three-dimensional space. The L* - axis is known as 'lightness' and extends from 0 (black) to 100 (white). The other two coordinates a* and b* represent redness-greenness and yellowness-blueness respectively. Samples for which a*=b*=0 are achromatic and thus the L* - axis represents the achromatic scale of greys from black to white (Figure 4-13).

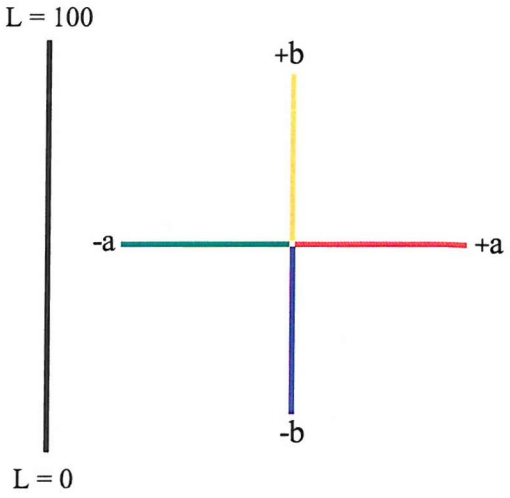

Figure 4-13: A diagrammatic representation of CIE L*, a*, b* 3-dimensional colour space.

Table 4-14: CIE L*, a*, b* Colour data for the $Cu_2Al_{1-x}Ga_xBO_5$ series.

x	0	0.2	0.4	0.6	0.8	1.0
L*	49.15	55.36	56.29	58.84	60.75	62.23
a*	-24.69	-24.27	-23.94	-24.93	-21.65	-21.09
b*	22.72	25.39	27.60	32.12	31.03	32.87

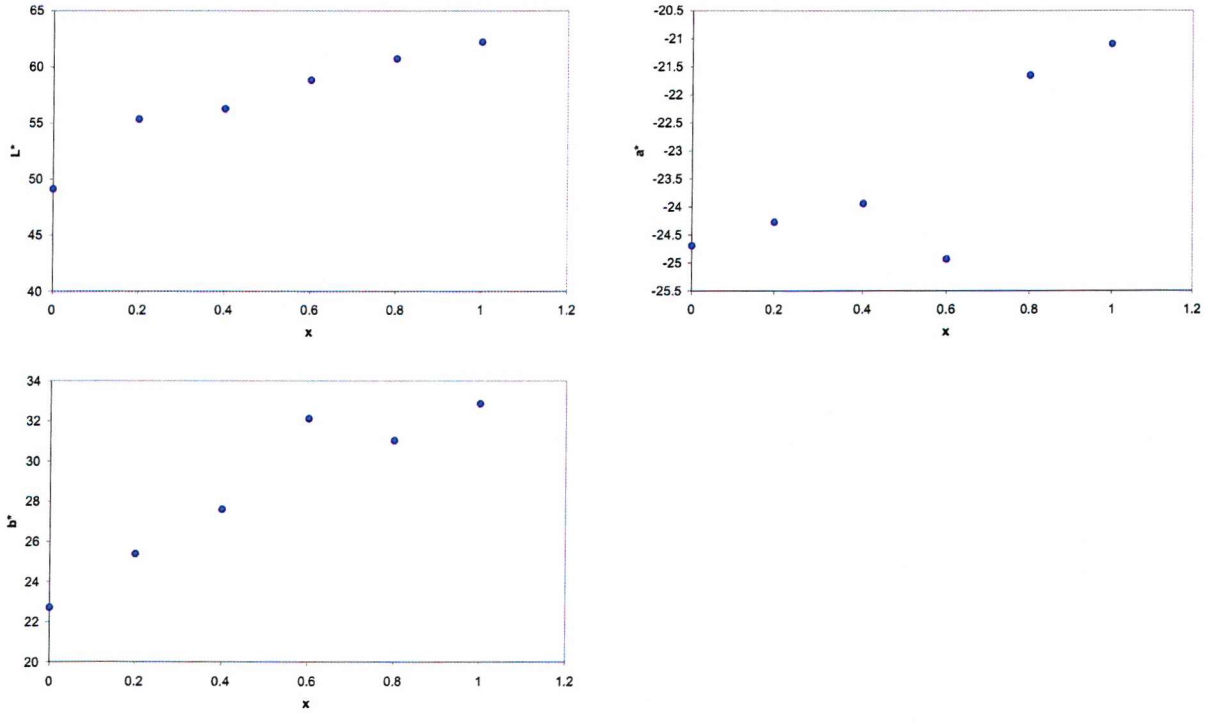

Figure 4-14: Plots of the CIELAB parameters as a function of x for the $Cu_2Al_{1-x}Ga_xBO_5$ series.

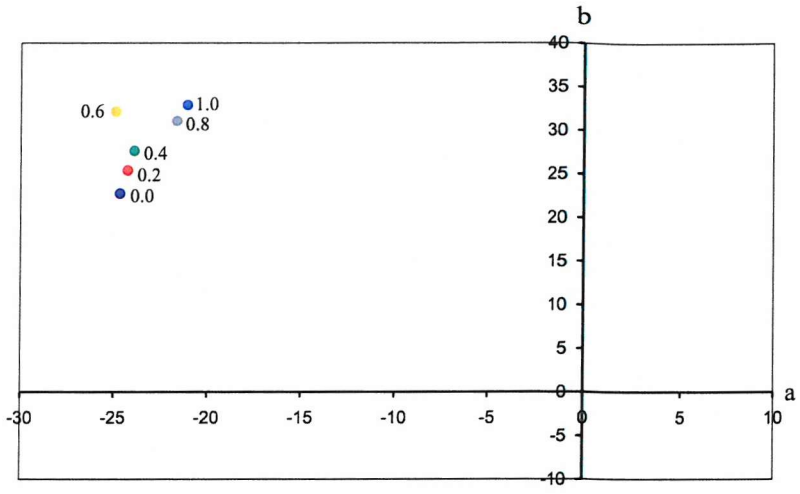

Figure 4-15: A plot of a* v b* for the $Cu_2Al_{1-x}Ga_xBO_5$ series.

The colour measurements reflect the shift in colour across the series from a dark intense green to an olive green colour. The a* values move in the direction of the red region of the axis and away from the green region. The b* values become more 'yellow' as the gallium content increases. There also appears to be some lightening of the pigment when considering the L* values obtained for the series - 49.15 for x = 0 to 62.23 for x = 1. The colour measurements for the sample x = 0.6 seem to be displaced from the trend line, which suggests that the reading for this sample is an anomaly and may be due to particle size irregularities.

4.1.9 Conclusions

The preparation of a completed solid solution in the system $Cu_2(Al,Ga)BO_5$ has been successfully completed. Compounds in the system range in colour from a dark intense green to a lighter olive green.

The substitution of Al^{3+} ions by Ga^{3+} ions has the effect of increasing the average metal-oxygen distances for sites 3 and 4. It also has some effect on the copper coordination environment (mainly sites 1 and 2) and thus the colour of the material produced.

Three impurity phases were identified in samples throughout the series - CuO, $Cu_2Al_6B_4O_{17}$ and $CuGa_2O_4$ – and were included in each of the PND refinements. Attempts to prepare single phase products were unsuccessful.

4.2 $Cu_2Al_6B_4O_{17}$

4.2.1 Introduction

The copper aluminium borate, $Cu_2Al_6B_4O_{17}$, was seen as an impurity phase for the system discussed in section 4.1 - $Cu_2Al_{1-x}Ga_xBO_5$. It is useful as a dehydrogenation catalyst [22] and the average structure has been known for some time [23]. Further characterisation using single-crystal and resonant scattering x-ray techniques [24] has confirmed the structure to a greater degree of accuracy and precision. However, there is no literature data to suggest that powder neutron diffraction has been used. In this case PND would enable more accurate location of the lighter elements present within the material, namely oxygen and boron.

$Cu_2Al_6B_4O_{17}$ is also of interest to this particular study due to the green colour of the material and the origins of that colour. The copper is seen to occupy around 50% of a five-coordinate site, the remaining 50% being occupied by Al^{3+}, and a small proportion (*ca.* 1%) of the octahedral site.

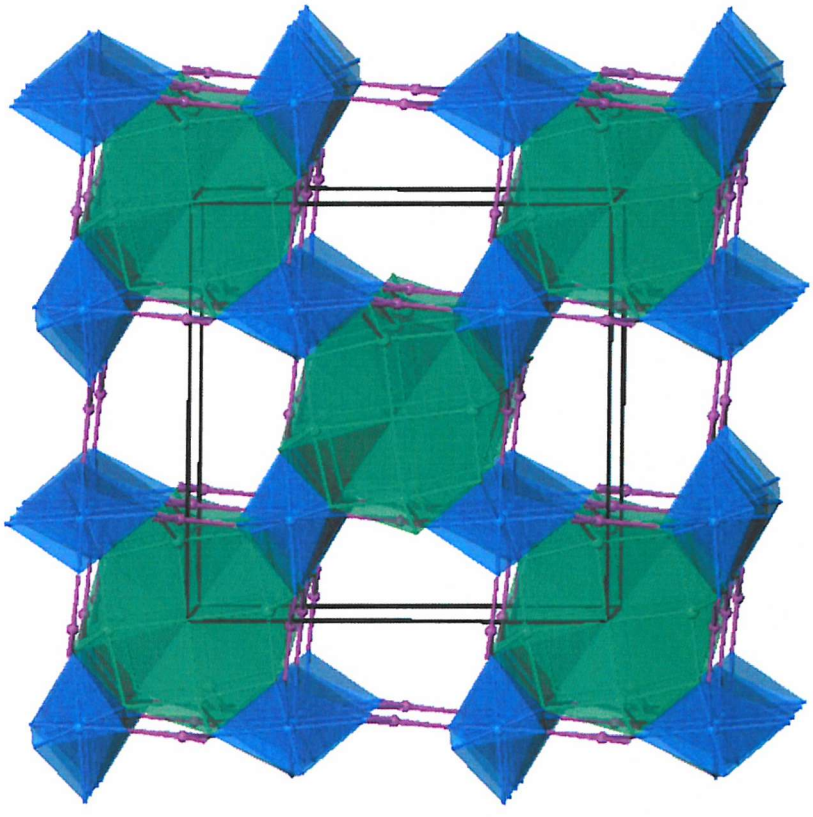

Figure 4-16: A view of the $Cu_2Al_6B_4O_{17}$ structure showing the Cu/Al shared sites: trigonal bipyramidal (green) and octahedral (blue). BO_3^{3-} units are shown in purple. Oxygen atoms are omitted for clarity.

4.2.2 Synthesis

$Cu_2Al_6B_4O_{17}$ was prepared by grinding a stoichiometric mixture of the reagents (Copper (II) Oxide, Aluminium Oxide and Boric Acid) to produce an intimate mixture. The resultant mixture was transferred to a small alumina crucible with a lid, before being heated to 950 °C for 24 hours. A lid was used on the crucible to help prevent the loss of $B(OH)_3$ at high temperatures. Phase identification by X-ray powder diffraction revealed that a single-phase sample of $Cu_2Al_6B_4O_{17}$ had been obtained.

4.2.3 Powder X-ray Diffraction

PXD data were acquired for $Cu_2Al_6B_4O_{17}$, as described in Chapter 2, and Rietveld refinement of the structure carried out using the model proposed by *Kaduk et al.* [24] as a starting point. Initially, the lattice parameters and diffractometer zero point correction were varied followed by the profile coefficients to fit the peaks. Atomic positions and thermal parameters were then added to the refinement. Finally, fractional site occupancies were added to the refinement. The refinement proceeded smoothly and convergence was achieved, giving a good fit to the observed data with chemically sensible bond distances and angles. Refinement details are presented in Table 4-15.

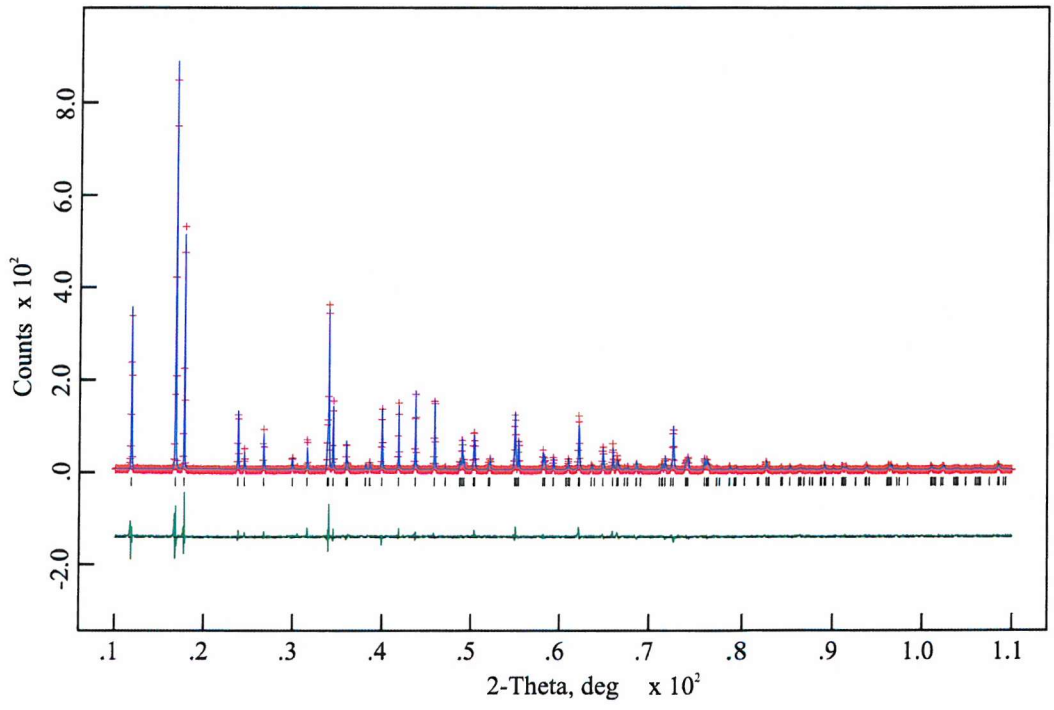

Figure 4-17: Observed (+++), Calculated (—), and difference (shown underneath) PXD profiles for $Cu_2Al_6B_4O_{17}$. Tick marks indicate reflection positions.

Table 4-15: Refined crystallographic data for $Cu_2Al_6B_4O_{17}$ (e. s. d. s are shown in parentheses).

Space group: I4/*m*

Lattice parameters a = 10.55469(8) Å, c = 5.66687(6) Å

Atom	*x*	*y*	*z*	*Frac.*	U_{iso} /Å^{2}x*100*
Cu1	.1916(3)	.0248(3)	0	.478(3)	2.65(8)
Al1	.1916(3)	.0248(3)	0	.522(3)	2.65(8)
Cu2	.25	.25	.25	.022(3)	1.5(1)
Al2	.25	.25	.25	.978(3)	1.5(1)
B	.240(2)	.495(2)	0	1	1.1(4)
O1	0	0	0	1	3.0(5)
O2	.1461(6)	.2095(7)	0	1	.95(3)
O3	.3745(5)	.2529(8)	0	1	.87(2)
O4	.2345(5)	.4328(4)	.2017(7)	1	1.34(2)

Final fit parameters:χ^2 = 0.2692, R_{wp} = 15.13 %, R_p = 11.79 %

4.2.4 Powder Neutron Diffraction

TOF PND data were collected as described in section 4.1.4. A sample of $Cu_2Al_6(^{11}B)_4O_{17}$ was prepared as described in the synthesis section.

A Rietveld refinement was performed using the model refined from the x-ray data as a starting point and the PC package, GSAS [18]. A uniform approach to the structure refinement was undertaken as described previously. Linear constraints were added to the refinement of the site occupancies to give the required stoichiometry, i.e. a 1:3 ratio of Cu:Al. The refinement proceeded smoothly to convergence giving a good fit to the observed data and chemically sensible bond distances and angles. The refinement profile for $Cu_2Al_6(^{11}B)_4O_{17}$ and tables of crystallographic data and refinement statistics are presented in Figure 4-18 and Table 4-16.

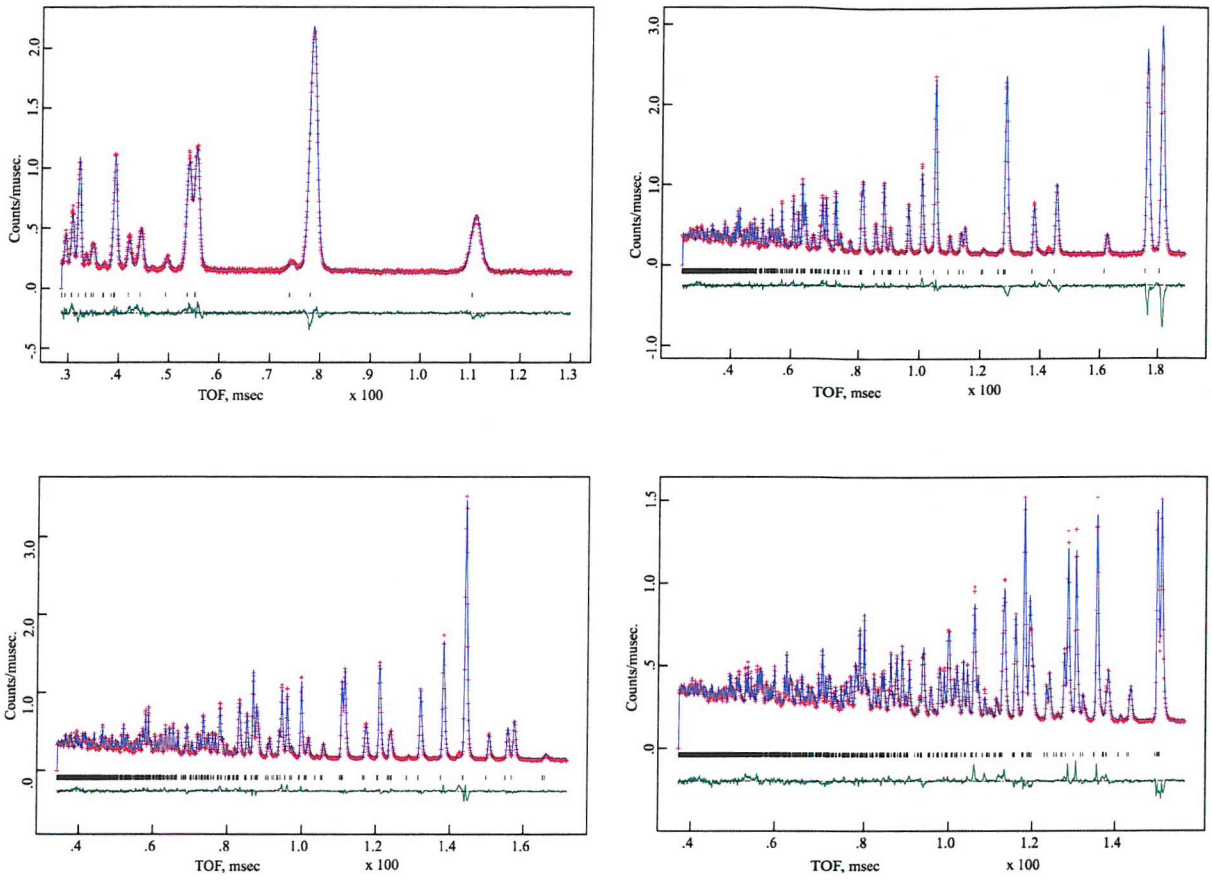

Figure 4-18: Observed (+++), Calculated (—), and difference (shown underneath) PND profiles from the low angle, 75 °, 90 ° and backscattering banks for $Cu_2Al_6(^{11}B)_4O_{17}$. Tick marks indicate reflection positions.

Table 4-16: Refined crystallographic data for $Cu_2Al_6(^{11}B)_4O_{17}$ (e. s. d. s are shown in parentheses).

Space group: I4/*m*

Lattice parameters a = 10.5636(7) Å, c = 5.6716(4) Å

Atom	*x*	*y*	*z*	*Frac.*	U_{iso} /Å^{2}x*100*
Cu1	.1919(2)	.0256(2)	0	.478(3)	1.10(4)
Al1	.1919(2)	.0256(2)	0	.522(3)	1.10(4)
Cu2	.25	.25	.25	.022(3)	.17(3)
Al2	.25	.25	.25	.978(3)	.17(3)
B	.2379(1)	.4965(1)	0	1	.42(2)
O1	0	0	0	1	2.54(8)
O2	.1464(2)	.2090(2)	0	1	.45(2)
O3	.3740(1)	.2438(2)	0	1	.28(2)
O4	.23740(9)	.43053(8)	.2086(2)	1	.81(2)

Final fit parameters:χ^2 = 5.432, R_{wp} = 4.21 %, R_p = 4.14 %

4.2.5 Discussion

$Cu_2Al_6(^{11}B)_4O_{17}$ crystallises in the tetragonal space group I4/*m* with lattice parameters *a* = 10.5636(7) Å, *c* = 5.6716(4) Å. The refined atomic coordinates, lattice parameters and site occupancies agree well with literature values [24].

The structure, shown in Figure 4-16, consists of infinite chains of edge sharing MO_6 (M = Al/Cu) octahedra, with the octahedra in adjacent chains being rotated by *ca.* 90 °, such that the axial bonds are aligned approximately parallel to the *a* and *b* axes. The chains are interlinked by edge sharing with M_4O_{13} (M = Al/Cu) units (Figure 4-19), which consist of four edge sharing MO_5 trigonal bipyramids orientated around a single oxygen atom (O1), and by corner sharing with the planar BO_3 units.

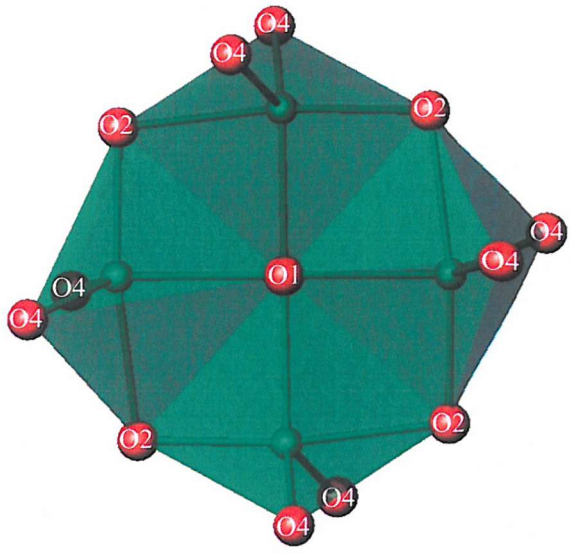

Figure 4-19: A view of the M(1) sites (green) (where M = Cu/Al) in $Cu_2Al_6(^{11}B)_4O_{17}$. Oxygen atoms are shown in red.

4.2.6 Interatomic Distances and Angles

The cation-oxygen distances and bond angles, derived from the Rietveld refinement of the PND data, are shown in Table 4-17 and Table 4-18. The distances shown for the trigonal bipyramidal Cu/Al site and the octahedral Al/Cu site are averages of the metal-oxygen bond lengths within the structure as the site contains both Cu^{2+} and Al^{3+} ions.

Table 4-17: Derived bond distances (Å) for the $M(1)O_5$, $M(2)O_6$ and BO_3 sites (where M = Cu, Al) in $Cu_2Al_6(^{11}B)_4O_{17}$. (e. s. d. s are shown in parentheses).

Distance	$Cu_2Al_6(^{11}B)_4O_{17}$	*Kaduk et al.* [24]
M1_O1	2.045(2)	2.038(1)
M1_O2	1.997(2)	1.998(3)
M1_O2	1.825(2)	1.854(3)
M1_O4	1.872(1)	1.872(2)
M1_O4	1.872(1)	1.872(2)
M2_O2 (x2)	1.8430(9)	1.822(2)
M2_O3 (x2)	1.9312(7)	1.934(2)
M2_O4 (x2)	1.9261(8)	1.943(2)
B_O3	1.370(1)	1.388(6)
B_O4 (x2)	1.373(1)	1.352(4)

Table 4-18: Derived bond angles (°) for the $M(1)O_5$, $M(2)O_6$ and BO_3 sites (where M = Cu or Al) in $Cu_2Al_6(^{11}B)_4O_{17}$. (e. s. d. s are shown in parentheses).

Angle	$Cu_2Al_6(^{11}B)_4O_{17}$
O1_M1_O2	83.65(7)
O1_M1_O2	88.10(8)
O1_M1_O4 (x2)	115.35(5)
O2_M1_O2	171.7(1)
O2_M1_O4 (x2)	81.71(5)
O2_M1_O4 (x2)	101.94(6)
O4_M1_O4	123.99(9)
O2_M2_O2	180.00(0)
O2_M2_O3	80.21(4)
O2_M2_O4	95.60(5)
O3_M2_O3	180.00(0)
O3_M2_O4	89.48(5)
O4_M2_O4	179.98(0)
O3_B_O4 (x2)	120.48(5)
O4_B_O4	119.0(1)

The metal-oxygen distances reported here are in agreement with those reported in the literature [24]. However, it is worth noting that there seems to be slight discrepancies in the boron-oxygen distances (Table 4-17). This may arise due to the different characterisation techniques used. Kaduk *et al.* utilised PXD and Cu K-edge EXAFS techniques, which are less able to accurately locate the light atoms - boron and oxygen - within the structure when compared to PND as utilised in this study. It is therefore assumed that the boron-oxygen distances reported here are more accurate and representative of the actual structure.

4.2.7 Discussion.

As mentioned in Chapter 1, Cu^{II} is often seen to occupy coordination environments that display a '4+1' type geometry as a result of the Jahn-Teller effect. When adopting this geometry Cu^{II} typically has four shorter coplanar bonds, which tend to have lengths within the range 1.90 – 2.05 Å and one elongated apical bond at around 2.1 – 2.4 Å [25]. The four

coplanar bonds would imply a square pyramidal arrangement of the Cu-O bonds. However, the five coordinate site observed here is distorted from this arrangement towards a trigonal bipyramidal one.

The M(1)-O bond lengths for the five-coordinate site do not seem to agree with those mentioned above for typical Cu^{II} coordinations. All five of the metal-oxygen distances are shorter than 2.05 Å and the M(1)-O(4) distance of 1.825 Å is particularly short for a Cu-O distance. These distances, however, are average values as the M(1) site is occupied in almost equal proportions by cations whose effective ionic radii [17] differ significantly - Cu^{2+} (0.65 Å) and Al^{3+} (0.48 Å). Thus one could expect the 'Cu-O' distances to appear to be somewhat shorter than those reported for sites containing solely Cu^{2+} ions.

The refined temperature factor for O(1) is large, which suggests some uncertainty about its position. This may be due to static disorder of some sort. Indeed, Kaduk *et al.* [24] proposed a model based upon EXAFS experiments that describes a different model for the M(1) local structure. Their EXAFS results seem to indicate that there is some degree of Cu^{II} clustering. Stoichiometry dictates that two of the four M(1) sites surrounding O(1) (Figure 4-19) will contain Cu^{II} and that the two remaining sites contain Al^{3+}. It also mandates that there will be only one oxygen atom at the centre of the 4-ring. The EXAFS data also indicates that two copper cations occur as a *cis*-pair in the 4-ring. Therefore, displacement of O(1) away from the *cis*-pair would allow for an elongated apical bond for each of the copper centres and shorter bonds for each of the aluminium containing sites; a new O(1) site of -0.018, 0.018, 0 was suggested, which has a fractional occupancy of ¼.

A repeat PND refinement was performed using the O(1) position suggested by Kaduk *et al.* Selected refinement details and revised interatomic distances for the M(1) site are presented in Table 4-19, Table 4-20 and Figure 4-20. Improved R factors were obtained indicating that the revised model is probably a more accurate description of the local structure.

Table 4-19: Refined crystallographic data (revised model) for $Cu_2Al_6(^{11}B)_4O_{17}$ (e. s. d. s are shown in parentheses).

Space group: I4/*m*

Lattice parameters a = 10.56(4) Å, c = 5.67(2) Å

Atom	*x*	*y*	*z*	*Frac.*	U_{iso} /Å^{2}x*100*
Cu1	.1920(2)	.0254(2)	0	.478(3)	1.04(4)
Al1	.1920(2)	.0254(2)	0	.522(3)	1.04(4)
Cu2	.25	.25	.25	.022(3)	.17(3)
Al2	.25	.25	.25	.978(3)	.17(3)
B	.2379(1)	.4967(1)	0	1	.43(2)
O1	-0.018	0.018	0	0.25	0.02(7)
O2	.1466(2)	.2090(2)	0	1	.46(2)
O3	.3740(1)	.2442(2)	0	1	.31(2)
O4	.23722(9)	.43063(8)	.2087(2)	1	.81(2)

Final fit parameters:χ^2 = 5.165, R_{wp} = 4.10 %, R_p = 4.10 %

Table 4-20: Derived (revised model) bond distances (Å) for the $M(1)O_5$ sites (where M = Cu or Al) in $Cu_2Al_6(^{11}B)_4O_{17}$. (e. s. d. s are shown in parentheses).

Distance	*Cu(a)*	*Cu(b)*	*Al(a)*	*Al(b)*
M1_O1	**2.265(9)**	**2.220(8)**	**1.840(7)**	**1.895(7)**
M1_O2	1.997(8)	1.997(8)	1.997(8)	1.997(8)
M1_O2	1.825(7)	1.825(7)	1.825(7)	1.825(7)
M1_O4	1.872(6)	1.872(6)	1.872(6)	1.872(6)
M1_O4	1.872(6)	1.872(6)	1.872(6)	1.872(6)

where 'a' and 'b' refer to the fact that the two Cu(1) sites (and the two Al(1) sites) surrounding O(1) have different M(1)_O(1) distances using the model proposed by Kaduk *et al.*

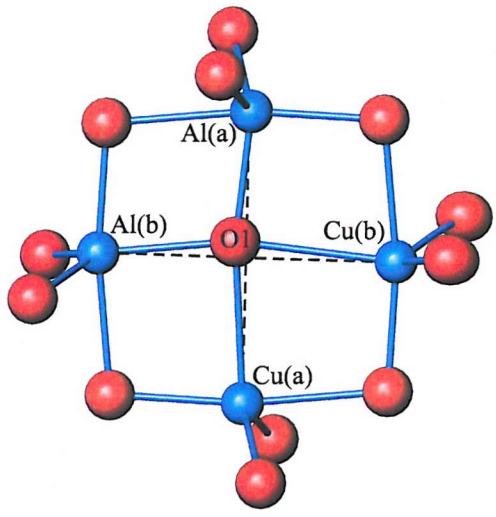

Figure 4-20: A view of the M(1) sites (blue) with O(1) displaced from 0, 0, 0 to -0.018, 0.018, 0. Oxygen atoms are shown as red spheres.

4.2.8 Site Occupancies

The fractional site occupancies obtained from the refinement of PND data agree well with those published by Kaduk *et al.* [24], although our data seems to suggest a slightly larger copper fractional occupancy on the M(2) site – 0.012(2) (Kaduk) compared with 0.022(3) (this work).

4.2.9 Conclusions

Single phase samples of $Cu_2Al_6B_4O_{17}$ and $Cu_2Al_6(^{11}B)_4O_{17}$ have been prepared by conventional solid state synthesis and the individual coordination environments for copper, aluminium and boron have been studied using PXD and PND. The PND refinement has refined the structure to a greater degree of accuracy than was previously reported and has confirmed that the structure proposed by Kaduk *et al.* appears to be the correct description of the local structure for the M(1) sites.

Further investigation of this material as a possible pigment was not performed due to the weak green/yellow colour produced.

4.3 Cobalt Pyroborate – $Co_2B_2O_5$

4.3.1 Introduction

The crystal structure of cobalt pyroborate ($Co_2B_2O_5$) was originally elucidated by Berger [26] and was the first example of its type, proving the existence of the $B_2O_5^{4-}$ composite ion. However, prior to this there are literature reports [27, 28, 29] to suggest that the borate was already known, although its structure had not been determined. Subsequent to the Berger paper a phase diagram of the CoO-B_2O_3 system was published [30], which defines the pyroborate as one of only two ternary compounds within the system; the second being the orthoborate $Co_3(BO_3)_2$. The stoichiometry of these borates were later confirmed by Hauck and Muller [31] who also identified a third cobalt borate; $Co(B_4O_7)$. A further cobalt borate material to have been reported is the mixed-valent ludwigite Co_3BO_5 [5, 32]. More recently Rowsell *et al.* [6] have performed a crystallographic investigation of the Co-B-O system and have reported the formation of $Co_4(BO_2)_6O$. None of these reports have utilised powder neutron diffraction in the characterisation of the borate materials, which would enable more accurate location of the lighter atoms present within the structure – boron and oxygen.

The intense violet colour of $Co_2B_2O_5$ is characteristic of octahedrally coordinated Co^{II} and can be attributed to the following spin-allowed, Laporte forbidden d-d electron transition [20]: $^4T_{1g}(F) \rightarrow {}^4T_{2g}(P)$.

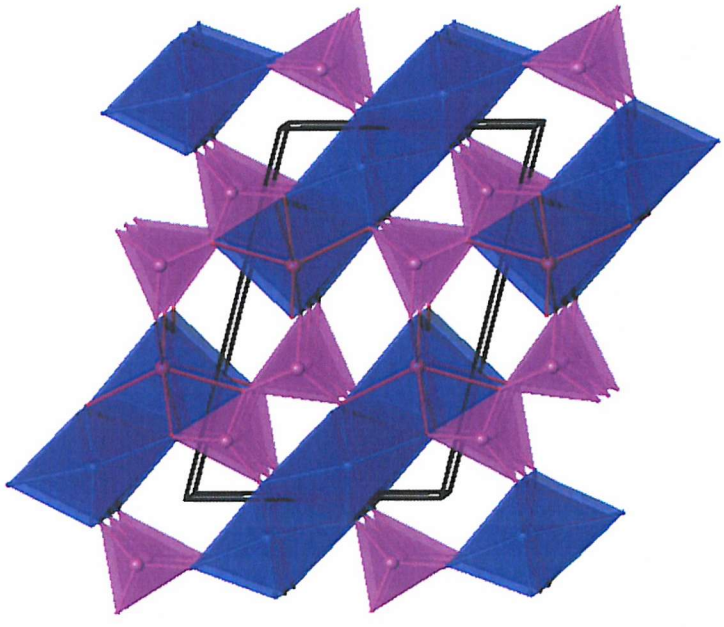

Figure 4-21: A view of the $Co_2B_2O_5$ structure. Cobalt sites 1 and 2 and boron atoms are represented as blue, red and purple spheres respectively. Oxygen atoms are omitted for clarity

4.3.2 Synthesis

To allow a PND study of cobalt pyroborate to be undertaken a sample containing no ^{10}B had to be prepared. This is due to the large absorption cross-section observed for natural isotope boron (767.(8.) barn). Natural isotope boron consists of ^{10}B (20 %) and ^{11}B (80 %), whose absorption cross-sections are 3835.(9.) barn and 0.0055 barn respectively.

$Co_2(^{11}B_2)O_5$ was prepared by heating a stoichiometric mixture of cobalt (II) oxide (Aldrich) and ^{11}B-boric acid (99 atom % ^{11}B, Aldrich). The precursors were intimately mixed by grinding before being transferred to an alumina crucible and heated in air to 800 °C for 15 hours. Initial phase identification PXD (2θ range 10-70°, SOL-X detector, Bruker-D8) revealed that the desired single-phase product had been formed.

Further characterisation was performed using PND, UV/Vis spectroscopy including colour measurement and IR spectroscopy.

4.3.3 Powder neutron diffraction

In order to delineate the oxygen and boron positions more accurately, time of flight (TOF) powder neutron diffraction data were collected on the POLARIS diffractometer at the Rutherford Appleton Laboratory, Oxfordshire, UK. All data sets were collected at room temperature and data obtained from the backscattering banks were used in the analysis. A Rietveld refinement was performed using the model determined by Berger [26] as a starting point and the PC package, GSAS [18]. A uniform approach to the structure refinement was undertaken as described previously. The refinement proceeded smoothly to convergence giving a good fit to the observed data and chemically sensible bond distances and angles. The refinement profile for $Co_2(^{11}B_2)O_5$, crystallographic data and refinement statistics are presented in Figure 4-22 and Table 4-21.

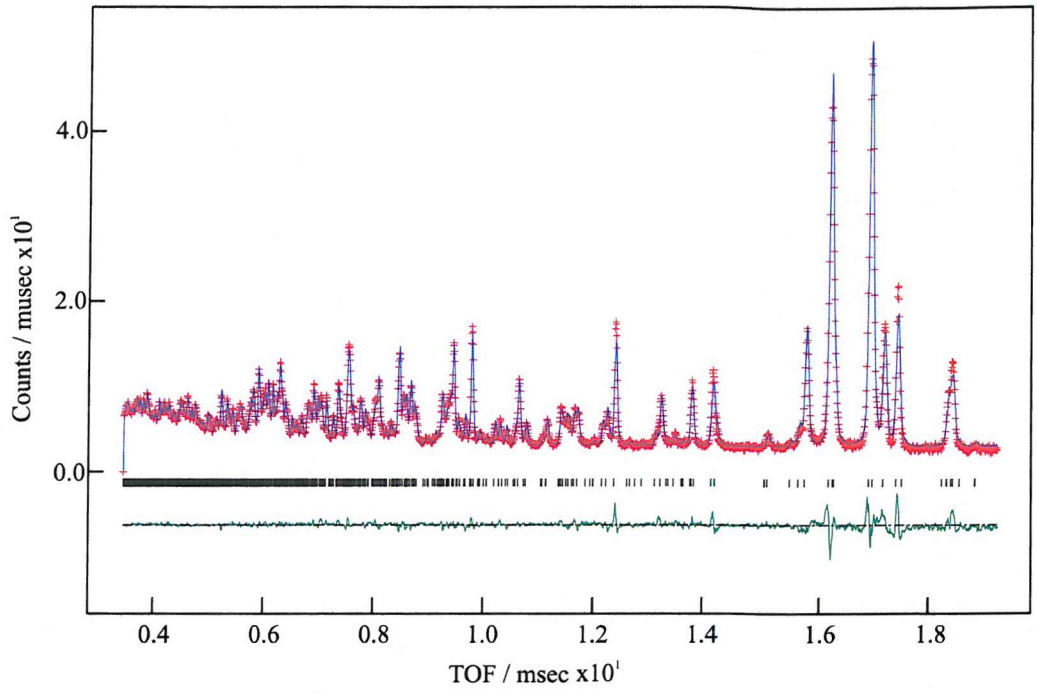

Figure 4-22: Observed (+++), Calculated (—), and difference (shown underneath) PND profiles for $Co_2(^{11}B)_2O_5$. Tick marks indicate reflection positions.

Table 4-21: Refined crystallographic data for $Co_2(^{11}B)_2O_5$. (e. s. d. s are shown in parentheses).

Space group: P –1

Lattice parameters a = 3.17343(5) Å, b = 6.1526(1) Å, c = 9.2792(2) Å, α = 104.339(2) °, β = 91.158(2) °, γ = 91.845(2) °.

Atom	*x*	*y*	*z*	U_{iso} /Å^{2}x*100*
Co1	0.732(2)	0.2139(8)	0.3600(4)	0.98(7)
Co2	0.239(2)	0.3709(6)	0.1015(4)	0.48(5)
B1	0.6993(4)	0.6826(3)	0.3560(2)	0.41(3)
B2	0.3335(5)	0.8802(3)	0.1683(2)	0.47(3)
O1	0.2621(5)	0.6965(3)	0.0543(2)	0.60(4)
O2	0.2185(6)	0.0931(3)	0.1804(2)	0.77(4)
O3	0.7401(6)	0.4767(4)	0.2587(2)	0.86(4)
O4	0.5636(5)	0.8600(3)	0.2978(2)	0.68(4)
O5	0.7704(6)	0.7253(3)	0.5032(3)	0.97(4)

Final fit parameters: $\chi^2 = 2.983$, $R_{wp} = 2.18$ %, $R_p = 4.35$ %

4.3.4 Interatomic Distances and Angles

The cation-oxygen distances and bond angles, derived from the Rietveld refinement of the PND data together with literature values are shown in Table 4-22 and Table 4-23. The derived values also agree well with those reported by Rowsell *et al.* [6].

Table 4-22: Derived bond distances (Å) for the $Co(1)O_6$, $Co(2)O_6$, $B(1)O_3$ and $B(2)O_3$ sites in $Co_2(^{11}B)_2O_5$. (e. s. d. s are shown in parentheses).

Distance	$Co_2(^{11}B)_2O_5$	Literature Values [26]*
Co1_O2	2.276(4)	2.22
Co1_O2	2.297(5)	2.13
Co1_O3	2.061(5)	2.02
Co1_O4	2.156(5)	2.20
Co1_O5	2.044(5)	2.14
Co1_O5	1.973(5)	2.01
Co2_O1	2.153(4)	2.12
Co2_O1	2.087(4)	2.02
Co2_O1	2.147(4)	2.13
Co2_O2	2.019(5)	2.02
Co2_O3	2.178(5)	2.00
Co2_O3	2.111(4)	2.12
B1_O3	1.373(3)	1.28
B1_O4	1.408(2)	1.30
B1_O5	1.338(3)	1.28
B2_O1	1.353(3)	1.30
B2_O2	1.349(2)	1.33
B2_O4	1.427(3)	1.29

* No errors are quoted for these values in the literature.

Table 4-23: Derived bond angles (°) for the $Co(1)O_6$, $Co(2)O_6$, $B(1)O_3$ and $B(2)O_3$ sites in $Co_2(^{11}B)_2O_5$. (e. s. d. s are shown in parentheses).

Angle	$Co_2(^{11}B)_2O_5$
O2_Co1_O2	87.9(2)
O2_Co1_O3	79.3(2)
O2_Co1_O4	62.3(2)
O2_Co1_O5	83.1(2)
O2_Co1_O5	170.3(3)
O2_Co1_O3	79.7(2)
O2_Co1_O4	80.2(2)
O2_Co1_O5	169.5(3)
O2_Co1_O5	84.1(2)
O3_Co1_O4	136.9(2)
O3_Co1_O5	103.7(3)
O3_Co1_O5	104.6(2)
O4_Co1_O5	90.9(2)
O4_Co1_O5	110.7(2)
O5_Co1_O5	104.3(2)
O1_Co2_O1	84.3(2)
O1_Co2_O1	83.7(2)
O1_Co2_O2	170.8(3)
O1_Co2_O3	90.3(2)

Angle	$Co_2(^{11}B)_2O_5$
O1_Co2_O3	89.5(2)
O1_Co2_O1	97.1(2)
O1_Co2_O2	101.7(2)
O1_Co2_O3	83.3(2)
O1_Co2_O3	173.7(3)
O1_Co2_O2	102.4(2)
O1_Co2_O3	173.9(3)
O1_Co2_O3	83.5(2)
O2_Co2_O3	83.5(2)
O2_Co2_O3	84.3(2)
O3_Co2_O3	95.4(2)
O3_B1_O4	117.9(2)
O3_B1_O5	124.5(2)
O4_B1_O5	117.6(2)
O1_B2_O2	129.2(2)
O1_B2_O4	119.3(2)
O2_B2_O4	111.5(2)

4.3.4.1 Cobalt Octahedra

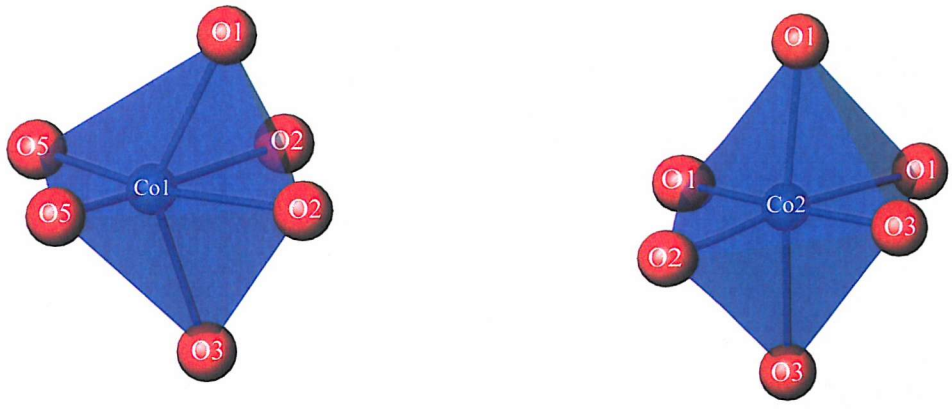

Figure 4-23: Co(1) (left) and Co(2) (right) sites in $Co_2(^{11}B)_2O_5$. Cobalt and oxygen are shown as blue and red spheres respectively.

There are two individual CoO_6 sites present in $Co_2B_2O_5$ as shown in Figure 4-21 and Figure 4-23. The Co(1) site is a very distorted octahedron with an octahedral distortion value (calculated using the expression below) of 32.56667; deviation from zero indicates some degree of distortion. The two Co(1)-O(2) distances are on average 0.228 Å longer than the remaining four cobalt-oxygen bonds.

$$Oh_{distortion} = [\Sigma (|\theta_{\llcorner} - 90| / 12) + \Sigma (|\theta_{—} - 180| / 3)]$$

where $\theta_{\llcorner}$ and $\theta_{—}$ are the observed O_M_O angles for the octahedra.

The Co(2) site displays a more regular octahedral coordination environment and has an octahedral distortion value of 13.4333. Unlike Co(1), the cobalt-oxygen distances observed for Co(2) all lie within 0.159 Å of each other, with the longest and shortest bonds being 2.178 Å and 2.019 Å respectively.

4.3.4.2 Pyroborate group

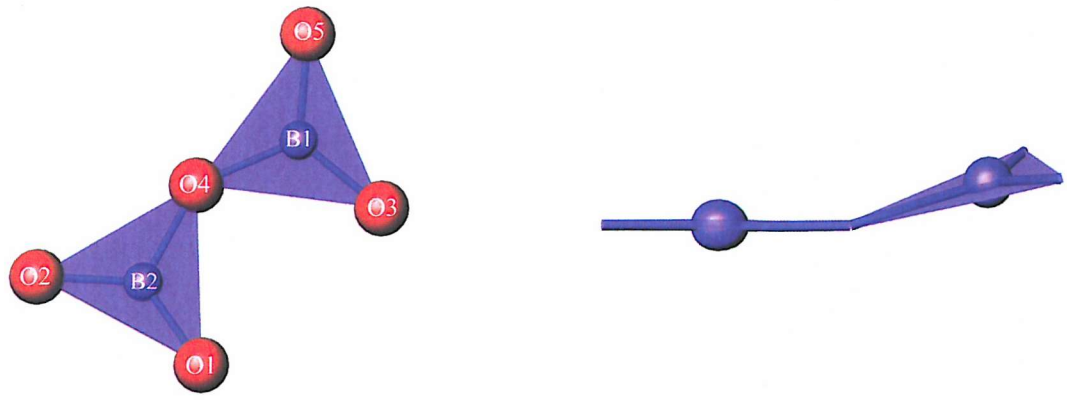

Figure 4-24: $B_2O_5^{4-}$ unit in $Co_2(^{11}B)_2O_5$. Boron and oxygen atoms are shown as purple and red spheres respectively.

Each boron atom is surrounded by a planar arrangement of three oxygen atoms. The two BO_3 triangles are linked by a bridging oxygen atom (O(4)) to form a $B_2O_5^{4-}$ pyroborate unit. The $B_2O_5^{4-}$ unit as a whole is not planar. The $B(2)O_3$ triangle is *ca.* 15 ° out of planarity with the $B(1)O_3$ triangle and is also twisted by *ca.* 14 ° relative to the $B(1)O_3$ unit. The $B_2O_5^{4-}$ acts as a bridge between the 4 x 1 sheets of edge-sharing CoO_6 octahedra by both corner- and edge-sharing. It is also worth noting that the two B_O(4) – the bridging oxygen – distances are on average *ca.* 5 % longer than the remaining four boron-oxygen distances. This was not the case for the refinement performed by Berger [26].

4.3.4.3 Bond valence calculations

Bond valance data were used to confirm the oxidation state of cobalt on the two metal sites. The presence of Co^{3+} would lead to charge transfer transitions between the two sites, which would lead to some darkening of the colour. For example the mixed-valent, Ludwigite-type, cobalt borates ($Co_{2.1}Al_{0.9}BO_5$ [11] and Co_3BO_5 [5]) are black in colour due to such transitions. Calculations were performed using PND data and the mathematical method described by Altermatt and Brown in their papers: The Automatic Searching for Chemical Bonds in Inorganic Structures [33] and Bond-Valence Parameters Obtained from a Systematic Analysis of the Inorganic Crystal Structure Database [34]. Results are presented in Table 4-24.

Table 4-24: Bond Valence Data for $Co_2{}^{11}B_2O_5$

Atom	*Assumed Oxidation State*	*Bond Valence Sum*	% Deviation from Assumed Ox. State
Co1	+2	+1.909	5
Co2	+2	+1.928	4
B1	+3	+2.993	0
B2	+3	+2.971	1
O1	-2	-1.974	1
O2	-2	-1.875	6
O3	-2	-1.955	2
O4	-2	-2.05	2
O5	-2	-1.965	2

No significant deviation from the expected values is observed, thus confirming the presence of Co^{2+} on the two metal sites.

4.3.5 UV visible spectroscopy

UV visible data were collected on undiluted samples for $Co_2{}^{11}B_2O_5$, according to the method outlined in Chapter 2. A broad absorption band centred at ca. 540nm dominates the visible part of the spectrum. This band is characteristic of Co^{II} in an octahedral coordination environment and can be attributed to the $^4T_{1g}(F)(t_{2g}{}^5e_g{}^3) \rightarrow {}^4T_{2g}(P)(t_{2g}{}^4e_g{}^3)$ transition. The broadness of the peak is likely to be due to the distorted nature of the two cobalt sites observed for $Co_2B_2O_5$.

4.3.5.1 Colour measurements

CIE L*, a*, b* (CIELAB) colour measurements were performed using a Perkin-Elmer Lambda 35 UV-Vis spectrometer. Results for $Co_2{}^{11}B_2O_5$, are presented in Table 4-25 and Figure 4-25.

Table 4-25: CIE L*, a*, b* Colour data for the $Co_2(^{11}B)_2O_5$.

	L*	**a***	**b***
$Co_2(^{11}B)_2O_5$	41.34	31.13	-32.89

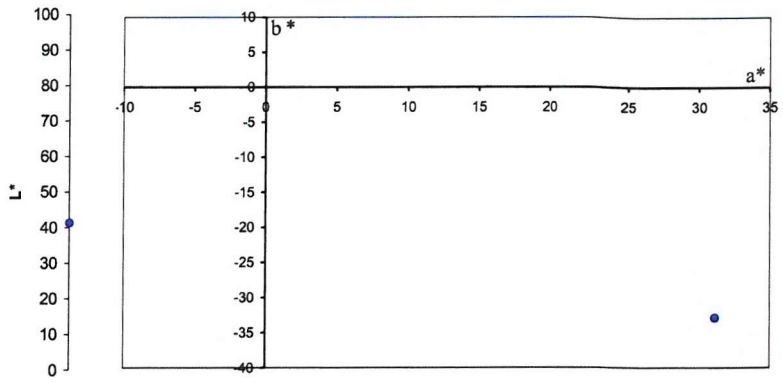

Figure 4-25: CIE L*, a*, b* Colour data for the $Co_2(^{11}B)_2O_5$.

4.3.6 IR spectroscopy

Infrared vibration spectra were obtained for $Co_2B_2O_5$, $Co_2(^{10}B)_2O_5$ and $Co_2(^{11}B)_2O_5$ using a Perkin-Elmer Spectrum One spectrometer in diffuse reflectance mode. Spectra for the three materials are presented in Figure 4-26.

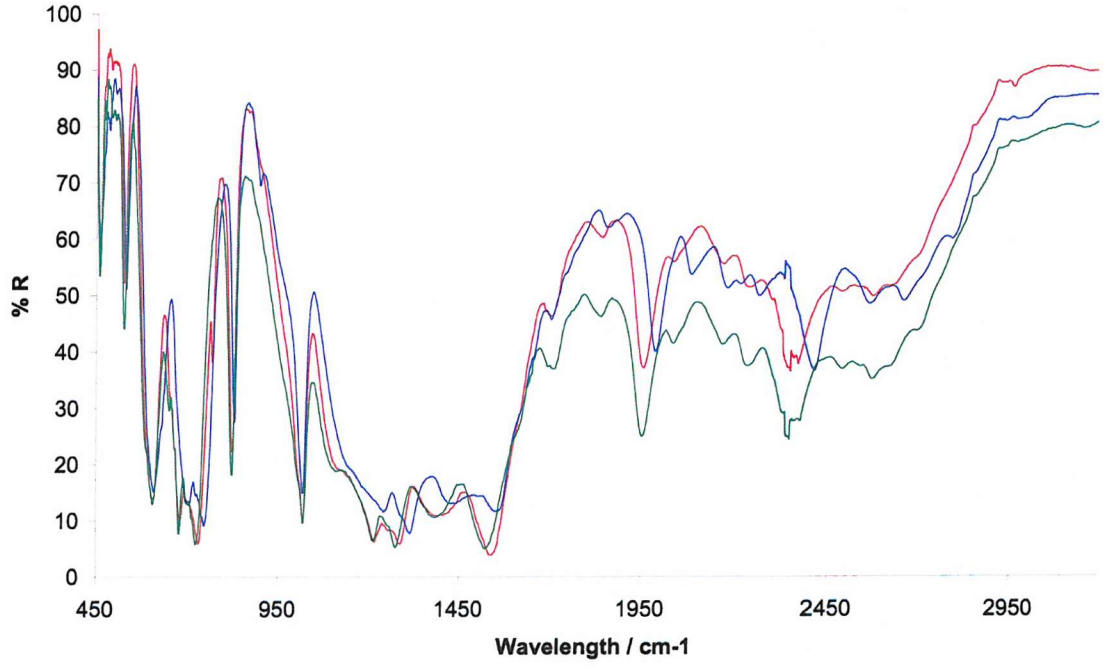

Figure 4-26: Infrared reflectance spectra for $Co_2B_2O_5$ (red), $Co_2(^{10}B)_2O_5$ (blue) and $Co_2(^{11}B)_2O_5$ (green).

The spectral regions and specific absorption bands are assigned according to those reported by Pascuta *et al.* and Motke *et al.* for borate glasses.

Table 4-26: Frequencies and their assignment for IR spectra of $Co_2B_2O_5$, $Co_2(^{10}B)_2O_5$ and $Co_2(^{11}B)_2O_5$.

Wavenumber / cm^{-1}	Assignment
***ca.* 1100-1600**	B-O stretching vibrations of trigonal BO_3 units
***ca.* 700-750**	B-O-B Bending vibrations
***ca.* 550-650**	B-O-B stretching vibrations

It can be seen from the observed data that the spectrum for the sample containing ^{10}B is shifted by a significant amount to shorter wavelengths when compared to the sample containing natural boron. Conversely, the ^{11}B spectrum is shifted only slightly to longer wavelengths. The shift observed for each of the spectra can be explained by considering the relative mass of the boron atoms in each sample. As the average mass of the boron atom is decreased the frequency with which the vibrations occur will increase, therefore the wavelength will become shorter. Natural boron consists of 20 % ^{10}B and 80 % ^{11}B, thus the relative atomic mass for natural boron will be 10.8 (actual value 10.811(7) [35]). It can, therefore be assumed that the behaviour of a ^{nat}B-O vibration will be closer to that of ^{11}B-O than ^{10}B-O.

4.3.7 Conclusions

Single phase samples of $Co_2B_2O_5$, $Co_2(^{10}B)_2O_5$ and $Co_2(^{11}B)_2O_5$ have been successfully prepared by conventional solid state synthesis. A complete structural characterisation of $Co_2(^{11}B)_2O_5$ has been undertaken using PND and UV-Vis and IR spectroscopy.

The cobalt pyroborate structure has been refined to a greater degree of accuracy than had been previously reported and the individual coordination environments of both cobalt and boron have been considered.

4.4 $Co_{2.45}BO_5$ Single Crystal

4.4.1 Introduction

One of the more common structure-types for borates of the first row transition metals is the ludwigite structure, as mentioned in section 4.1.1. One of the ternary phases found in the C-B-O system [6] is a mixed-valent cobalt borate (Co_3BO_5), which has the ludwigite structure. Gotz and Hermann [5] were the first to detect this material and present its structure, which has been refined since [32]. Other cobalt-containing ludwigite-type compounds include $Cu_{2-x}Co_xGaBO_5$ [4] and $Co_{2.1}Al_{0.9}BO_5$ [11]. These materials contain both Co^{II} and Co^{III} ions, which are distributed across four individual MO_6 sites within the ludwigite structure. As mentioned previously (section 4.3.4.3) the colour – black – of these materials is due to mixed-valent charge transfer transitions between sites containing Co^{2+} and sites containing Co^{3+}.

In an attempt to prepare a single-phase powdered sample of the intensely coloured cobalt borate CoB_2O_4, a black, metallic-looking, molten sample was produced. From this was isolated a single needle-like single crystal, which appeared to be very dark red in colour. Details of the method used are given in section 4.4.2.

4.4.2 Synthesis

The reagents, cobalt (II) oxide (0.50 g) and boric acid (0.8252 g), were intimately mixed by grinding under acetone to yield a homogenous mixture. The acetone was allowed to evaporate in a drying oven ($\approx$ 150 °C) and the mixture was transferred to an alumina boat. The sample was then heated to 950 °C for 15 hours under flowing nitrogen gas. The sample melted to form a black metallic-effect glass with a small cluster of dark red crystals at one edge of the boat. The largest single crystal was isolated and studied using single-crystal X-ray diffraction. The crystal has an overall elemental composition of $Co_{2.45}BO_5$ and is seen to crystallise in the orthorhombic space group P*bam*, as described for the ludwigite structure.

4.4.3 Single Crystal X-ray Diffraction

Single crystal X-ray diffraction data were collected using a Nonius Kappa CCD diffractometer. The X-ray source is a rotating anode giving molybdenum K_α radiation (λ= 0.71073 Å). The crystal was mounted on a glass fibre and fixed in a goniometer, which was used to orient the crystal over a range of angles relative to the X-ray beam. An area detector measured the intensities of the diffracted X-rays. Initially a single position scan was done to check the quality of the diffraction from the crystal, before the collection of a full data set

was initiated. Analysis of the collected data was carried out using SHELXS/L-97 and the WINGX system (Ver. 1.64.03) [36]. The collection of single crystal data and its refinement was performed in association with Lee A. Gerrard, Southampton University.

Crystallographic data and refinement statistics for $Co_{2.45}BO_5$ are presented in Table 4-27.

Table 4-27:Refined crystallographic data for $Co_{2.45}BO_5$ (e.s.d.s are shown in parentheses).

Space group: P*bam*

Lattice parameters a = 9.191(1) Å, b = 12.038(2) Å, c = 2.9945(3) Å

Atom	*x*	*y*	*z*	*Frac.*	U_{eq} /Å^2
Co(1)	0	0	0.5	0.86(1)	0.0046(6)
Co(2)	0.5	0	0	0.75(1)	0.0066(7)
Co(3)	0.2381(1)	0.11428(9)	0	0.68(1)	0.0048(5)
Co(4)	-0.00200(8)	0.27872(8)	0.5	0.88(1)	0.0043(5)
B	-0.2297(8)	0.1369(6)	0	1	0.010(2)
O(1)	-0.3786(5)	0.1376(3)	0	1	0.014(1)
O(2)	-0.1522(5)	0.0406(4)	0	1	0.014(1)
O(3)	0.1101(5)	0.1427(3)	0.5	1	0.015(1)
O(4)	0.3423(5)	0.2613(4)	0	1	0.013(1)
O(5)	0.3846(6)	0.0748(4)	-0.5	1	0.022(1)

Final fit parameters:χ^2 =1.138, R_{wp} = 9.57 %, R_p = 3.96 %

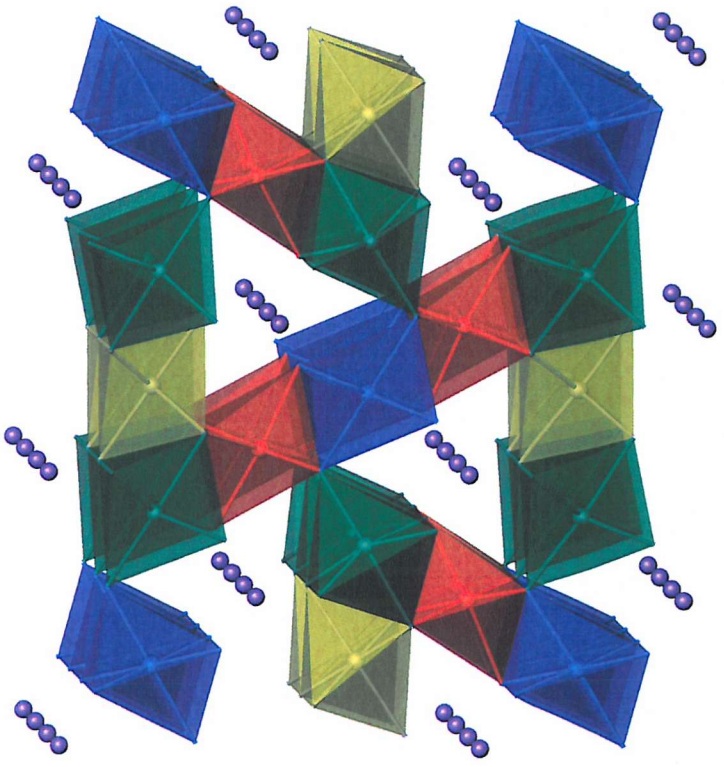

Figure 4-27: A view of the $Co_{2.45}BO_5$ showing the four individual cobalt octahedral sites (blue, red, green and yellow). Boron atoms are shown as purple spheres and oxygen atoms are omitted for clarity.

4.4.4 Interatomic Distances and Angles

Derived interatomic distances and angles for $Co_{2.45}BO_5$ and literature values for the related ludwigite-type phases $Co_{2.1}Al_{0.9}BO_5$ and Co_3BO_5 are presented in Table 4-28.

Table 4-28: Derived bond distances (Å) for the $Co(1)O_6$, $Co(2)O_6$, $Co(3)O_6$, $Co(4)O_6$ and BO_3 sites in $Co_{2.45}BO_5$. (e. s. d. s are shown in parentheses).

Distance	$Co_{2.45}BO_5$	$Co_{2.1}Al_{0.9}BO_5$	Co_3BO_5
Co(1)_O2 (x4)	2.107(3)	2.113(3)	2.115(3)
Co(1)_O3 (x2)	1.993(4)	1.993(3)	1.982(3)
Co(2)_O1 (x2)	1.997(4)	1.984(3)	1.996(3)
Co(2)_O5 (x4)	2.044(4)	2.036(3)	2.055(3)
Co(3)_O2	2.025(5)	1.997(4)	2.024(4)
Co(3)_O3 (x2)	1.935(3)	1.936(3)	1.940(3)
Co(3)_O4	2.012(5)	2.013(4)	2.029(4)
Co(3)_O5 (x2)	2.069(4)	2.070(3)	2.054(3)
Co(4)_O1 (x2)	2.131(3)	2.139(3)	2.124(3)
Co(4)_O3	1.935(5)	1.932(4)	1.941(4)
Co(4)_O4 (x2)	2.127(3)	2.131(3)	2.126(3)
Co(4)_O5	2.048(5)	2.049(4)	2.040(4)
B_O1	1.368(9)	1.370(7)	1.370(7)
B_O2	1.360(9)	1.369(7)	1.379(7)
B_O4	1.393(9)	1.378(6)	1.361(6)

Table 4-29: Derived bond angles (°) for the $Co(1)O_6$, $Co(2)O_6$, $Co(3)O_6$, $Co(4)O_6$ and BO_3 sites in $Co_{2.45}BO_5$. (e. s. d. s are shown in parentheses).

Angle	$Co_{2.45}BO_5$
O2_Co1_O2	180.0
O2_Co1_O2	90.6(2)
O2_Co1_O2	89.4(2)
O2_Co1_O3	97.9(2)
O2_Co1_O3	82.1(2)
O3_Co1_O3	180.0
O1_Co2_O1	180.0(3)
O1_Co2_O5	94.3(2)
O1_Co2_O5	85.7(2)
O5_Co2_O5	180.0(3)
O5_Co2_O5	85.8(2)
O5_Co2_O5	94.2(2)
O2_Co3_O3	85.7(2)
O2_Co3_O4	174.5(2)
O2_Co3_O5	92.4(2)
O3_Co3_O3	101.4(2)
O3_Co3_O4	97.7(2)
O3_Co3_O5	175.2(2)
O3_Co3_O5	82.9(2)
O4_Co3_O5	83.8(2)
O5_Co3_O5	92.7(2)

Angle	$Co_{2.45}BO_5$
O1_Co4_O1	89.3(2)
O1_Co4_O3	96.7(2)
O1_Co4_O4	163.7(2)
O1_Co4_O4	88.3(2)
O1_Co4_O5	82.2(2)
O3_Co4_O4	99.6(2)
O3_Co4_O5	178.4(2)
O4_Co4_O4	89.5(2)
O4_Co4_O5	81.5(2)
O1_B_O2	121.9(6)
O1_B_O2	120.1(6)
O1_B_O2	118.0(6)

4.4.5 Discussion

$Co_{2.45}BO_5$ adopts the Ludwigite structure as described previously and, due to charge balancing constraints, must contain both Co^{II} and Co^{III}. This is also the case for the mixed-valent cobalt borates mentioned in section 4.4.1, where $Co_{2.1}Al_{0.9}BO_5$ has a Co^{II}:Co^{III} ratio of 1:1.1 and Co_3BO_5 has a Co^{II}:Co^{III} ratio of 1:2. For the material $Co_{2.45}BO_5$, a greater presence of Co^{3+} must be true. Indeed, calculations to determine the amount of each oxidation state

present lead to the following composition: $Co^{2+}_{0.34}Co^{3+}_{2.11}BO_5$. This material therefore has a Co^{II}:Co^{III} ratio of 1:6.21.

As previously mentioned (section 4.1.6) for the Ludwigite structure, the covalency of the B-O bond affects the distribution of cations over the four octahedral metal sites. Therefore, due to the metal-oxygen-boron interactions, it is probable that sites 1 and 4 will contain a higher proportion of Co^{2+} cations than sites 2 and 3. However, due to the fact that the sites are only partially occupied in each case, bond valence calculations do not help to solve the distribution of Co^{2+} and Co^{3+} over the four sites.

4.4.6 Conclusions

The $Co_{2.45}BO_5$ single crystal has been characterised using X-ray diffraction and is a further example of a mixed-valent cobalt borate that adopts the ludwigite structure. The interatomic distances and angles presented here are in accordance with those presented for other cobalt containing ludwigites. Indeed, they are extremely similar to those reported for $Co_{2.1}Al_{0.9}BO_5$. Due the limited sample size and nature it was not possible to obtain UV-Visible data to further study the colour of the sample. Nor was it possible to prepare an equivalent powder sample.

4.5 References

[1] Takeuchi Y., Watanabe T., Ito T.: Acta Crystallogr. 3, 473 (1950)

[2] Bertaut E.F.; *Acta Cryst.*, **3** 98 (1950).

[3] Fernandes J.C., Guimarães R.B., Continentino M.A., Borges H.A., Sulpice A., Tholence J-L, Siqueira J.L., Zawislak L.I., da Cunha J.B.M., dos Santos C.A.; *Phys. Rev.*, **B58,** 287-292 (1998).

[4] Bezmaternykh L.N., Ovchinnikov S.G., Balaev A.D., Beluschenko S.V., Gudim I.A., Vasiliev A.D., Potseluyko A.M., Zabluda V.N.; *ICFM conference proceedings, Ukraine* (2003).

[5] Gotz W., Hermann V.; *Naturwissenschaf.*, **53** 475 (1966).

[6] Rowsell J.L.C., Taylor N.J., Nazar L.F.; *J. Solid State Chem.*, **174**, 189-197, (2003).

[7] Continentino M.A., Fernandes J.C., Guimarães R.B., Borges H.A., Sulpice A., Tholence J-L, Siqueira J.L., da Cunha J.B.M., dos Santos C.A.; *Eur. Phys. J.*, **B9,** 613-618 (1999).

[8] Bordet P., Anterion B., Mir M, Guimarães R.B., Fernandes J.C., Continentino M.A.; *Acta Cryst.*, **A58**, Supp. C363, (2002).

[9] Stenger C.G.F., Verschoor G.C., Ijdo D.J.W.; *Mat. Res. Bull.*, **8**, 1285-1292 (1973).

[10] Norrestam R., Kritikos M., Nielsen K., Søtofte I., Thorup N.; *J. Solid State Chem.*, **111** 217-223 (1994).

[11] Brown R.D., Cheetham A.K., Hriljac J.A., Satek L.C.: *J. Solid State Chem.* **84**, 289 (1990).

[12] Satek L.C.: US Patent 4,590,324 (1986).

[13] Hussman G.P., McMahon P.E.: US Patent 4,740,647 (1988).

[14] Bluhm K., Schaefer J.: *Z. Anorg. Allg. Chem.* **621**, 571 (1995).

[15] Uhig; *JCPDS Grant-in-Aid Report* (1976).

[16] CELL (Program to calculate cell parameters from indexed powder data), University of Oxford.

[17] Shannon R.D.; *Acta Cryst.*, **A32** 751-767 (1976).

[18] Larson A.C., Von Dreele R.B.; *General Structure Analysis System (GSAS).* Los Alamos National Laboratory Report LAUR, 86 (2000).

[19] Lever A.B.B.P.; *Inorganic Electronic Spectroscopy, 2nd Ed.*, Elsevier, Amsterdam (1984).

[20] Cotton F.A., Wilkinson G., Murillo C.A., Bochmann M.; *Advanced Inorganic Chemistry 6th Ed.*, J. Wiley, New York (1999).

[21] Pearson R.G., *Inorg. Chem.*, **27**, 734 (1988)

[22] Satek L.C., Kaduk J.A., McMahon P.E.; *Catalysis of Organic Reactions*, Pascoe WE (ed.), 235-243. New York, Marcel Dekker (1992).

[23] Richter L.; *"Synthese und Strukturuntersuchungen von Eisen- und Kupfer Aluminum Boraten"*, Technische Hochschule, Aachen (1977).

[24] Kaduk J.A., Satek L.C., McKenna S.T.; *The Rigaku Journal*, **16**, 17 (1999).

[25] *Inorganic Crystal Structure Database*, Fachinformationszentrum (FIZ) Karlsruhe, Germany, (2003).

[26] Berger S.V.; *Acta Chemica Scand.*, **4** 1054-1065 (1950).

[27] Ebelmen J.J.; *Ann. Chim. et Phys. 3*, **33** 34 (1851).

[28] Ouvrard L.; *Compt. Rend.*, **130** 172 (1900).

[29] Guertler W.Z.; *Z. Anorg. Chem.*, **40** 239 (1904).

[30] Konovalov P.F.; *Dokl. Akad. Nauk SSSR*, **70** 847 (1950); Belyaev IN; *Zh. Fiz. Khim.*, **30** 1419 (1956).

[31] Hauck D., Muller F.; *Z. Anorg. Allg. Chem.*, **466** 163 (1980).

[32] Norrestam R., Nielsen K., Sotofte I, Thorup N; *Z. Kristallogr.*, **189** 33 (1989).

[33] Altermatt D., Brown I.D.; *Acta Cryst.* **B41**, 240-244, (1985).

[34] Altermatt D., Brown I.D.; *Acta Cryst.* **B41**, 244-247, (1985).

[35] Coplen T.B. for IUPAC; *Pure & Appl. Chem.*, **73**, 667-683, (2001).

[36] Farrugia L.J., *J. Appl. Cryst.* **32**, 837-838, (1999).

Chapter 5

Mixed Spinel Systems

5 Mixed Spinel Systems

Spinel-type systems, as described in Chapter 1, are extremely useful as inorganic pigments due to their high chemical and thermal stability. The diverse nature of the colours available through the incorporation of certain metal cations into the spinel structure is impressive and is an area of great scientific interest. Some research groups have studied the effect of the synthetic method upon pigment colour and structure [1, 2, 3, 4], whilst others have concentrated upon substitution of both 'coloured' [5, 6, 7, 8] and 'colourless' [9, 10] cations. Also a number of groups have been concerned with gaining a better understanding of the spinel structure itself and of existing pigment systems [11, 12, 13]. In most of these cases the aim has been to develop methods that can improve the properties – chemical and physical stability and/or colour – of the pigment in some way.

The distribution of the metal cations across the octahedral and tetrahedral sites within the spinel structure obviously has a large influence upon the colour produced by a particular pigment. The ability to predict the preferred coordination geometry of a given cation and additionally to restrict that cation to a desired site in preference to another has important implications for the coloured properties of the system. In the case of the cobalt compounds considered in this Chapter, being able to direct the cobalt ions onto sites that are tetrahedral or highly distorted in preference to octahedral sites, using a colourless metal species as the driving force, might allow the production of a more intensely coloured pigment with the minimum amount of cobalt incorporation within the structure.

In this section two complex inverse spinel systems ($(Co_{1-x}(MgZn)_x)_2TiO_4$ and $Co(Mg_{1-x}Zn_x)TiO_4$) are studied using PXD, PND and combined EXAFS/PND techniques in an effort to solve the cation distributions and also to begin to model the local lattice distortions caused by Ti^{4+} ions within the spinel structure.

5.1 $(Co_{1-x}(MgZn)_x)_2TiO_4$ and $Co(Mg_{1-x}Zn_x)TiO_4$

5.1.1 Introduction

The incorporation of cobalt into the tetrahedral and octahedral sites of the inverse titanium spinels Mg_2TiO_4 and Zn_2TiO_4 produces compounds that have intense green colours.

Two complex pigment systems are studied here, $(Co_{1-x}(MgZn)_x)_2TiO_4$ and $Co(Mg_{1-x}Zn_x)TiO_4$ (where x = 0, 0.2, 0.4, 0.6, 0.8, 1.0), with the aim of solving the cation distributions over the tetrahedral and octahedral spinel sites and, ultimately to determine the distribution of cobalt over the sites, as a function of zinc and magnesium content.

5.1.2 Synthesis

The two systems, $(Co_{1-x}(MgZn)_x)_2TiO_4$ and $Co(Mg_{1-x}Zn_x)TiO_4$ (where x = 0.0, 0.2, 0.4, 0.6, 0.8, 1.0), were prepared by heating stoichiometric mixtures of cobalt (II) oxide, magnesium (II) oxide, nickel (II) oxide and titanium (IV) oxide (all >99% purity). The ground mixtures were formed into pellets, firstly to aid reaction and secondly to enable the simultaneous firing of multiple samples to ensure that reaction conditions were consistent for each composition. The pellets were heated in air to 1200 °C for 48 hours.

The colour of the resulting materials for the $(Co_{1-x}(MgZn)_x)_2TiO_4$ system ranged from a very dark and intense green for the composition Co_2TiO_4 (x = 0) to white for $MgZnTiO_4$ (x = 1). For the $Co(Mg_{1-x}Zn_x)TiO_4$ system colours ranged from an intense dark green ($CoMgTiO_4$, x = 0) to an olive-like green/brown colour ($CoZnTiO_4$, x = 1.0)

Initial phase identification X-ray powder diffraction data revealed that the desired inverse spinel type phase had been formed in each case. The products were studied further using PND and EXAFS/PND combined refinement.

5.1.3 Powder X-ray Diffraction

PXD data for the $(Co_{1-x}(MgZn)_x)_2TiO_4$ and $Co(Mg_{1-x}Zn_x)TiO_4$ (x = 0, 0. 2, 0.4, 0.6, 0.8, 1.0) systems were recorded on a Siemens D5000 diffractometer using Cu $K\alpha_1$ radiation (λ = 1.5406 Å) over the two-theta range 10° – 110° for 15 hours. The diffraction patterns obtained for samples containing cobalt have relatively high signal-to-noise ratios for such a regular and well-defined structure. This is caused by the fluorescence of cobalt when exposed to X-radiation at a particular wavelength. Rietveld refinements were performed using the PC package, GSAS [14] as described in Chapter 2. Literature [8, 15] values were used as the initial models for Co_2TiO_4 (x = 0 for the $(Co_{1-x}(MgZn)_x)_2TiO_4$ system) and $CoZnTiO_4$ (x = 1.0 for the $Co(Mg_{1-x}Zn_x)TiO_4$ system) respectively. Subsequent refinements

utilised the values obtained in the preceding refinement. The fractional site occupancies for the tetrahedral and octahedral sites were fixed at values based upon the intended composition in each case and the site preferences displayed by the cations in the end-member compounds (x = 0 and x = 1.0). It was not possible to refine these site occupancies due to the complexity of the cation distribution. The refinements proceeded smoothly to convergence giving a good fit to the observed data and chemically sensible bond distances and angles in each case.

The refinement profiles for $Co_{1.2}Mg_{0.4}Zn_{0.4}TiO_4$, $MgZnTiO_4$, $CoMg_{0.8}Zn_{0.2}TiO_4$ and $CoMg_{0.8}Zn_{0.2}TiO_4$ are shown in Figure 5-1. Tables of cyrstallographic data and refinement statistics for each phase are presented in Table 5-1 and Table 5-2.

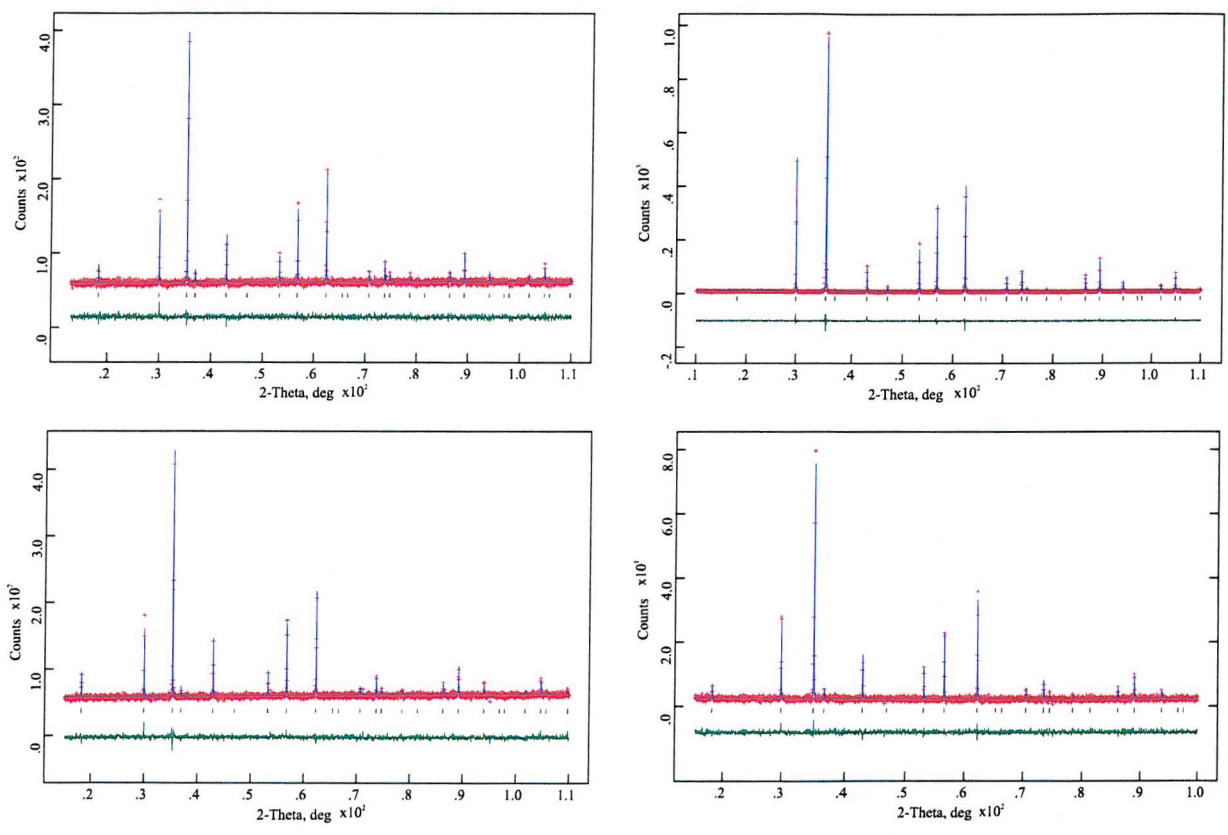

Figure 5-1: Observed (+++), Calculated (—), and difference (shown underneath) PXD profiles for $Co_{1.2}Mg_{0.4}Zn_{0.4}TiO_4$ (top left), $MgZnTiO_4$ (top right), $CoMg_{0.8}Zn_{0.2}TiO_4$ (bottom left) and $CoMg_{0.8}Zn_{0.2}TiO_4$ (bottom right). Tick marks indicate reflection positions.

Table 5-1: Refined crystallographic data (PXD) for the $(Co_{1-x}(MgZn)_x)_2TiO_4$ (x = 0, 0.2, 0.4, 0.6, 0.8, 1.0) series as a function of x). (e. s. d. s are shown in parentheses). Cation positions Td (1/8,1/8,1/8) and Oh (1/2,1/2,1/2).

Space group: *Fd-3m*

Parameter	0	0.2	0.4	0.6	0.8	1.0
Cell Parameter (Å)	8.42243(9)	8.4242(3)	8.42349(5)	8.41978(4)	8.4171(2)	8.41133(3)
Tetrahedral Site						
U_{iso}*	0.7(2)	0.7(2)	0.5(2)	0.8(1)	0.5(2)	1.13(5)
Occupancy # (Co / Mg / Zn)	1.0 / 0 / 0	0.80 / 0.05 / 0.15	0.60 / 0.10 / 0.30	0.40 / 0.10 / 0.50	0.15 / 0.15 / 0.70	0 / 0.09(6) 0.991(6)
Octahedral Site						
U_{iso}*	2.5(3)	1.6(2)	1.8(2)	3.9(2)	5.3(2)	0.89(7)
Occupancy # (Co / Mg / Zn)	0.5 / 0 / 0	0.400 / 0.075 / 0.025	0.30 / 0.15 / 0.05	0.20 / 0.25 / 0.05	0.125 / 0.325 / 0.05	0 / 0.496(3) / 0.004(3)
Oxygen Site						
x (= y= z)	0.2554(9)	0.2576(7)	0.2566(6)	0.2529(5)	0.2452(5)	0.2589(4)
U_{iso}*	3.3(4)	1.4(4)	2.8(3)	3.5(3)	4.6(3)	2.2(2)
R_{wp} (%)	3.62	3.65	3.96	4.46	6.56	11.19
R_p (%)	2.87	2.92	3.14	3.50	5.11	8.67
χ^2	0.1028	0.0945	0.0977	0.1121	0.1298	0.1463

* Isotropic temperature factors are quoted with units - $Å^2x100$. # Ti fractional occupancies are assumed to be zero on the tetrahedral site and 0.5 on the octahedral site.

Table 5-2: Refined crystallographic data (PXD) for the $Co(Mg_{1-x}Zn_x)TiO_4$ (x = 0, 0.2, 0.4, 0.6, 0.8, 1.0) series as a function of x. (e. s. d. s are shown in parentheses). Cation positions Td (1/8,1/8,1/8) and Oh (1/2,1/2,1/2).

Space group: *Fd*-3*m*

Parameter	0	0.2	0.4	0.6	0.8	1.0
Cell Parameter (Å)	8.42441(5)	8.42255(5)	8.44224(9)	8.4427(3)	8.4428(2)	8.4431(3)
Tetrahedral Site						
U_{iso}*	1.4(2)	0.4(2)	0.3(3)	0.4(3)	0.8(2)	0.7(3)
Occupancy # (Co / Mg / Zn)	0.61(2) / 0.39(2) / 0	0.50 / 0.40 / 0.10	0.50 / 0.20 / 0.30	0.40 / 0.10 / 0.50	0.25 / 0.05 / 0.70	0.02(2) / 0 0.98(2)
Octahedral Site						
U_{iso}*	1.1(2)	2.1(2)	4.7(4)	3.3(3)	3.2(3)	3.3(3)
Occupancy # (Co / Mg / Zn)	0.196(6) / 0.304(6) / 0	0.25 / 0.20 / 0.05	0.25 / 0.20 / 0.05	0.30 / 0.15 / 0.05	0.375 / 0.075 / 0.05	0.492(6) / 0 / 0.008(6)
Oxygen Site						
x (= y= z)	0.2613(5)	0.2563(5)	0.2567(9)	0.2546(9)	0.2520(9)	0.2518(9)
U_{iso}*	1.6(3)	3.0(3)	5.2(5)	2.8(4)	3.9(5)	3.1(4)
R_{wp} (%)	4.63	4.10	19.97	19.26	4.36	5.96
R_p (%)	3.77	3.24	15.81	15.05	3.57	4.74
χ^2	0.1021	0.1037	0.1023	0.0997	0.1028	0.1185

* Isotropic temperature factors are quoted with units - $Å^2x100$. # Ti fractional occupancies are assumed to be zero on the tetrahedral site and 0.5 on the octahedral site.

5.1.4 Powder Neutron Diffraction

Time of flight (TOF) powder neutron diffraction data were collected on the POLARIS diffractometer at the Rutherford Appleton Laboratory, Oxfordshire, UK. All data sets were collected at room temperature. Rietveld refinements were performed using the PC package, GSAS [14] as described in Chapter 2. Literature [8, 15] values were used as the initial models for Co_2TiO_4 (x = 0 for the $(Co_{1-x}(MgZn)_x)_2TiO_4$ system) and $CoZnTiO_4$ (x = 1.0 for the $Co(Mg_{1-x}Zn_x)TiO_4$ system) respectively. Subsequent refinements utilised the values obtained in the preceding refinement. A uniform approach to the structure refinement was

undertaken for each of the data sets obtained with different x values to ensure consistent results. Initially the background was modelled and the lattice parameters were refined to accurately locate the reflections. The peak profiles were then refined and the atomic positions varied. Finally, isotropic temperature factors and fractional site occupancies for the tetrahedral and octahedral metal sites were added to the refinement. Linear constraints were added to the refinement of fractional occupancies for the end member compounds of each series (x = 0, 1.0) to give the required stoichiometry. Due to the complexity of the cation distribution over the tetrahedral and octahedral sites for the remaining members of each series (x = 0.2, 0.4, 0.6, 0.8) the site occupancy values were fixed according to the reactant levels. In each case the values were also fixed according to the site preferences shown by each cation in the end-member compounds of each series.

The refinements proceeded smoothly to convergence giving a good fit to the observed data and chemically sensible bond distances and angles. The refinement profiles for $Co_{1.6}Mg_{0.2}Zn_{0.2}TiO_4$ and $CoZnTiO_4$ are shown in Figure 5-2 and Figure 5-3 respectively. Tables of cyrstallographic data and refinement statistics for each phase are presented in Table 5-3 to Table 5-14.

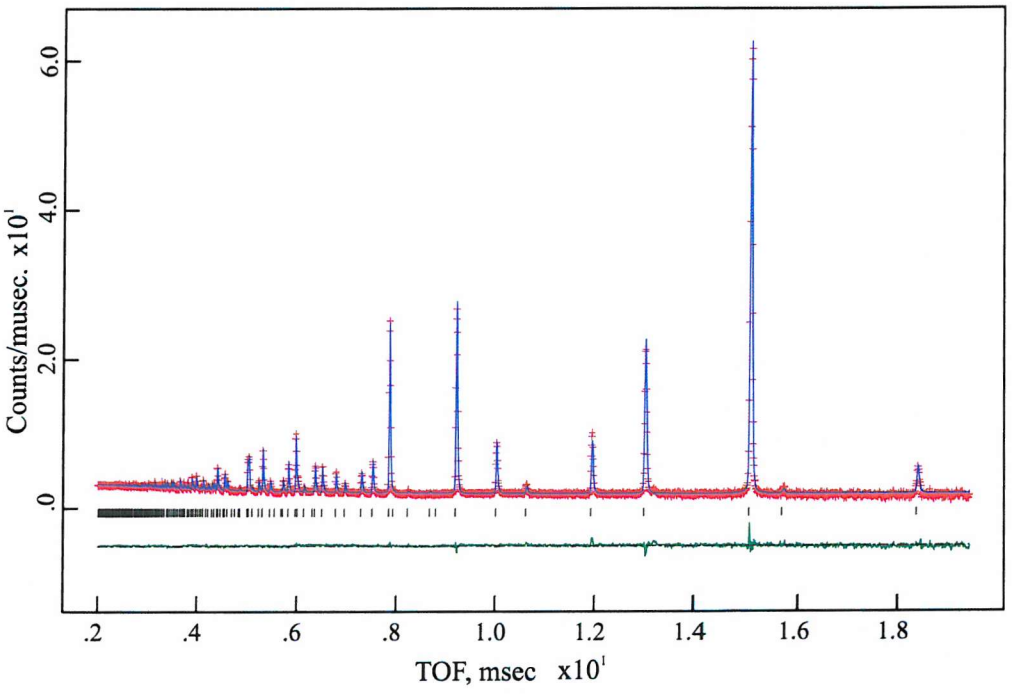

Figure 5-2: Observed (+++), Calculated (—), and difference (shown underneath) PND profiles for $Co_{1.6}Mg_{0.2}Zn_{0.2}TiO_4$. Tick marks indicate reflection positions.

Table 5-3: Refined crystallographic data (PND) for Co_2TiO_4 (e. s. d. s are shown in parentheses).

Space group: *F*d-3m

Lattice parameters a = 8.44858(5) Å

Atom	*x*	*y*	*z*	*Frac.*	U_{iso} /Å^{2}x100
Co(1)	0.5	0.5	0.5	0.500(3)	0.79(9)
Ti(1)	0.5	0.5	0.5	0.500(3)	0.79(9)
Co(2)	-0.125	-0.125	-0.125	1.000(6)	0.96(4)
Ti(2)	-0.125	-0.125	-0.125	0.000(6)	0.96(4)
O	0.26059(3)	0.26059(3)	0.26059(3)	1	1.06(1)

Final fit parameters:χ^2 = 1.739, R_{wp} = 2.74 %, R_p = 5.00 %

Table 5-4: Refined crystallographic data (PND) for $Co_{1.6}Mg_{0.2}Zn_{0.2}TiO_4$ (e. s. d. s are shown in parentheses).

Space group: *F*d-3m

Lattice parameters a = 8.44607(4) Å

Atom	*x*	*y*	*z*	*Frac.**	U_{iso} /Å^{2}x100
Co(1)	0.5	0.5	0.5	0.400	.09(9)
Mg(1)	0.5	0.5	0.5	0.075	.09(9)
Zn(1)	0.5	0.5	0.5	0.025	.09(9)
Ti(1)	0.5	0.5	0.5	0.500	.09(9)
Co(2)	-0.125	-0.125	-0.125	0.800	0.68(3)
Mg(2)	-0.125	-0.125	-0.125	0.050	0.68(3)
Zn(2)	-0.125	-0.125	-0.125	0.150	0.68(3)
O	0.26069(3)	0.26069(3)	0.26069(3)	1	1.07(1)

Final fit parameters:χ^2 = 1.943, R_{wp} = 2.84 %, R_p = 5.11 %

Table 5-5: Refined crystallographic data (PND) for $Co_{1.2}Mg_{0.4}Zn_{0.4}TiO_4$ (e. s. d. s are shown in parentheses).

Space group: *F*d-3m

Lattice parameters a = 8.44750(4) Å

Atom	*x*	*y*	*z*	*Frac.**	U_{iso} /Å^{2}x100
Co(1)	0.5	0.5	0.5	0.300	1.6(4)
Mg(1)	0.5	0.5	0.5	0.150	1.6(4)
Zn(1)	0.5	0.5	0.5	0.050	1.6(4)
Ti(1)	0.5	0.5	0.5	0.500	1.6(4)
Co(2)	-0.125	-0.125	-0.125	0.600	0.55(2)
Mg(2)	-0.125	-0.125	-0.125	0.100	0.55(2)
Zn(2)	-0.125	-0.125	-0.125	0.300	0.55(2)
O	0.26075(3)	0.26075(3)	0.26075(3)	1	1.00(1)

Final fit parameters:$\chi^2 = 2.206$, $R_{wp} = 3.11$ %, $R_p = 5.44$ %

Table 5-6: Refined crystallographic data (PND) for $Co_{0.8}Mg_{0.6}Zn_{0.6}TiO_4$ (e. s. d. s are shown in parentheses).

Space group: *F*d-3m

Lattice parameters a = 8.44515(5) Å

Atom	*x*	*y*	*z*	*Frac.**	U_{iso} /Å^{2}x100
Co(1)	0.5	0.5	0.5	0.200	0.9(2)
Mg(1)	0.5	0.5	0.5	0.250	0.9(2)
Zn(1)	0.5	0.5	0.5	0.050	0.9(2)
Ti(1)	0.5	0.5	0.5	0.500	0.9(2)
Co(2)	-0.125	-0.125	-0.125	0.400	0.40(2)
Mg(2)	-0.125	-0.125	-0.125	0.100	0.40(2)
Zn(2)	-0.125	-0.125	-0.125	0.500	0.40(2)
O	0.26085(3)	0.26085(3)	0.26085(3)	1	0.85(2)

Final fit parameters:$\chi^2 = 3.125$, $R_{wp} = 3.64$ %, $R_p = 6.13$ %

Table 5-7: Refined crystallographic data (PND) for $Co_{0.4}Mg_{0.8}Zn_{0.8}TiO_4$ (e. s. d. s are shown in parentheses).

Space group: *F*d-3m

Lattice parameters a = 8.43693(4) Å

Atom	*x*	*y*	*z*	*Frac.**	U_{iso} /Å^{2}x100
Co(1)	0.5	0.5	0.5	0.125	1.79(9)
Mg(1)	0.5	0.5	0.5	0.325	1.79(9)
Zn(1)	0.5	0.5	0.5	0.050	1.79(9)
Ti(1)	0.5	0.5	0.5	0.500	1.79(9)
Co(2)	-0.125	-0.125	-0.125	0.150	0.55(2)
Mg(2)	-0.125	-0.125	-0.125	0.150	0.55(2)
Zn(2)	-0.125	-0.125	-0.125	0.700	0.55(2)
O	0.26095(3)	0.26095(3)	0.26095(3)	1	0.90(2)

Final fit parameters:χ^2 = 2.969, R_{wp} = 3.46 %, R_p = 6.12 %

Table 5-8: Refined crystallographic data (PND) for $MgZnTiO_4$ (e. s. d. s are shown in parentheses).

Space group: *F*d-3m

Lattice parameters a = 8.43497 (4) Å

Atom	*x*	*y*	*z*	*Frac.*	U_{iso} /Å^{2}x100
Mg(1)	0.5	0.5	0.5	0.49(3)	1.00(5)
Zn(1)	0.5	0.5	0.5	0.01(3)	1.00(5)
Ti(1)	0.5	0.5	0.5	0.500	1.00(5)
Mg(2)	-0.125	-0.125	-0.125	0.02(6)	0.60(2)
Zn(2)	-0.125	-0.125	-0.125	0.98(6)	0.60(2)
O	0.26109(3)	0.26109(3)	0.26109(3)	1	0.824(8)

Final fit parameters:χ^2 = 2.906, R_{wp} = 3.83 %, R_p = 6.15

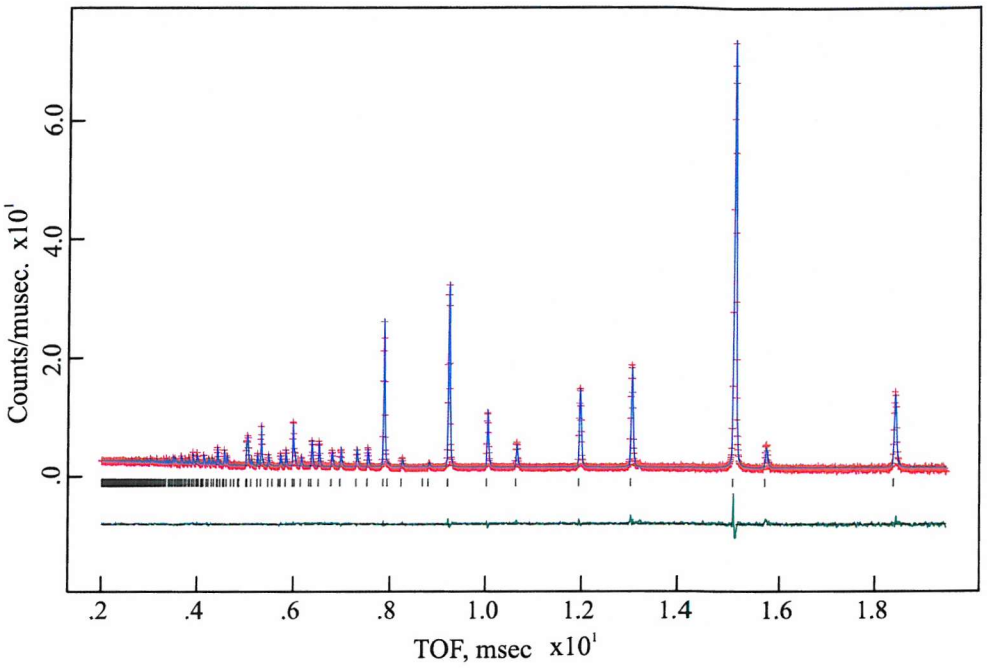

Figure 5-3: Observed (+++), Calculated (—), and difference (shown underneath) PND profiles for $CoZnTiO_4$. Tick marks indicate reflection positions.

Table 5-9: Refined crystallographic data (PND) for $CoMgTiO_4$ (e. s. d. s are shown in parentheses).

Space group: *F*d-3m

Lattice parameters a = 8.44650 (5) Å

Atom	*x*	*y*	*z*	*Frac.*	U_{iso} /Å^{2}x100
Co(1)	0.5	0.5	0.5	0.215(7)	0.7(3)
Mg(1)	0.5	0.5	0.5	0.285(7)	0.7(3)
Ti(1)	0.5	0.5	0.5	0.500	0.7(3)
Co(2)	-0.125	-0.125	-0.125	0.57(2)	0.74(4)
Mg(2)	-0.125	-0.125	-0.125	0.43(2)	0.74(4)
O	0.26074(3)	0.26074(3)	0.26074(3)	1	0.91(2)

Final fit parameters: $\chi^2 = 3.874$, $R_{wp} = 4.24$ %, $R_p = 7.01$ %

Table 5-10: Refined crystallographic data (PND) for $CoMg_{0.8}Zn_{0.2}TiO_4$ (e. s. d. s are shown in parentheses).

Space group: *F*d-3m

Lattice parameters a = 8.44696 (5) Å

Atom	*x*	*y*	*z*	*Frac.**	U_{iso} /Å^{2}x100
Co(1)	0.5	0.5	0.5	0.25	0.9(2)
Mg(1)	0.5	0.5	0.5	0.20	0.9(2)
Zn(1)	0.5	0.5	0.5	0.05	0.9(2)
Ti(1)	0.5	0.5	0.5	0.500	0.9(2)
Co(2)	-0.125	-0.125	-0.125	0.50	0.72(3)
Mg(2)	-0.125	-0.125	-0.125	0.40	0.72(3)
Zn(2)	-0.125	-0.125	-0.125	0.10	0.72(3)
O	0.26079(3)	0.26079(3)	0.26079(3)	1	0.90(1)

Final fit parameters:$\chi^2 = 2.582$, $R_{wp} = 3.77$ %, $R_p = 6.37$ %

Table 5-11: Refined crystallographic data (PND) for $CoMg_{0.6}Zn_{0.4}TiO_4$ (e. s. d. s are shown in parentheses).

Space group: *F*d-3m

Lattice parameters a = 8.44706(4) Å

Atom	*x*	*y*	*z*	*Frac.**	U_{iso} /Å^{2}x100
Co(1)	0.5	0.5	0.5	0.25	0.8(2)
Mg(1)	0.5	0.5	0.5	0.20	0.8(2)
Zn(1)	0.5	0.5	0.5	0.05	0.8(2)
Ti(1)	0.5	0.5	0.5	0.50	0.8(2)
Co(2)	-0.125	-0.125	-0.125	0.50	0.58(2)
Mg(2)	-0.125	-0.125	-0.125	0.20	0.58(2)
Zn(2)	-0.125	-0.125	-0.125	0.30	0.58(2)
O	0.26083(3)	0.26083(3)	0.26083(3)	1	0.95(2)

Final fit parameters:$\chi^2 = 2.735$, $R_{wp} = 3.30$ %, $R_p = 5.65$ %

Table 5-12: Refined crystallographic data (PND) for $CoMg_{0.4}Zn_{0.6}TiO_4$ (e. s. d. s are shown in parentheses).

Space group: *F*d-3m

Lattice parameters a = 8.44573(4) Å

Atom	*x*	*y*	*z*	*Frac.**	U_{iso} /Å^{2}x100
Co(1)	0.5	0.5	0.5	0.30	1.1(3)
Mg(1)	0.5	0.5	0.5	0.15	1.1(3)
Zn(1)	0.5	0.5	0.5	0.050	1.1(3)
Ti(1)	0.5	0.5	0.5	0.500	1.1(3)
Co(2)	-0.125	-0.125	-0.125	0.40	0.58(2)
Mg(2)	-0.125	-0.125	-0.125	0.10	0.58(2)
Zn(2)	-0.125	-0.125	-0.125	0.50	0.58(2)
O	0.26077(3)	0.26077(3)	0.26077(3)	1	0.968(9)

Final fit parameters:$\chi^2 = 2.808$, $R_{wp} = 3.48$ %, $R_p = 5.68$ %

Table 5-13: Refined crystallographic data (PND) for $CoMg_{0.2}Zn_{0.8}TiO_4$ (e. s. d. s are shown in parentheses).

Space group: *F*d-3m

Lattice parameters a = 8.44565(4) Å

Atom	*x*	*y*	*z*	*Frac.**	U_{iso} /Å^{2}x100
Co(1)	0.5	0.5	0.5	0.375	0.2(3)
Mg(1)	0.5	0.5	0.5	0.075	0.2(3)
Zn(1)	0.5	0.5	0.5	0.050	0.2(3)
Ti(1)	0.5	0.5	0.5	0.500	0.2(3)
Co(2)	-0.125	-0.125	-0.125	0.250	0.67(2)
Mg(2)	-0.125	-0.125	-0.125	0.050	0.67(2)
Zn(2)	-0.125	-0.125	-0.125	0.700	0.67(2)
O	0.26067(3)	0.26067 (3)	0.26067(3)	1	1.061(9)

Final fit parameters:$\chi^2 = 2.940$, $R_{wp} = 3.39$ %, $R_p = 5.51$ %

Table 5-14: Refined crystallographic data (PND) for $CoZnTiO_4$ (e. s. d. s are shown in parentheses).

Space group: *F*d-3m

Lattice parameters a = 8.45116(4) Å

Atom	*x*	*y*	*z*	*Frac.*	U_{iso} /Å^{2}x*100*
Co(1)	0.5	0.5	0.5	0.477(5)	1.0(2)
Zn(1)	0.5	0.5	0.5	0.023(5)	1.0(2)
Ti(1)	0.5	0.5	0.5	0.500	1.0(2)
Co(2)	-0.125	-0.125	-0.125	0.046(9)	0.79(2)
Zn(2)	-0.125	-0.125	-0.125	0.954(9)	0.79(2)
O	0.26056(3)	0.26056(3)	0.26056(3)	1	1.015(9)

Final fit parameters:$\chi^2 = 2.523$, $R_{wp} = 3.23$ %, R_p 5.21 %

5.1.5 Fractional Occupancies

Due to the complexity of these systems it was only possible to refine the fractional site occupancies for the end member compounds of each group – x = 0 and x = 1.0.

5.1.5.1 $(Co_{1-x}(MgZn)_x)_2TiO_4$ – Co_2TiO_4 and $MgZnTiO_4$

The PND refinement data obtained for Co_2TiO_4 suggests an ideal inverse-spinel arrangement of cations. The cobalt 2+ ions occupy the tetrahedral site and half of the available octahedral sites, whilst Ti^{4+} occupies the remaining octahedral sites. No site mixing is observed, therefore for the remaining members of each series the octahedral fractional site occupancy was fixed at 50 % titanium for all samples. This allows the fractional site occupancies for the remaining ternary compounds to be refined.

Refined fractional site occupancies for $MgZnTiO_4$ indicate that zinc shows strong preference for a tetrahedral coordination and the magnesium appears to prefer octahedral sites. Indeed the tetrahedral site is occupied almost exclusively by zinc 2+ ions - $[Zn_{0.98}Mg_{0.02}]^{tet}[Zn_{0.02}Mg_{0.98}]^{oct}TiO_4$. It has been reported that this preference is due to the covalent properties exhibited by Zn^{2+} ions in a tetrahedral oxygen environment [16].

5.1.5.2 $Co(Mg_{1-x}Zn_x)TiO_4$ – $CoMgTiO_4$ and $CoZnTiO_4$

Given that magnesium was seen to occupy the octahedral site in preference to the tetrahedral site in $MgZnTiO_4$, a similar distribution was expected for $CoMgTiO_4$. However this was not observed. In fact both the cobalt and magnesium ions are distributed almost equally between

the two sites - $[Co_{0.57}Mg_{0.43}]^{tet}[Co_{0.43}Mg_{0.57}]^{oct}TiO_4$. This result highlights the fact that neither cobalt nor magnesium shows a particularly strong preference for either site, although a slightly larger fraction of cobalt tends to occupy the tetrahedral site.

In a similar fashion to that observed for $MgZnTiO_4$, zinc shows strong preference for the tetrahedral site in $CoZnTiO_4$ causing the cobalt to be displaced onto the octahedral site - $[Co_{0.046}Zn_{0.954}]^{tet}[Co_{0.954}Zn_{0.046}]^{oct}TiO_4$.

It can be seen from these results that the addition of zinc to each of these materials has the effect of displacing those cations currently occupying the tetrahedral site such that Zn^{2+} can occupy the site. This will greatly affect the colour of the pigment produced in each case. The magnesium ions seem to show a slight preference for the octahedral site and, for $CoMgTiO_4$, they seem to simply 'dilute' the cobalt presence on each site. Again this has important implications as far as the colour properties of the pigment are concerned, although the main effect may be a dilution/lightening of the colour rather than any actual colour change.

5.1.6 Interatomic Distances and Angles

The metal-oxygen distances and bond angles, derived from the Rietveld refinements, are shown in Table 5-15 and Table 5-16. The distances shown for the shared octahedral (M(1)) and tetrahedral (M(2)) sites are averages of the metal-oxygen bond lengths within the structure as the sites contain up to three different metal ions. It is expected that the derived values will lie somewhere between the values for the singly occupied sites of the end member compounds.

Table 5-15: Derived bond distances (Å) and angles (°), as a function of x, for the $(Co_{1-x}(MgZn)_x)_2TiO_4$ series. (e. s. d. s are shown in parentheses).

Distance / Angle	*0*	*0.2*	*0.4*	*0.6*	*0.8*	*1.0*
M(1)_O (x 6)	2.0266(2)	2.0252(2)	2.0252(2)	2.0238(3)	2.0211(2)	2.0193(2)
M(2)_O (x 4)	1.9841(4)	1.9851(4)	1.9862(4)	1.9871(4)	1.9867(4)	1.9888(4)
O_M(1)_O (x 6)	84.83(2)	84.78(2)	84.75(2)	84.70(3)	84.65(2)	84.55(2)
O_M(1)_O (x 3)	180	180	180	180	180	180
O_M(1)_O (x 6)	95.17(2)	95.22(2)	95.25(2)	95.30(2)	95.35(2)	95.45(2)
O_M(2)_O (x 6)	109.471	109.471	109.471	109.471	109.471	109.471

Table 5-16: Derived bond distances (Å) and angles (°), as a function of x, for the $Co(Mg_{1-x}Zn_x)TiO_4$ series. (e. s. d. s are shown in parentheses).

Distance / Angle	*0*	*0.2*	*0.4*	*0.6*	*0.8*	*1.0*
M(1)_O (x 6)	2.0249(3)	2.0247(2)	2.0244(2)	2.0245(2)	2.0253(2)	2.0275(2)
M(2)_O (x 4)	1.9859(5)	1.9867(4)	1.9873(4)	1.9861(4)	1.9846(4)	1.9843(4)
O_M(1)_O (x 6)	84.75(2)	84.73(2)	84.71(2)	84.74(3)	84.79(2)	84.85(2)
O_M(1)_O (x 3)	180	180	180	180	180	180
O_M(1)_O (x 6)	95.25(2)	95.27(2)	95.29(2)	95.26(2)	95.21(2)	95.15(2)
O_M(2)_O (x 6)	109.471	109.471	109.471	109.471	109.471	109.471

5.1.6.1 $(Co_{1-x}(MgZn)_x)_2TiO_4$ series

It can be seen from the derived interatomic distances and angles that there is a consistent variation of both the tetrahedral and octahedral coordination environments as the value of x is varied (Figure 5-4). The octahedral bond length (M(1)_O) displays an overall decrease in size as the cobalt content is decreased. Conversely the tetrahedral bond distance increases. The octahedral environment tends towards a more distorted situation when considering the O_M(1)_O bond angle; the difference between this angle and 90° increases as x increases. These observations can be explained in terms of the site occupancies and the effective ionic radii of the cations involved (Table 5-17).

Table 5-17:Effective ionic radii values [17] for the $(Co_{1-x}(MgZn)_x)_2TiO_4$ system. Values are quoted in Angstroms.

Metal Cation	*Coordination Number*	
	4	*6*
Co^{2+}	0.58	0.745
Mg^{2+}	0.57	0.72
Ti^{4+}	0.42	0.605
Zn^{2+}	0.60	0.74

The refined fractional site occupancies for the end member compounds of this series (Co_2TiO_4 and $MgZnTiO_4$) reveal that, in the absence of any zinc or magnesium, cobalt is distributed equally between the tetrahedral and octahedral sites. Also, for x = 1.0 the Zn^{2+} ions show preference for the tetrahedral site whilst the majority of the Mg^{2+} ions tend to occupy the octahedral site. Therefore, as the magnesium ions are smaller than the Co^{2+} ions that they replace on the octahedral site, it follows that the average metal-oxygen distances for that site will be shorter. Similarly, the tetrahedral metal-oxygen distances increase because the Co^{2+} ions are replaced by Zn^{2+} ions, which are slightly larger.

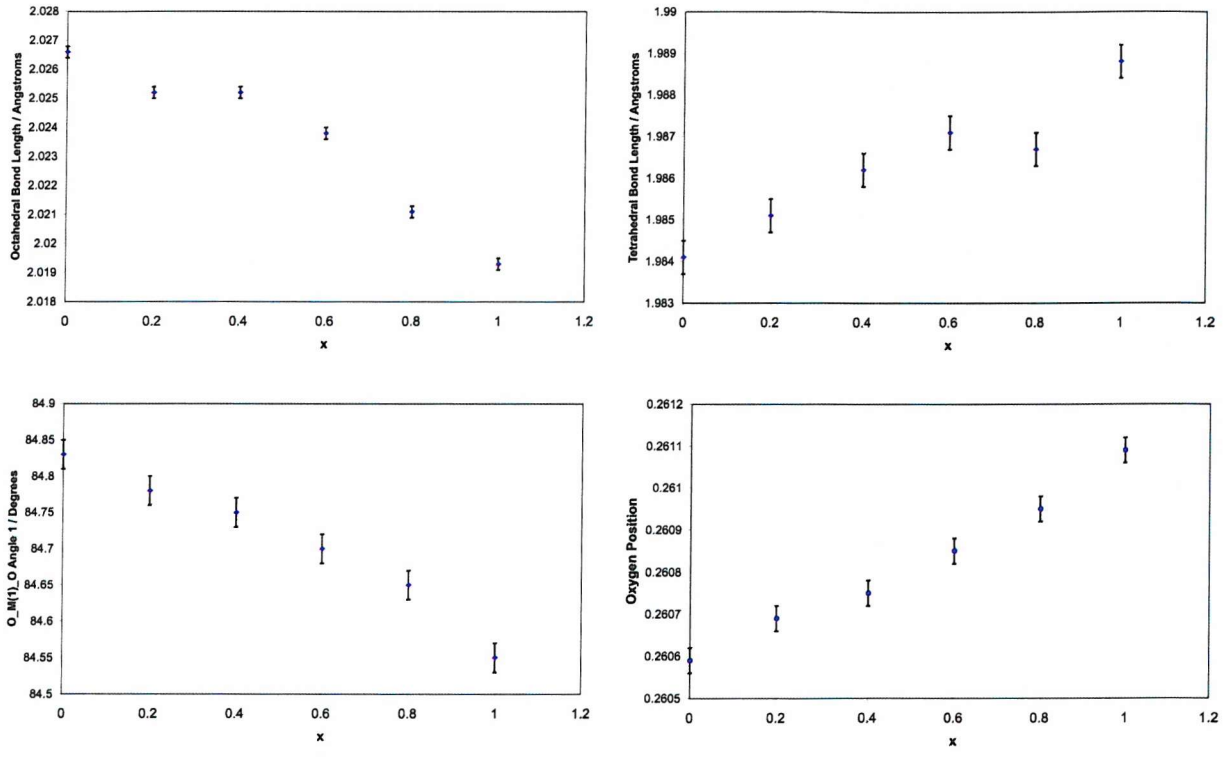

Figure 5-4: Variation of the M(1)-O distance (top left), the M(2)-O distance (top right), the O_M(1)_O bond angle (bottom left) and the oxygen position as a function of x for the $(Co_{1-x}(MgZn)_x)_2TiO_4$ system. M = Co, Zn, Mg, Ti.

5.1.6.2 $Co(Mg_{1-x}Zn_x)TiO_4$ series

For the $Co(Mg_{1-x}Zn_x)TiO_4$ series the variation in octahedral and tetrahedral bond length, octahedral bond angle and oxygen position appears to be more complicated than for the $(Co_{1-x}(MgZn)_x)_2TiO_4$ series (Figure 5-5). The increase in the size of the octahedral metal-oxygen distance (M(1)-O) is expected; as the zinc concentration increases the Mg^{2+} and Co^{2+} ions that occupy the tetrahedral site are displaced onto the octahedral site. Therefore the greater

ionic radii of Co^{2+}, when compared to Mg^{2+}, causes an overall increase in the average M(1)-O distance as the magnesium concentration decreases.

On closer inspection it can be seen that the average M(1)-O distance decreases on moving from x = 0 to x = 0.4; at x = 0.6 it begins to increase. It is thought that this occurs due to the strong tetrahedral site preference observed for zinc. As the zinc concentration increases, it is likely that the smaller magnesium ions will be effectively displaced onto the octahedral site before the cobalt ions. Thus causing the M(1)-O distance to decrease. When the zinc concentration exceeds x = 0.5, cobalt ions will begin to be displaced from the tetrahedral site onto the octahedral site (for x = 0 the site occupancy for the tetrahedral site was ≈ 50 % Co and ≈ 50 % Mg), thus causing the average M(1)-O distance to increase.

The metal-oxygen distance for the tetrahedral site (M(2)-O) does not behave as expected. The fractional site occupancies for the tetrahedral site in $CoZnTiO_4$ (x = 1.0) indicate that the site is occupied almost exclusively by zinc rather than ≈ 50 % Co and ≈ 50 % Mg as in $CoMgTiO_4$ (x = 0). Therefore, one would expect the average M(2)-O distance to increase as the overall zinc content is increased. However, this is not the case here. For the samples where x = 0, 0.2 and 0.4 the higher zinc content of the site causes an increase in the average M(2)-O distance, as expected. Beyond this, however, a decrease in size is observed, which may be due to the increasing size of the octahedral site or possibly some degree of local distortion caused by the Ti^{4+} ions on the octahedral site.

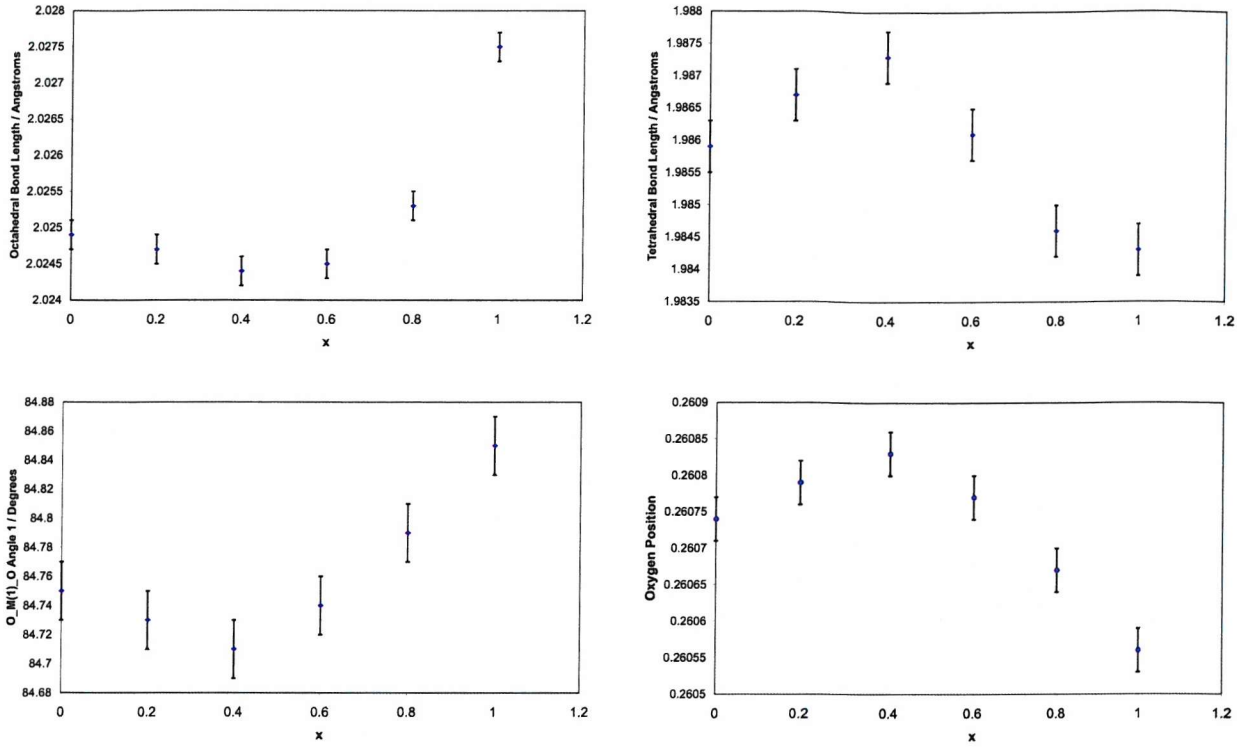

Figure 5-5: Variation of the M(1)-O distance (top left), the M(2)-O distance (top right), the O_M(1)_O bond angle (bottom left) and the oxygen position as a function of x for the $Co(Mg_{1-x}Zn_x)TiO_4$ system. M = Co, Zn, Mg, Ti.

5.1.7 Discussion

The refined (PXD and PND) temperature factor for the octahedral site is relatively large and indicates some degree of uncertainty regarding the positional coordinates. A possible explanation for this is that the octahedral environment observed using either PXD or PND is an average one; each of the metal cations present on an octahedral site will impart some influence upon its own coordination environment, therefore in some cases there will be up to three different coordination environments averaged to provide the data presented in the tables above. Indeed, titanium is often seen to occupy a distorted octahedral environment, rather than the regular octahedron suggested by this model. Combined EXAFS/PND refinements were performed to help model these possible distortions.

5.1.8 Combined EXAFS/PND Refinements

Due to the complexity of these systems in terms of the distribution of cations across the tetrahedral and octahedral sites, it was not possible to obtain refined fractional site occupancies for the quaternary systems using PXD or PND alone. To enable a better understanding of the cation distribution throughout each series combined EXAFS/PND

refinements were performed for a number of materials using 'P' the combined refinement program (see Chapter 2).

A further reason for using the combined refinement is that it can give specific data regarding a particular element in a given site. PND or PXD alone, provide bond lengths and angles that are averaged for a mixed site across the structure as a whole, which leads to the suggestion, for instance, that the Co-O (Td) bonds may become longer as x increases across the $(Co_{1-x}(MgZn)_x)2TiO_4$ series and as more zinc occupies the tetrahedral site. However, what in fact may be happening is that the Co-O bond lengths remain exactly the same and tetrahedral sites containing Zn^{2+} have a longer cation-oxygen bond length, which would in turn cause the average metal-oxygen bond length to increase.

In each case N. Binsted performed the combined refinement in association with the author.

5.1.8.1 Data Collection

Room temperature cobalt K-edge, zinc K-edge and titanium K-edge EXAFS were collected on stations 7.1, 8.1, 9.2 and 9.3 at the SRS Daresbury Laboratory in transmission mode as described in Chapter 2. Up to six scans were collected in each case and the data averaged to improve the signal to noise ratio. Background subtraction of the EXAFS data was performed using PAXAS [18]. PND data were collected on POLARIS at the ISIS facility, Rutherford Appleton Laboratory (RAL) as described in Chapter 2. Results are presented for a binary (Co_2TiO_4), a ternary ($CoZnTiO_4$) and a quaternary ($Co_{0.8}Mg_{0.6}Zn_{0.6}TiO_4$) system.

5.1.8.2 Co_2TiO_4

An initial model was taken from the PND refinement performed earlier in this Chapter. Both the background-subtracted EXAFS and the PND data were entered into the program and the scattering phase shifts calculated using a common value of the interstitial potential for all atoms. Both combined (EXAFS + PND) and PND-only refinements were performed; the combined refinement used equal weightings for the spectra with $W_{EXAFS} = W_{PND} = 0.5$, while PND-only refinements used $W_{EXAFS} = 0$ and $W_{PND} = 1.0$. A cluster radius of either 5 or 6 angstroms was used to calculate the EXAFS spectra. Contributions were identified to at least 10 Å, but regular use of such large clusters is prohibitive in terms of CPU time. As with all regular solids, multiple scattering effects are important beyond the first shell of atoms, and paths involving up to 3 different scattering atoms were always included.

5.1.8.2.1 Results and Discussion

The fits to the EXAFS data for both the Co-K and the Ti-K edges are shown in Figure 5-6. The fit to the cobalt-edge data is reasonably good and indicates that the standard spinel model is more or less sufficient to describe the Co^{2+} environments present. There are anomalies however, especially in paths that contribute to the *ca.* 5.5 Å peak in the Fourier transform. However, this model fails to describe the Ti^{4+} environment adequately. This can be seen in Figure 5-6 where the oscillations shown for the fit to EXAFS data (Ti-K) appear to be out of phase, especially between ≈ 4-6 $Å^{-1}$.

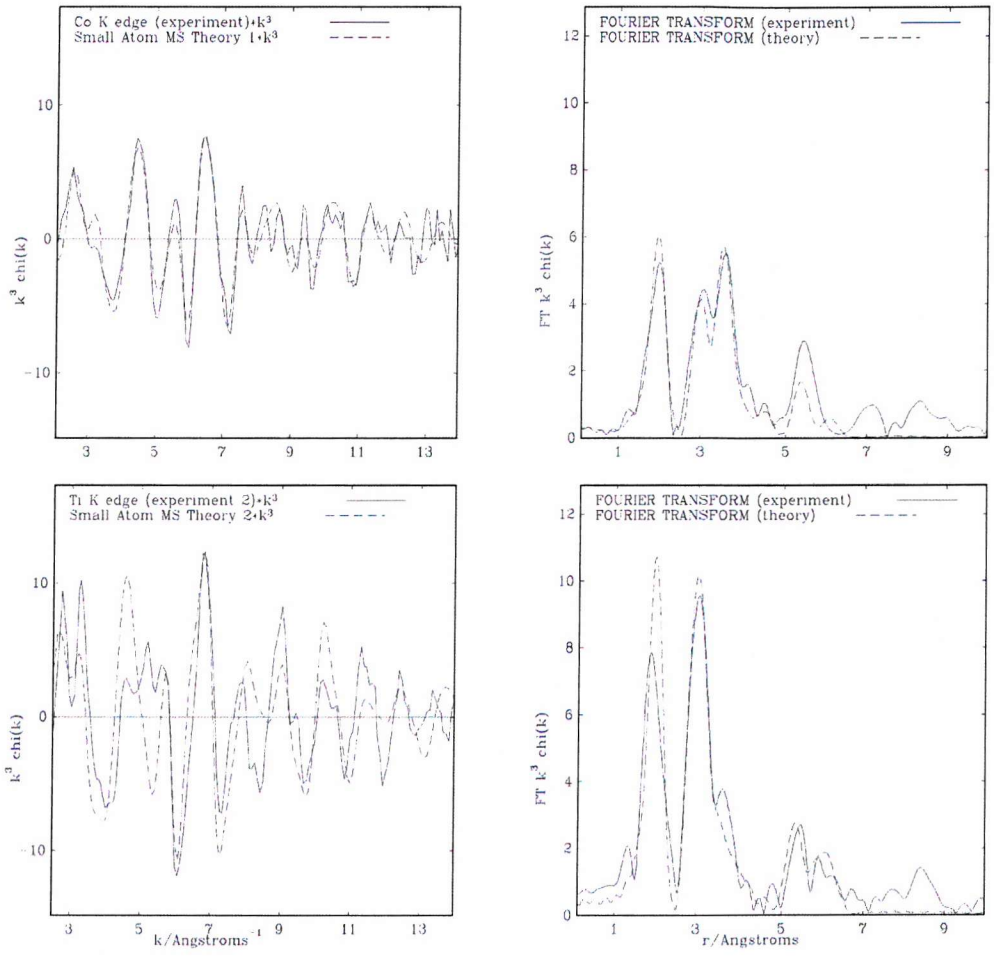

Figure 5-6: EXAFS plots (left) and Fourier transformed EXAFS plots (right) for Co_2TiO_4. Co K-edge (top) and Ti K-edge (bottom). The solid and dotted lines represent the observed data and calculated fit respectively.

The Fourier transform shows that the first shell has been modelled incorrectly; the peak shape and size calculated for the first shell are incorrect and the experimental data seem to suggest a shorter average Ti – O distance than is being calculated. For these refinements the physical requirement that Co*-Ti and Ti*-Co Debye-Waller (DW) factors are identical was assumed.

It was also assumed that Co-O and Ti-O DW factors for the same distance (i.e. same site to same oxygen for mixed sites) were the same, which should be approximately true. An improvement could be obtained with physically unreasonable DW factors.

Both EXAFS and PND data agree that Ti^{4+} prefers to occupy the octahedral environment almost exclusively. However, Co^{2+} cations also occupy the octahedral site in Co_2TiO_4, therefore the environment observed by refining PND data is an average one despite the fact that one would expect the Ti-O distance to be shorter than the Co-O distance; Ti^{4+} is a smaller ion with a greater nuclear charge. EXAFS should allow the two environments to be determined independently, however in this case the model is producing an average Ti-O distance that is similar to the Co-O distance and slightly longer than that indicated by the experimental data.

In a number of pseudobrookite-type oxide materials ($A^{2+}Ti^{4+}{}_2O_5$, where A = Co, Mg, Fe or $A^{3+}Ti^{4+}O_4$, where A = Ga or Al) [19, 20, 21] the Ti^{4+} ion adopts a distorted octahedron of oxygen ligands, where by one of the Ti-O distances is noticeably longer than the remaining five distances. Kunz *et al.* [22] also note that sites containing Ti typically have high bond-length distortion (BLD) [23] values. The symmetry constrictions and cubic nature of the standard inverse spinel model used do not allow for the sort of local lattice distortions described, therefore a second model was developed to allow the O atom to move along the (111) axis by an amount dependent upon the neighbouring atom. Thus, the calculated model would be a statistical mixture of Co-O-Co, Co-O-Ti, Ti-O-Co and Ti-O-Ti entities. This is an approximate model for both the local and long-range structure. The undistorted value was used for the PND refinement. EXAFS fits to the data for the second model are shown in Figure 5-7:.

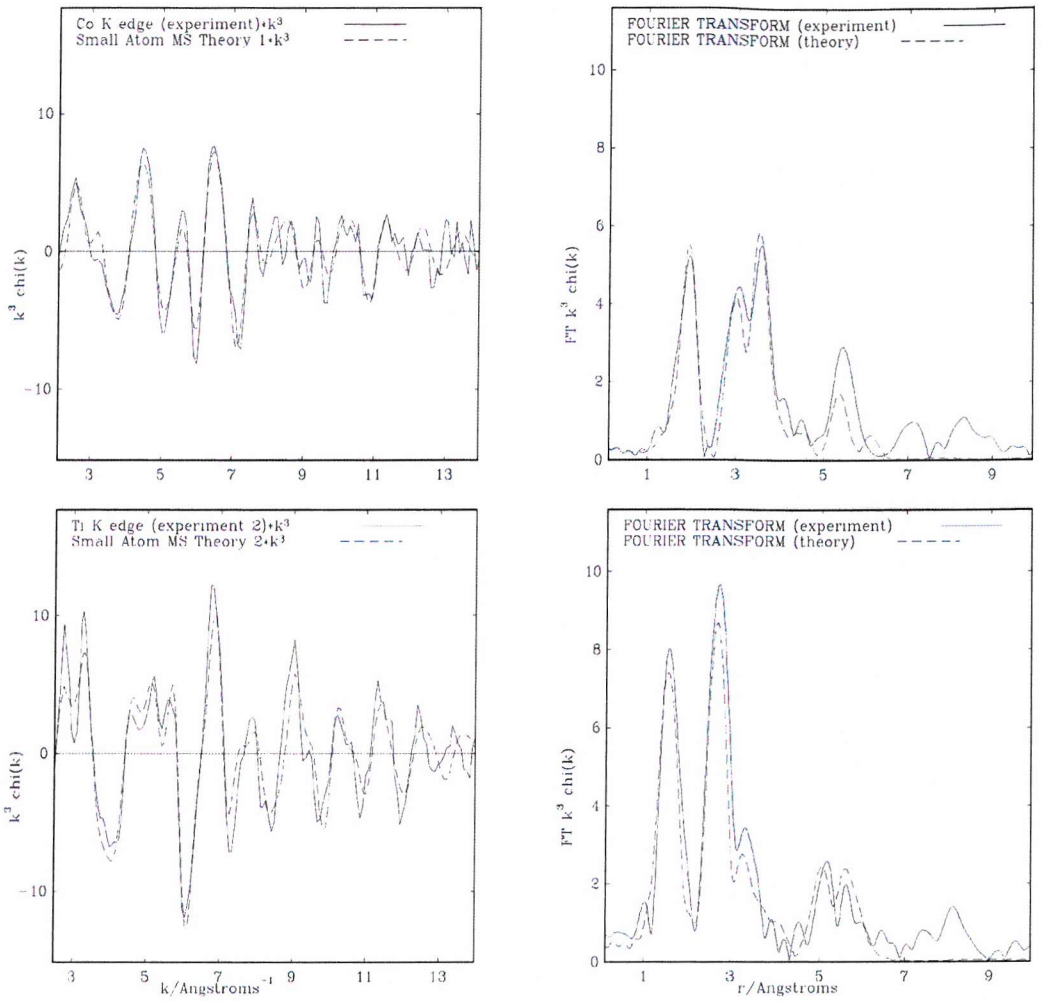

Figure 5-7: (Model 2) EXAFS plots (left) and Fourier transformed EXAFS plots (right) for Co_2TiO_4. Co K-edge (top) and Ti K-edge (bottom). The solid and dotted lines represent the observed data and calculated fit respectively.

The second model produces a much better fit to the observed EXAFS data (R_{EXAFS} (1st model) = 71.3, R_{EXAFS} (2nd model) = 40.7) and appears to model both of the cations reasonably well. Selected data for each of the combined refinements are shown in Table 5-18.

Table 5-18: Refined data derived from combined EXAFS/PND refinements for Co_2TiO_4.

Parameter	*Standard Model*	*Local Lattice Distortion Model*
Cell	8.448(3) Å	8.448(3) Å
O, *x*	0.261(1)	0.261(1)
Dp (Ti-O-Ti)	0	0.024(1) Å
Dp (Ti-O-Co)	0	0.005(1) Å
Dp (Co-O-Co)	0	-0.002(2) Å
BL(Oh) (**Co-O**-Co)	2.025 Å	2.04 Å
BL(Oh) (**Co-O**-Ti)	2.025 Å	2.063 Å
BL(Oh) (**Ti-O**-Co)	2.025 Å	1.989 Å
BL(Oh) (**Ti-O**-Ti)	2.025 Å	1.867 Å
BL(Td) (**Co-O**)	1.983	1.983
BVS (Co(Oh))	2.44	2.27
BVS (Co(Td))	1.80	1.80
BVS (Ti(Oh))	3.40	4.48
R_{EXAFS}	71.3	40.7
R_{PND}	5.9	5.9

NB. Dp = displacement of the O atom away from the first cation in the 111 direction, relative to the oxygen position. BL = first-cation oxygen distance when attached to a specific second cation in a neighbouring octahedron. BVS = bond valence sum.

Despite a well-modelled first shell and an improved fit to the observed data when using the second model, the model itself has a number of limitations. The movement of the O atom is limited to being along the 111 axis due to symmetry constraints and the subsequent complexity of the model if it were otherwise. This gives rise to anomalous results where **Ti-O**--Ti distances differ from Ti--**O-Ti** distances, thus creating an unsymmetrical Ti-O-Ti situation rather than a perfectly symmetrical one, as should be the case. There are also clear anomalies in the first and second shell distances for Ti.

A similar situation was observed for the remaining compounds being considered.

5.1.9 Reverse Monte-Carlo Simulation

In an effort to better model the local lattice distortions for each material a Reverse Monte-Carlo (RMC) approach [24, 25, 26, 27, 28, 29, 30, 31] was adopted. With this method the starting model for crystalline materials is a supercell of the crystal lattice, presumed to have periodic boundary conditions. A fitting function χ^2 is calculated, utilising the sum of squares of residuals from the fits to experimental data, together with those for any restraints that are to be applied to the solution. Random changes are made to the coordinates of the model, which are accepted with probability $P(\Delta\chi^2) \geq 0$ if $\Delta\chi^2$ is positive or 1 if $\Delta\chi^2$ is negative. The procedure is then repeated until convergence to a minimum is achieved.

5.1.9.1 Results

RMC EXAFS plots and Fourier transformed EXAFS plots for $Co_{0.8}Mg_{0.6}Zn_{0.6}TiO_4$ are shown in Figure 5-8 and Figure 5-9 respectively. Tables of cyrstallographic data and refinement statistics for Co_2TiO_4, $CoZnTiO_4$ and $Co_{0.8}Mg_{0.6}Zn_{0.6}TiO_4$ are presented in Table 5-19 to Table 5-21

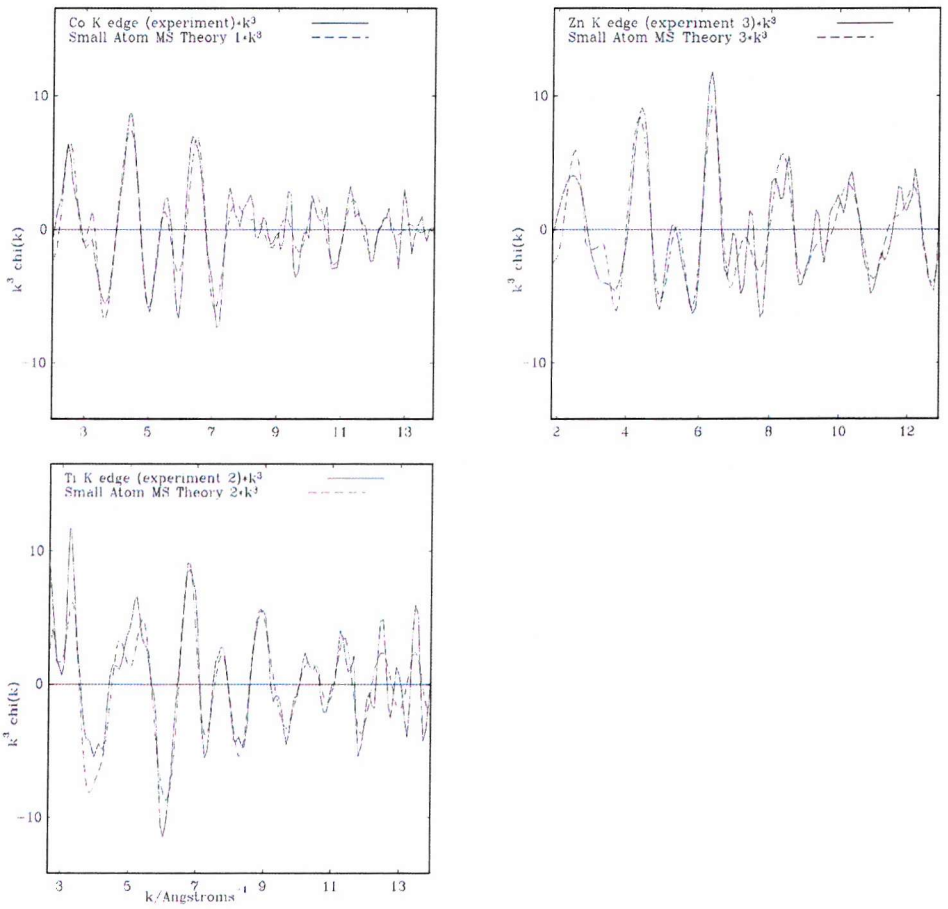

Figure 5-8: (RMC) EXAFS plots for $Co_{0.8}Mg_{0.6}Zn_{0.6}TiO_4$. Co K-edge (top left), Zn K-edge (top right) and Ti K-edge (bottom). The solid and dotted lines represent the observed data and calculated fit respectively.

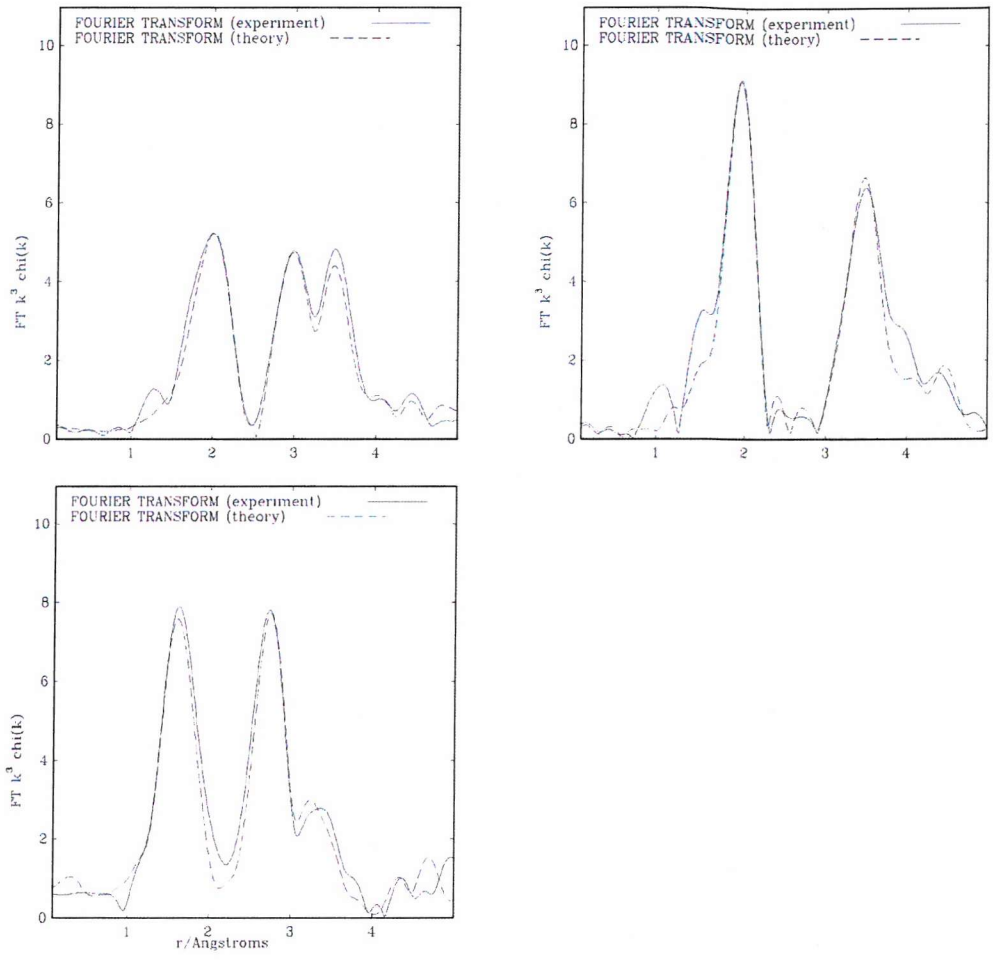

Figure 5-9: Fourier Transformed (RMC) EXAFS plots for $Co_{0.8}Mg_{0.6}Zn_{0.6}TiO_4$. Co K-edge (top left), Zn K-edge (top right) and Ti K-edge (bottom). The solid and dotted lines represent the observed data and calculated fit respectively.

Table 5-19: Determined (RMC) site positions (x, y, z) for Co_2TiO_4 – M(1) = Octahedral, M(2) Tetrahedral

Lattice parameter a = 8.4479 Å

Atom	*x*	*y*	*z*	*Multiplicity*
Co(1)	0.5011	0.4999	0.4992	8
Ti(1)	0.5009	0.5013	0.5007	8
Co(2)	-0.1246	-0.1250	-0.1247	8
O	0.2598	0.2595	0.2608	32

Final fit parameters:χ^2 = 0.381 x 10^{-8}, R_{EXAFS} = 37.138, Partial R_{EXAFS} = 42.656 (Co) and 33.420 (Ti), R_{PND} = 5.929

Table 5-20: Determined (RMC) site positions (x, y, z) for $CoZnTiO_4$ – M(1) = Octahedral, M(2) Tetrahedral

Lattice parameter a = 8.4508 Å

Atom	*x*	*y*	*z*	*Multiplicity*
Co(1)	0.5009	0.5001	0.4998	8
Ti(1)	0.5004	0.5004	0.4998	8
Zn(2)*	0.1240	0.1258	0.1247	8
O	0.2578	0.2592	0.2604	32

Final fit parameters:χ^2 = 0.2189 x 10^{-7}, R_{EXAFS} = 40.155, Partial R_{EXAFS} = 41.698 (Co), 38.878 (Ti) and 39.367 (Zn), R_{PND} = 5.235.

* It is assumed that zinc is 100 % tetrahedral and that Co is 100 % octahedral.

Table 5-21: Determined (RMC) site positions (x, y, z) for $Co_{0.8}Mg_{0.6}Zn_{0.6}TiO_4$ – M(1) = Octahedral, M(2) Tetrahedral

Lattice parameter a = 8.4508 Å

Atom	*x*	*y*	*z*	*Multiplicity*
Co(1)	0.4989	0.4987	0.4985	4.70
Mg(1)	0.5019	0.5010	0.5004	3.11
Zn(1)	0.5021	0.4984	0.4928	0.19
Ti(1)	0.5006	0.5011	0.5008	8
Co(2)	0.1249	0.1263	0.1251	1.70
Zn(2)	0.1241	0.1242	0.1254	4.63
Mg(2)	0.1225	0.1228	0.1246	1.67
O	0.2609	0.2600	0.2608	32

Final fit parameters:χ^2 = 0.2782 x 10^{-7}, R_{EXAFS} = 40.963, Partial R_{EXAFS} = 39.818 (Co), 42.231 (Ti) and 40.463 (Zn), R_{PND} = 4.5188

For the material $CoZnTiO_4$, Zn was assumed to occupy only the tetrahedral site. However, slight discrepancies in the Fourier transform at *ca.* suggest the possible presence of a small amount (< 10 %) of octahedral zinc. This is in agreement with the refined fractional occupancies obtained from the powder neutron diffraction data refinement (section 5.1.4) - $[Co_{0.046}Zn_{0.954}]^{tet}[Co_{0.954}Zn_{0.046}]^{oct}TiO_4$ – which indicate that approximately 5 % of the zinc atoms lie on the octahedral site.

5.1.9.2 Multiplicity Values

The multiplicity values quoted in the tables above are equivalent to the fractional occupancy values quoted for the PND refinements (section 5.1.5). However they refer to a fraction of the total site multiplicity rather than being a fraction of 1.0. In each case the multiplicity can be converted into an equivalent fractional occupancy by dividing the value by eight (for the tetrahedral site) or by sixteen (for the octahedral site). Calculated fractional occupancy values derived from the RMC calculations are presented below and are compared with the predicted values used for the refinement of PND data in section 5.1.4.

Figure 5-10: Calculated fractional occupancy values for $Co_{0.8}Mg_{0.6}Zn_{0.6}TiO_4$ derived from RMC calculations. PND values were predicted. M(1)-Octahedral, M(2)-Tetrahedral.

Element (site)	Co(1)	Mg(1)	Zn(1)	Ti(1)	Co(2)	Mg(2)	Zn(2)
(RMC) EXAFS/PND	0.2937	0.1944	0.0119	0.5	0.2125	0.2088	0.5787
PND	0.200	0.25	0.050	0.5	0.400	0.100	0.500

The RMC-derived values imply a greater concentration of cobalt on the octahedral site than was previously predicted for this material and serves to highlight the preference shown by zinc for the tetrahedral site.

5.1.9.3 Interatomic Distances

The metal-oxygen distances and bond angles, derived from the RMC simulations, are shown in Table 5-22 to Table 5-24. The distances shown for the shared octahedral (M(1)) and tetrahedral (M(2)) sites, unlike those derived from PND refinements (section 5.1.6), are element specific rather than averages of the metal-oxygen bond lengths within the structure. However, in each case the presented value *is* an average of the metal-oxygen distances for that particular element on a particular site. The skewness value quoted for each element gives a measure of deviation from a perfectly symmetrical coordination environment – deviation from zero indicates a degree of distortion.

Table 5-22: Refined distances obtained from the RMC simulation for Co_2TiO_4 (DW = EXAFS Debye-Waller factor). M(1) = Octahedral, M(2) Tetrahedral

Vector	*Distance / Å*	*DW*	*Skewness*
Co(1) – O	2.0619	0.0150	0.0005
Ti(1) – O	2.0155	0.0249	0.0039
Co(2) – O	1.9832	0.0080	0.0000

Table 5-23: Refined distances obtained from the RMC simulation for $CoZnTiO_4$ (DW = EXAFS Debye-Waller factor). M(1) = Octahedral, M(2) Tetrahedral

Vector	*Distance / Å*	*DW*	*Skewness*
Co(1) – O	2.0662	0.0185	0.0000
Ti(1) – O	2.0266	0.0314	0.0057
Zn(2) – O	1.9806	0.0136	0.0006

Table 5-24: Refined distances obtained from the RMC simulation for $Co_{0.8}Mg_{0.6}Zn_{0.6}TiO_4$ (DW = EXAFS Debye-Waller factor). M(1) = Octahedral, M(2) Tetrahedral.

Vector	*Distance / Å*	*DW*	*Skewness*
Co(1) – O	2.0752	0.0105	0.0002
*Mg(1) – O	-	-	-
Zn(1) – O	2.0713	0.0204	0.0018
Ti(1) – O	2.0018	0.0301	0.0043
Co(2) – O	1.9916	0.0060	0.0000
*Mg(2) – O	-	-	-
Zn(2) – O	1.9960	0.0091	0.0007

* Data not available; Mg EXAFS data not collected.

For each of the materials under consideration the DW factor for titanium on the octahedral site is relatively large, which suggests some uncertainty about its position. This is probably due to static disorder caused by local lattice distortions. In addition to this, the skewness values for the titanium site indicate deviation from perfectly octahedral symmetry.

The high DW value for octahedrally coordinated zinc in $Co_{0.8}Mg_{0.6}Zn_{0.6}TiO_4$ is probably due to the small fraction of zinc associated with the octahedral site – fractional sites occupancy = 0.0119.

5.1.9.4 Radial Distribution Function

Radial distribution functions (RDF) were generated from the RMC simulations for each phase. RDF diagrams for Co_2TiO_4 and $Co_{0.8}Mg_{0.6}Zn_{0.6}TiO_4$ are presented in Figure 5-11 and Figure 5-12 respectively.

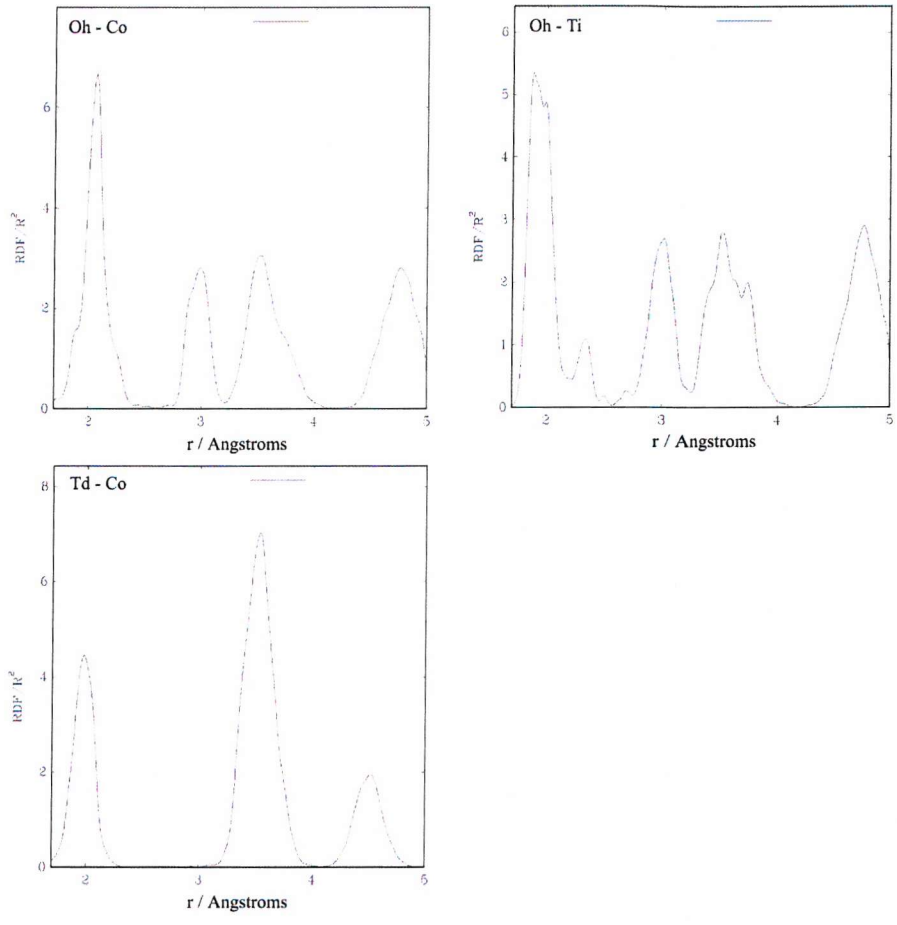

Figure 5-11: RDF diagrams for octahedral Co-O (top left), octahedral Ti-O (top right) and tetrahedral Co-O distances obtained from the RMC simulation for Co_2TiO_4.

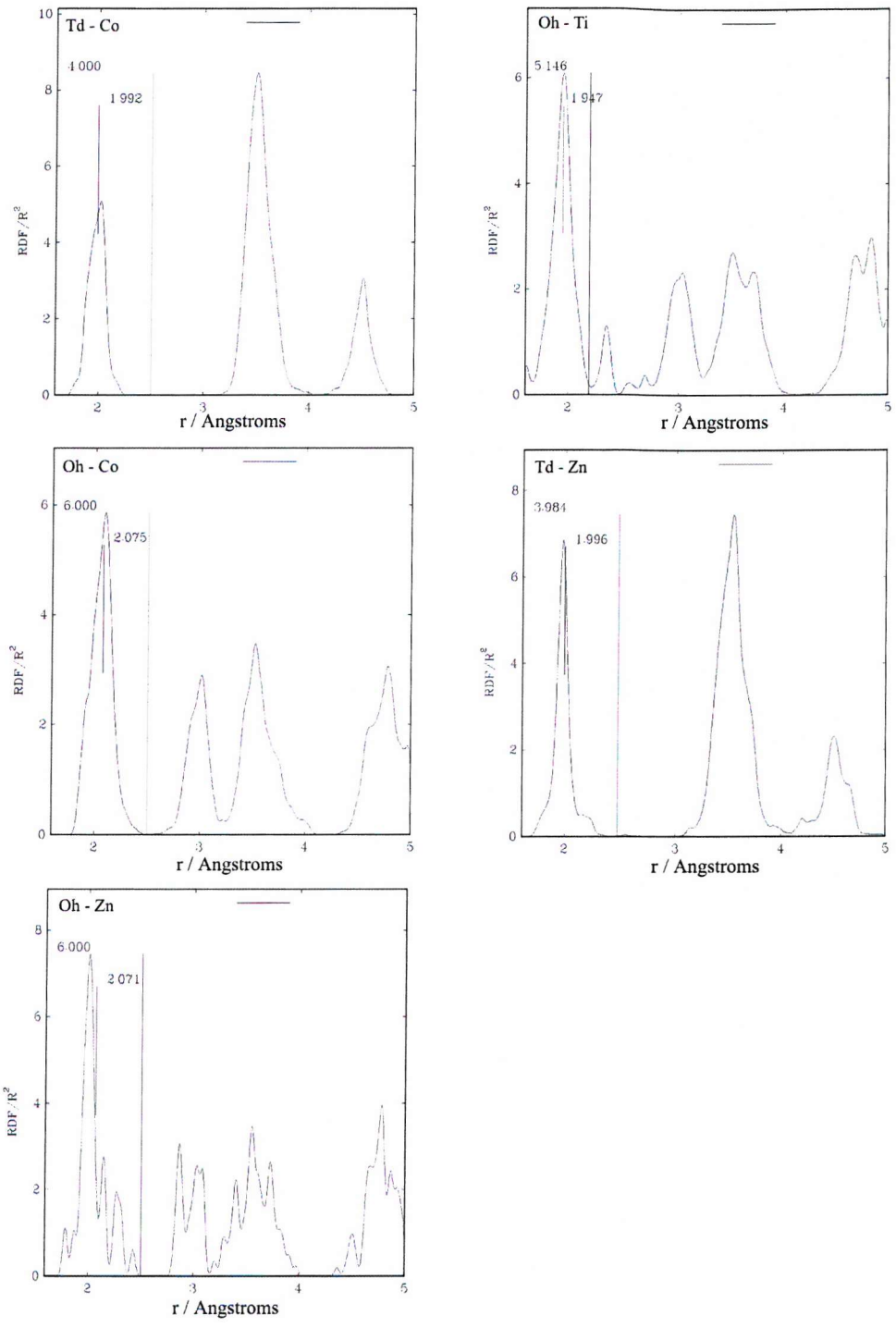

Figure 5-12: RDF diagrams for tetrahedral Co-O (top left), octahedral Ti-O (top right), octahedral Co-O (middle left), Tetrahedral Zn-O (middle right) and octahedral Zn-O (bottom) distances obtained from the RMC simulation for $Co_{0.8}Mg_{0.6}Zn_{0.6}TiO_4$.

For each phase the RDF diagram for octahedral titanium reveals a small secondary peak at *ca.* 2.3 Å. Integration of the peak areas indicates that the primary peak, at *ca.* 1.9 Å, is equivalent to approximately five oxygen atoms and that the secondary peak equates to approximately one oxygen atom. This suggests that titanium probably occupies a distorted

six-coordinate environment that has five shorter Ti-O distances and one long Ti-O distance. Titanium oxygen distances for each phase are shown in Table 5-25.

Table 5-25: Titanium – Oxygen distances (Å) derived from RDF calculations.

Distance	Co_2TiO_4	$CoZnTiO_4$	$Co_{0.8}Mg_{0.6}Zn_{0.6}TiO_4$
'Short' Ti-O (x5)	1.950	1.936	1.947
Long Ti-O (x1)	2.330	2.353	2.332

5.1.9.5 Discussion

The titanium coordination environment in each of the materials considered appears to be a distorted '5+1' arrangement where by one of the Ti-O distances is *ca.* 0.4 Å longer than the remaining five interactions. This contradicts previous data that suggested a regular octahedral arrangement of oxygen atoms around the titanium centre and indicates that titanate type spinel materials are described by a model that deviates from the accepted regular inverse-spinel structure.

The octahedral metal-oxygen distances obtained for cobalt and zinc are around 0.04 Å longer than those derived from PND refinements. It was not possible to derive Mg-O distances from the combined refinements due to the lack magnesium EXAFS data. The average titanium-oxygen distances are in agreement with those mentioned in section 5.1.6. However, the RMC combined refinements have yielded a more accurate model for the titanium coordination environment.

5.1.10 Conclusions

Twelve materials in the system $(Co,Mg,Zn)_2TiO_4$ have been prepared by conventional solid state synthesis and were characterised by the Rietveld refinement of both PXD and PND data. Combined EXAFS/PND refinements and RMC simulations were performed to help solve the cation distribution for a quaternary system and to help model the local lattice distortions caused by octahedrally coordinated Ti^{4+}.

The observed colour of the materials is greatly affected by the substitution of the metal cations. It is possible to direct the Co^{2+} species onto the octahedral site of the spinel structure by the addition of Zn^{2+} cations, which show a high degree of preference for the tetrahedral site. The addition of Mg^{2+} to the system has the effect of diluting the presence of Co^{2+} on each of the metal sites, rather than being able to direct the Co^{2+} species. The addition of

either zinc or magnesium seems to have a detrimental effect upon the observed colour of the material, although it does provide some degree of colour 'tunability'.

Combined EXAFS/PND RMC simulations have yielded a new model for the titanium coordination environment present in these systems. Instead of occupying a regular octahedral site, Ti^{4+} adopts a '5+1' arrangement of oxygen atoms with one Ti-O distance being *ca.* 0.4 Å longer than the remaining five Ti-O distances.

The cation distribution for the quaternary system $Co_{0.8}Mg_{0.6}Zn_{0.6}TiO_4$ has been determined by the combined refinement of EXAFS and PND data using a Reverse Monte Carlo approach.

5.2 References

[1] Mimani T., Ghosh S.; *Curr. Science* **78** 892-896 (2000).

[2] Pacurariu C., Lazau I., Bescherescu D., Bobos I.; *Rev. Romaine de Chim.* **42** 447-454 (1997).

[3] Zayat M., Levy D.; *Chem. Mater.* **12** 2763-2769 (2000).

[4] Marco J.F., Gancedo J.R., Gracia M., Gautier J.L., Rios E, Berry FJ; *J. Solid. State Chem.* **153** 74-81 (2000).

[5] Garcia Casado P., Rasines I.; *J. Solid State Chem.* **52** 187-193 (1984).

[6] Kawai H., Tabuchi M., Nagata M., Tukamoto H., West AR; *J. Mater. Chem.* **8** 1273-1280 (1998).

[7] Hirota K., Inoue T., Mochida N., Ohtsuka A.; *J. Ceram. Soc. Jpn.* **98** 976-86 (1990).

[8] Eppler R.A.; *J. Am. Ceram. Soc.* **66** 794-801 (1983).

[9] Yan G.J., Cheng J.J., Zhang J.C., Chun S.L.; *J. Inorg. Mater.* **15** 660-664 (2000).

[10] De Strooper K., van Alboom A., Henriet-Iserentant C., Vanleerberghe R., Vandenberghe R.; *Phys. Stat. Sol.* **44** 215-220 (1977).

[11] Wei S-H, Zhang S.B.; *Phys. Rev. B* **63** 045112 (2001).

[12] Sawada H.; *Mater. Res. Bull.* **31** 355-360 (1996).

[13] Binsted N., Stange M., Owens C., Fjellvåg H., Weller M.T.; *J. Synchrotron Rad.* **8** 305-307 (2001).

[14] Larson A.C., Von Dreele R.B.; *General Structure Analysis System (GSAS).* Los Alamos National Laboratory Report LAUR, 86 (2000).

[15] Marin S.J., O'Keefe M., Partin D.E.; *J. Solid State Chem.* **113** 413-419 (1994).

[16] De Strooper K., Robbrect G.; Physica 86-88b 934 (1977)

[17] Shannon R.D.; *Acta Crystallogr.* **A32** 751-767 (1976).

[18] Binsted N.; PAXAS (Program for the Analysis of X-ray Absorption Spectra), University of Southampton, (1988)

[19] Müller-Buschbaum H.k., Freund H-R.; Zeit. Naturforsch. 29b 590-593 (1974)

[20] Müller-Buschbaum Hk., Waburg M.; Monat. Chemie 114 21-25 (1983)

[21] Morosin B., Lynch R.W.; Acta Crystallogr. B28 1040-1046 (1972)

[22] Kunz M., Armbruster T., Lager G.A., Schultz A.J., Goyette R.J., Lotermoser W., Amthauer G.; Phys. Chem. Miner. 18 199-213 (1991)

[23] Renner B., Lehmann G.; Zeit. fur Krystallogr. 175 43-59 (1986)

[24] McGreevy R.L.; *J. Phys. Condens. Matter* **13** R877 (2001).

[25] Mellergård A., McGreevy R.L., Eriksson SG; *J. Phys. Condens. Matter* **12** 4975 (2000).

[26] Wicks J.D., McGreevy R.L.; *J. Non-Cryst. Solids* **192** 23 (1995).

[27] McGreevy R.L.; *Nucl. Instr and Methods in Phys. Res.* **A354** 1 (1995)

[28] Zetterström P., McGreevy R.L.; *Physica B,* **276** 187 (2000)

[29] Swenson J., McGreevy R.L., Börjesson L., Wicks JD; *Solid State Ionics,* **105** 55 (1998).

[30] Winterer M., Delaphane R., McGreevy R.L.; *J. Appl. Cryst.,* **35** 434 (2002).

[31] Binsted N., Stange M., Fjellvåg H., Weller M.T.; *Yet to be published.*

Chapter 6

Cobalt Aluminate

6 Cobalt Aluminate

6.1 Introduction

Cobalt Blue is a readily available industrial pigment with applications ranging from coatings and ceramics to plastics and paints. The colour of this pigment, due to the $^4A_2(F) \rightarrow {}^4T_1(P)$ absorption for tetrahedrally co-ordinated cobalt, is well known to be at its most intense when there is a deficiency of cobalt such that the composition is close to '$Co_{0.7}Al_2O_4$' rather than the ideal spinel composition of $CoAl_2O_4$. However the reason for this phenomenon is little understood. It is therefore the aim of this study to provide an insight into this phenomenon and its effect upon the colour of the resulting pigment.

In this section the cation distribution throughout the $Co_{1-x}Al_2O_4$ series is considered as a function of x and a theory to explain the perceived darkening in colour as x decreases is presented.

6.2 $Co_{1-x}Al_2O_4$

6.2.1 Synthesis

The $Co_{1-x}Al_2O_4$ (x = 0, 0.1, 0.2, 0.3) series was prepared by heating stoichiometric mixtures of cobalt (II) oxide and aluminium (III) oxide (both >99% purity). The reagents were intimately mixed by grinding after which they where transferred to an alumina crucible and heated to 1100 °C for 15 hours. Grinding was performed under an inert atmosphere to prevent oxidation of the CoO reagent to Co_3O_4. The materials produced ranged from an intense royal blue colour (x = 0.3) to a dark blue/black colour (x = 0). Initial phase identification X-ray powder diffraction data revealed that the desired spinel type phase had been formed in each case.

The products were studied further using PND, EXAFS and UV-visible spectroscopy.

6.2.2 Powder Neutron Diffraction

Time of flight (TOF) powder neutron diffraction data were collected on the POLARIS diffractometer at the Rutherford Appleton Laboratory, Oxfordshire, UK. All data sets were collected at room temperature. Rietveld refinements were performed using the PC package, GSAS [1]. Literature [2] values were used as the initial model for $CoAl_2O_4$ (x = 0), subsequent refinements utilised the values obtained in the preceding refinement. A small Al_2O_3 impurity phase was identified in each sample; this was included in the refinements as

an additional phase. A uniform approach to the structure refinement was undertaken for each of the data sets obtained with different x values to ensure consistent results. Initially the background was modelled and the lattice parameters were refined to accurately locate the reflections. The peak profiles were then refined and the atomic positions varied. Finally, isotropic temperature factors and fractional site occupancies for the tetrahedral and octahedral metal sites were added to the refinement. Linear constraints were added to the refinement of the site occupancies to give the required stoichiometry. Three separate refinements were performed for each sample:

Refinement 1

The final stoichiometry of the sample was assumed to be that intended at the point of synthesis. However, to enable the tetrahedral and octahedral sites to be fully occupied whilst conserving the intended Co/Al ratio the compositions (x = 0.1, 0.2, 0.3) were slightly adjusted in each case:

$Co_{0.9}Al_2O_4$ becomes $Co_{0.93}Al_{2.07}O_4$

$Co_{0.8}Al_2O_4$ becomes $Co_{0.86}Al_{2.14}O_4$

$Co_{0.7}Al_2O_4$ becomes $Co_{0.78}Al_{2.22}O_4$

Refinement 2

The presence of aluminium (III) oxide as an impurity in each sample may indicate that the excess Al_2O_3 included in each synthesis is not incorporated into the final product. For this reason the final stoichiometry of each sample was assumed to be the ideal spinel composition – $CoAl_2O_4$.

Refinement 3

The fractional occupancies for each of the metal sites were constrained to sensible values by assuming that the fractional occupancy sum for each metal site was 1, whilst the cobalt and aluminium fractions were allowed to vary independently of each other.

The refinements proceeded smoothly to convergence giving a good fit to the observed data and chemically sensible bond distances and angles. The refinement profile for $Co_{0.8}Al_2O_4$ (refinement 2) and tables of crystallographic data and refinement statistics for each phase are presented in Figure 6-1 and Table 6-3, Table 6-1, Table 6-2.

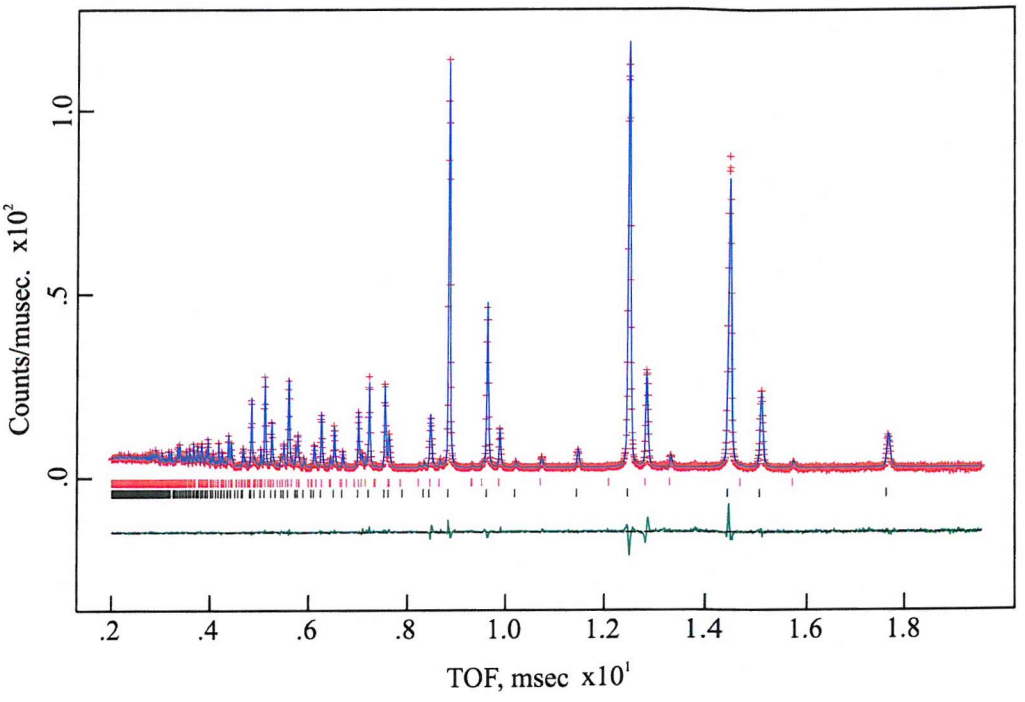

Figure 6-1: Observed (+++), Calculated (—), and difference (shown underneath) PND profiles for $Co_{0.8}Al_2O_4$. Tick marks indicate reflection positions – main phase (black) and Al_2O_3 impurity (red).

Table 6-1: Refinement 1 – Refined crystallographic data (PND) for the $Co_{1-x}Al_2O_4$ (x = 0, 0.1, 0.2, 0.3) series as a function of x). (e. s. d. s are shown in parentheses). Cation positions Td (1/8,1/8,1/8) and Oh (1/2,1/2,1/2).

Space group: *Fd*-3*m*

Parameter	$CoAl_2O_4$	$Co_{0.93}Al_{2.07}O_4$	$Co_{0.86}Al_{2.14}O_4$	$Co_{0.78}Al_{2.22}O_4$
Lattice Parameter (Å)	8.10239(3)	8.10354(3)	8.10251(3)	8.10215(2)
Tetrahedral Site				
U_{iso}*	0.41(2)	0.41(2)	0.41(2)	0.43(2)
Occupancy (Co/Al)	0.82(2) / 0.18(2)	0.88(2) / 0.12(2)	0.84(2) / 0.16(2)	0.86(2) / 0.14(2)
Octahedral Site				
U_{iso}*	0.41(1)	0.406(8)	0.361(8)	0.403(7)
Occupancy (Co/Al)	0.092(8) / 0.908(8)	0.025(7) / 0.975(7)	0.009(7) / 0.991(7)	0 / 1[#]
Oxygen Site				
x (= y= z)	0.26303(2)	0.26321(2)	0.26345(2)	0.26352(2)
U_{iso}*	0.746(6)	0.694(5)	0.613(4)	0.604(3)
R_{wp} (%)	2.72	2.34	2.54	1.97
R_p (%)	4.50	4.08	4.20	3.18
χ^2	3.345	2.472	3.239	4.849

* Isotropic temperature factors are quoted with units - $Å^2$x100. [#] Values fixed at 0 and 1 as Co(Oh) occupancy refines to a value less than zero.

Table 6-2: Refinement 2 – Refined crystallographic data (PND) for the $Co_{1-x}Al_2O_4$ (x = 0, 0.1, 0.2, 0.3) series as a function of x). (e. s. d. s are shown in parentheses). Cation positions Td (1/8,1/8,1/8) and Oh (1/2,1/2,1/2).

Space group: *Fd*-3*m*

Parameter	**0**[+]	**'0.1'**	**'0.2'**	**'0.3'**
Lattice Parameter (Å)	8.10239(3)	8.10354(3)	8.10251(3)	8.10215(2)
Tetrahedral Site				
U_{iso}*	0.41(2)	0.40(2)	0.39(2)	0.39(2)
Occupancy (Co/Al)	0.82(2) / 0.18(2)	0.91(2) / 0.09(2)	0.89(2) / 0.11(2)	0.94(2) / 0.06(2)
Octahedral Site				
U_{iso}*	0.41(1)	0.396(8)	0.340(8)	0.368(6)
Occupancy (Co/Al)	0.092(8) / 0.908(8)	0.047(7) / 0.953(7)	0.053(7) / 0.947(7)	0.029(6) / 0.971(6)
Oxygen Site				
x (= y= z)	0.26303(2)	0.26321(2)	0.26346(2)	0.26353(2)
U_{iso}*	0.746(6)	0.698(5)	0.619(4)	0.614(3)
R_{wp} (%)	2.72	2.34	2.53	1.95
R_p (%)	4.50	4.07	4.16	3.08
χ^2	3.345	2.471	3.225	4.753

* Isotropic temperature factors are quoted with units - $Å^2$x100. [+] Results are the same as for refinement 1.

Table 6-3: Refinement 3 – Refined crystallographic data (PND) for the $Co_{1-x}Al_2O_4$ (x = 0, 0.1, 0.2, 0.3) series as a function of x). (e. s. d. s are shown in parentheses). Cation positions Td (1/8,1/8,1/8) and Oh (1/2,1/2,1/2).

Space group: *Fd-3m*

Parameter	**0**	**0.1**	**0.2**	**0.3**
Lattice Parameter (Å)	8.10238(3)	8.10354(3)	8.10251(3)	8.10214(2)
Tetrahedral Site				
U_{iso}*	0.39(2)	0.40(2)	0.38(2)	0.38(2)
Occupancy (Co/Al)	0.86(2) / 0.14(2)	0.90(2) / 0.10(2)	0.89(2) / 0.11(2)	0.96(2) / 0.04(2)
Octahedral Site				
U_{iso}*	0.39(2)	0.398(9)	0.340(9)	0.362(8)
Occupancy (Co/Al)	0.13(2) / 0.87(2)	0.04(2) / 0.96(2)	0.05(2) / 0.95(2)	0.04(1) / 0.96(1)
Oxygen Site				
x (= y= z)	0.26304(2)	0.26321(2)	0.26345(2)	0.26354(2)
U_{iso}*	0.755(7)	0.698(5)	0.619(4)	0.616(3)
R_{wp} (%)	2.71	2.34	2.53	1.95
R_p (%)	4.50	4.07	4.16	3.07
χ^2	3.340	2.471	3.227	4.753

* Isotropic temperature factors are quoted with units - $Å^2x100$

6.2.2.1 Al_2O_3 Impurity phase

Aluminium (III) oxide was identified as an impurity phase in each of the samples. Phase fractions are presented in Table 6-4. No cobalt containing impurities were identified therefore it is assumed that the final composition in each case differs from that intended. For this reason the stoichiometric compositions observed for refinement 2 are assumed to be a better representation of the material in each case. This assumption is further supported by the impurity phase fractions (Table 6-4), which increase as the cobalt content is decreased. This suggests that the 'excess' Al_2O_3 present in each synthesis is not incorporated into a sub-

stoichiometric compound. Instead, it is observed as an impurity phase for a stoichiometric material. Calculated phase fractions, assuming a main phase of $CoAl_2O_4$, are also shown in Table 6-4. The calculated values seem to differ somewhat from the refined values, which may imply that the situation in each case is not as clear-cut as 'stoichiometric composition + impurity' or 'defined sub-stoichiometric composition + no impurity'.

Table 6-4: Phase fraction values (refinement 1) derived from PND refinements for the $Co_{1-x}Al_2O_4$ (x = 0, 0.1, 0.2, 0.3) system.

x	*Phase Fraction*	
	Al_2O_3	*Calculated**
0	0.18142	0
0.1	0.19206	0.1111
0.2	0.25927	0.2500
0.3	0.34113	0.4286

*The calculated phase fractions give the number of moles of Al_2O_3 per mole of $CoAl_2O_4$ in the obtained sample.

6.2.2.2 Interatomic Distances and Angles

The metal-oxygen distances and bond angles, derived from the Rietveld refinements (refinement 2), are shown in Table 6-5. The distances shown for the octahedral ($M(1)O_6$) and tetrahedral ($M(2)O_4$) sites are averages of the metal-oxygen bond lengths within the structure as the sites contain both cobalt and aluminium ions. One would expect the values therefore, to lie between the bond lengths for non-mixed CoO_x and AlO_x polyhedra.

Table 6-5: Derived bond distances (Å) and angles (°), as a function of x, for the $Co_{1-x}Al_2O_4$ series. (e. s. d. s are shown in parentheses). M(1) = Octahedral site, M(2) = Tetrahedral site.

Distance / Angle	*0*	*0.1*	*0.2*	*0.3*
M(1)_O (x 6)	1.92583(11)	1.92479(9)	1.92280(10)	1.92215(8)
M(2)_O (x 4)	1.93705(21)	1.93989(18)	1.94307(19)	1.94408(15)
O_M(1)_O (x 6)	83.552(8)	83.455(7)	83.324(7)	83.283(6)
O_M(1)_O (x 3)	180	180	180	180
O_M(1)_O (x 6)	96.448(8)	96.545(7)	96.676(7)	96.717(3)
O_M(2)_O (x 6)	109.471	109.471	109.471	109.471

It can be seen from the observed data that there is consistent variation of the tetrahedral and octahedral bond lengths and angles (octahedral only) as the initial Co/Al ratio is varied.

The octahedral bond length (M(1)_O) displays a steady decrease in size as x is increased (Figure 6-2), whilst the tetrahedral metal oxygen distance (M(2)_O) shows a gradual increase in size (Figure 6-3). These variations can be explained by considering the fractional occupancies of each site and the relative sizes of each cation present (Table 6-6).

Table 6-6: Effective ionic radii values (Å) [3] for the $Co_{1-x}Al_2O_4$ system.

Metal Cation	*Coordination Number*	
	4	*6*
Co^{2+}	0.58	0.745
Al^{3+}	0.39	0.535

As x is increased the amount of cobalt on the octahedral site is decreased, therefore the average metal-oxygen distance also decreases as a result of the increased occupancy by the smaller cation. Conversely the amount of cobalt seen to occupy the tetrahedral site increases as x increases. As the cobalt cation has a greater effective ionic radius than Al^{3+} the average bond length for the site is increased.

An almost linear variation of the octahedral bond angles is also observed as the initial composition of the sample is changed (Figure 6-4).

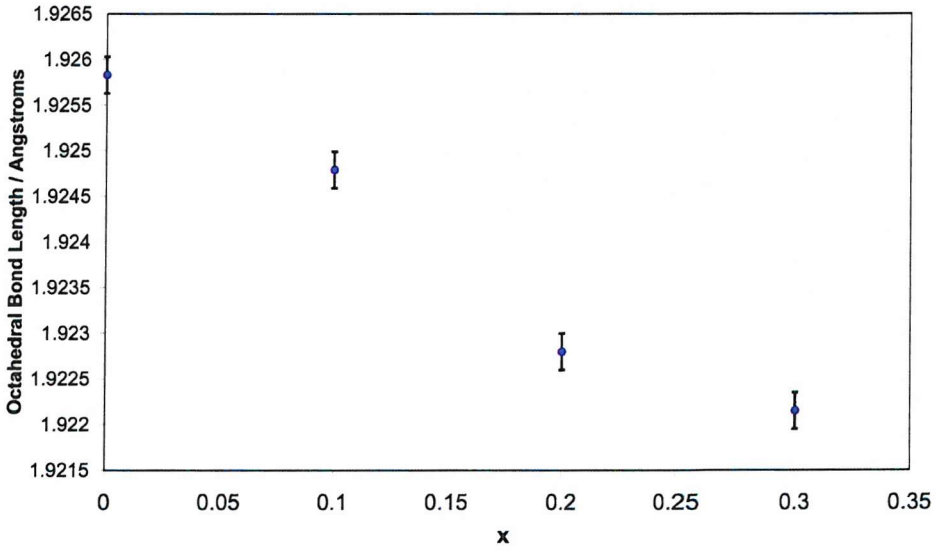

Figure 6-2: Variation of the octahedral metal-oxygen distance (M(1)_O) (where M = Co, Al) as a function of x for the $Co_{1-x}Al_2O_4$ system.

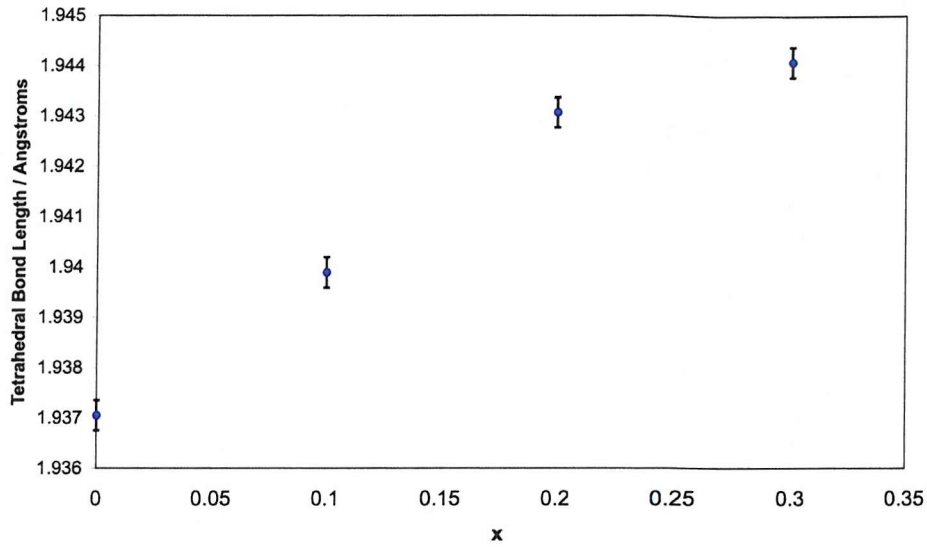

Figure 6-3: Variation of the tetrahedral metal-oxygen distance (M(2)_O) (where M = Co, Al) as a function of x for the $Co_{1-x}Al_2O_4$ system.

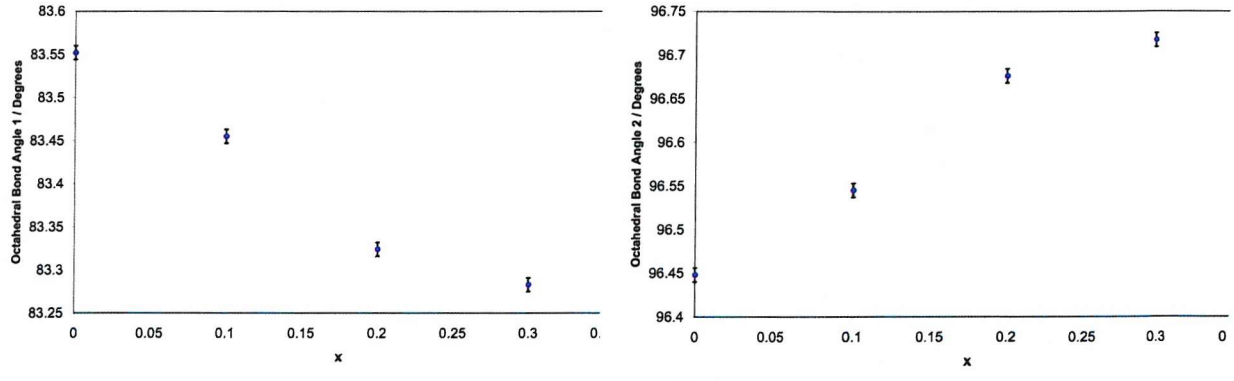

Figure 6-4: Variation of the octahedral bond angles (O_M(1)_O) (where M = Co, Al) as a function of x for the $Co_{1-x}Al_2O_4$ system.

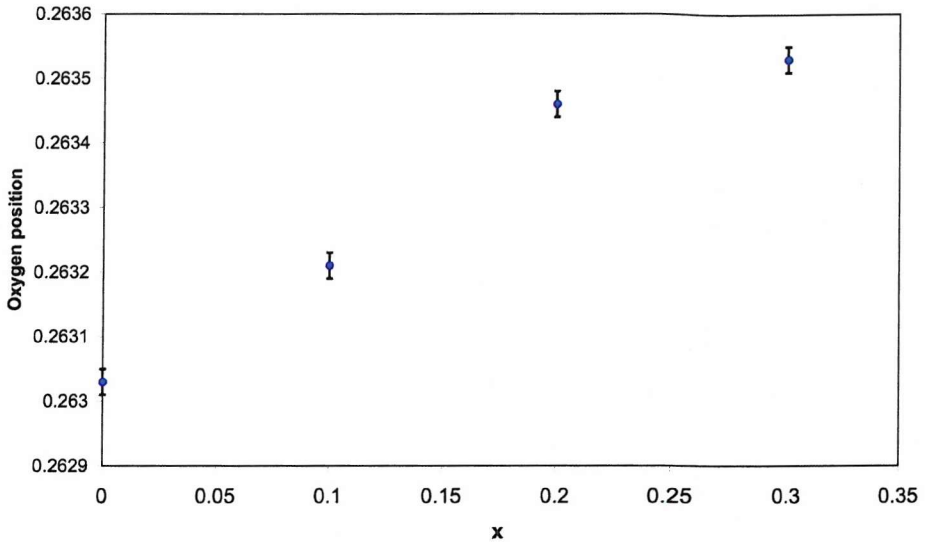

Figure 6-5: Variation of the oxygen position (x, x, x) as a function of x for the $Co_{1-x}Al_2O_4$ system.

6.2.2.3 Fractional Occupancies

Refinement 1

The cobalt and aluminium occupancies for the tetrahedral site remain approximately constant across the series. However, the refined fractional occupancies for the octahedral site show that the cobalt presence on the site is much reduced as the overall cobalt content is reduced. Indeed for x = 0.3, the value for cobalt occupancy on the octahedral site refines to a value below zero, indicating that all of the cobalt in this sample is situated on the tetrahedral site.

Refinement 2

The cobalt fractional occupancy of the tetrahedral site shows an overall increase (0.82(2) to 0.94(2)) as x is increased, which is in agreement with the bond distances mentioned previously. The octahedral site, as expected given the tetrahedral values, has a decreased cobalt fractional occupancy as x is increased; again this is in agreement with the previously mentioned bond distances. For the sample where x = 0.3 a small fraction of octahedrally coordinated cobalt is detected (0.029(6)). This contradicts the results of refinement 1, which suggested that cobalt does not occupy the octahedral site of that sample.

Refinement 3

This refinement was performed to help clarify the validity of refinements 1 and 2. When allowed to refine freely the occupancies tend toward the values obtained in refinement 2, which suggests that those occupancies are probably more correct than those obtained in the first refinement. However, the refined stoichiometry (Table 6-7) obtained for each sample

fails to identify any pattern, although in each case the values are closer to the ideal spinel composition than to the intended sub-stoichiometric composition.

Table 6-7: Refined stoichiometries (refinement 3) for compounds in the $Co_{1-x}Al_2O_4$ (x = 0, 0.1, 0.2, 0.3) series.

Sample (x =)	*Composition*
0	$Co_{1.12(4)}Al_{1.88(4)}O_4$
0.1	$Co_{0.98(4)}Al_{2.02(4)}O_4$
0.2	$Co_{0.99(4)}Al_{2.01(4)}O_4$
0.3	$Co_{1.04(3)}Al_{1.96(3)}O_4$

6.2.2.4 Bond Valence Calculations

Bond valence data was used to help identify the oxidation state of cobalt on the octahedral site. The presence of Co^{3+} would lead to charge transfer transitions between the octahedral and tetrahedral sites, which would lead to some darkening of the colour. This occurs in cobalt (II, III) oxide (Co_3O_4), which has a spinel structure and is black in colour. Calculations were performed using PND data and the mathematical method described by Altermatt and Brown [4, 5]. Results for sample x = 0 are presented in Table 6-8.

Table 6-8: Bond valence data for $CoAl_2O_4$ (refinement 2). Site 1 = Octahedral, Site 2 = Tetrahedral.

Atom	*Assumed Oxidation State*	*Bond Valence Sum*	% Deviation from Assumed Ox. State
Co(1)	2	3.186	59
Co(1)	3	3.258	9
Al(1)	3	2.622	13
Co(2)	2	2.064	3
Al(2)	3	1.7	43

Charge-balance calculations demand that most of the octahedrally coordinated cobalt is divalent. However, the bond valence sum seems to favour the presence of Co^{3+} on the octahedral site. Small amounts of trivalent cobalt on the octahedral site could lead to one of a

number of possible situations in terms of charge balancing. Two possible situations are mentioned below.

Example 1

The final composition of the sample may be slightly sub-stoichiometric such that the composition would be $[Co^{2+}_{1-1.5y}Al^{3+}_{y}]^{tet}[Al^{3+}_{2-y}Co^{3+}_{y}]^{oct}O_4$, where y describes the amount of trivalent cobalt occupying the octahedral site. This expression assumes that all of the cobalt occupying the octahedral site is trivalent. It also assumes that Co^{2+} is lost from the tetrahedral site to allow for charge balancing. Thus the final composition would be slightly sub-stoichiometric – $Co_{1-0.5y}Al_2O_4$ – but would remain charge balanced.

Example 2

The final stoichiometry of the sample may become cobalt rich due to the substitution of Al^{3+} by Co^{3+} on the octahedral site such that the composition would be $Co^{2+}Al^{3+}_{2-y}Co^{3+}_{y}O_4$. Again this composition assumes that only trivalent cobalt will replace aluminium ions on the octahedral site to conserve charge balancing. However, in this case it is assumed that the tetrahedral site is occupied by cobalt only. This process would also contribute to the observed Al_2O_3 impurity phase. Thus the final composition would be $Co_{1+y}Al_{2-y}O_4$.

These results and suggestions are considered later after further characterisation of the materials has taken place.

6.2.3 UV-Visible Spectroscopy

UV visible data were collected on undiluted samples for the $Co_{1-x}Al_2O_4$ system (x = 0, 0.1, 0.2, 0.3), according to the method outlined in Chapter 2. These are shown in Figure 6-6.

A broad, intense absorption band in the region 500 – 700 nm dominates the spectra, which is characteristic of tetrahedrally coordinated cobalt and leads to samples that are blue in colour. As described in Chapter 2, the spin allowed d-d transitions of Co^{2+} in tetrahedral coordination are [6]:

$$\nu_1: \ {}^4A_2(F) \rightarrow {}^4T_2(F)$$
$$\nu_2: \ {}^4A_2(F) \rightarrow {}^4T_1(F)$$
$$\nu_3: \ {}^4A_2(F) \rightarrow {}^4T_1(P)$$

The ν_3 transition is responsible for the observed colour of these materials [7, 8]. The ν_1 and ν_2 transitions occur in the infrared region and therefore do not contribute to the colour of each sample.

Throughout the series there appears to be no shift of the absorption band (500-700 nm), although for x = 0 the absorption is broader than for the other samples. As there is no shift it can be assumed that the position of the d-d transitions is unaffected as the cobalt content changes and that the observed darkening of the colour is not caused by a change in coordination geometry.

The intensity of the broad absorption observed between 300-400 nm increases as the initial cobalt content increases. Zayat et al. [9] observed a similar situation for $Co_{3-s}Al_sO_4$ and noted that the absorption is probably due to octahedrally coordinated Co^{3+} ions. They also mention that it may be due to the presence of Co_3O_4 in cobalt rich samples. However, the presence of Co_3O_4 as a second phase would be easily detected using PND data and is not thought to be the case here. The absorption is probably caused by mixed-valence charge transfer transitions occurring due to the presence of both Co^{2+} and Co^{3+} in the sample.

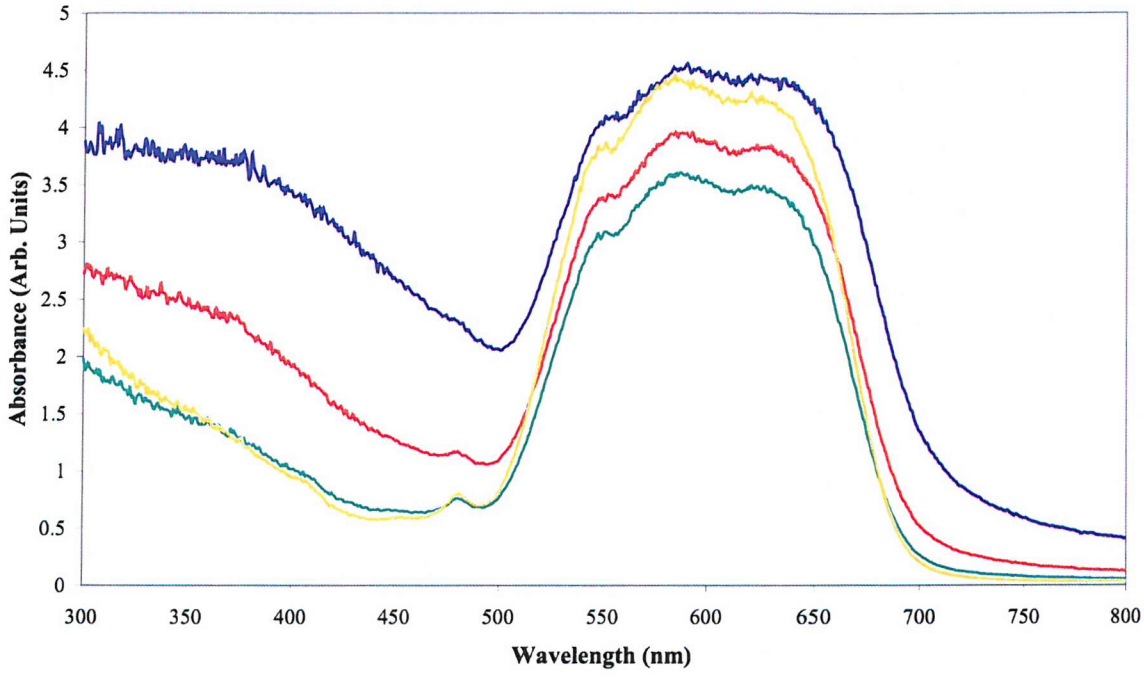

Figure 6-6: Diffuse reflectance spectra of the $Co_{1-x}Al_2O_4$ system transformed according to the Kubelka-Munk function. (0-blue, 0.1-red, 0.2-green, 0.3-yellow)

6.2.4 EXAFS and Combined Refinements

Due to the complexity of these systems in terms of the distribution of cations across the tetrahedral and octahedral sites, combined EXAFS/HRPXD refinements were performed to help confirm the PND results. Refinements were performed for the $Co_{1-x}Al_2O_4$ system (x = 0, 0.1, 0.2, 0.3) using 'P' the combined refinement program (see Chapter 2).

A further reason for using the combined refinement is that it can give specific data regarding a particular element in a given site. PND alone, provides bond lengths and angles that are averaged for a mixed site across the structure as a whole, rather than element specific data regarding coordination environments. In each case N. Binsted performed the combined refinement with the assistance of the author.

6.2.4.1 Data Collection

Room temperature cobalt K-edge EXAFS were collected on station 8.1 at the SRS Daresbury Laboratory in transmission mode as described in Chapter 2. Up to six scans were collected in each case and the data averaged to improve the signal to noise ratio. Background subtraction of the EXAFS data was performed using PAXAS [10]. High-resolution PXD data were collected on station 9.1 at x-ray wavelength 0.4858Å using a curved image-plate camera system at room temperature.

6.2.4.2 $Co_{1-x}Al_2O_4$

An initial model was taken from the PND refinement performed earlier in this Chapter. Both the background-subtracted EXAFS and the PXD data were entered into the program and the scattering phase shifts calculated using a common value of the interstitial potential for all atoms. Both combined (EXAFS + PXD) and PXD-only refinements were performed; the combined refinement used equal weightings for the spectra with $W_{EXAFS} = W_{PXD} = 0.5$, while PXD-only refinements used $W_{EXAFS} = 0$ and $W_{PND} = 1.0$. A cluster radius of 6 Angstroms was used to calculate the EXAFS spectra. Contributions were identified to 12 Å. As with all regular solids, multiple scattering effects are important beyond the first shell of atoms, and paths involving 2 different scattering atoms were always included.

6.2.4.3 Results

Simultaneous fits to the cobalt K-edge EXAFS and PXD data are shown in Figure 6-7 for the composition '$Co_{0.7}Al_2O_4$' and selected refinement data for all phases are presented in Table 6-9.

The fractional occupancies are in agreement with those obtained from the refinement of PND data. The combined refinements indicate that cobalt has a greater fractional occupancy of the octahedral site as the overall cobalt content is increased. Therefore, as x increases the degree of octahedral cobalt decreases. It is reasonable to assume that this observed change will have some bearing upon the colour of the final material. The metal oxygen distances (BL values, Table 6-9) also agree, within calculated errors, with those derived from the PND refinements. Again the observed trends are that the tetrahedral site shows an overall increase in the length

of the M-O bond, whilst the octahedral site appears to become more compact with increasing x. The contraction of the octahedral distance is consistent with the reduced presence of cobalt on that site, as mentioned in section 6.2.2.2. In a similar fashion to the values obtained from the PND refinements, the Al_2O_3 phase fraction is reduced as the ideal spinel composition is approached, i.e. as x approaches zero.

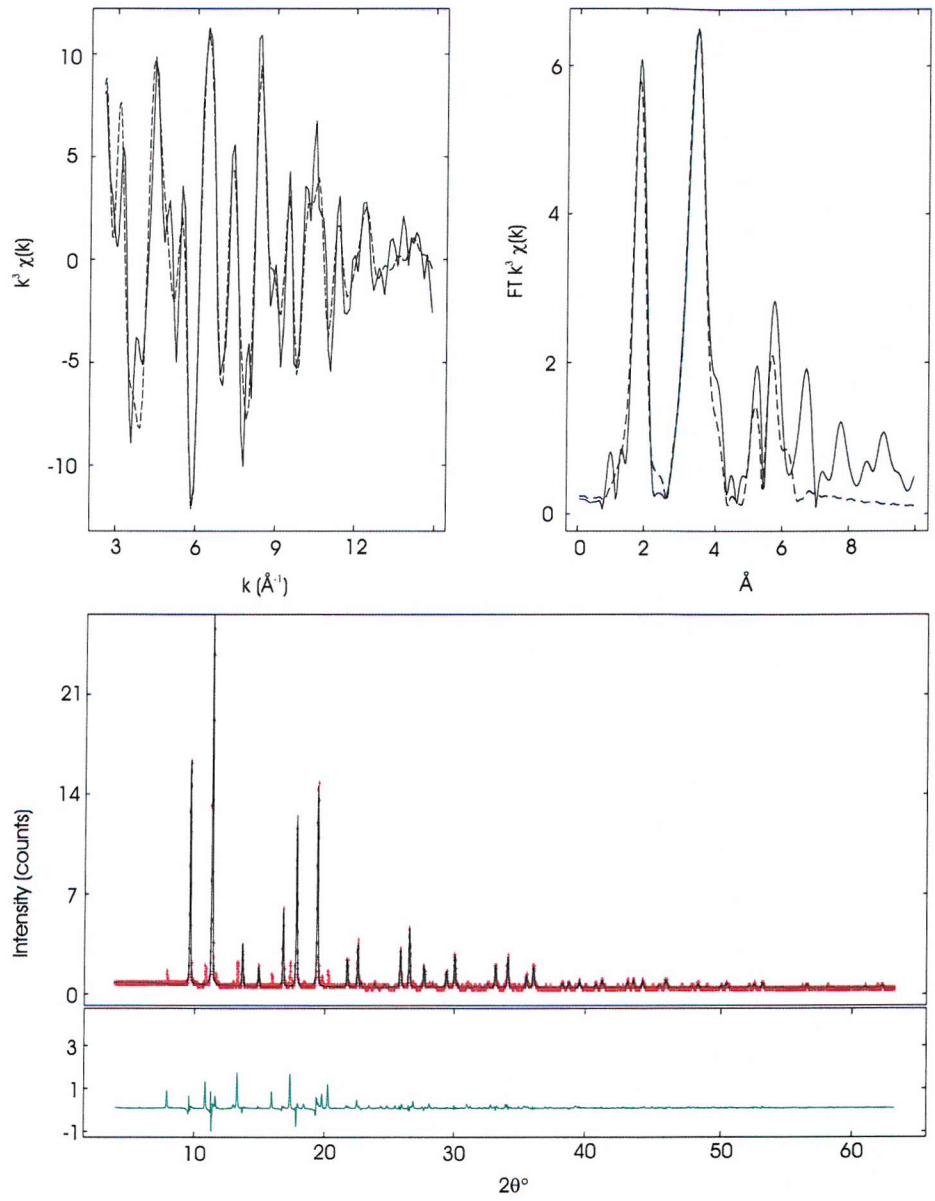

Figure 6-7: Fits to cobalt K-edge EXAFS (top) and HR PXD data (bottom) for $Co_{0.7}Al_2O_4$.

Table 6-9: Refined data derived from combined EXAFS/HR PXD refinements for $Co_{1-x}Al_2O_4$ (x = 0, 0.1, 0.2, 0.3).

Parameter	*0*	*0.1*	*0.2*	*0.3*
Cell*	8.1060(4)	8.1058(2)	8.1051(6)	8.0989(6)
O, *x*	0.2653(2)	0.2654(2)	0.2652(2)	0.2650(2)
Frac Co (Td)	0.84(1)	0.81(1)	0.84(1)	0.85(1)
Frac Al (Td)	0.16(1)	0.19(1)	0.16(1)	0.15(1)
Frac Co (Oh)	0.15(1)	0.10(1)	0.07(1)	0.06(1)
Frac Al (Oh)	0.85(1)	0.90(1)	0.93(1)	0.94(1)
PF_{Al2O3}	0.21(2)	0.15(2)	0.23(2)	0.33(2)
BL_{Td}*	1.970[5]	1.971[3]	1.968[3]	1.965[3]
BL_{Oh}*	1.911[10]	1.910[11]	1.911[15]	1.913[17]
R_{EXAFS}	31.5942	34.5426	35.3659	34.1216
R_{PXD}	5.7157	5.1409	4.8565	4.4310

* Cell parameter and Bond Length (BL) values are quoted in Angstroms

Derived errors [ ] and refined errors ( ) are given by $2\sigma^2$.

6.2.5 Discussion

Both PND and combined EXAFS/PXD refinements show a steady increase of octahedrally coordinated cobalt as the overall cobalt content is increased. An overall increase in the size of the unit cell also observed. Both the refined fractional occupancies (PND and EXAFS/PXD) and the bond lengths (PND) indicate the presence of cobalt on the octahedral site.

Octahedrally coordinated Co^{2+} gives rise to reddish-pink, weakly coloured compounds (eg. Co_2GeO_4) and would, therefore, not explain the darkening in colour. However, bond-valence calculations favour the presence of Co^{3+} on the octahedral site (as in Co_3O_4), which would allow for charge-transfer (mixed-valence) with the tetrahedral site and would lead to discolouration of the pigment. This is evident in the UV-Vis data, where the broad absorption between 300-400 nm increases as the amount of octahedrally coordinated cobalt increases.

The final stoichiometry of each sample must differ from that intended due to the presence of aluminium (III) oxide in each case. However, the actually stoichiometry of each sample is difficult to predict given that both Co^{2+} and Co^{3+} are present in varying amounts. Both the PND and the EXAFS/PXD combined refinements tend towards an ideal spinel composition,

although the UV-Vis data and BV calculations, which suggest that Co^{3+} occupies the octahedral site, favour a sub-stoichiometric composition similar to that presented in section 6.2.2.4 - $[Co^{2+}_{1-1.5y}Al^{3+}_{y}]^{tet}[Al^{3+}_{2-y}Co^{3+}_{y}]^{oct}O_4$.

6.2.6 Conclusions

The preparation of the $Co_{1-x}Al_2O_4$ (x = 0, 0.1, 0.2, 0.3) series from CoO and Al_2O_3 using conventional solid-state synthesis at 1100 °C results in the formation of sub-stoichiometric compounds with scrambling of the cations over the tetrahedral and octahedral sites.

The observed darkening of colour occurs due to the occupation of octahedral sites in the spinel lattice by Co^{3+}, which leads to mixed-valence charge transfer between Co^{2+} on the tetrahedral sites and Co^{3+} on the octahedral sites.

Al_2O_3 is present in all samples as an impurity confirming that the composition of the products formed is different to that intended and that the sample formed is more cobalt-rich in each case.

6.3 References

[1] Larson A.C., Von Dreele R.B.; *General Structure Analysis System (GSAS).* Los Alamos National Laboratory Report LAUR, 86 (2000).

[2] Toriumi K., Ozima M., Akaogi M., Saito Y.; Acta Cryst. B34 1093-1096 (1978).

[3] Shannon R.D.; *Acta Crystallogr.* **A32** 751-767 (1976).

[4] Altermatt D., Brown I.D.; *Acta Cryst.* **B41**, 240-244, (1985).

[5] Altermatt D., Brown I.D.; *Acta Cryst.* **B41**, 244-247, (1985).

[6] Carlin R.L.; Electronic structure and stereochemistry of cobalt (II), *Transition Metal Chemistry*, **1** 1-33 (1965)

[7] Mimani T., Ghosh S.; *Current Science,* **78** 7 892-896 (2000)

[8] Corma F., Lambies V.; *Rev. Chim. Miner.*, **17** 110-117 (1980)

[9] Zayat M., Levy D.; *Chem. Mater.* **12** 2763-2769 (2000).

[10] Binsted N.; PAXAS (Program for the Analysis of X-ray Absorption Spectra), University of Southampton, (1988)

Chapter 7

Other Possible Pigment Systems

7 Other Possible Pigment Systems

7.1 Introduction

In addition to those systems studied and presented in the previous chapters, a number of other materials underwent preliminary studies in an attempt to identify other possible pigment systems. In some cases the intention was to further the available literature data, but in most cases the study was purely investigatory and yielded little or no improvement upon already known systems. They are presented here simply to highlight the vast and diverse nature of mixed-metal oxide pigments and the study of such materials.

7.2 Preparation of the inverse spinel series $(Fe, Zn)_2TiO_4$

The properties of the inverse spinels Fe_2TiO_4 and Zn_2TiO_4 have been studied in detail previously [1, 2, 3, 4]. It has been reported [5] that the solid solution Fe_2TiO_4-Zn_2TiO_4 produces colours ranging from bright oranges and yellows to dark browns and brick-reds. The intention of this study was to investigate the cation distribution and its affect upon the observed colour of the material produced

7.2.1 Synthesis

A series of compounds in the system $Fe_{2-x}Zn_xTiO_4$ (where x = 0, 0.2, 0.4, 0.6, 0.8, 1.0, 1.2, 1.4, 1.6, 1.8 and 2.0) were prepared by grinding together stoichiometric mixtures of ZnO, FeO, and TiO_2 (all >99 % purity). The mixtures were transferred to alumina crucibles and heated to 1100°C for 18hrs in air.

7.2.2 Structural Characterisation

Powder X-ray diffraction (PXD) data were collected for all samples and revealed that the desired inverse spinel phase was formed in all samples, except those with high iron content (where x = 0, 0.2 and 0.4), which appeared to adopt the pseudobrookite structure of Fe_2TiO_5 [6].

The colours obtained from this synthesis ranged from white for x = 2, through various shades of sandy brown to black for the compound containing no zinc. Further, attempts were made to obtain the reported colours by varying the synthesis time and temperature. A brighter orange colour was obtained for $FeZnTiO_4$, when the firing time was reduced to 3hrs, possibly due to less oxidation of the Fe (II).

Whilst this system is very structurally interesting, the colours obtained were not of the required shade or intensity to be employed as replacement pigments for the intense red and yellow cadmium pigments.

7.3 Lithium Spinels

7.3.1 Introduction

The crystal chemistry of binary spinel oxides, of general formula $M^{2+}M^{3+}{}_2O_4$ and $M^{4+}M^{2+}{}_2O_4$, has been studied in great detail [5, 7, 8, 9]. Ternary spinel oxides, in contrast, are less well understood, examples include materials of type $Li_2MM'_3O_8$ (where M = Mg, Co, Ni, Zn and M' = Ti, Ge).

This system of materials was prepared with the aim of studying the cation distribution through the series and its effect upon the colour.

7.3.2 Synthesis

Three materials in the series $Li_2MTi_3O_8$ were successfully prepared, where M = Co, Zn or $Co_{0.5}Zn_{0.25}Ni_{0.25}$. The third composition being that of an existing pigment system.

In each case, the reagents (Li_2CO_3, CoO, $2NiCO_3.3Ni(OH)_2.4H_2O$, ZnO, TiO_2 – all >99% purity) were intimately mixed by grinding under acetone in an agate pestle and mortar, transferred to an alumina crucible and fired, first of all, in air at 650°C for 3 hours then at 800°C for 12 hours. The resultant mixed was then reground, pelletised and fired in air at 900°C for 3 days.

Attempts to prepare the nickel analogue of this material were unsuccessful, which is in agreement with literature data [10].

7.3.3 Powder X-ray Diffraction

PXD data for $Li_2CoTi_3O_8$, $Li_2ZnTi_3O_8$ and $Li_2Co_{0.5}Zn_{0.25}Ni_{0.25}Ti_3O_8$ were recorded on a Siemens D5000 diffractometer using Cu $K\alpha_1$ radiation (λ = 1.5406 Å) over the two-theta range 10° – 110° for 15 hours. Rietveld refinements were performed using the PC package, GSAS [11] as described in chapter 2. Literature [10] values were used as the initial models for $Li_2CoTi_3O_8$, $Li_2ZnTi_3O_8$. The refinement of data for $Li_2Co_{0.5}Zn_{0.25}Ni_{0.25}Ti_3O_8$ utilised the values obtained from the $Li_2CoTi_3O_8$ refinement as a starting point. The fractional site occupancies for the tetrahedral and octahedral sites of $Li_2Co_{0.5}Zn_{0.25}Ni_{0.25}Ti_3O_8$ were fixed at values based upon the intended composition in each case and the site preferences displayed by the cations in $Li_2CoTi_3O_8$ and $Li_2ZnTi_3O_8$. It was not possible to refine these site occupancies due to the complexity of the cation distribution. The refinements proceeded

smoothly to convergence giving a good fit to the observed data and chemically sensible bond distances and angles in each case.

The PXD refinement profiles for $Li_2ZnTi_3O_8$ are shown in Figure 7-1. Tables of cyrstallographic data and refinement statistics for each phase are presented in Table 7-1, Table 7-2 and Table 7-3.

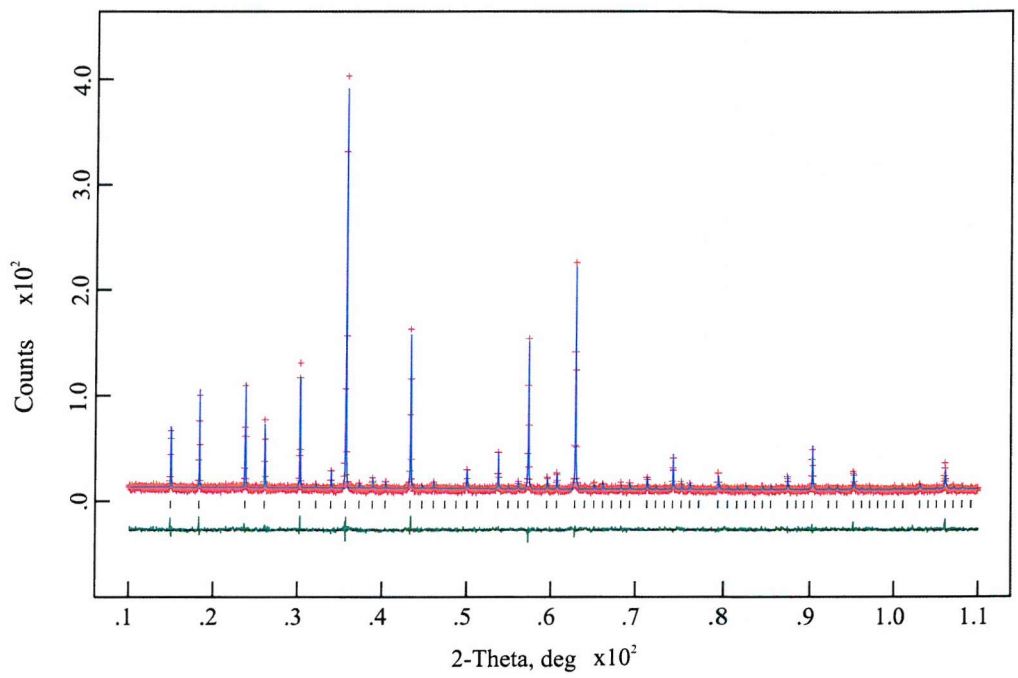

Figure 7-1: Observed (+++), Calculated (—), and difference (shown underneath) PXD profiles for $Li_2ZnTi_3O_8$. Tick marks indicate reflection positions.

Table 7-1: Refined crystallographic data (PXD) for $Li_2CoTi_3O_8$ (e. s. d. s are shown in parentheses).

Space group: $P4_332$

Lattice parameters a = 8.3927(9) Å

Atom	*x*	*y*	*z*	*Frac.*	U_{iso} /Å^{2}x*100*
Li(1)	-0.005(2)	-0.005(2)	-0.005(2)	0.506(7)	1.3(3)*
Co(1)	-0.005(2)	-0.005(2)	-0.005(2)	0.494(7)	1.3(3)*
Li(2)	0.625	0.625	0.625	0.98(2)	1.3(3)*
Co(2)	0.625	0.625	0.625	0.02(2)	1.3(3)*
Ti	0.125	0.369(2)	0.880(2)	1	2.9(3)
O	0.384(4)	0.384(4)	0.384(4)	1	2.9(2)
O	0.103(3)	0.123(3)	0.391(3)	1	1.0(5)

Final fit parameters:$\chi^2 = 0.1371$, $R_{wp} = 5.84$ %, $R_p = 4.45$ %

* Temperature factors for the mixed metal sites were constrained to the same value as site 2 refines to an reasonable value when varied separately.

Table 7-2: Refined crystallographic data (PXD) for $Li_2ZnTi_3O_8$ (e. s. d. s are shown in parentheses).

Space group: $P4_332$

Lattice parameters a = 8.34645(4) Å

Atom	*x*	*y*	*z*	*Frac.*	U_{iso} /Å^{2}x*100*
Li(1)	-0.0012(4)	-0.0012(4)	-0.0012(4)	0.504(3)	1.4(1)
Zn(1)	-0.0012(4)	-0.0012(4)	-0.0012(4)	0.496(3)	1.4(1)
Li(2)	0.625	0.625	0.625	0.992(5)	2(2)
Zn(2)	0.625	0.625	0.625	0.008(5)	2(2)
Ti	0.125	0.3672(3)	0.8828(3)	1	1.68(8)
O	0.390(1)	0.390(1)	0.390(1)	1	0.8(4)
O	0.108(1)	0.1285(7)	0.3900(7)	1	1.8(2)

Final fit parameters:$\chi^2 = 0.1216$, $R_{wp} = 9.42$ %, $R_p = 7.36$ %

Table 7-3: Refined crystallographic data (PXD) for $Li_2(Co_{0.5}Ni_{0.25}Zn_{0.25})Ti_3O_8$ (e. s. d. s are shown in parentheses).

Space group: $P4_332$

Lattice parameters a = 8.34762(6) Å

Atom	*x*	*y*	*z*	*Frac.*	U_{iso} /Å^{2}x100
Li(1)	-0.002(2)	-0.002(2)	-0.002(2)	0.625*	1.5(2)
Co(1)	-0.002(2)	-0.002(2)	-0.002(2)	0.250*	1.5(2)
Zn(1)	-0.002(2)	-0.002(2)	-0.002(2)	0.125*	1.5(2)
Li(2)	0.625	0.625	0.625	0.700*	2.9(8)
Ni(2)	0.625	0.625	0.625	0.250*	2.9(8)
Ti	0.125	0.3697(8)	0.8803(8)	1	1.8(2)
O	0.388(3)	0.388(3)	0.388(3)	1	1.7(9)
O	0.107(3)	0.129(2)	0.31(2)	1	1.6(4)

Final fit parameters: $\chi^2 = 0.1084$, $R_{wp} = 6.09$ %, $R_p = 4.77$ %

* Fractional occupancies for the two mixed metal sites were fixed at values according to the values obtained for the ternary compounds and those reported by Kawai *et al* [10] for $Li_2NiGe_3O_8$.

7.3.3.1 Interatomic Distances and Angles

The metal-oxygen distances and bond angles, derived from the Rietveld refinements, are shown in Table 7-4 and Table 7-5. The distances shown for the shared tetrahedral (M(1)) and octahedral (M(2)) sites are averages of the metal-oxygen bond lengths within the structure as the sites contain up to three different metal ions.

Table 7-4: Derived bond distances (Å) for $Li_2MTi_3O_8$ (M = Co, Zn, Ni). (e. s. d. s are shown in parentheses).

Distance	$Li_2CoTi_3O_8$	$Li_2ZnTi_3O_8$	$Li_2(Co_{0.5}Ni_{0.25}Zn_{0.25})Ti_3O_8$
M(1)_O1	1.88(5)	2.01(2)	1.96(4)
M(1)_O2 (x 3)	2.04(2)	1.951(7)	1.97(2)
M(2)_O2 (x 6)	2.10(3)	2.124(6)	2.13(2)
Ti_O1 (x 2)	2.06(3)	2.032(8)	2.03(2)
Ti_O2 (x 2)	1.88(2)	1.894(9)	1.90(2)
Ti_O2 (x 2)	1.98(2)	1.974(6)	1.96(2)

Table 7-5: Derived bond angles (°) for for $Li_2MTi_3O_8$ (M = Co, Zn, Ni). (e. s. d. s are shown in parentheses).

Angle	$Li_2CoTi_3O_8$	$Li_2ZnTi_3O_8$	$Li_2(Co_{0.5}Ni_{0.25}Zn_{0.25})Ti_3O_8$
O1_M(1)_O2 (x3)	110.7(7)	108.2(3)	108.4(6)
O1_M(1)_O2 (x3)	108.2(7)	110.7(3)	110.5(6)
O2_M(2)_O2 (x6)	80.9(9)	82.7(3)	82.0(7)
O2_M(2)_O2 (x3)	97.9(9)	97.0(3)	97.6(7)
O2_M(2)_O2 (x3)	100(2)	97.6(5)	98.3(9)
O2_M(2)_O2 (x3)	178.1(9)	179.527(3)	179.517(7)
O1_Ti_O1	92(2)	93.6(5)	94(2)
O1_Ti_O2	175.1(7)	174.0(2)	174.6(5)
O1_Ti_O2 (x2)	91.3(9)	90.9(3)	90.9(7)
O1_Ti_O2 (x2)	83.4(9)	82.6(3)	82.9(5)
O1_Ti_O2 (x2)	81.1(7)	80.7(3)	81.4(4)
O1_Ti_O2	175.1(7)	174.0(2)	174.6(5)
O2_Ti_O2 (x2)	90(2)	93.0(4)	92.6(9)
O2_Ti_O2	101(1)	101.6(4)	101.0(8)
O2_Ti_O2 (x2)	96.8(9)	94.7(3)	94.5(6)
O2_Ti_O2	169(2)	167.8(4)	168.8(9)

7.3.3.2 Fractional Occupancies

The refinement of fractional site occupancies for the tetrahedral (8c) and octahedral (4b) sites reveals that both cobalt and nickel show preference for the tetrahedral site. This appears to agree well with the observed trends seen in chapter 5 for the mixed spinel systems. These values also agree well with those reported by Kawai *et al* [10]. Due to the complexity of the expected cation distribution for $Li_2(Co_{0.5}Ni_{0.25}Zn_{0.25})Ti_3O_8$ these values could not be refined and were fixed at values which assume that nickel occupies only the octahedral site whilst both cobalt and nickel lie 100% on the tetrahedral site. It is also assumed for each material, that titanium is not involved in any cation scrambling and that it occupies the octahedral 12d site only.

For each material, the temperature factor for the octahedral 4b site refines to a relatively large value. This can be attributed to the poor sensitivity of X-ray diffraction when trying to accurately locate atoms with low atomic numbers; the octahedral site (4b) is occupied to a large extent by lithium – atomic number 3.

A more detailed analysis of the cation distribution for $Li_2(Co_{0.5}Ni_{0.25}Zn_{0.25})Ti_3O_8$ could be performed by using the combined EXAFS/PND (RMC) method described in chapter 5.

7.3.4 Discussion

The data presented here is in agreement with that reported in the literature and although the preparation of $Li_2(Co_{0.5}Ni_{0.25}Zn_{0.25})Ti_3O_8$ is a novel one, further data is required to fully understand the cation distribution.

7.4 $(Mg, Cu)_3(PO_4)_2$ and $(Zn, Cu)_3(PO_4)_2$ Solid Solutions

The incorporation of Cu^{2+} into distorted co-ordination environments gives rise to blue/green coloured compounds. The two systems to be studied here have previously been studied [12, 13] but the extent of the solid solution was limited possibly due to the relatively low reaction temperatures employed (800 °C). The intention here was to extend the limit of the solid solution by employing elevated reaction temperaturs and varying the reaction conditions in general.

7.4.1 $Mg_{3-x}Cu_x(PO_4)_2$

Four samples were prepared corresponding to x = 0, 1, 2 and 3.

7.4.1.1 Synthesis

A stoichiometric mixture of the metal acetate hydrates ($Cu(CH_3CO_2)_2.H_2O$, $Mg(CH_3CO_2)_2.4H_2O$) was dissolved in the minimum amount of distilled water. $(NH_4)_2HPO_4$

was also dissolved in the minimum amount of distilled water in a separate beaker. The two solutions were then mixed to produce a precipitate. The excess water was removed by evaporation and the resultant mixtures were heated to 1000 °C for 60 hours in air. The two copper rich samples (x = 2, 3) melted at 1000 °C, which is contrary to the synthesis performed by Moquine *et al* [13]. These samples were subsequently prepared at 950 °C for 48 hours. Colours of the materials obtained ranged from white (x = 0) to a pale green colour (x = 3). The poor colour intensity associated with these materials precludes them from use as inorganic pigments.

7.4.1.2 Powder X-ray Diffraction

PXD data revealed that the desired phase has been formed in each case. However, the sample $MgCu_2(PO_4)_2$ is biphasic; containing one phase which is isotypic with $Mg_3(PO_4)_2$ and one that is isotypic with $Cu_3(PO_4)_2$. This indicates that a complete solid solution has not been formed and is in agreement with the results observed by Moquines *et al* [13].

7.4.2 $Zn_{3-x}Cu_x(PO_4)_2$

Four samples were prepared corresponding to x = 0, 1, 2 and 3.

7.4.2.1 Synthesis

Stoichiometric amounts of $Zn(CH_3CO_2)_2.2H_2O$ and $Cu(CH_3CO_2)_2.H_2O$ were dissolved in the minimum amount of distilled water. $(NH_4)_2HPO_4$ was also dissolved in the minimum amount of distilled water in a separate beaker. The two solutions were then mixed causing precipitation. The excess water was evaporated gradually and the resultant mixture was heated to 950 °C for 48 hours.

Table 7-6: Colours obtained from the $(Zn, Cu)_3(PO_4)_2$ system

Composition	*Colour*
$Zn_3(PO_4)_2$	White
$Zn_2Cu(PO_4)_2$	Pale green
$ZnCu_2(PO_4)_2$	Sky blue
$Cu_3(PO_4)_2$	Turquoise

7.4.2.2 Powder X-ray Diffraction

PXD data for $Zn_3(PO_4)_2$ revealed the formation of 2 phases: α - $Zn_3(PO_4)_2$ and β - $Zn_3(PO_4)_2$, with the β phase being a high temperature metastable phase [14]. The transition from α to β occurs at 942°C.

The data obtained for $Cu_3(PO_4)_2$ revealed that the desired product had been formed.

The patterns obtained for $ZnCu_2(PO_4)_2$ and $Zn_2Cu(PO_4)_2$ do not appear to correspond to either of the end member compounds. These phases could not be identified.

7.5 Ca-Cu-Te-O Phase diagram

7.5.1 M_2CuTeO_6 (where M = Ca, Sr, Ba)

A calcium analogue of this system has not been reported in the literature. Therefore the intention here was to prepare the calcium analogue and to study its structural and optical properties. Although the barium and strontium analogue have similar crystal structures it is likely that the size of the calcium cation will lead to the formation of a completely different structure type.

7.5.1.1 Synthesis

The methods used to prepare the calcium and strontium analogues were based upon that used by Maria J. Pack, Southampton University, in the preparation of similar materials. The barium analogue was not prepared.

A stoichiometric mixture of the reactants (CuO, SrO, CaO and TeO_2 all >99% purity) were intimately mixed by grinding before being transferred to an alumina crucible and heated to 600 °C, under oxygen, for 15 hours. The resultant mixture was then placed in a silica tube that was subsequently evacuated and sealed before being heated to 1000 °C for 48 hours.

The strontium analogue was olive green in colour, whilst the calcium analogue had an intense dark green colouration.

7.5.2 Powder X-ray Diffraction

PXD data revealed that the desired phase had been formed for the strontium analogue. However, the pattern observed for Ca_2CuTeO_6 could not be identified by comparison with the JCPDS database. It is possible that the material is a mixture of compounds, although no single phases could be identified.

Attempts to identify this phase through the preparation of a phase diagram were unsuccessful, largely due to the complexity of the observed PXD patterns and the presence of impurity phases in each sample. The stoichiometry of the materials produced is listed in Table 7-7. In each case the materials were prepared using the method described above as well as by conventional solid-state synthesis.

Table 7-7: A list of compositions prepared during the attempted preparation of a Ca-Cu-Te-O phase diagram.

Composition	*Composition*
Ca_3TeO_6	$CuCaO_3$
Ca_2CuTeO_6	Ca_2CuO_3
$CaCu_2TeO_6$	$CaCuO_2$
$Ca_{2.5}Cu_{0.5}TeO_6$	$Ca_5Cu_3Te_2O_{14}$
$Ca_{1.5}Cu_{1.5}TeO_6$	Ca_3CuTeO_7
$Ca_{0.5}Cu_{2.5}TeO_6$	$Ca_5Cu_4TeO_{12}$
Cu_3TeO_6	

7.6 $M_3(VO_4)_2$ (M = Cu or Zn)

These materials, which contain VO_4 tetrahedral units, were prepared with the intention of ultimately replacing the VO_4^{3-} complex ion with the intensely coloured MnO_4^{3-} unit (chapter 3).

7.6.1 Synthesis

Stoichiometric mixtures of the reagents (ZnO, V_2O_5, CuO – all >99 % purity) were intimately mixed by grinding under acetone. The resultant mixtures were transferred to alumina crucibles and heated to 800 °C for 36 hours. A dark red/brown coloured material was obtained for the copper analogue and the zinc compound had a pale yellow colouration. PXD data recorded on a Siemens D5000 diffractometer using Cu $K\alpha_1$ radiation (λ = 1.5406 Å), revealed a single-phase product had been produced in each case.

7.6.2 Cation Substitution

The colour of the copper-containing material was assumed to be too intensely coloured to allow any blue/green colour – produced by the MnO_4^{3-} - to be seen. Therefore no attempt perform the substitution for $Cu_3(VO_4)_2$ was made.

The zinc analogue has a pale yellow colouration, therefore the incorporation of MnO_4^{3-} could be easily identified by the production of a green/blue coloured material. The preparation of $Zn_3(V_{0.98}Mn_{0.02}O_4)_2$ was attempted to test the feasibility of the idea. This resulted in the production of a yellow/brown coloured material, which had the same structure type as $Zn_3(VO_4)_2$. The colour produced is an indication that manganese (V) is not the

manganese species present. Further attempts to prepare Mn^{5+} containing samples, utilised oxygen atmospheres and higher temperatures; none were successful.

The reason manganese (V) could not be stabilised in these structures is probably due to the relatively low basicity of the copper and zinc ions; a feature that seems to be a requirement for the stabilisation of the MnO_4^{3-} complex ion.

7.6.3 VO_4 Containing Materials

A number of other materials were identified as possible substrates for the incorporation of manganese (V), these are listed in Table 7-8 along with the relevant V-O distances.

Table 7-8: Materials containing VO_4^{3-} units. Bond distances are quoted in Angstroms.

Composition	V-O(1)	V-O(2)	V-O(3)	V-O(4)	Reference.
$LiVO_3$	1.662	1.628	1.764	1.848	15
LiV_3O_8	1.592	1.781	1.884	1.884	16
	1.647	1.705	1.879	1.879	
Li_3VO_4	1.714	1.720	1.720	1.721	17
$BiVO_4$	1.703	1.703	1.703	1.703	18
$BiCaVO_5$	1.693	1.700	1.704	1.744	19
$BiCa_4V_3O_{13}$	1.672	1.703	1.706	1.723	20
$BiCa_2VO_6$	1.697	1.707	1.722	1.722	21
$NaCdVO_4$	1.554	1.554	1.567	1.567	22
$Cd_4Na(VO_4)_3$	1.653	1.712	1.730	1.765	23
	1.686	1.686	1.737	1.760	24
$Cd_{3.23}Na_{1.41}V_{0.36}(VO_4)_3$	1.702	1.712	1.721	1.735	25
	1.715	1.715	1.718	1.718	
$Zn_3(VO_4)_2$	1.736	1.749	1.749	1.797	26
$Zn_2V_2O_7$	1.658	1.704	1.727	1.775	27
α-$Zn_2V_2O_7$	1.658	1.704	1.728	1.775	28
$Zn_4V_2O_9$	1.683	1.716	1.728	1.740	29
	1.680	1.717	1.735	1.740	
	1.646	1.740	1.755	1.756	
	1.670	1.701	1.740	1.835	
$Cu_2V_2O_7$	1.650	1.711	1.737	1.745	30

β-$Cu_2V_2O_7$	1.644	1.694	1.741	1.770	28
$Cu_3(VO_4)$	1.643	1.741	1.783	1.743	31
	1.795	1.742	1.697	1.670	32
$Cu_5V_2O_{10}$	1.658	1.717	1.744	1.761	33
	1.650	1.725	1.742	1.778	
$Ba_3(VO_4)_2$	1.694	1.694	1.694	1.698	34
$FeVO_4$	1.653	1.653	1.791	1.791	35
$Fe_2V_4O_{13}$	1.647	1.652	1.766	1.780	36
	1.644	1.657	1.764	1.783	
	1.664	1.673	1.776	1.780	
	1.646	1.666	1.770	1.776	
$Sr_3(VO_4)_2$	1.695	1.717	1.717	1.717	37
$NaVO_3$	1.620	1.646	1.774	1.814	38
	1.631	1.653	1.801	1.805	39
$KSbV_2O_8$	1.750	1.591	1.756	1.756	40
	1.711	1.592	1.777	1.777	
$RbSbV_2O_8$	1.764	1.585	1.763	1.763	40
	1.710	1.596	1.775	1.775	
$TlSbV_2O_8$	1.741	1.598	1.760	1.756	40
	1.702	1.767	1.602	1.773	
$CsSbV_2O_8$	1.736	1.608	1.790	1.757	40
	1.773	1.696	1.598	1.760	
$Na_3Ca_2V_3O_{11}$	1.681	1.814	1.691	1.680	41
	1.838	1.669	1.692	1.686	
	1.723	1.731	1.712	1.697	
$NaCaVO_4$	1.690	1.690	1.734	1.734	42
$Sr_{10}(VO_4)_6F_2$	1.716	1.721	1.703	1.703	43
$Ca_2(VO_4)Cl$	1.711	1.711	1.703	1.703	44
$Sr_2(VO_4)Cl$	1.726	1.726	1.715	1.715	45
$Cs_2V_4O_{11}$	1.788	1.59	1.755	1.755	46

7.7 References

[1] MacChesney J.B., Muan A.; *Amer. Mineral.* **44** (5) 926-45 (1959)

[2] MacChesney J.B., Muan A.; *Amer. Mineral.* **46** (3) 572-82 (1961)

[3] Rossiter M.J., Clarke P.T.; *Nature*, **207** (4995) 402 (1965)

[4] Dulin F.H., Rase D.E.; *J. Am. Ceram. Soc.*, **43** (3) 125-31 (1960)

[5] Eppler R.A.; *J. Am Ceram. Soc.*, **66** (11) 794-801 (1983)

[6] Teller R.G. et al; *J. Solid State Chem.*, **88** 334-350 (1990)

[7] Garcia Casado P., Rasines I.; *J.Solid State Chem.*, **52** 187-193 (1984).

[8] Sawada H.; *Mats. Res. Bull.*, **31** 355-360 (1996).

[9] McClure D.S.; J. *Phys. Chem. Solids,* **3** 311 (1957).

[10] Kawai H., Tabuchi M., Nagata M., Tukamoto H., West AR; *J. Mater. Chem.,* **8**(5), 1273–1280 (1998).

[11] Larson A.C., Von Dreele R.B.; *General Structure Analysis System (GSAS).* Los Alamos National Laboratory Report LAUR, 86 (2000).

[12] Nord A.G., Stefanidis T.; *Mat. Res. Bull.* **16** 1121-1129 (1981)

[13] Moquine A., Boukhari A., Flandrois S.; *Mat. Res. Bull.* **22** 965-971 (1987)

[14] Nord A.G.; *Mat. Res. Bull.* **12** 563-568 (1977)

[15] Shannon R.D., Calvo C.. *Can. J. Chem.* **51** 265-273 (1973)

[16] Wadsley A.D.. *Acta Crystallogr.* **10** 261-267 (1957)

[17] Shannon R.D., Calvo C. *J. Solid State Chem.* **6** 538-549 (1973)

[18] Dreyer G., Tillmans E.. *Neues. Jahrbuch fuer Miner. Monat.* 151-154 (1981)

[19] Boje J., Mueller-Buschbaum H.k. *Zeit. fur. Anorg. Allge. Chem.* **619** 521-524 (1993)

[20] Huang J-F., Sleight A.W. *J. Solid State Chem.* **104** 52-58 (1993)

[21] Radosavljevic I., Evans J.S.O., Sleight A.W. *J. Solid State Chem.* **137** 143-147 (1998)

[22] le Flem G., Olazcuaga R. *Bull. Soc. Chim. France.* 2769-2780 (1968)

[23] Ben-Amara M., Vlasse M., Olazcuaga R., le Flem G. *Acta Crystallogr.* **B35** 50-52 (1979)

[24] Abrahams S.C., Marsh P., Ravez J. *Acta Crystallogr.* **C39** 680-683 (1983)

[25] El Ammari L., Azrour M., Depmeier W., Hesse K.F., Elouadi B. *Acta Crystallogr.* **C55** 1743-1746 (1999)

[26] Gopal R., Calvo C. *Can. J. Chem.* **49** 3056-3059 (1971)

[27] Gopal R., Calvo C. *Can. J. Chem.* **51** 1004-1009 (1973)

[28] Schindler M., Hawthorne F.C., *J. Solid State Chem.* **146** 271-276 (1999)

[29] Waburg M., Mueller-Buschbaum H.k. *Monat. fur Chem. Verwand. Teile Ander. Wissen.* **117** 131-138 (1986)

[30] Robinson P.D., Hughes J.M., Malinconico M.L. *Amer. Miner.* **72** 397-400 (1987)

[31] Coing-Boyat J., *Acta Crystallogr.* **B38** 1546-1548 (1982)

[32] Shannon R.D., Calvo C., *Can. J. Chem.* **50** 3944-3949 (1972)

[33] Shannon R.D., Calvo C. *Acta Crystallogr.* **B29** 1338-1345 (1973)

[34] Suesse P., Buerger M.J. *Zeit. fur Kristall.* **131** 161-174 (1970)

[35] Oka Y., Yao T., Yamamoto N., Ueda Y., Kawasaki S., Azuma M., Takano M. *J. Solid State Chem.* **123** 54-59 (1996)

[36] Wang X.D., Heier K.R., Stern C.L., Poeppelmeier K.R. *Inorg. Chem.* **37** 6921-6927 (1998)

[37] Carrillo-Cabrera W., von Schnering H.G. *Zeit. fur Kristall.* **205** 271-276 (1993)

[38] Ramani K., Shaikh A.M., Reddy B.S., Viswamitra M.A. *Ferroelectrics* **9** 49-56 (1975)

[39] Marumo F., Isobe M., Iwai S.I. *Acta Crystallogr.* **B30** 1628-1630 (1974)

[40] Nandini Devi R., Vidyasagar K. *J. Chem. Soc., Dalton Trans.,* 3013-3019 (1998)

[41] Murashova E.V., Velikodnyi YuA., Trunov V.K., *Russ. J. Inorg. Chem.* **33** 1621-1623 (1988)

[42] Ijdo D.J.W, *Acta Crystallogr.* **B38** 923-925 (1982)

[43] Corker D., Chai B.H.T, Nicholls J.F.H., Loutts G.B. *Acta Crystallogr.* **C51** 549 (1995)

[44] Banks E., Greenblatt M., Post B., *Inorg. Chem.* **9** 2259 (1970)

[45] Albrecht C., Cohen S., Mayer I., Reinen D., *J. Solid State Chem.* **107** 218-228 (1993)

[46] Oka Y., Saito F., Yao T., Yamamoto N., *J. Solid State Chem.* **134** 52-58 (1997)